

**Targeting Bid for mitoprotection -  
Bid crystallization, new mechanisms and inhibitory  
compounds**

Dissertation

zur

Erlangung des Doktorgrades  
der Naturwissenschaften  
(Dr. rer. nat.)

dem

Fachbereich Pharmazie  
der Philipps-Universität Marburg

vorgelegt von

**Sina Oppermann**

aus Haiger

Marburg/Lahn 2014

Erstgutachter: Prof. Dr. Carsten Culmsee

Zweitgutachter: Prof. Dr. Moritz Bünemann

Drittgutachter: Prof. Dr. Nikolaus Plesnila

Eingereicht am 25.04.2014

Tag der mündlichen Prüfung am 11.06.2014

Hochschulkennziffer: 1180

Meinen Eltern





## ERKLÄRUNG

Ich versichere, dass ich meine Dissertation

**„Targeting Bid for mitoprotection -**

**Bid crystallization, new mechanisms and inhibitory compounds “**

selbständig ohne unerlaubte Hilfe angefertigt und mich dabei keiner anderen als der von mir ausdrücklich bezeichneten Quellen bedient habe.

Die Dissertation wurde in der jetzigen oder einer ähnlichen Form noch bei keiner anderen Hochschule eingereicht und hat noch keinen sonstigen Prüfungszwecken gedient.

Marburg, den 25.04.2014

.....

(Sina Oppermann)



## Table of content

<b>1</b>	<b>Introduction</b>	<b>1</b>
1.1	Neuronal cell death mechanisms	1
1.1.1	Oxidative stress, mitochondria and the point of no return	4
1.2	Bcl-2 family proteins – regulators of life and death	5
1.2.1	The BH3-only protein Bid	7
1.2.2	Pharmacological Bid inhibition – a strategy for mitoprotection	11
1.3	Voltage-dependent anion channels (VDACs)	13
1.4	HT-22 cells – a model for and Bid-mediated cell death	15
1.5	Aims of the thesis	17
<b>2</b>	<b>Materials and methodes</b>	<b>19</b>
2.1	Chemicals and reagents	19
2.1.1	Transfection reagents	19
2.1.2	PCR-primer	21
2.1.3	Primary antibodies	22
2.1.4	Secondary antibodies	23
2.2	Supplies	23
2.2.1	Kits	23
2.2.2	Materials for recombinant proteins	24
2.2.3	Cell culture materials	25
2.3	Cell culture	26
2.3.1	Cell culture media and cultivation of HT-22 cells	26
2.3.2	Cell culture medium and cultivation of primary mouse embryonic cortical neurons	28
2.3.3	Induction and inhibition of cell death in HT-22 neurons	31
2.3.4	Induction of cell death in primary cortical neurons (PCN)	33
2.3.5	Transfection protocols	33
2.4	Cell viability assays	35

2.4.1	Analysis of cell morphology .....	35
2.4.2	MTT assay .....	35
2.4.3	Real-time measurements of cell impedance (xCELLigence).....	36
2.4.4	ATP- luminescence measurements.....	37
2.4.5	Measurements of oxygen consumption (Seahorse Bioscience).....	38
2.5	Flow cytometric measurements (FACS) .....	40
2.5.1	Analysis of apoptotic and necrotic cell death with Annexin-V-FITC staining ....	40
2.5.2	Analysis of lipid peroxidation with BODIPY.....	41
2.5.3	Analysis of mitochondrial membrane potential with TMRE .....	41
2.6	Immunocytochemistry .....	42
2.6.1	Visualization of mitochondria.....	42
2.6.2	Characterization of mitochondrial morphology.....	42
2.6.3	Immunocytochemistry of Bid and VDAC1 .....	43
2.7	Epifluorescence and confocal laser scanning microscopy (CLSM) .....	44
2.7.1	Epifluorescence microscopy.....	44
2.7.2	Confocal laser scanning microscopy .....	44
2.8	Protein analysis.....	45
2.8.1	Protein sample preparation from HT-22 cells .....	45
2.8.2	Protein sample preparation from cortex and hippocampal mice brain tissue ...	46
2.8.3	Determination of protein amount in cell lysates .....	47
2.8.4	Immunoprecipitation of Bid, VDAC1 and FLAG-VDAC1 .....	47
2.8.5	Gel electrophoresis and western blot .....	48
2.8.6	Dot blot analysis.....	52
2.8.7	Coomassie staining.....	52
2.8.8	Ponceau S staining .....	53
2.9	RNA analysis.....	53
2.9.1	RNA preparation and determination of RNA amount .....	53
2.9.2	One Step reverse transcriptase polymerase chain reaction (RT-PCR) .....	54
2.9.3	Agarose gel electrophoresis.....	56
2.10	Transient focal cerebral ischemia in mice.....	57

2.11	Concentration-response curves and EC50 values .....	57
2.12	Molecular docking .....	58
2.13	Statistical analysis .....	58
2.14	Molecular Biology .....	59
2.14.1	Recombinant proteins .....	59
2.14.2	Competent cells .....	59
2.14.3	Culture medium for bacteria .....	59
2.14.4	Cloning and site-directed mutagenesis of Bid constructs.....	60
2.14.5	Transformation of plasmids in Rosetta2 (DE3) .....	63
2.14.6	Inoculating a liquid bacterial culture.....	63
2.14.7	Long-term storage of plasmids via Cryo-stocks .....	64
2.14.8	Determination of optical density of bacteria (OD <sub>600</sub> ).....	64
2.14.9	Expression of recombinant proteins .....	64
2.14.10	Expression tests .....	65
2.15	Purification of recombinant proteins .....	66
2.15.1	Buffers for protein purification.....	66
2.15.2	Protein purification using the ÄKTA prime plus.....	69
2.15.3	Purification of recombinant His <sub>6</sub> -tagged proteins .....	70
2.15.4	Purification of recombinant GST-tagged proteins .....	74
2.16	Thrombin cleavage of His <sub>6</sub> - and GST-fusion proteins .....	77
2.17	Dialysis of recombinant proteins.....	78
2.18	Cut-off concentration of recombinant proteins .....	79
2.19	Cleavage of full length Bid with Caspase 8.....	79
2.20	Determination of protein concentration .....	80
2.20.1	Bradford assay .....	80
2.20.2	Nanodrop photometry.....	80
2.21	Acetone precipitation.....	81
2.22	Functional analysis of recombinant proteins.....	82
2.22.1	Models of membrane permeabilization .....	82
2.22.2	Analysis of protein-protein interactions.....	84

2.23	Crystallographic methods .....	87
2.23.1	Protein crystallization .....	87
2.23.2	Optimizing and reproducing crystallization .....	90
2.23.3	Scoring and interpretation of crystallization drop results.....	94
2.23.4	Differentiation between of protein and salt crystals.....	96
2.23.5	Mounting crystals and diffractometric measurements .....	98
2.23.6	Data collection and processing.....	98
<b>3</b>	<b>Results .....</b>	<b>99</b>
3.1	Targeting Bid for mitoprotection.....	99
3.1.1	Neuroprotective potency of BI-6c9 .....	99
3.1.2	tBid-induced cell death in HT-22 cells .....	100
3.1.3	Synthesis strategy for development of novel small Bid inhibitors.....	104
3.1.4	<i>N</i> -acyl derivatives of 4-phenoxyaniline as neuroprotective agents.....	106
3.1.5	<i>N</i> -phenyl substituted thiazolidindiones provide protection against tBid-mediated cell death pathways.....	117
3.1.6	<i>N</i> -aryl substituted pyrazolopyrimidinones promise a novel class of neuroprotectants .....	129
3.2	Expression, purification and crystallization of recombinant Bid constructs.....	132
3.2.1	Expression of recombinant full-length Bid and its active form tBid .....	132
3.2.2	Purification of full length Bid yields reasonable protein amounts .....	134
3.2.3	Crystallization of full-length Bid .....	138
3.2.4	Design of modified truncated Bid constructs promise successful crystallization.. .....	139
3.2.5	Effective expression of GST-tagged Bid constructs.....	142
3.2.6	Purification of the Bid construct pGEX $\Delta$ 12-Y47 (Bid 1).....	143
3.2.7	Crystallization screening of pGEX $\Delta$ 12-Y47 (Bid 1) .....	145
3.2.8	Optimization strategies of Bid 1 crystals .....	147
3.2.9	Data collection and processing.....	148

3.2.10	Purification and crystallization of pGEX $\Delta$ 12-D51 (Bid 2) and pGEX $\Delta$ 13-D51 (Bid 4) .....	150
3.2.11	Functional analysis of Bid constructs in HT-22 cells .....	154
3.3	Functional analysis of recombinant Bid and Bax – a model system for membrane permeabilization .....	156
3.3.1	Liposome channel activity demonstrates cBid- and Bax-mediated membrane permeabilization to be dependent on the presence of cardiolipin.....	156
3.4	Role of VDAC1 in Bid-mediated mitochondrial demise and cell death .....	162
3.4.1	Expression of VDAC1 and VDAC2 in HT-22 cells .....	162
3.4.2	The anion channel blocker DIDS provides neuroprotection in HT-22 cells.....	163
3.4.3	Direct and functional interaction between Bid/tBid and VDAC1 .....	175
3.4.4	Direct interaction of Bid and VDAC1 in cultured neurons.....	179
3.4.5	Direct interaction of Bid and VDAC1 during ischemic brain damage <i>in vivo</i> ...	181
3.4.6	Interaction of Bid and VDAC1 determines mitochondrial demise and cell death in HT-22 cells .....	182
3.5	VDAC2 plays a minor role in neuronal intrinsic cell death pathways .....	199
3.5.1	VDAC2 gene silencing provides only transient protective effects against glutamate-induced toxicity .....	199
3.5.2	Mitochondrial membrane potential is not affected by VDAC2 silencing .....	204
<b>4</b>	<b>Discussion .....</b>	<b>206</b>
4.1	Targeting Bid for protection against mitochondrial injury and neuronal cell death .	208
4.2	Bid protein crystallization – a pipeline for structural knowledge and structure-guided drug design .....	211
4.3	Mechanisms of Bid-mediated MOMP and mitochondrial impairments .....	216
4.3.1	Role of cardiolipin in cBid/Bax mediated pore formation – a model system of membrane permeabilization .....	217
4.4	The role of the voltage-dependent anion channel VDAC1 in Bid-mediated mitochondrial demise and cell death .....	220
4.4.1	Direct interaction of Bid and VDAC1 determines mitochondrial demise.....	222
4.5	Bid-mediated mitochondrial demise in neurons is independent on VDAC2.....	225

<b>5</b>	<b>Summary</b> .....	<b>228</b>
<b>6</b>	<b>Zusammenfassung</b> .....	<b>231</b>
<b>7</b>	<b>Abbreviations</b> .....	<b>233</b>
<b>8</b>	<b>Appendix</b> .....	<b>237</b>
<b>9</b>	<b>References</b> .....	<b>251</b>
<b>10</b>	<b>Index of Tables</b> .....	<b>270</b>
<b>11</b>	<b>Index of Figures</b> .....	<b>272</b>
<b>12</b>	<b>Publications</b> .....	<b>276</b>
	12.1.1 Original papers.....	276
	12.1.2 Poster presentations .....	276
	12.1.3 Oral presentations .....	278
<b>13</b>	<b>Grants</b> .....	<b>278</b>
<b>14</b>	<b>Acknowledgements</b> .....	<b>279</b>
<b>15</b>	<b>Curriculum vitae</b> .....	<b>281</b>



# 1 Introduction

## 1.1 Neuronal cell death mechanisms

Neuronal viability is maintained through a complex interactive network of signaling pathways and can be disturbed in response to multiple cellular stress factors and pathologies. Although neuronal death is required for the normal development of the central nervous system (CNS), as well as for the removal of dysfunctional cells in pathological conditions, excessive loss of neurons underlies the symptoms of many human neurological disorders, including acute brain injury as well as neurodegenerative diseases, such as Alzheimer's disease (AD), Parkinson's diseases (PD), Huntington's disease (HD) and amyotrophic lateral sclerosis (ALS)<sup>1, 2</sup>. Oxidative stress and perturbed calcium homeostasis are environmental factors of neuronal death that ultimately compromise mitochondrial function, energy metabolism and nuclear integrity<sup>2</sup>. Although extensive research has provided insights into several key factors and targets that play important roles in mediating neuronal injury, and recent advances have improved the management of the neurological diseases mentioned above, there is no effective treatment available so far that prevents neuronal death. Since current treatments are mostly symptomatic and achieve only mild to moderate effects in patients, it is indispensable to further explore the biological pathways of neuronal disorders and to validate novel therapeutic perspectives against the progressive loss of brain function in both acute and chronic brain injury<sup>3, 4</sup>.

Although it is well recognized that neurons die after acute brain damage and in neurodegenerative diseases, the mode of cell death is not always clear. Neuronal cell death has been commonly delineated into two distinct categories: apoptosis and necrosis. However, limitations of such nomenclature became apparent when apoptotic mechanisms were associated with necrotic cell death features, leading to an expanding number of additional neuronal cell death classifications based on morphological and biochemical considerations<sup>5</sup>. Therefore, neuronal cell death has also been described in terms of regulated necrosis or necroptosis and autophagy.

Necrosis is an acute and passive form of cell death associated with the loss of ATP, loss of ionic homeostasis, membrane disruption, and organelle and cell swelling. Thus, necrosis causes inflammation in the surrounding region due to the release of cellular contents into the environment<sup>6</sup>. As there is no defined biochemical pathway, necrosis is not termed as a programmed form of cell death in contrast to the recently identified forms of regulated necrosis or necroptosis that occur in a RIP1 and/or RIP3-dependent manner<sup>5, 7</sup>. However, both pathways are described in neurons and have been associated to several neurodegenerative diseases, indicating their relevance for further therapeutic interventions<sup>8</sup>

In contrast to necrosis, apoptosis is a highly conserved and uniform type of programmed cell death, characterized by nuclear condensation and DNA fragmentation as well as membrane blebbing and formation of apoptotic bodies<sup>12</sup>. Cells undergoing apoptosis secrete signals that initiate their phagocytic removal by macrophages or neighboring cells, thereby preventing cell lysis and inflammatory response<sup>1</sup>. Thus, apoptosis serves as an important physiological function in the replacement of senescent and excessive cells. In the nervous system, apoptosis is essential during development, removing unnecessary cells thereby controlling the formation of synapses and neuronal plasticity<sup>1, 13</sup>. In contrast to its physiological role, pathological pathways of apoptosis have been associated with the progressive neuronal loss during several neuronal disorders including AD and PD as well as with delayed cell death after acute brain damage caused by cerebral ischemia or traumatic brain injury (TBI)<sup>2, 14-16</sup>.

Apoptosis can result from the activation of two biochemical cascades, which are known as the extrinsic pathway and the intrinsic mitochondrial pathway (Figure 1). The extrinsic apoptotic pathway is initiated by the activation of specific cell surface receptors, specifically by the members of the tumor necrosis factor (TNF) family. Fas-ligand (FasL) activation of the Fas receptor leads to the association with the adaptor protein FADD (Fas-associated protein death domain) and the initiator caspases 8 or 10 to form a complex known as DISC (death-inducing signaling complex)<sup>17</sup>. The activation of downstream effector caspases (3, 6, or 7) triggers the proteolytical cleavage of many cellular substrates and the activation of nucleases like caspase-activated deoxyribonuclease (CAD), thereby mediating DNA cleavage and cell death<sup>5, 18</sup>. While extrinsic apoptosis can occur irrespective of any contribution by mitochondria, caspase-8 can also cleave and activate the pro-apoptotic protein Bid to its active truncated form tBid. tBid in turn causes changes in mitochondrial permeability, thereby initiating the cascade of intrinsic apoptosis<sup>5, 17</sup>.

In contrast, intrinsic apoptosis involves a cascade of molecular events occurring within the cells, independent of plasma membrane receptor stimulation. Various conditions trigger intrinsic cell death pathways, including accelerated oxidative stress, intracellular  $[Ca^{2+}]$  deregulation and DNA damage, but converge at mitochondria where the permeabilization of the mitochondrial outer membrane (MOMP) is considered as the 'point of no return' in the cell's commitment to die<sup>5, 19</sup>. Breakdown of the mitochondrial membrane potential ( $\Delta\psi_m$ ) is associated with impaired oxidative phosphorylation and diminished energy supplies, enhanced production of reactive oxygen species (ROS), and the release of mitochondrial proteins, such as cytochrome c, Omi/HtrA2, Smac/DIABLO, and apoptosis-inducing factor (AIF)<sup>5, 17, 20-24</sup>. Upon mitochondrial release, AIF rapidly translocates to the nucleus and induces chromatin condensation and large-scale DNA fragmentation, resulting in the final execution steps of caspase-independent intrinsic cell death<sup>25</sup>.

In contrast, intrinsic apoptotic pathways can also occur in a caspase-dependent manner as cytosolic cytochrome c might interact with the apoptosis protease-activating factor-1 (APAF-1) as well as with pro-caspase-9 to form the apoptosome. This results in the sequential activation of execution caspases 3, 6 and 7, which in turn induce the breakdown of the framework through degradation of several substrates, executing the final cell death process<sup>5, 18</sup>. Alternatively, caspase activation is mediated by the mitochondrial release of Omi/HtrA2 or Smac/DIABLO, which are capable of blocking the anti-apoptotic protein XIAP (x-chromosomal linked inhibitor of apoptosis) and other IAPs (inhibitors of apoptosis), thereby releasing caspase-3 from its physiological inhibitors<sup>17</sup>.

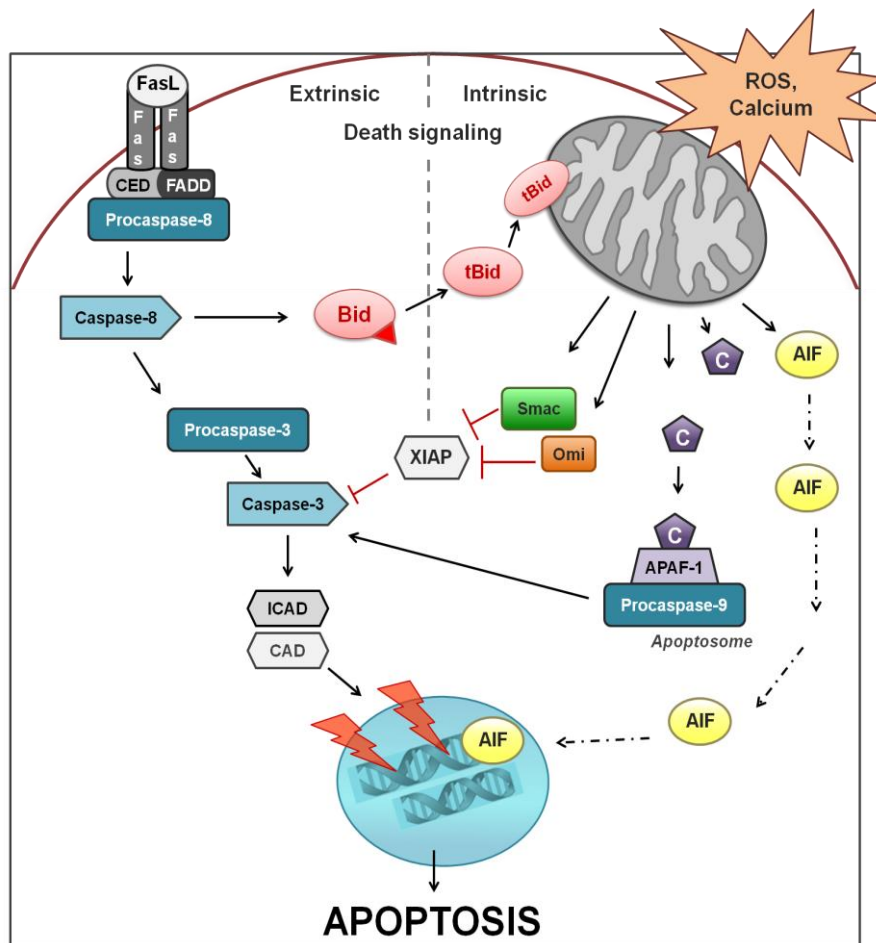


**Figure 1: Intrinsic and extrinsic pathways of apoptotic cells death.**

Apoptosis can result from the activation of two biochemical cascades, the extrinsic pathway and the intrinsic (mitochondrial) pathway. The extrinsic pathway is initiated at the plasma membrane: The death receptor Fas is activated by its ligand (FasL), which in turn leads to the association of the Fas associated death domain (FADD). Procaspase-8 is bound by the death effector domain (CED) and activated through FADD complex binding. Activation of caspase-8 triggers the cleavage and activation of downstream effector caspase-3, inducing the release of CAD (caspase-activated deoxyribonuclease) from its inhibitory ligand ICAD. This induces the CAD-mediated nuclear DNA fragmentation, accelerating cell death. The intrinsic mitochondrial pathway is triggered by intracellular stimuli such as  $\text{Ca}^{2+}$  overload and increased generation of reactive oxygen species (ROS). Caspase-8 mediated cleavage of the pro-apoptotic protein Bid into its active truncated form tBid links the extrinsic and intrinsic pathway. tBid translocation to the mitochondria induces the detrimental mitochondrial outer membrane permeabilization (MOMP), which marks the point of no return in the intrinsic cell death machinery. Permeabilization of MOM allows the mitochondrial release of death promoting proteins such as AIF,

Smac/DIABLO (Smac), Omi /HtrA2 and cytochrome c (C) in the cytosol. Smac/DIABLO or Omi/HtrA2 scavenge the inhibitors of apoptosis (IAPs) such as XIAP, thereby enhancing the activation of caspase-3. Further, cytosolic cytochrome c, APAF-1 and procaspase-9 interact to form the apoptosome that additionally drives the activation of caspase-3. Upon mitochondrial release, AIF translocates into the nucleus where it induces chromatin condensation and DNA fragmentation thereby resulting in caspase-independent cell death.

### 1.1.1 Oxidative stress, mitochondria and the point of no return

In humans, oxidative stress has been associated with a variety of pathologies, including chronic inflammatory processes, cancer, type II diabetes or arteriosclerosis, as well as ischemic injury, brain trauma and several neurodegenerative diseases<sup>26</sup>. Under physiological conditions, low levels of ROS are involved in signaling processes mediating cellular growth and adaptation responses<sup>27</sup>. However, the imbalance of excessive ROS production over antioxidant defense can lead to oxidation of macromolecules and has been implicated in the damage of intracellular structures, mitochondrial dysfunction and cell death<sup>28</sup>. In neurons, enhanced production of ROS occurs in both, developmental apoptosis as well as in various neuropathological conditions<sup>29-34</sup>, indicating the relevance of oxidative stress in neuronal damage. Given the importance of mitochondria as the prime source of intracellular ROS, mainly generated at complex I and III of the respiratory chain, mitochondria are at the same time important targets of ROS-mediated damaging effects and placed in the focus of cell death regulation<sup>1, 35, 36</sup>. Extensive formation of ROS and lipid peroxides affect vital mitochondrial functions, such as respiration and oxidative phosphorylation and perturb the maintenance of the mitochondrial membrane potential ( $\Delta\psi_m$ )<sup>28</sup>. Thus, besides their essential role in the cells' ATP supply and their involvement in several metabolic reactions<sup>20, 37</sup>, mitochondria play a central role in intrinsic pathways of apoptosis triggered by oxidative stress<sup>38</sup>. Furthermore, increasing evidence points to a crucial role of mitochondrial dynamics and integrity for the maintenance of cellular viability. Mitochondrial fission and fusion defects limit mitochondrial motility, decrease energy production and enhance oxidative stress, thereby promoting cell death<sup>20, 24</sup>. Thus, it is obvious, that the preservation of mitochondrial integrity and function, called mitoprotection, is essential for cell survival.

Mitochondria consist of two membranes, the outer and the inner membrane, composed of phospholipid bilayers and proteins. While the mitochondrial outer membrane (MOM) is freely permeable to small molecules such as ions and sugar, the inner mitochondrial membrane (IMM) is highly impermeable. The permeabilization of MOM allows the release of protein from the intermembrane space (IMS), such as cytochrome c, Smac/DIABLO and AIF, which immediately initiate the cell death machinery<sup>21</sup>. While it is likely, that the permeabilization is achieved by the formation of membrane-spanning pores, the involvement of appropriate pore-forming proteins as well as the correlation between MOMP and the breakdown of  $\Delta\psi_m$  is not well defined.

It is well described that MOMP is initiated by multi-domain pro-apoptotic members of the Bcl-2 family, such as Bax and Bak as well as BH3-only proteins, such as tBid or Bim, that directly activate Bax or Bak<sup>21, 23, 39</sup>. However, the precise mechanisms of how Bcl-2 family proteins trigger MOMP and subsequent mitochondrial impairment are still not fully understood. An alternative model for the initiation of MOMP is the opening of the mitochondrial permeability transition pore (mPTP), consisting of the voltage-dependent anion channel (VDAC) present in the outer membrane, the adenine nucleotide transporter (ANT) located in the inner membrane and the matrix protein cyclophilin D (CypD), among other proteins<sup>23, 40</sup>. Under normal conditions, CypD is reported to reside in the mitochondrial matrix and the mPTP remains closed. Opening of the mPTP upon cell death stimuli such as calcium overload or intracellular oxidative stress, results in a sudden increase in the IMM permeability, loss of  $\Delta\psi_m$ , mitochondrial swelling and rupture of the MOM<sup>41, 42</sup>. The present thesis addresses the disputed question, how these proposed mechanisms of MOMP are related to each other.

## 1.2 Bcl-2 family proteins – regulators of life and death

An important regulatory mechanism of mitochondrial integrity and function is represented by the B-cell lymphoma-2 (Bcl-2) family proteins<sup>36</sup>. An imbalance between multiple pro- and anti-apoptotic members of this family has been explored for their involvement in the underlying mechanisms of diverse pathologies such as tumor formation as well as autoimmune pathologies, infectious diseases and neurological disorders<sup>43</sup>. The Bcl-2 family includes more than 20 members and is subdivided into three groups on the basis of their pro- or anti-apoptotic action and the presence of conserved Bcl-2 homology (BH1-BH4) domains (Figure 2)<sup>44</sup>. The first group includes the anti-apoptotic proteins (e.g. Bcl-2, Bcl-xl, Bcl-w, Mcl-1, and A1/Bfl-1), which contain all four Bcl-2-homology domains (BH1-4) and preserve MOM integrity by directly binding and inhibiting either pro-apoptotic Bax/Bak or activator BH3-proteins. They are generally integrated within the MOM, but also displaced in the cytosol or ER membranes<sup>36, 45</sup>. In contrast, the second and third group contain the pro-apoptotic members, which are divided into multi-domain proteins with all four homology regions (e.g. Bax, Bak and Bok) and those that contain only the BH3 domain (e.g. tBid, Bim, Bad, Bik/Nbk, Noxa, Puma)<sup>46</sup>. While the multi-domain proteins Bax and Bak are thought to undergo conformational changes and oligomerization thereby promoting pore-formation and MOMP, the BH3-only proteins are described to either interact with anti-apoptotic proteins to inhibit their function and/or to directly interact with the effector proteins Bax/Bak to provoke their apoptotic activity<sup>21, 44, 47</sup>. In healthy cells pro-apoptotic Bcl-2 family members are cytosolic, whereas cell death stimuli can trigger their translocation (e.g. Bid or Bim) to membranes. In

contrast to the BH3-only protein tBid, full-length Bid shares structural similarities with the multi-domain family members as described in detail below<sup>44</sup>. Opposed to their abundant presence in non-neuronal cells, neuronal cells reveal highly dynamic expression of the main family members Bcl-xl, Bcl-2, Bax, Bak, Mcl-1 and Bid during neuronal development. While Bid, Bax and Bcl-xl continue to be highly expressed in the adult brain, significant expression levels of Bcl-2 and Mcl-1 as well as full-length Bak have not been observed<sup>48-52</sup>. In contrast, neurons express an unusual splice variant of Bak depicting anti-apoptotic functions when over-expressed<sup>52</sup>. In regard to the expanding interest in the BH3-only proteins and their pro-apoptotic effects within neurons, this thesis focuses on the pro-apoptotic protein Bid and addresses Bid-dependent mechanisms of neuronal cell death.

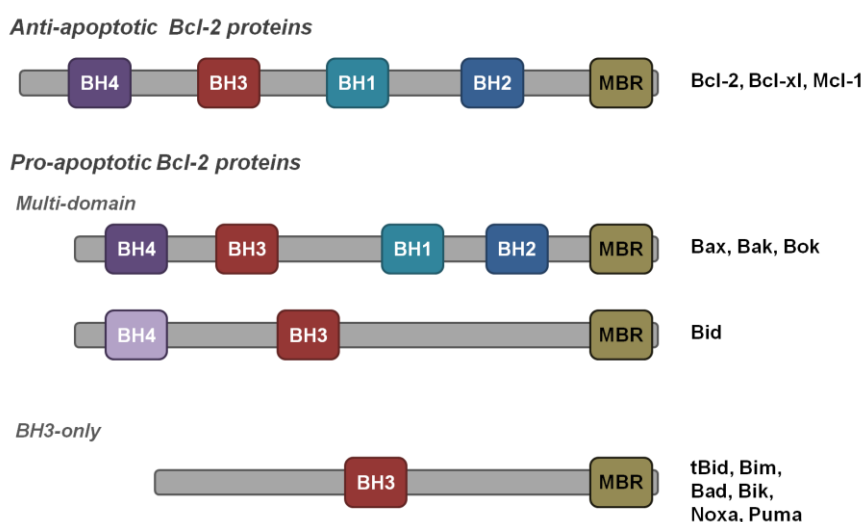


**Figure 2: Simplified overview of the Bcl-family proteins.**

Bcl-2 family proteins can be classified into three subtypes based on structural and functional features. To date, four Bcl-2 homology (BH)-domains have been identified (BH1-BH4). The anti-apoptotic family members Bcl-2, Bcl-xl, A1, MCL-1 and Bcl-w contain four BCL-2 homology domains and are thought to exert their effect at the mitochondrial outer membrane where they contribute to maintenance of membrane integrity. The pro-apoptotic proteins are subdivided into the multi-domain proteins Bax, Bak, Bok and the BH3-only proteins e.g. tBid, Bim, Bad, Bik, Noxa, Puma, Bik and Bnip3. Pro-apoptotic members such as Bax and Bak oligomerize and permeabilize the MOM, whereas tBid, Bim, Bad or Noxa are thought to either activate Bax or Bak or inhibit the anti-apoptotic proteins. In contrast to tBid, full-length Bid shares structural and functional similarities to the pro-apoptotic protein Bax. Most members of the Bcl-2 family consist of a carboxy-terminal membrane-binding region (MBR) that triggers the translocation and binding of the proteins to membranes. (modified from Chikpuk et al., 2010 and Shamas-Din et al., 2013)<sup>53, 54</sup>.

### 1.2.1 The BH3-only protein Bid

The BH3-interacting domain death agonist, Bid, first reported by Wang et al. 1996<sup>55</sup>, is a widely expressed cytosolic pro-apoptotic protein, consisting of 195 amino acid residues (22 kDa) in its full length form. Although Bid has been reported to participate in a mitosis checkpoint and maintenance of genomic stability<sup>56, 57</sup>, the main function of Bid appears to be its crucial involvement in the regulation of mitochondrial cell death pathways. Even though some pro-apoptotic function is reported for full-length Bid<sup>58, 59</sup>, detrimental activation of Bid is accelerated by proteolytic cleavage of the native protein to a truncated C-terminal p15 fragment (tBid), which translocates to the mitochondria<sup>60</sup>. There, tBid mediates mitochondrial membrane permeabilization and the subsequent release of apoptotic factors from the mitochondrial intermembrane space to the cytosol<sup>61-63</sup>.

The structure of Bid, which has been elucidated using NMR spectroscopy<sup>64, 65</sup>, consists of eight  $\alpha$  helices arranged in three layers, with two central hydrophobic helices ( $\alpha$  6 and  $\alpha$  7) surrounded by the amphipatic helices on either side<sup>66</sup>. Beside this highly ordered core structure, Bid contains a large unstructured loop between the helices  $\alpha$  2 and  $\alpha$  3 (amino acids 42-79), as well as a disordered N-terminal region (Figure 3 A). The structural arrangement of Bid shares high similarity to the structure of multi-domain Bcl-2 family proteins, such as Bcl-2, Bcl-xl, Mcl-1 and Bax, and is thereby contrasting the unstructured composition of almost all BH3-only proteins<sup>44, 66, 67</sup>. In accordance to the structures of Bax and Bak, recent studies further suggested a redefined BH4 region at the N-terminus of Bid, a feature that was previously observed only by the anti-apoptotic Bcl-2 family proteins<sup>61</sup>. Further, the structural arrangement of Bid is similar to that of bacterial toxins such as the colicins and diphtheria toxin<sup>65, 68</sup> and implies the role of Bid in pore-formation. This suggestion has been substantiated by reports describing high similarities between Bid and Bax regarding their migration to and insertion into the MOM, thereby indicating Bid as a 'Bax-like protein'<sup>61</sup>. While the BH3-domain of Bid, located in helix 3, is required for its interactions with the Bcl-2 family proteins Bax and Bcl-xl, the unstructured loop contains a variety of sites that are subjected to post-translation modifications regulating Bid localization and apoptotic function (Figure 3 B)<sup>66, 68</sup>.

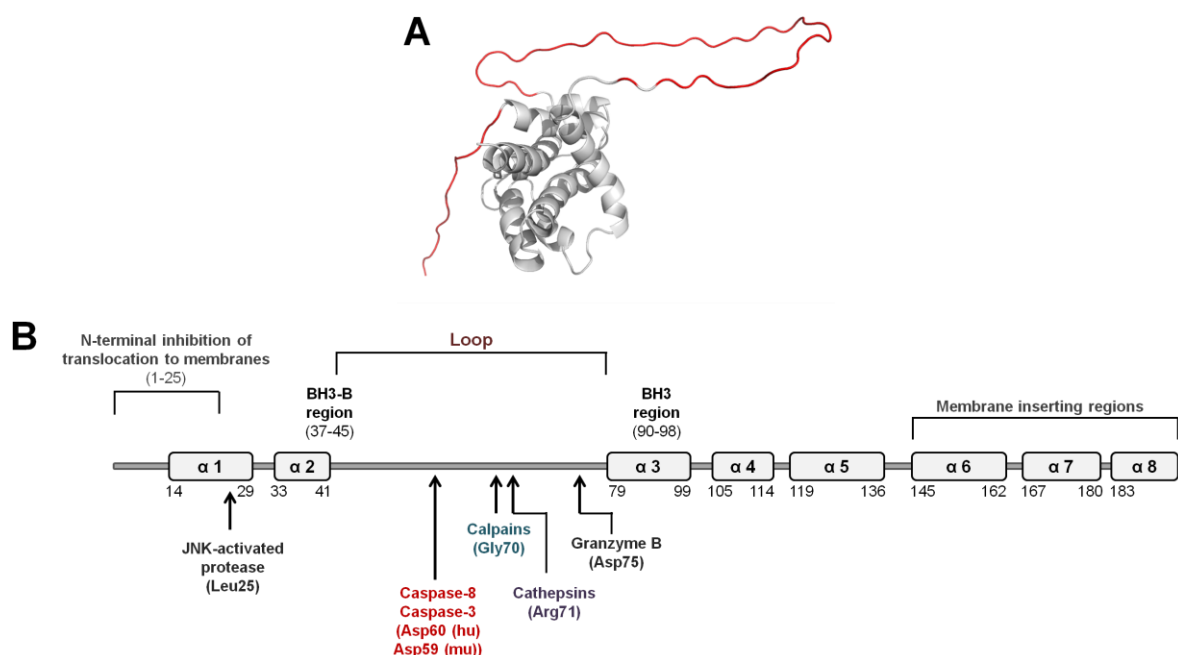


**Figure 3: Molecular structure and protease-cleavage sites of Bid.**

**A**, NMR- solution structure of mouse Bid (PDB entry 1DDB)<sup>65</sup>. The flexible loop region between helix  $\alpha 2$  and  $\alpha 3$  and the flexible N-terminal region are marked in red. The core structure consisting of 8  $\alpha$ -helices is stained in grey. The schematic drawing reveals one of 20 NMR solution structures of mouse Bid. **B**, Human Bid (hu) and mouse Bid (mu) consists of 195 amino acids and 8  $\alpha$ -helices. Numbers below each  $\alpha$ -helix indicates the starting and ending amino acid sequence of the helix. The BH3-domain is domain is required for interactions with other Bcl-2 family members, whereas helix  $\alpha 2$  is thought to interact with membrane lipids, particularly cardiolipin. Mostly all proteases cleave Bid in the loop region, cleavage sites are indicated with black arrows (modified from billen et al 2009)<sup>61</sup>.

Within this highly flexible region, proteolytic activation and cleavage of Bid can be exerted by different proteases (Figure 3 B). The first mentioned and best studied example of Bid activation is its cleavage by caspase-8<sup>60</sup>, which itself is activated by the engagement of Fas/TNF death receptors. Caspase-8 cleavage of Bid, resulting in the C-terminal p15 tBid fragment, triggers the exposure of the BH3-domain and drives the membrane binding of tBid by relieving its auto-repression mediated by the un-cleaved N-terminal p7 fragment<sup>61, 64, 65, 69</sup>. Upon cleavage, the smaller p7 fragment of tBid is not necessarily completely separated from the active C-terminal moiety<sup>66</sup>, as both fragments are held together by hydrophobic interactions<sup>70</sup>. However, recent studies revealed that in the presence of a membrane, both fragments of caspase-8 cleaved Bid (cBid) spontaneously dissociate, thereby exposing sufficient hydrophobicity to drive the insertion of tBid into membranes<sup>71, 72</sup>. Beside caspase-8, Bid can also be cleaved by the effector caspase-3<sup>61</sup>, as well as by caspase-10<sup>66</sup>, caspase-2 and caspase-1. In addition, Bid cleavage has also been shown to be exerted by several non-caspase proteases, namely granzyme B<sup>73</sup>, calpains<sup>74, 75</sup> or lysosomal hydrolases such as cathepsins<sup>76</sup>, and finally by a JNK-dependent unknown protease<sup>61</sup>. Mostly all of them cleave Bid in the loop region between helices  $\alpha 1$  and  $\alpha 2$  and notably all proteases trigger the accumulation of the C-terminal cleavage product at mitochondria<sup>44, 61</sup>.



### 1.2.1.1 Bid interactions with lipids and proteins - recruitment to mitochondrial membranes

There are several hypotheses proposed to explain the recruitment of Bid and tBid to mitochondrial membranes and the subsequent MOMP. While protein-protein interactions are discussed in being involved in the specific translocation of Bid and tBid to mitochondria<sup>66</sup>, increasing evidence indicates that mitochondrial lipids might play an important role in the molecular cell death pathway driven by pro-apoptotic Bcl-2 family members culminating with MOMP and the release of apoptogenic factors<sup>77</sup>.

For example it has been postulated that post-transcriptional myristinylation of tBid enhances its targeting to mitochondria<sup>70</sup>, and many *in vitro* studies revealed Bid-lipid binding and a membrane destabilization or even a pore-forming ability of tBid on artificial lipid membranes<sup>66, 69</sup>. Furthermore, a relevance of a Bid-lipid interaction was also suggested for the activation of mitochondria and a tBid-induced mitochondrial dysfunction in the absence of Bak or Bax<sup>78</sup>. In particular, the glycerol-based phospholipid cardiolipin (CL) has been shown to play a crucial role for the specific targeting of tBid to mitochondria<sup>79, 80</sup>. Cardiolipin is synthesized and exclusively present in the IMM, but also found in the MOM and even more at the contact sites connecting the outer with inner mitochondrial membrane. A Bid-cardiolipin interaction was initially demonstrated by *in vitro* studies, revealing the necessity of CL in liposome membranes for the effective tBid-induced release of trapped indicators<sup>71, 79</sup> and confirmed by cell based assays demonstrating the requirement of CL for tBid-induced cytochrome c release<sup>80-82</sup>. In accordance to the mitochondrial localization of CL, it has been suggested that tBid binds to CL at the contact sites of the IMM and MOM<sup>81, 83</sup> and further studies have linked the Bid-CL interaction to mitochondrial cristae reorganization, permeability transition and the subsequent release of CL-bound cytochrome c<sup>84, 85</sup>. Notably, also full-length Bid as well as the non-separated cBid retain the capacity of binding tightly to CL and display interactions with other Bcl-2 family proteins and lipid membranes<sup>86-89</sup>. Therefore it is obvious, that CL plays a role in the modulation of the pro-apoptotic action of Bid<sup>90, 91</sup>, although it remains unclear whether the pro-apoptotic action of Bid is directly dependent on CL.

Despite the apparent important role of mitochondrial lipids, it is well accepted that the pro-apoptotic activity of Bid, and in particular tBid-mediated membrane permeabilization and the release of cytochrome c, is based on its interactions with other Bcl-2 family members or mitochondrial proteins. tBid can interact with the anti-apoptotic proteins Bcl-2 and Bcl-xl, thereby releasing Bax to promote Bax activation, but is also able to directly activate the apoptotic effector proteins Bax and Bak to trigger their oligomerization and mitochondrial activation<sup>61, 92</sup>. Besides the necessity of other Bcl-2 family members, it has also been shown

that the voltage-dependent anion channel 2 (VDAC2) is required for tBid-induced mitochondrial apoptosis by inducing Bak translocation to mitochondria<sup>66, 93</sup>. Furthermore, the mitochondrial carrier homolog 2 (Mtch2) has been recently reported as a binding partner for tBid and appears to be important for its mitochondrial recruitment<sup>72, 94, 95</sup>. After cleavage of Bid and the spontaneous separation of the p7 and p15 fragment upon the initial binding of tBid to MOM, Mtch2 is thought to act as a direct receptor for tBid, catalyzing its conformational change and anchoring the membrane binding helices of tBid in the membrane<sup>72</sup>. Finally, latest reports demonstrated a direct interaction of tBid with caspase-cleaved arrestin-2, which does not induce tBid recruitment to mitochondria but enhances the ability of tBid to induce cytochrome c release<sup>96</sup>.

These studies suggest the importance of both, mitochondrial lipids and other proteins for the crucial role of Bid in the mitochondrial cell death machinery. However, it is not clear if the described Bid-lipid and –protein interactions depend on each other, occur in parallel or if there are multiple mechanisms for the mitochondrial recruitment of Bid and its apoptotic function depending on cell type and cell death stimuli. It is therefore of interest to address the precise mechanism of Bid participation in MOMP and especially to explore the essential binding partners that facilitate the mitochondrial recruitment and pro-apoptotic action of Bid in neurons.

### **1.2.1.2 Involvement of Bid in neuronal cell death**

In contrast to other cells where Bax and Bak are reported to be the key players of intrinsic cell death pathways, recent studies highlighted a pivotal role of Bid in mitochondrial demise, the subsequent acceleration of oxidative stress and neuronal cell death. It has been shown that Bid-deficient neurons are highly resistant to cell death stimuli including oxygen-glucose deprivation (OGD), glutamate-induced excitotoxicity or oxidative stress *in vitro*<sup>97, 98</sup>. Pharmacological Bid inhibition and Bid gene silencing using small interfering RNA (siRNA) provides neuroprotective effects by inhibiting tBid-induced mitochondrial fragmentation, loss of mitochondrial membrane integrity, mitochondrial AIF release, and cell death<sup>97, 99</sup>. *In vivo*, a pivotal role for Bid in mechanisms of delayed neuronal death has been confirmed in models of cerebral ischemia and brain trauma, where Bid knockout mice revealed significantly reduced brain damage compared to wild-type controls<sup>98, 100, 101</sup>. In addition, activation of Bid and tBid translocation to mitochondria has been detected in seizure-induced neuronal death and in human brain tissue after temporal lobe epilepsy<sup>102, 103</sup>, indicating a key role of Bid in neurological disorders.

## 1.2.2 Pharmacological Bid inhibition – a strategy for mitoprotection

The findings above highlight the pivotal role of Bid in the control point of life and death and identified Bid as a key regulator of mitochondrial injury and mitochondrial pathways of neuronal cell death. The transactivation of Bid to mitochondria, Bid-induced mitochondrial fragmentation and MOMP and the accelerated production of reactive oxygen species (ROS) mediate the release of death promoting factors into the cytosol that trigger the final steps of the mitochondrial cell death machinery. Bid deficiency and pharmacological Bid inhibition were shown to provide protection against such mitochondrial demise, indicating Bid as a target for mitoprotection and cell survival. Therefore, inhibition of Bid may serve as a promising strategy for the development of novel therapeutic approaches for neuroprotection with high relevance for the treatment of age-related diseases of the nervous system, where intrinsic death pathways cause impaired mitochondrial integrity and neuronal death.

While several selective inhibitors for other members of the Bcl-2 family proteins, such as Bcl-2, Bcl-xl or Mcl-1 have been described<sup>104-113</sup>, so far, only a few small molecules targeting Bid have been developed by Becattini et al.<sup>99, 114</sup>. While the discovery of Bcl-2 and Bcl-xl inhibitors has been based on the structural knowledge of their molecular function<sup>104, 106, 115</sup>, analogous strategies for Bid were missing so far as the molecular basis for its function is not fully understood<sup>99</sup>. In contrast, the design of small-molecules targeting Bid was based on the abovementioned NMR-solution structure of mouse Bid (PDB entry, 1DDB)<sup>65</sup>, revealing the presence of a deep hydrophobic crevice on the surface of the Bid protein. First Bid-targeting ligands (**1-3**), capable of occupying this hydrophobic pocket, were identified by an NMR-based approach named “structure-activity relationships by interligand-Nuclear-Overhauser Effects” (SAR-by-ILOE) (Figure 4). Combination of these small Bid-binding fragments (**1-3**) resulted in several substances with diverse potentials for Bid-binding and inhibition of mitochondrial Smac/DIABLO release<sup>99, 114</sup>. The most promising substances obtained from this strategy were the 4-phenylsulfanyl-phenylamine derivatives BI-11A7 (**4**) and BI-6c9 (**5**) (Figure 4). Both BI-6c9 and BI-11A7 demonstrated protective efficiency, positively influencing cell survival and mitochondrial integrity. Furthermore, these small-molecule Bid inhibitors provided protection against neuronal cell death in models of glutamate toxicity and oxygen-glucose deprivation (OGD) in neuronal cell lines *in vitro*<sup>24, 97, 99, 114, 116</sup> and attenuated genotoxic drug induced apoptosis in HeLa cells<sup>117, 118</sup>. However, the protective activities of the Bid-inhibiting compounds developed so far, were only achieved at high micromolar concentrations and the small-molecules were only applicable in enzyme assays and in cell culture. Applications of BI-6c9 in model systems of neuronal degeneration *in vivo* have failed so far, likely due to a limited affinity and bioavailability of the compound. Based on these findings the first part of this thesis focused on Bid as a molecular druggable target and the

screening of novel small Bid inhibitors which were developed based on further optimization of the available Bid-targeting molecules.

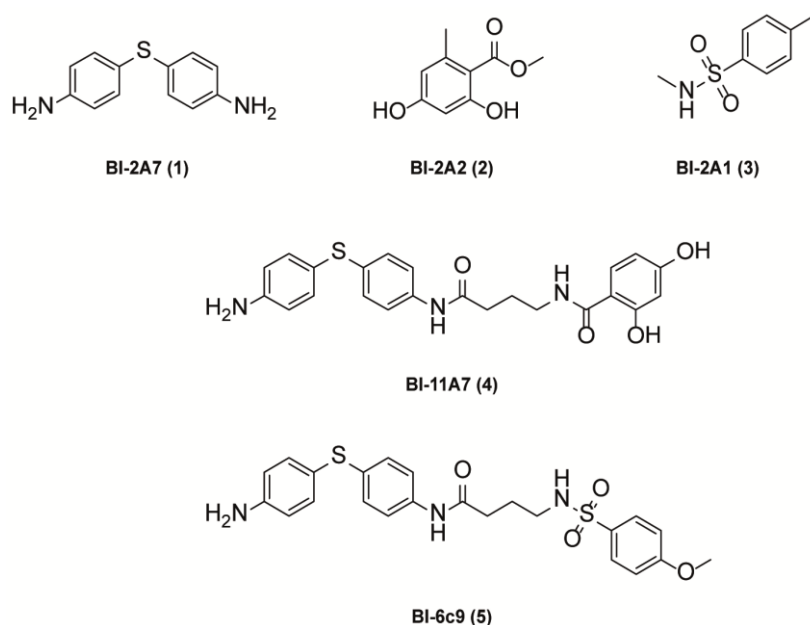


**Figure 4: Structures of Bid-binding fragments and the resulting Bid inhibitors.**

By the combined approaches of NMR-fragment-based screening and *in vitro* assays, Becatiini et al. identified the fragments BI-2A7, BI-2A2 and BI-2A1 as binding ligands for Bid. Combinations of these fragments yielded in the Bid inhibitors BI-11A7 and BI-6c9<sup>99, 114</sup>

Another aspect in the demanding development of novel small-molecules that selectively target Bid is the absence of an appropriate crystal structure of isolated Bid. It is well accepted that elucidation of the atomic structure of proteins is not only a powerful tool for understanding the macromolecular function but has undoubtedly an important role in drug discovery and pharmacological research<sup>119, 120</sup>. So far, only small Bid-BH3 peptides have been crystallized in complex with the Bax protein and were used to explore the pro-apoptotic activation of Bax<sup>121</sup>, but no crystal structure of the Bid helical core has been obtained to date. However, deep structural knowledge would enable the structure-guided drug design as it has been performed for the related Bcl-2 family proteins Bcl-xl or Mcl-1<sup>109, 122-124</sup>. Thus, a crystal structure of Bid would facilitate the rational design of lead candidates with acceptable physicochemistry, selectivity, and affinity properties.

### 1.3 Voltage-dependent anion channels (VDAC) and their role in mitochondrial apoptosis

Voltage-dependent anion channels, also known as mitochondrial porins, are the most abundant proteins in the outer mitochondrial membrane and can be subdivided into three isoforms: VDAC1, VDAC2 and VDAC3. All three proteins have a similar molecular weight (30-35 kDa) and are highly conserved across species, albeit in different amounts, with VDAC1 being the most prevalent sub-type and the least common form being VDAC3<sup>125, 126</sup>. While so far very little is known about the three-dimensional structure of VDAC2 and VDAC3, intensive structural investigations were performed on the isoform VDAC1 in recent years<sup>127-129</sup>. X-ray structures revealed VDAC1 as an atypical 19 stranded  $\beta$ -barrel with a 25 residue-long N-terminal  $\alpha$ -helical region spanning the middle of the pore which is supposed to be involved in channel gating behavior<sup>127-129</sup>. Beside their abundant presence in the MOM, VDACS are also localized in compartments other than mitochondria, such as plasma membranes and the endoplasmic reticulum (ER), yet the exact functions of extra-mitochondrial VDAC remain unclear<sup>125</sup>. The physiological function of mitochondrial VDACS is their involvement in the cross-talk between mitochondria and the cytosol by regulating the exchange of energy carrying molecules like ATP, ADP, pyruvate or succinate and other small molecules<sup>130-132</sup>. Further reports connect VDACS to many physiological and pathophysiological processes, including  $\text{Ca}^{2+}$  homeostasis<sup>133-136</sup> or energy metabolism<sup>135-140</sup> and increasing evidence points to VDAC as a key protein in the regulation of intrinsic cell death pathways<sup>130, 135, 136, 138, 141-144</sup>. Several lines of experimental data suggested the isoform VDAC1 as the most likely candidate involved in mitochondrial apoptosis, as siRNA mediated VDAC1 gene silencing efficiently prevented Bax activation, cytochrome c release and cell death induced by various stimuli, such as cisplatin<sup>145</sup>, endostatin<sup>146</sup> or selenite<sup>147</sup>. In contrast, VDAC1 over-expression triggers apoptotic cell death<sup>132, 141, 148, 149</sup>, and release of cytochrome c could be induced by purified VDAC1 reconstituted into cytochrome c containing liposomes<sup>132, 150</sup>. Although these data indicate the critical involvement of VDAC1 in cell death, the precise mechanisms of how VDAC1-mediated apoptosis is regulated is a matter of controversial discussion<sup>126, 130, 131, 151</sup>.

VDAC1 is regarded as the major pore-forming component of the mPTP, suggesting that its activation by apoptotic stimuli, such as over-production of  $\text{Ca}^{2+}$  and ROS, results in mPTP opening and subsequent cell death<sup>125, 130, 131, 152</sup>. Another hypothesis indicates that VDAC1 closure prevents the efficient exchange of ATP and ADP between mitochondria and cytosol, thereby leading to osmotic matrix swelling, rupture of MOM and the non-specific diffusion of intermembrane proteins that trigger cell death<sup>132, 153</sup>. Alternatively, it has been suggested that VDAC1 oligomerization mediates the release of apoptogenic factors<sup>154-156</sup>, as an increase in

VDAC1 homo-oligomers was observed upon STS-induced apoptosis and could be blocked by the anion channel blocker 4,4'-diisothiocyanostilbene-2,2'-disulfonic acid (DIDS)<sup>136, 155</sup>. Finally, both VDAC1 and VDAC2 have been reported as key functional targets of the Bcl-2 family proteins and increasing evidence indicates that both anti- and pro-apoptotic proteins are involved in the regulation of VDAC mediated apoptosis<sup>142, 157-160</sup>. Although a close interplay of VDAC with Bcl-2 family proteins such as Bcl-xl, Bax or Bid has been proposed<sup>157, 159, 161, 162</sup>, a direct interaction of VDAC with any of these Bcl-2 family members has not yet been demonstrated at the cellular level. Furthermore, the relationship between Bcl-2 family proteins and the VDAC gating behavior is contradictory. While it has been described that the pro-apoptotic proteins triggers VDAC channel closure thereby leading to MOM rupture and cell death, and anti-apoptotic proteins maintains the functional open state of VDAC channels<sup>153, 161</sup>, other reports claim, that the pro-apoptotic members Bax and Bak induce VDAC channel opening and the formation of a large pore permeable for cytochrome c<sup>144, 159</sup> in contrast to the anti-apoptotic proteins Bcl-xl and Bcl-2 which facilitate the close state of VDACS<sup>144, 160</sup>. Despite all abovementioned indications, it should be noted, that VDAC isoforms were also reported to be dispensable for mitochondria-dependent cell death<sup>163</sup>, suggesting that multiple pathways and mechanisms of mPTP opening and cytochrome c release can co-exist within the proposed cell death models depending on the cell type and death stimulus<sup>151, 163</sup>.

The particular involvement of VDAC1 and VDAC2 in intrinsic cell death pathways and especially their connection to the pro-apoptotic activity of the Bcl-2 family protein Bid will be elucidated in the last part of the present thesis.

#### 1.4 HT-22 cells – a model for and Bid-mediated cell death

In order to investigate the mechanisms of Bid-mediated neuronal cell death, immortalized mouse HT-22 neurons were used as a well established model system to study intrinsic cell death pathways triggered by oxidative stress. Since HT-22 cells lack functional ionotropic glutamate receptors, glutamate induced cell death occurs independently of NMDA-receptor stimulation through competitive inhibition of the glutamate/cystine antiporter system  $X_c^-$ , which exchanges extracellular cystine and intracellular glutamate across the plasma membrane. High extracellular glutamate concentrations at millimolar ranges consequently reduce the intracellular cystine levels required for glutathione (GSH) synthesis<sup>164-167</sup>. As glutathione serves as a radical scavenger that sequesters free radicals and ROS, GSH depletion results in a pronounced and significant increase in free radicals and detrimental reactive oxygen species (ROS) within a few hours after glutamate treatment of cells<sup>164</sup>. The dramatic GSH depletion leads to the loss of function of glutathione peroxidase 4 (GPX4) and an increased activity of 12/15-lipoxygenases (12/15-LOX), resulting in ROS-mediated lipid peroxidation. Upon 12/15-LOX activation, the pro-apoptotic protein Bid translocates to mitochondria, induces mitochondrial fragmentation and mitochondrial membrane permeabilization and thereby accelerates the glutamate-induced ATP depletion, the second pronounced increase in ROS production and, finally, the release of death-promoting factors, such as AIF in the cytosol. Nuclear translocation of AIF induces the DNA fragmentation and nuclear condensation, ultimately triggering the final execution step of caspase-independent cell death within a few minutes<sup>97</sup>.

This delayed form of glutamate-induced toxicity is clearly different from glutamate-induced excitotoxicity in primary neurons, where excessive or even prolonged physiological glutamate-mediated activation of ionotropic NMDA-receptors leads to a massive calcium influx and rapid neuronal cell death<sup>168, 169</sup>. However, despite the absence of functional NMDA-receptors, it has also been shown that glutamate-induced cell death signaling is accompanied with increases in cyclic GMP and cytosolic calcium levels<sup>34, 170, 171</sup>. Although the initial signaling of glutamate-induced cell death in primary neurons and HT-22 cells are different, they both share a high similarity in the downstream cell death pathways. Since enhanced ROS formation, increased  $Ca^{2+}$  levels as well as Bid-mediated mitochondrial dysfunction are well established features of neuronal toxicity, the glutamate-treatment of the present HT-22 cells serves as a valuable and applicable *in vitro* model for studying molecular mechanisms of PCD triggered by oxidative stress and the activation of the pro-apoptotic protein Bid.

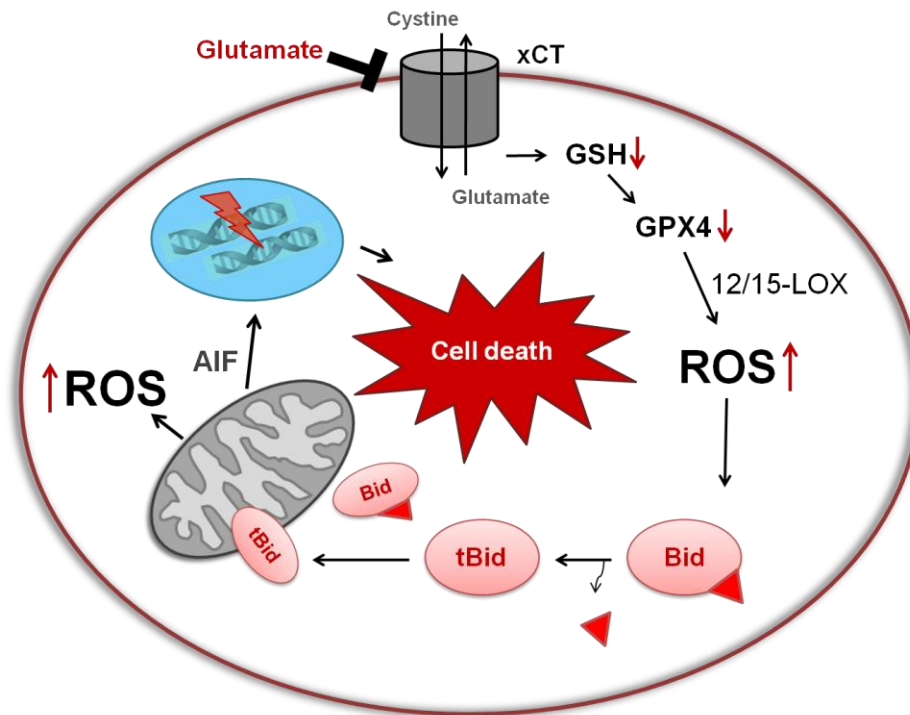


**Figure 5: Simplified model of glutamate-induced toxicity in HT-22 cells.**

In HT-22 cells, the xCT- antiporter mediates the import of extracellular cystine and the export of intracellular glutamate. Exposure to high concentrations of glutamate triggers oxidative stress by a competitive inhibition of the cystine import, resulting in a GSH depletion, which reduces GPX4 activity and increases the 12/15-LOX activation. These events enhance the generation of highly detrimental ROS and increase the formation of lipid peroxides. Downstream of the first ROS formation, the pro-apoptotic protein Bid is activated to its truncated form tBid, which subsequently translocates to mitochondria, where tBid induces the permeabilization of the mitochondrial outer membrane, mitochondrial dysfunction and the accelerated ROS production, consequently releasing death promoting factors, such as AIF, into the cytosol. AIF in turn immediately translocates to the nucleus, leading to DNA fragmentation and nuclear condensation, thereby causing the final execution of caspase-independent cell death. Red arrows indicate the increases and decreases in cellular molecule levels caused by the exposure of HT-22 cells to glutamate. (modified from Tobaben et al., 2011).



## 1.5 Aims of the thesis

The pivotal role of the pro-apoptotic Bcl-2 family protein Bid in intrinsic cell death pathways has become increasingly apparent over the last couple of years, as Bid has been identified as a key regulator of mitochondrial integrity and function and detrimental accumulation of reactive oxygen species (ROS). Previous studies revealed an important role of Bid in delayed neuronal death after oxygen-glucose-deprivation, glutamate-induced excitotoxicity or oxidative stress *in vitro*. *In vivo*, major roles of Bid-dependent cell death mechanisms were confirmed in models of cerebral ischemia and traumatic brain injury. These data highlight Bid as a potential target for novel therapeutic strategies aiming at preserved mitochondrial function and neuronal survival with high relevance for the treatment of age-related diseases of the nervous system, where mitochondrial injury and associated neuronal dysfunction are prominent.

To achieve efficient pharmacological strategies to inhibit Bid-mediated cell death pathways, novel drug discovery campaigns are required to overcome the limitations of the few Bid inhibiting compounds developed so far. While other Bcl-2 family members are intensively investigated in various structure-guided drug development approaches, until now similar strategies for Bid were hampered by the absence of appropriate crystal structures of isolated Bid. Moreover, a better knowledge of mechanisms involved in Bid activation and Bid-dependent impairments of mitochondrial membrane integrity are mandatory for sustaining the therapeutic potential of Bid inhibition.

Therefore, the present thesis is aimed to bridge crucial gaps of knowledge regarding the precise mechanisms of Bid-dependent mitochondrial demise and cell death and to initiate important requisites for Bid crystallization with the principal purpose of identifying novel Bid-targeting compounds for mitoprotection and cell survival:

### 1) Evaluation of new chemical compounds that target Bid for mitoprotection and cell survival

The first aim of the present thesis was the identification of novel Bid-targeting molecules that provide protection against mitochondrial cell death. Based on the structure of available Bid inhibitors, compounds of three chemical classes were developed. These molecules were screened in this thesis for their protective efficiency in the model of glutamate toxicity in HT-22 neurons. In order to investigate the interference with the pro-apoptotic activities of Bid, the effects of the novel structures were further examined after tBid over-expression. Moreover, the work addresses the ability of the most promising compounds to prevent Bid-mediated impairments in mitochondrial integrity and function.

### **1) Design, expression and purification of different Bid constructs for crystallization and functional assays**

In order to provide insights into the structural properties of Bid and its pro-apoptotic activities, the second aim of this thesis was the design of different Bid constructs and the establishment of protocols for expression and purification of recombinant Bid protein. Highly pure protein was used for initiation of the first Bid crystallization studies and the development of primary assays of Bid activity, and Bid-interactions with other proteins.

### **2) Development of model systems for membrane permeabilization**

Since Bid was identified as a key trigger of apoptotic cell death via detrimental effects at the mitochondrial membrane, the third goal of the project was to investigate the effect of recombinant full length Bid and cBid on artificial lipid bilayer structures which mimic the mitochondrial membrane. For this approach, a liposome channel activity assay was validated as a screening system for membrane permeabilization. As many previous studies claimed the pro-apoptotic protein Bax as the main pore-forming protein required for MOMP, a further purpose during this research was to examine the role of Bax in Bid/cBid-mediated permeabilization of fluorescent liposomes. Another question of interest was the role of cardiolipin in Bid-mediated membrane integration and permeabilization.

### **3) Mechanisms of Bid mediated mitochondrial dysfunction and cell death and the link to the voltage-dependent anion channel VDAC**

So far, the precise mechanism by which Bid initiates MOMP and the subsequent mitochondrial demise is not fully understood. Therefore, the thesis was proposed to investigate whether the voltage-dependent anion channel VDAC1 is a direct mitochondrial receptor for activated Bid at the control point of life and death. The approach of the anion channel blocker DIDS as well as VDAC1 gene silencing was used to explore the impact of VDAC in glutamate-induced and Bid-accelerated cell death pathways in cultured neurons. The interplay between Bid and VDAC was additionally verified in a model of ischemic brain injury *in vivo* as well as by *in vitro* studies using recombinant proteins.

As previous studies reported a direct interplay between the isoform VDAC2, tBid and Bak in non-neuronal cells, the last part of the work was aimed at the role of VDAC2 in glutamate-induced cell death in HT-22 neurons.

## 2 Materials and methodes

### 2.1 Chemicals and reagents

All standard chemicals were obtained from Sigma-Aldrich (Taufkirchen, Germany) and Roth (Karlsruhe, Germany), if not described otherwise. All buffers and solutions were prepared using demineralized, ultrapure water that was prepared with the SG Ultra Clear UV plus pure water system (VWR, Darmstadt, Germany).

Ultrapure, demineralized water for aseptic preparation of solutions was sterilized before use by a steam autoclave (Systec V-40, Systec GmbH, Wetttenberg, Germany). In addition, all media and solutions that were used in cell culture were sterilized by filtration using 0.22 µm filter sets (Sarstedt, Nümbrecht, Germany).

#### 2.1.1 Transfection reagents

Opti-MEM I (Invitrogen, Karlsruhe, Germany) was used to allow formation of DNA- or siRNA transfection complexes. For siRNA transfections, the cationic lipid formulation Lipofectamine RNAiMax (Invitrogen, Karlsruhe, Germany) was used. Transfection of plasmid vectors were performed using the attractene transfection reagent (Qiagen, Hilden, Germany).

##### 2.1.1.1 Plasmid vectors

Plasmid pCDNA 3.1+ was obtained from Invitrogen (Karlsruhe, Germany). The mitoGFP (mGFP) vector was a kind gift from Andreas Reichert (Goethe University Frankfurt, Frankfurt, Germany). The tBid vector (pIRES-tBid) was generated as previously described<sup>172</sup>. The ApoAlert<sup>®</sup> pDSRed2-Bid vector which encodes a biologically active fluorescent fusion protein of Bid and DsRed monomer was derived from Clontech (Palo Alto, California, USA). The mouse VDAC1 plasmid (mVDAC1) was kindly provided by Dr. Jeff Abramson (University of California LA). For the generation of Flag-VDAC1, full-length mouse VDAC1 was amplified with two primers (VDAC1-fwd and VDAC1-Flag-rev, see 2.1.2) of which the C-terminal one encoded also a Flag epitope. The PCR product was subcloned into pcDNA3 (Invitrogen) using the inserted BamHI and NotI sites. Plasmids containing either the gene sequence for full length Bid or truncated Bid were ordered from Addgene (Cambridge, MA): pET15b Bid p22 (Addgene plasmid 8784) encodes full-length mouse Bid, pET15b Bid p15 (Addgene plasmid 8782) encodes mouse tBid<sup>173</sup>. A plasmid containing the caspase 8 gene was also purchased from Addgene in a pET15b vector (Addgene plasmid 11827, pET15b-Casp8 delta DED). The plasmid vector encoding the Bax sequence was ordered from Addgene in a pCEP4-HA vector (Addgene plasmid 16587, pCEP4-HA-Bax). The construction of plasmids encoding GST fusion proteins of various Bid constructs is described in more detail in section

2.14.3. The following plasmids were constructed: pGEX  $\Delta$ 12-Y47 (also called Bid 1), pGEX  $\Delta$ 12-D51 (Bid 2), pGEX  $\Delta$ 13-Y47 (Bid 3) and pGEX  $\Delta$ 13-D51 (Bid 4).

All plasmids were amplified using a Quiagen Plasmid Plus Midi kit (Quiagen, Hilden, Germany) according to the manufacturer's protocol. Prior to use, the plasmid DNA-concentrations were determined using the NanoVue Plus Spectrophotometer (Implen, GE Healthcare Europe GmbH, Freiburg, Germany), and digestion by restriction enzymes with subsequent gel electrophoresis analysis was performed. Additionally all plasmid constructs were verified by sequencing.

### 2.1.1.2 SiRNA

VDAC1 and VDAC2 siRNA sequences were synthesized by Eurofins MWG Operon (Eurofins MWG Operon, Ebersberg, Germany). Specific VDAC1 knockdown was achieved by the following siRNA sequences: 5'-GAUUGGCUUAGG GUACACUCA-3' (VDAC1 siRNA 1) and 5'-GUGAAUGACGGGACAGAGUUU-3' (VDAC1 siRNA 2). For specific knockdown of VDAC2 the following siRNA sequences were used: 5'-UGAUUAUUCGUUCCCAGAGGUU-3' (VDAC2 siRNA a) and 5'-AGAGUGUUAUCGGUGUCCUU-3' (VDAC2 siRNA b). For knockdown of Bid two siRNA sequences were purchased from Sigma-Aldrich (Taufkirchen, Germany): 5'-GAGUGUAUCUAAGAGUUU[dT][dT]-3' (SASI\_Mm01\_0011519) and 5'-AAACUCUUCAGAUACACUC[dT][dT]-3' (SASI\_Mm01\_00115200). Non-functional scrambled siRNA (*scr* siRNA, 5'-AAGAGAAAAGCGAAGAGCCA-3') was purchased from Dharmacon (Thermo Scientific, Bonn, Germany).

### 2.1.2 PCR-primer

For RT-PCR all primers were synthesized at by Eurofins MWG Operon (Eurofins MWG Operon, Ebersberg, Germany). Primer sequences were used as listed in Table 1:

**Table 1: Primers used for RT-PCR**

Primers	Sequences
VDAC1 fwd	5'-GGACTGAGTATGGGCTGACG -3'
VDAC1 rev	5'-AAGTTGCTCTGGGTCACCTCG-3'
VDAC2 fwd	5'-ACTTTGCAGTCGGCTACAGG-3'
VDAC2 rev	5'-CTCTTCCCGTCTACCAGAGC-3'
Bid fwd	5'-GGGAACTGCCTGTGCAAGCTTAC-3'
Bid rev	5'-CAGTGAGGCCTTGTCTCTGAA-3'
GAPDH fwd	5'-AGGCCGGTGCTGAGTAT-3'
GAPDH rev	5'-TGCCTGCTTCACCACCTTCT-3'

#### Primers used for the construction of expression vectors:

Primer	Sequence
mVDAC fwd	5'-TTA ATA CTC GAG TTA TGC TTG AAA TTC CAG TCC TAG GC-3'
mVDAC rev	5'-ATA AAT CAT ATG GCC GTG CCT CCC AC-3'
VDAC1 fwd	5'-AAA TAA _GGA TCC_ ATG GCC GTG CCT CCC-3'

VDAC1-Flag rev	5'-AAA ATT _GCG GCC GC_T TAC TTA TCA TCA TCA TCC TTA TAA TC_T CTA GA_T GCT TGA AAT TCC AGT CC-3'
G12-mBid fwd	5'-AAAAAAGGATCCGGGGCCGAGCACATCACAGACC-3'
A13-mBid fwd	5'-AAAAAAGGATCCGCCGAGCACATCACAGACCTGCTGG-3'
mBid-EcoRI	5'-AAAAAAGAATTCTCAGTCCATCTCGTTTCTAACCAAGTTCC-3'
Y47-mBid fwd	5'-AAAAAAAAGCTTACAGTCAGGAAGAAATCATCCACAACATTGCC- 3'
D51-mBid fwd	5'-AAAAAAAAGCTTACTGGGAGGCAGACAGTCAGGAAGAAATCATC CACAACATTGCC-3'
KpnI-M13Bid	5'-AAAAAA GGTACC ATG GCCGAGCACATCACAGACCTGCTGG-3'

---

### 2.1.3 Primary antibodies

All primary antibodies were diluted in Tris-buffered saline containing 0.05 % Tween 20 (TBST) and 5 % skim milk powder or Tris-buffered saline containing 5 % BSA (all Sigma-Aldrich) as indicated in the company's protocol. For Western blot analysis in this study, the VDAC1-antibody (VDAC1-N18, polyclonal, Santa Cruz Biotechnology, Santa Cruz, CA, USA) was diluted 1:200, of monoclonal and polyclonal Flag-antibody (Flag M2 monoclonal, Flag polyclonal both Sigma-Aldrich, Munich, Germany) 1:1000. VDAC2-, Bid-, Bax and Bak-antibodies (all polyclonal, Cell Signaling, Danvers, Massachusetts, USA, and New England Biolabs GmbH, Frankfurt, Germany) were diluted 1:1,000. The dilution of the Drp1-antibody (BD Bioscience Laboratories, Heidelberg, Germany) was 1:500 and the anti-actin antibody (Cell Signaling, Danvers, Massachusetts, USA, and New England Biolabs GmbH, Frankfurt, Germany) was used at a dilution of 1:10,000.

For immunoprecipitation experiments the Bid-antibody (polyclonal, Cell Signaling, Danvers, Massachusetts, USA) and Flag-antibody (polyclonal Sigma-Aldrich, Munich, Germany) were used at concentrations of 7.5 µg/sample and the VDAC1(N18)-antibody (Santa Cruz Biotechnology, Santa Cruz, CA, USA) was used at concentrations of 10 µg/sample (see also 2.8.4)

## 2.1.4 Secondary antibodies

All secondary antibodies were purchased from Vector Labs (Burlingame, California, USA), if not otherwise described. Horse radish peroxidase (HRP) labeled anti-mouse IgG (H+L), anti-goat IgG (H+L) and anti-rabbit IgG (H+L) secondary antibodies were used for Western blot analysis at dilutions of 1:2,500 - 1:5,000 in Tris-buffered saline with 0.05 % Tween 20 and 5 % skim milk powder (Sigma-Aldrich). For immunocytochemistry biotinylated anti-rabbit IgG (H+L) antibody was used in a 1:200 dilution in phosphate buffered saline (1 x PBS, Table 5) containing 3 % horse serum (Invitrogen, Karlsruhe, Germany) and DyLight 649 anti-mouse antibody (Merck Millipore, Darmstadt, Germany) in a dilution of 1:200 in phosphate buffered saline (1 x PBS) containing 3 % heat inactivated fetal calf serum (FCS).

## 2.2 Supplies

### 2.2.1 Kits

All kits used in this work are provided in Table 2 and were applied following the manufacturer's instructions:

**Table 2: Kits**

Kit	Company
Annexin-V-FITC Detection Kit	Promokine, Heidelberg, Germany
BODIPY (581/591 C11)	Invitrogen, Karlsruhe, Germany
MitoPT™ TMRE kit	Immunochemistry Technologies, Hamburg, Germany
ViaLight™ Plus-Kit	Lonza, Verviers, Belgium
XF Cell Mito Stress Kit	Seahorse Biosciences, North Billerica, MA
Pierce BCA Kit	Perbio Science, Bonn, Germany
NucleoSpin RNA II Kit	Machery & Nagel, Düren, Germany
SuperScript III One Step RT-PCR System with Platinum® Taq	Invitrogen, Karlsruhe, Germany
QIAGEN Plasmid Plus Midi	Qiagen, Hilden, Germany
QIAGEN Gel Extraction Kit	Qiagen, Hilden, Germany
Ultra Free DNA Extraction Kit	Millipore, Schwalbach, Germany

### 2.2.2 Materials for recombinant proteins

Consumables used for purification and concentration of recombinant proteins are provided in Table 3. Materials for crystallographic methods are depicted in Table 4.

**Table 3: Materials for protein purification**

Columns and filters	Company
His-Catcher Nickel Gravity columns	PJK GmbH, Kleinbittersdorf, Germany
HisTrap™ FF, 1 ml and 5 ml column	GE Healthcare Bio-Science AB, Uppsala, Sweden
GSTrap™ FF, 5 ml column	GE Healthcare Bio-Science AB, Uppsala, Sweden
Glutathione HiCap Cartridge, 5 ml	Qiagen, Hilden, Germany
HiTrap Q HP, 1 ml and 5 ml column	GE Healthcare Bio-Science AB, Uppsala, Sweden
HiLoad 16/600 Superdex 75 prep grade	GE Healthcare Bio-Science AB, Uppsala, Sweden
Collection tubes 14 ml, 105x16 mm, Polystyrol	Sarstedt, Newton, NC, USA
Poly-Prep® Chromatography column	BioRad Laboratories, Munich, Germany
PD MidiTrap G-25 column	GE Healthcare Europe GmbH, Freiburg, Germany
3 kDa Amicon® Ultra Centrifugal Filter Units – 4 ml	Millipore, Schwalbach, Germany
3 kDa and 10 kDa Amicon® Ultra Centrifugal Filter Units – 15 ml	Millipore, Schwalbach, Germany
0.22 µm Whatman Puradisc™ sterile-filter	Whatman, Dassel, Germany



**Table 4: Materials for protein crystallization**

Crystal equipment	Company
MRC2 96-well crystallization plate	Jena Bioscience GmbH, Jena, Germany
24-well EasyXtal plate	Quiagen, Hilden Germany
VIEWseel™ adhesive sheets	Greiner Bio-one, Frickenhausen, Germany
96-Deep well plate	Abgene, Schwerte, Germany
CrystalWand Magnetic™	Hampton Research, Aliso Viejo, CA, USA
CrystalCapHT™	Hampton Research, Aliso Viejo, CA, USA
Mounted CryoLoop™ - 10 and 20 micron with EasySnap Micro Tube	Hampton Research, Aliso Viejo, CA, USA
CrystalCap™ Copper Magnetic™	Hampton Research, Aliso Viejo, CA, USA
CrystalCap Magnetic™	Hampton Research, Aliso Viejo, CA, USA
Micro-Tools	Hampton Research, Aliso Viejo, CA, USA

### 2.2.3 Cell culture materials

Sterile plastic ware was used as indicated in Table 5.

**Table 5: Sterile plastic ware**

Plastic ware	Company
T75 flasks	Greiner, Frickenhausen, Germany
T175 flasks	Greiner, Frickenhausen, Germany
6-well plates	Greiner, Frickhausen, Germany
24-well plates	Greiner, Frickenhausen, Germany
96-well plates	Greiner, Frickenhausen, Germany
IbiTreat 8-well	Ibidi, Munich, Germany
6 cm dishes	Sarstedt, Newton, NC, USA
10 cm dishes	Sarstedt, Newton, NC, USA

96-well plates white	Greiner, Frickenhausen, Germany
96- well plates black	Greiner, Frickenhausen, Germany
XF96-well microplates	Seahorse Biosciences, North Billerica, MA
E-plate 96 well	Roche, Applied Science, Penzberg, Germany
15 ml tubes	Greiner, Frickenhausen, Germany
50 ml tubes	Greiner, Frickenhausen, Germany
0.5, 1.5, 2 ml tubes	Sarstedt, Nümbrecht, Germany
0.22 µm Whatman Puradisc™ sterile-filter	Whatman, Dassel, Germany
0.45 µm filter	Whatman, Dassel, Germany
Cell scraper	Sarstedt, Nümbrecht, Germany
1, 5, 10 ml Injekt®	Braun, Melsungen, Germany

---

## 2.3 Cell culture

### 2.3.1 Cell culture media and cultivation of HT-22 cells

HT-22 cells were obtained from Gerald Thiel (Homburg/Saar) with kind permission of David Schubert (Salk Institute, San Diego, California, USA). The HT-22 cell line was originally selected from HT-4 cells based on glutamate sensitivity. HT-4 cells were immortalized from primary hippocampal neurons using a temperature-sensitive SV-40 T antigen<sup>174</sup>.

HT-22 cells were cultured in Dulbeccos' modified Eagle medium (DMEM, Invitrogen, Karlsruhe, Germany) supplemented with 10 % heat-inactivated fetal calf serum, 100 U/ml penicillin, 100 µg/ml streptomycin and 2 mM glutamine (all from PAA Laboratories GmbH, Germany) as indicated in Table 6. For standard cultivation HT-22 cells were kept in 75 cm<sup>2</sup> culture flasks in a standard unified incubator at 37°C and 5 % CO<sub>2</sub>. Cells were split twice per week in a ratio 1:10 - 1:20. Splitting of HT-22 cells was performed as follows: Growth medium was removed and cells were washed once with 2 ml phosphate buffered saline (1 x PBS, Table 7) to fully remove the growth media. For detachment of cells from the bottom of the flasks, 2 ml of trypsin/EDTA solution (Table 8) was added and cells were incubated 2-5 min. at 37°C. After detaching of the cells, the protease activity was stopped by adding the 3-fold amount of DMEM growth medium (Table 6). Afterwards, the cell suspension was centrifuged at 1.000 x rpm for 5 minutes and the cell pellet resuspended in fresh growth medium. For

determination of cell number a counting chamber (Neubauer Zählkammer, Brand, Wertheim, Germany) was used. Afterwards, cells were seeded into the appropriate culture dishes with a cell density of  $6 \times 10^3$  –  $6 \times 10^4$  cells per well or  $5 \times 10^5$  –  $1.5 \times 10^6$  cells per dishes, depending on the respective experiments (Table 9).

**Table 6: HT-22 standard growth medium**

DMEM-medium with 4.5mg/l glucose and 110 mg/l sodium pyruvate	440 ml
Heat inactivated fetal calf serum (FCS)	50 ml
L-alanyl-L-glutamine 200 mM	5 ml
Penicillin 10.000 U/ml / Streptomycin 10 mg/ml (Pen/Strep)	5 ml

**Table 7: Phosphate buffered saline (PBS), pH 7.4**

NaCl	9 g
Na <sub>2</sub> HPO <sub>4</sub>	0.527 g
KH <sub>2</sub> PO <sub>4</sub>	0.144 g
HCl (0.1M)	q.s. for pH adjustment
Aqua demin	add to a final volume of 1,000 ml

**Table 8: Standard Trypsin/EDTA solution**

Trypsin (7.500 U/mg)	100 mg
Ethylenediamine-tetra-acetic acid (EDTA)	40 mg
PBS	Table 3

**Table 9: HT-22 cells – cell densities**

Cell culture format	cell density cells/cm <sup>2</sup> (cells/well)
96-well plate	~ 6,000 – 12,000 cells/well
24-well plate	~ 40,000 – 60,000 cells/well
6-well plate	~ 180,000 cells/well
ibidi $\mu$ -slide 8-well plates	~ 16,000 – 20,000 cells/well
6 cm dish	~ 500,000 cells/dish
10 cm dish	~ 1,000,000 – 1,500,000 cells/ dish
XF96-well microplates	~ 10,000 cells/well
E-Plate 96-well	~ 10,000 cells/well

### 2.3.2 Cell culture medium and cultivation of primary mouse embryonic cortical neurons

For culturing of primary mouse embryonic cortical neurons, cell culture dishes were coated one day before preparation with 5 % polyethylenimine (PEI, Table 10). Coating was performed by incubation with 5 % PEI for 2-3 h at 37°C. Afterwards the dishes were washed three times with sterile bidest water and dried for 30 min under UV-light. Cell dishes were filled up with MEM+ and incubated overnight in the cell incubator at 37 °C and 5 % CO<sub>2</sub>.

**Table 10: 5% PEI**

Borac acid	3.1 g
Borax	9.0 g
PEI	1 ml
Aqua demin	add to a final volume of 1,000 ml

Cortices were removed from embryonic day 14-16 wild type C57BL/6 mice (Charles River Laboratories, Sulzfeld, Germany) and dissociated by trypsinization and trituration as followed: Isolated cortices were incubated in Hank's balanced salt solution (HBSS, diluted from 10 x HBSS, Invitrogen, Karlsruhe, Germany, Table 12 ) containing 1 mg/ml trypsin (Sigma-

Aldrich, Taufkirchen, Germany) for 15 min. at 37°C. Afterwards, DNase was added for 30 seconds and the cortices were washed with HBSS and mixed with HBSS containing 1 mg/ml trypsin inhibitor (Sigma-Aldrich, Taufkirchen, Germany), and the cell suspension was incubated for further 2 min. at room temperature. Afterwards, the cortices were washed once with HBSS, and triturated in MEM+ obtained from Eagle's minimum essential medium (Invitrogen, Germany, Table 13) by addition of 1 mM HEPES (Biomol, Hamburg, Germany), 26 mM NaHCO<sub>3</sub>, 40 mM glucose, 20 mM KCl, 1.2 mM L-glutamine (each Sigma-Aldrich, Taufkirchen, Germany), 1 mM sodium pyruvate (Biochrom, Berlin, Germany), 10% (v/v) fetal calf serum (FCS) (Invitrogen, Karlsruhe, Germany) and 10 mg/l gentamicin sulfate (Sigma-Aldrich, Taufkirchen, Germany). The titrated cells were centrifuged at 1,000 x g for 5 min. at room temperature. The supernatant was removed and cells cultured in neurobasal medium supplemented with 2 % (v/v) B-27 (Table 11). Afterwards, cells were counted in a cell counting chamber (Neubauer Zählkammer) and seeded into T75 flasks with a density of 10 to 15 x 10<sup>6</sup> cells per flask containing 20 ml MEM+. One day after incubation, the medium was exchanged with neurobasal medium (Table 11) containing 0.5 µM cytosine arabinofuranoside (CAF) to avoid glia cell growth. On day 5 and 7 after seeding of cells, half of the medium was exchanged with fresh neurobasal medium, respectively. Since cultures of primary neurons develop functional NMDA receptors after 6-8 days in culture and are therefore susceptible to glutamate-induced excitotoxicity, experimental treatments were performed with 7-9 day old cultures.

All mediums were obtained from Invitrogen (Karlsruhe, Germany), if not described otherwise. Chemical substances were obtained from Sigma-Aldrich (Taufkirchen, Germany).

**Table 11: Neurobasal medium**

Neurobasal medium (Gibco®)	490 ml
2 % (v/v) B-27 (Gibco®)	10 ml
1 % (v/v) L-glutamine	5 ml
1 % (v/v) Pen/Strep	5 ml

**Table 12: Hank's balanced salt solution (1 x HBSS) pH 7.2**

---

10 x HBSS	50 ml
HEPES	1.2 g
1 % (v/v) Pen/Strep	5 ml
Aqua demin	add to a final volume of 500 ml

---

**Table 13: Eagle's minimum essential medium (MEM)**

---

MEM- Phenolrot	4.695 mg
1 mM HEPES	4.75 mg
26 mM NaHCO <sub>3</sub>	1.1 g
40 mM Glucose	5.0 g
20 mM KCL	0.605 g
1 mM Na-pyruvate	0.6 g
1.2 mM L-glutamine	0.088 g
10 % (v/v) FCS	50 ml
1% (v/v) Pen/Strep	5 ml
Aqua demin	add to a final volume of 500 ml

---

### **2.3.3 Induction and inhibition of cell death in HT-22 neurons**

#### **2.3.3.1 Induction of neuronal cell death**

Neuronal cell death was induced 24 – 48 h after seeding of the HT-22 cells. Induction of cell death was either performed by glutamate-induced toxicity or by tBid over-expression.

##### **2.3.3.1.1 Glutamate-induced toxicity**

Glutamate-induced toxicity in HT-22 cells was performed when cells reached about 70-80 % confluency. For induction of cell death, glutamate solution at a final concentration range from 3-7 mM was used. For glutamate stock solution, D,L-glutamic acid monohydrate (Sigma-Aldrich, Taufkirchen, Germany) was dissolved in Dulbeccos's modified eagle medium (DMEM; PAA Laboratories GmbH; Cölbe, Germany) to a stock concentration of 1 M. The pH was adjusted to 7.2 with concentrated sodium hydroxid solution (NaOH). The stock solution was stored at -20°C. For measuring glutamate toxicity the stock solution was diluted in DMEM to final concentrations of 3 mM to 7 mM instantaneously before treatment, and cell growth medium was removed and replaced by the final glutamate solution. To investigate neuroprotective properties of the inhibitors used in this study (0), growth medium of HT-22 cells was exchanged with cell culture medium containing glutamate and/or substances in the final concentrations, respectively. Between 4 h and 24 h after treatment, cells were analyzed following the the described procedures for protein or RNA analysis, cell viability, flow cytometry, epi- and confocal microscopy or immunoprecipitation and immunoblots.

##### **2.3.3.1.2 tBid induced-toxicity**

For induction of tBid-mediated cell death, HT-22 cells were seeded in 24-well plates with a density of 40,000 cells per well. Twenty-four hours after seeding, tBid overexpression was induced by transfection of cells with a tBid- encoding plasmid (pIRES-tBid, 2.3.5.1). Between 17 h to 24 h after tBid overexpression cell morphology, cell viability and mitochondrial membrane potential ( $\Delta\psi_m$ ) was analyzed as described below.

### 2.3.3.2 Inhibition of neuronal cell death

To inhibit neuronal cell death in HT-22 cells, the Bid inhibitor BI-6c9 (Sigma-Aldrich, Taufkirchen, Germany; Figure 6) was dissolved in dimethyl sulfoxide (DMSO) to a stock concentration of 10 mM. The stock solution was stored at -20°C. To achieve neuroprotection against glutamate- and tBid-induced toxicity BI6c9 was used at final concentrations of 10  $\mu$ M in DMEM (Table 6). The Bid inhibitor BI-6c9 was used as a positive control for neuroprotection in all experiments performed in this study.

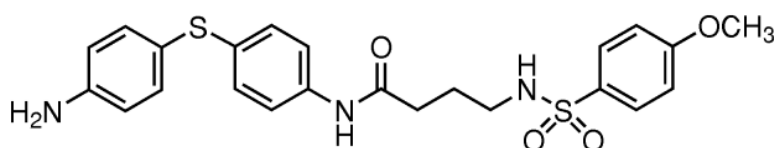


**Figure 6: Chemical structure of the Bid inhibitor BI-6c9**

Novel small-molecule Bid inhibitors used in this study (3.1.3) were dissolved in dimethyl sulfoxide (DMSO) to a stock concentration of 100 mM and stored at -20°C, respectively. To screen the newly synthesized structures for their ability to provide neuroprotection against glutamate- and tBid-induced toxicity, compounds were diluted in cell culture medium to final concentration ranges of 0.1  $\mu$ M to 100  $\mu$ M. Chemical structures of all novel small-molecule inhibitors are provided in Table 67 - Table 70 (Appendix).

The unspecific anion channel blocker and VDAC inhibitor 4,4'-Diisothio-cyanatostilbene-2,2'-disulfonic acid (DIDS; Figure 2) was dissolved in DMSO to a stock concentration of 100 mM. The stock solution was stored at -20°C and diluted with cell culture medium prior to each experiment to final concentrations of 100  $\mu$ M up to 1 mM.

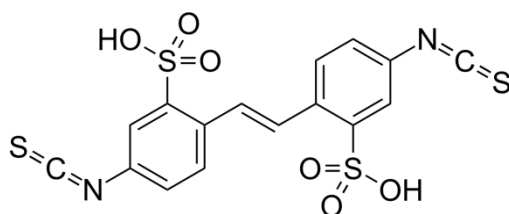


**Figure 7: Chemical structure of 4,4'-Diisothio-cyanatostilbene-2,2'-disulfonic acid (DIDS).**

DIDS was used to analyze the impact of the voltage-dependent anion channel (VDAC) in glutamate- and tBid-induced toxicity in HT-22 cells.



In order to exclude specific effects of the solvent of the different chemical substances and inhibitors, vehicle controls (DMSO controls) were always treated with medium containing the highest concentration of the solvent that was present at the highest applied concentration of the active compounds during the experiment.

### 2.3.4 Induction of cell death in primary cortical neurons (PCN)

Cell death in primary cortical neurons was performed by glutamate-induced excitotoxicity via activation of NMDA receptors that are functionally expressed at 6-8 days *in vitro* (DIV). Therefore treatments of primary cortical neurons were performed with 7-9 old cell cultures and excitotoxicity was induced by glutamate (20-25  $\mu\text{M}$ ) in neurobasal medium supplemented with 2 % B-27 (Table 11). Cultured neurons were harvest 4 h and 22- 24 h after glutamate exposure, and 30-45 x 10<sup>6</sup> cells per treatment condition were analyzed following the described procedures for immunoprecipitation studies.

### 2.3.5 Transfection protocols

HT-22 neurons were transfected either in 96-well plates, 24-well plates, ibidi  $\mu$ -slide 8-well plates, 6 cm<sup>2</sup> or 10 cm<sup>2</sup> dishes, depending on the respective experiments. Plasmid transfections were performed 24 h after seeding of cells and siRNA transfections were performed as reverse transfections instantaneous prior to seeding of cells.

#### 2.3.5.1 Plasmid and gene transfection

For plasmid transfections HT-22 cells/well were seeded in 24-well plates at a density of 4 x 10<sup>4</sup> or in ibidi  $\mu$ -slide 8-well plates (Ibidi, Munich, Germany) at a density of 16.000 cells/well 24 h before transfection, and incubated under normal growth conditions (37°C, 5% CO<sub>2</sub>). On the day of transfection growth medium was replaced with 500  $\mu\text{l}$  fresh standard growth medium and substance pre-treatment (BI-6c9, DIDS, novel Bid inhibitors) was performed 1 h before the following plasmid transfection. The plasmids pIRES-tBid, pDSRed2-Bid, pc-mBid13-y47, pc-mBid13-D51, FLAG-VDAC1, FLAG-control or empty vector pcDNA 3.1+ were dissolved separately in antibiotic- and serum-free medium and Attractene transfection reagent (Qiagen, Hilden, Germany) was added to the DNA solution. To allow complex formation samples were incubated for 10 to 15 minutes at RT. 24-60  $\mu\text{l}$  of the transfection mixture was added to the cell culture medium to a final concentration of 0.5-2  $\mu\text{g}$  DNA/well and 0.75-4.5  $\mu\text{l}$  Attractene/well. Controls were treated with 24-60  $\mu\text{l}$  antibiotic- and serum-free cell culture medium only and vehicle controls additionally with 0.75-4.5  $\mu\text{l}$  Attractene/well. Cells were incubated under normal growth conditions until further

experiments. Cell morphology and cell viability was analyzed 16 h to 20 h after over-expression tBid or novel Bid constructs, respectively. Immunostaining and immunoprecipitation of FLAG-VDAC1 was performed 24 h – 48 h after over-expression of FLAG-VDAC1. Immuno-analysis of pDSRed2-Bid was performed 24 h – 48 h after transfection.

### **2.3.5.2 SiRNA transfection**

For siRNA transfections Lipofectamine RNAiMax (Invitrogen, Karlsruhe, Germany) was used. VDAC1 siRNA (VDAC1 siRNA1 and VDAC1 siRNA2), VDAC2 siRNA (VDAC2 siRNA a and VDAC2 siRNA b), Bid siRNA (SASI 115198 and SASI 115200) or non-functional scrambled siRNA were separately dissolved in Opti-MEM I (Invitrogen, Karlsruhe, Germany). After 10 min. of equilibration at RT, each siRNA solution was combined with the respective volume of the Lipofectamine RNAiMax solution and mixed gently. For reverse transfection the transfection mixture was filled into the cell culture wells or dishes, depending on the respective experiments, and allowed to form siRNA liposome complexes for further 20 min. at room temperature. After addition of antibiotic-free cell suspension, a final concentration of 20 nM to 80 nM siRNA and 2 µl/ml Lipofectamine was reached. Controls were treated with 100 µl/ml Optimem only, and vehicle controls additionally with 2µl/ml Lipofectamine RNAiMax. SiRNA sequences see 2.3.5.2.

SiRNA transfections were performed in 10 cm<sup>2</sup> dishes for protein analysis or in 24-well plates for RNA analysis. Gene silencing was verified by RT-PCR and Western blotting. For functional analysis of protein depletion, siRNA transfections were carried out in cell culturing formats depending on the respective experiment.

## 2.4 Cell viability assays

### 2.4.1 Analysis of cell morphology

After different cell death stimuli, such as glutamate- or tBid-induced toxicity, HT-22 neurons show excessive alterations in cell morphology: Cells clearly appear shrunken, rounded up and detached from the bottom of the culture plate. Therefore, analysis of cell morphology can be used for estimating cell viability of HT-22 cells.

For analysis of cellular morphology, transmission light microscopy of living HT-22 cells, growing as monolayers, was performed using an Axiovert 200 microscope (Carl Zeiss, Jena, Germany) equipped with a Lumenera Infinity 2 digital camera (Lumenera Corporation, Ottawa, Canada). Light was collected through a 10 x 0.25 NA objective (Carl Zeiss, Jena, Germany), and images were captured using phase contrast. The INFINITY ANALYZE software (Lumenera Corporation, Ottawa, Canada) was used for digital image recording and image analysis. Images were captured using phase contrast.

### 2.4.2 MTT assay

The 3-(4,5-dimethylthiazol-2-yl)-2,5-diphenyltetrazolium bromide (MTT) assay is a well accepted colorimetric method to determine cell proliferation, cell viability and cytotoxicity. The cellular reduction of the yellow colored monotetrazolium salt MTT to purple colored formazan is performed by either a lysosomal/endosomal cell compartment or active mitochondria in living cells<sup>175</sup>. Since only viable cells with active metabolism convert MTT into a purple formazan product with an absorbance maximum near 570 nm that can be easily detected by absorptive spectroscopy, color formation serves as a useful and convenient marker of the metabolic activity in viable cells.

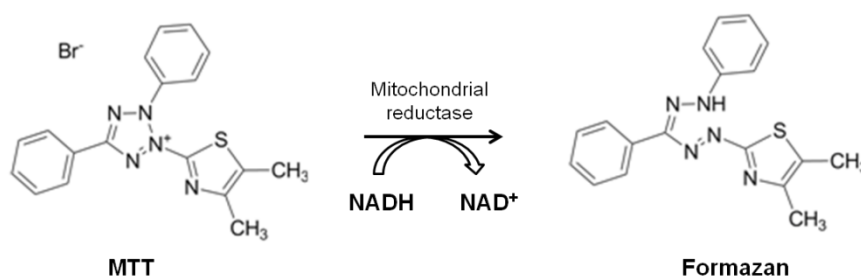


**Figure 8: Reduction of yellow MTT to purple colored formazan**

Cell viability of HT-22 cells was evaluated 16-24 h after glutamate- or tBid-induced toxicity and respective substance pre- or co-treatments. Quantification of cell viability in HT-22 cells was performed either in standard 96-well plates or standard 24-well plates. MTT (Sigma-Aldrich, Munich, Germany) was dissolved in 1 x PBS at a concentration of 2.5 mg/ml. When

morphological changes of the cells indicated cell death, the MTT reagent was added to the media at final concentrations of 0.25 mg/ml, followed by 1 h incubation at 37°C. After terminating the reaction was terminated by removing the media from cells and freezing the plate at -80 °C for at least 1 h. The formazan crystals were dissolved in dimethyl sulfoxide (DMSO) and absorbance was determined at 570 nm (FluoStar OPTIMA, BMG Labtech, Offenburg, Germany). Background was detected at 630 nm and subtracted accordingly. Cell viability levels were demonstrated as percentage of absorption levels in untreated control cells (100 % cell viability). A DMSO control was used as solvent control. For statistical analysis the experiments were repeated at least three times.

### **2.4.3 Real-time measurements of cell impedance (xCELLigence)**

Impedance-based real-time detection of cellular events was conducted using the xCELLigence system Real-Time Cell Analyzer RTCA-MP (Roche Diagnostics, Penzberg, Germany), which measures the electrical impedance between gold micro-electrodes integrated into the bottom of custom made tissue culture plates (E-plates 96)<sup>176</sup>. Due to a high electrical resistance of cells, the electrical impedance is the higher the more cells are attached to the bottom of the E-plates. Therefore this system allows for monitoring changes in cell proliferation, cell viability and morphology as well as alterations in cell number and cell adhesion, and especially the kinetics of these processes in a large number of tissue culture wells simultaneously throughout the experiments. Differences in the electrical impedance of cells are displayed as cell index (CI) as function of time.

HT-22 cells were cultured with a density of 10,000 – 12,000 cells/well in 96- well E-plates and recordings were started immediately after seeding. At twenty-four hours after seeding of cells, when the cell index exceeded a value of about one, cells were treated with glutamate (3-7 mM) and/or with different inhibitor substances dependent on the experiment. Since the system is very sensitive to changes in temperature, a complete removal of the medium was avoided to prevent a persistent breakdown of the impedance. Recording of cell index (CI) values and normalization was performed using the RTCA Software 1.2 (Roche Diagnostics, Penzberg, Germany). Background impedance caused by the media was recorded before seeding of the cells and subtracted automatically by the RTCA software.

After concluding each experiment, E-plates were recycled by removing media, washing the plates twice with aqua demin. and adding standard Trypsin/EDTA for 15-20 minutes. Afterwards 1xTE was removed, plates were washed 3 times. To reassure sterility the plates were irradiated with UV light for 30 minutes. For statistical analysis the experiments were repeated at least three times.

#### 2.4.4 ATP- luminescence measurements

Adenosinetriphosphate (ATP) can be used to assess the functional integrity of living cells since all cells require ATP for survival and their energy-dependent specialized functions. Any form of cell injury results in a rapid decrease in cytoplasmic ATP-levels. The detection of cellular ATP is based on a bioluminescent assay, which utilizes an enzyme, luciferase, to catalyze the formation of light from ATP and luciferin according to the following reaction:



**Figure 9: Formation of light from ATP and luciferin**

The emitted light intensity is linearly related to the cellular ATP concentration and can be easily detected by a plate reader measuring the luminescence. As each individual cell contains ATP, the method can not only be used for detection of cellular ATP-levels, but also for the direct assessment of cell numbers.

For analysis of total ATP levels, HT-22 neurons were seeded in white 96-well plates (Greiner, Frickenhausen, Germany) for luminescence measurements. Twenty four hours after seeding, cells were treated with 5 mM glutamate and when indicated additionally with the Bid inhibitor BI-6C9 (10  $\mu\text{M}$ ), novel compounds (20  $\mu\text{M}$ ) or the VDAC inhibitor DIDS (500  $\mu\text{M}$  – 1000  $\mu\text{M}$ ) respectively. Cellular ATP levels were detected approximately 20 h after glutamate exposure using the ViaLight™ Plus-Kit (Lonza, Verviers, Belgium) according to the manufacturer's protocol. Briefly, the culture plate was allowed to cool down to room temperature for at least 5 minutes. In this time all reagents were prepared following the manual instructions. Afterwards, cells were treated with the nucleotide releasing reagent, and incubated for 5 min. at room temperature. The ATP monitoring reagent was then injected into each well and luminescence was detected immediately by the FluoStar plate reader (BMG Labtech, Offenburg, Germany). The emitted light intensity was recorded for quantification of ATP-levels and values were given as relative values in % to control cells. The experiments were repeated at least three times with an n=8 per treatment condition.

### 2.4.5 Measurements of oxygen consumption (Seahorse Bioscience)

Measurement of oxygen consumption from intact cells enables evaluation of mitochondrial bioenergetics and metabolism under conditions that are more physiologically realistic compared to isolated mitochondria. Metabolic substrate uptake (oxygen, glucose, fatty acids) and energy conversion through oxidation and reduction reactions are executed by several intracellular biochemical processes (glycolysis, Krebs cycle, electron transport, OXPHOS) that result in the production of ATP and the release of heat and chemical by-products (lactate and CO<sub>2</sub>) into the extracellular environment. Using the Extracellular Flux Analyzer (Seahorse Bioscience, North Billerica, MA, USA) the uptake and excretion of metabolic end products can be measured in real-time. The XF Cell Mito Stress Test Kit (Seahorse Bioscience) was used to detect extracellular flux changes of oxygen and protons in the media immediately surrounding adherent cells by using fluorescent biosensors (oxygen and pH) and a sensor cartridge coupled to a fiber-optic waveguide<sup>177</sup>. From this waveguide light at various excitation wavelength (oxygen = 532 nm, pH = 470 nm) is delivered and a fluorescent signal is transmitted to a set of highly sensitive photodetectors<sup>177</sup>. In cells, oxygen consumption and proton extrusion cause rapid but measurable changes in oxygen tension and pH which are detected within a transient micro chamber in each well of a microplate. Additionally, each sensor cartridge is equipped with four reagent delivery chambers per well for injection of different reagents to analyze the respective mitochondrial bioenergetics. Thereby, four key parameters of mitochondrial function, namely basal respiration, ATP production, proton leak, and maximal respiration, were measured in a microplate (Figure 10). Thus a complete mitochondrial stress profile can be recorded:

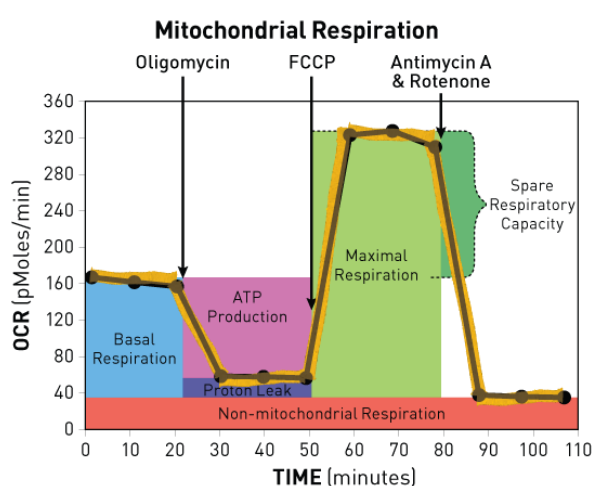


**Figure 10: Mito Stress Profile**

Key parameters of mitochondrial function: basal respiration, ATP turnover, proton leak, and maximal respiration, and spare respiratory. (Picture from Seahorse Bioscience, [www.seahorsebio.com](http://www.seahorsebio.com))

Measurements of oxygen consumption rate (OCR) in HT-22 cells were assessed using an XF96 Extracellular Flux Analyzer (Seahorse Biosciences, North Billerica, MA, USA), which directly records the OCR in cells that remain attached to the culture plate by using calibrated optical sensors. The OCR recordings were carried out as previously described with minor modifications<sup>178</sup>. Briefly, HT-22 cells were seeded in XF96-well cell culture microplates (Seahorse Bioscience, North Billerica, MA) at a density of 10,000 cells/well in standard growth medium and incubated at 37°C and 5 % CO<sub>2</sub> for ~24 h. For measuring effects of gene depletion on OCR of HT-22 cells, siRNA transfections were performed in the XF96-well microplates instantaneously prior to seeding of cells. Twenty-four hours after seeding, cells were treated with glutamate (5-7 mM) and/or BI-6c9 (10 µM), novel compounds (20 µM) or DIDS (500 µM and 1000 µM) for 20 h, respectively. Before starting the measurements, the growth medium was washed and replaced with ~180 µl of assay medium (with 4.5 g/L glucose as the sugar source, 2 mM glutamine, 1 mM pyruvate, pH 7.35) and cells were incubated at 37°C for 60 min. Three baseline measurements were recorded before the addition of compounds. To assess mitochondrial dysfunction, respiratory chain poisons were used. The ATP synthase inhibitor Oligomycin was injected in Port A at a final concentration of 3 µM to measure OCR in the absence of oxidative phosphorylation. The protonophore FCCP was subsequently injected in Port B at a concentration of 0.4 µM to dissipate the proton gradient across the inner mitochondrial membrane and thereby to assess maximal respiratory capacity (MRC). Co-injection of the complex I/III inhibitors Rotenone/Antimycin A in Port C at concentrations of 1 µM, respectively, was used to inhibit O<sub>2</sub> consumption by the mitochondrial electron transport chain and thus to address non-mitochondrial respiration. Three measurements were performed after the addition of each compound by a 4-minute mix cycle used to oxygenate the medium and 3-minute measurement cycle to assess respiration. For comparing OCR after compound exposure to OCR in non-treated cells, the absolute cell number is insignificant since the same population of cells is compared. Therefore, most of the results are indicated as normalized OCR (% baseline rate) for each individual cell population to minimize variability due to slight differences in plating and viability during culture and treatment time (~48 h). The experiments were independently repeated at least three to five times.

## 2.5 Flow cytometric measurements (FACS)

For Fluorescence-activated cell sorting (FACS) the Guava Easy Cyte 6-2 L system (Merck Millipore, Schwalbach, Germany) was used. For FACS measurements cells were treated with glutamate (3-5 mM) or transfected with pIRES-tBid 24 h after seeding in 24-well plates. SiRNA transfections were directly performed in the 24-well plates. Treatment of cells with the Bid inhibitor BI-6c9 (10  $\mu$ M), novel compounds (20  $\mu$ M) or DIDS (500  $\mu$ M, 1000  $\mu$ M) was performed simultaneously or 1 h prior to the cell death stimulus, dependent on the respective experiments. Seventeen to twenty hours after treatment, cells were analyzed as further described. Data were always collected from 10,000 cells per sample and 3-4 samples per condition were measured for each experiment. For quantitative analysis the GuavaSoft Software package was used. Measurements shown in this thesis are representative of at least three to five independent experiments, each with  $n = 3-4$ .

### 2.5.1 Analysis of apoptotic and necrotic cell death with Annexin-V-FITC staining

To determine apoptotic and necrotic cell death, cells were stained with Annexin-V-FITC and propidium iodide (PI) and subsequently analyzed by flow cytometry. In apoptotic cells, the membrane phospholipid phosphatidylserin (PS) is translocated from the inner to the outer leaflet of the plasma membrane, thereby exposing PS to the external cellular environment. Annexin-V (AV) is a calcium dependent phospholipid-binding protein with high affinity for PS on the cell surface in early phases of apoptosis. The conjugation of annexin-V to the green-fluorescent FITC dye allows for flow cytometric analysis of cells that undergo apoptosis. The red-fluorescent propidium iodide dye (PI) is used to stain late apoptotic or necrotic cells. Viable cells with intact membranes exclude PI, whereas the membranes of dead and damaged cells are permeable to PI. After treatment of cells with both AV and PI, apoptotic cells show green fluorescence ( $AV^+$ ), dead cells show red and green fluorescence ( $AV^+/PI^+$ ) and viable cells depict no fluorescence.

After respective treatments, HT-22 cells from 3 wells per condition were harvest using trypsin/EDTA, washed once with 1 x PBS and loaded with 2  $\mu$ l of annexin V-fluorescein isothiocyanate (FITC) and 2  $\mu$ l of propidium iodide (PI) according to the manufacturer's protocol (Annexin-V-FITC Detection Kit, Promokine, Heidelberg, Germany). After incubation for 5 min. at RT in the dark, cells were analyzed by FACS. Annexin-V-FITC was excited at 488 nm and emission was detected with the green filter at 525/530 nm. Fluorescence of PI was excited at 488 nm and fluorescence emission was detected with the red filter at 690/650 nm. To exclude cell debris and doublets, cells were appropriately gated by forward versus side scatter and pulse width, and 10,000 gated events per sample were collected.



### 2.5.2 Analysis of lipid peroxidation with BODIPY

For detection of cellular lipid peroxidation, BODIPY 581/591 C11 (Invitrogen, Karlsruhe, Germany) was used. BODIPY is a sensitive fluorescent reporter for lipid peroxidation, undergoing a shift from red to green fluorescence emission upon oxidation of the phenylbutadiene segment of the fluorophore. This oxidation-dependent emission shift enables fluorescence ratio imaging of lipid peroxidation in living cells. For detection of cellular lipid peroxidation cells were stained with 2 mM BODIPY 581/591 C11 (Invitrogen, Karlsruhe, Germany) for 60 minutes in standard growth medium at indicated time points after glutamate- or tBid-induced toxicity and/or substance treatment. Afterwards, cells were harvested by using trypsin/EDTA, washed once with 1 x PBS and resuspended in 1 x PBS. Flow cytometry was performed using 488 nm UV line argon laser for excitation, and BODIPY emission was recorded at 530 nm (green) and 585 nm (red) by flow cytometry (FACS). Data were collected from at least 10,000 events per sample at three independent experiments each with  $n = 3-4$ . Increases in green fluorescence indicated formation of lipid peroxides.

### 2.5.3 Analysis of mitochondrial membrane potential with TMRE

For detection of mitochondrial membrane potential ( $\Delta\psi_m$ ) in whole cells the MitoPT™ TMRE kit (Immunochemistry Technologies, Hamburg, Germany) followed by flow cytometric measurements (FACS) was used. The kit contains tetramethylrhodamin ethyl ester (TMRE) which is a lipophilic, cationic fluorescent redistribution dye. This dye has a delocalized positive charge dispersed throughout its molecular structure, and due to its lipophilic solubility TMRE is able to penetrate into living cells. As the mitochondrial membrane potential collapses and cells enter apoptosis or other oxidative stress driven mechanism, the amount of fluorescence will drop as the concentrated TMRE dye equilibrates back out of the mitochondria and into the cytosol, where it is diluted to a lower dye concentration. Therefore, cells with healthy mitochondria appear red (high TMRE fluorescence), whereas dead cells are depicted by a reduced magnitude of red fluorescence, indicating loss of  $\Delta\psi_m$ .

When cell death occurred after the respective treatments (see outlined above), HT-22 cells were collected and washed with 1 x PBS. After incubation of cells with 0.2  $\mu\text{M}$  TMRE for 30 min at 37 °C, cells were washed and resuspended in assay buffer. As a positive control for a complete loss of  $\Delta\psi_m$ , the protonophore carbonyl cyanide m-chlorophenylhydrazone (CCCP, 50  $\mu\text{M}$ ) was applied to intact cells 30 min. prior to harvesting. To exclude autofluorescence of the cells a non-treated negative control, which was not stained by TMRE, was prepared. Flow cytometry was performed using fluorescence excitation at 488 nm and TMRE emission at 680 nm. To exclude cell debris and doublets, cells were appropriately gated by forward versus side scatter and pulse width, and 10,000 events were gated per

sample and data were collected from 3-4 independent samples per treatment condition and the experiments were repeated at least three times.

## **2.6 Immunocytochemistry**

### **2.6.1 Visualization of mitochondria**

For detection of mitochondrial morphology changes during cell death, HT-22 neurons were seeded in ibidi  $\mu$ -slide 8-well plates (Ibidi, Munich, Germany) at a density of 16,000 – 20,000 cells per well 24 hours before treatment. For visualization of mitochondria, cells were transfected with the green fluorescent mGFP plasmid. Alternatively, mitochondria were visualized by MitoTracker Green/DeepRed according to the manufacturer's protocol (Invitrogen, Karlsruhe, Germany). Nuclei were stained with DAPI (4',6-diamidino-2-phenylindole dihydrochloride) for endpoint analysis on a fluorescence microscope (DMI6000B, Leica, Wetzlar, Germany). MitoTracker DeepRed was dissolved in DMSO at a final stock concentration of 50  $\mu$ M and kept protected from light. For applications on cells the MitoTracker reagent was diluted 1:250 in culture medium (final working concentration 200 nM) together with DAPI (1  $\mu$ g/ml) for counterstaining of the nuclei. Staining solution was added to the cells and incubated for 20-30 minutes at 37°C before starting the respective treatment. After completing the experiment, cells were washed with 1 x PBS, fixed with 4 % paraformaldehyde (PFA) and washed again twice with PBS. Mitochondria were visualized by epifluorescence microscopy (DMI6000B Leica, Wetzlar, Germany) for characterization and counting of mitochondria (see 2.6.2). Images were taken using a confocal laser scanning microscope (Leica SP5, Leica, Wetzlar, Germany).

### **2.6.2 Characterization of mitochondrial morphology**

For evaluation and classification of mitochondrial morphology, mitochondria of HT-22 cells, cells were seeded in ibidi  $\mu$ -slide 8-well plates (Ibidi, Munich, Germany) at a density of 16,000 – 20,000 cells per well. Twenty-four hours after seeding, cells were treated with glutamate (3-5 mM) and/or BI-6c9 (10  $\mu$ M) or DIDS (500  $\mu$ M and 1000  $\mu$ M) for 17-20 h, respectively. Mitochondria and nuclei were visualized as described before (2.6.1). Endpoint pictures were taken after fixation of cells with 4% paraformaldehyde (PFA) using confocal fluorescence microscopy (Leica SP5, Leica, Wetzlar, Germany). Three categories of mitochondrial morphology were defined as follows: Healthy cells display category I: elongated tubulin-like mitochondria, which are equally distributed throughout the cytosol. Category II mitochondria are defined as intermediate and round mitochondria, the cells do not show apoptotic features, e.g. shrunken nuclei, and are not detached. In contrast, damaged and dying cells contain category III mitochondria, which are strongly fragmented. In

these cells, mitochondrial fragmentation is accompanied by an apoptotic phenotype, showing nuclear condensation and the peri-nuclear arrangement of the mitochondrial fragments. For quantification of mitochondrial morphology, at least 500 cells per condition were counted by two investigators blinded towards the treatment condition in at least three independent experiments.

### 2.6.3 Immunocytochemistry of Bid and VDAC1

For detection of Bid and VDAC1 localization in healthy cells and during cell death, HT-22 neurons were seeded in ibidi  $\mu$ -slide 8-well plates (Ibidi GmbH, Munich, Germany) at a density of 16,000-20,000 cells/well and transfected with the pDSRed2-Bid or the FLAG-VDAC1 plasmid. Twenty-four hours after transfection cells were treated with glutamate (5 mM) or in case of Flag-VDAC1 transfection with BI-6c9 (10  $\mu$ M). To visualize mitochondria, cells were co-transfected with mGFP or alternatively, mitochondria were stained with MitoTracker Green as described before. For fixation of cells, culture medium was removed, cells were washed once with 1x PBS and fixed with 4 % PFA for 20 min. and washed again with 1 x PBS. After fixation, pDSRed2-Bid and mGFP-transfected cells were instantaneously analyzed by confocal fluorescence microscopy. In contrast, membranes of cells transfected with Flag-VDAC1 were permeabilized by exposure for 5 min. to 0.4 % Triton X-100 (Sigma-Aldrich, Taufkirchen, Germany) in 1x PBS. After fixation, cells were placed in blocking solution (3 % horse serum (Invitrogen, Karlsruhe, Germany) in 1x PBS) for 30-60 minutes. To visualize FLAG-VDAC1, cells were exposed to a monoclonal anti-FLAG antibody (1:200 in block solution, Sigma-Aldrich, Munich, Germany), for 2 h at room temperature. Afterwards, cells were washed three times with 1 x PBS followed by incubation for 1-2 hours with the secondary Dylight 649 anti-mouse antibody (1:200, Merck Millipore, Darmstadt, Germany). After washing of cells three times with 1 x PBS, cells were analyzed by confocal fluorescence microscopy. For immunocytochemistry of endogenous Bid, cells were exposed to a polyclonal anti-Bid antibody (1:200, Cell signaling, Danvers, Massachusetts, USA) overnight at 4°C and subsequent 2.5 h at room temperature, followed by an incubation for 2 hours with a secondary biotinylated anti-rabbit IgG antibody (1:200, Vector Labs, Burlingame, CA. USA) and 30 min. in the presence of streptavidin oregon green 514 conjugate (Invitrogen, Karlsruhe, Germany) according to the manufacturers protocol. The specificity of the respective Bid or FLAG-VDAC1 immune reactivity was controlled by emission of the primary antibody in parallel staining of negative controls. Images were acquired using a confocal laser scanning microscope (Leica SP5, Leica, Wetzlar, Germany) as described below.

## **2.7 Epifluorescence and confocal laser scanning microscopy (CLSM)**

### **2.7.1 Epifluorescence microscopy**

Imaging of mitochondrial morphology or TMRE stained HT-22 neurons was performed using a Leica DMI6000B fluorescence microscope, equipped with a DCF360FX-camera (both Leica, Wetzlar, Germany). TMRE red fluorescence and MitoTracker Deep Red fluorescence were excited using a  $620 \pm 60$  nm band pass filter and fluorescence emission was collected using a  $700 \pm 75$  nm band pass filter (Filter Cy5, Leica, Wetzlar, Germany). DAPI fluorescence was excited using  $360 \pm 40$  nm band pass filter, and emission was collected using a  $470 \pm 40$  nm band pass filter (Filter A4, Leica, Wetzlar, Germany). MitoTracker Green and mGFP fluorescence was excited at a wavelength of 488 nm and emission was detected using a 560 nm long pass filter. For digital imaging the software LAS AF (Leica, Wetzlar, Germany) was used.

### **2.7.2 Confocal laser scanning microscopy**

For detection of mitochondrial morphology changes, VDAC1-induced toxicity as well as VDAC1 and Bid localization in healthy and dead cells, HT-22 neurons were immunostained as described before. Images were acquired using a confocal laser scanning microscope (Leica SP5, Leica, Wetzlar, Germany) equipped with a diode (405 nm), an argon laser (458/476/488/496/514 nm) and two helium-neon lasers (543 nm and 633 nm). An Acousto-Optical-Beam-Splitter (AOBS) serves as tunable dichroic for all lasers. Light was collected through a 63 x 1.4 NA, oil immersion objective. MGFP, MitoTracker Green and oregon green fluorescence was excited at 488 nm and emissions were detected between 500 nm and 535 nm bandwidth. DyLight-stained Flag-VDAC1 was excited at 543 nm and emission was detected between 555 nm and 620 nm. MitoTracker DeepRed fluorescence was detected by excitation at 633 nm and emission between 640 nm and 750 nm. For digital imaging the software LSM Image Browser 4.2.0 (Carl Zeiss, Jena, Germany) was used.

## 2.8 Protein analysis

### 2.8.1 Protein sample preparation from HT-22 cells

For obtaining total protein extracts from HT-22 cells, cells were seeded either at a density of  $7 \times 10^4$  cells per well in 24-well plates or at a density of  $1-1.5 \times 10^6$  cells per dish in  $10 \text{ cm}^2$  dishes for western blot analysis, and at a density of  $1.5 \times 10^6$  cells per flask in T75 flask or at a density of  $4 \times 10^6$  cells per T175 flask for immunoprecipitation experiments. After respective treatments, cells were washed with cold  $1 \times$  PBS, lysed with protein lysis buffer (Table 14) supplemented with 1 mM DTT, 1% Triton-X-100, Complete Mini Protease Inhibitor Cocktail and Phosstop Phosphatase Inhibitor Cocktail (1 tablet per 10 ml, both Roche, Mannheim, Germany) and detached with a cell scraper. For immunoprecipitation studies, cells from 3 flasks per condition were pooled. All steps were performed at  $4^\circ\text{C}$ . After centrifugation at  $15.000 \times g$  for 15 min at  $4^\circ\text{C}$  supernatants were stored at  $-80^\circ\text{C}$  until further use.

**Table 14: Protein lysis stock-buffer for HT-22 cells; pH 7.8**

0.25 M D-Mannitol	4.56 g
0.05 M Tris	0.788 g
1 M EDTA	0.038 g
1 M EGTA	0.038 g
Bidest H <sub>2</sub> O ad	100 ml

### 2.8.2 Protein sample preparation from primary mouse cortical neurons (PCN)

For total protein extracts from primary mouse cortical neurons (PCN), neurons were cultured in PEI-coated T75 flask at a density of  $10-15 \times 10^6$  cells per flask. For immunoprecipitation studies and western blot analysis, neurons from three flasks per conditions were pooled. After respective glutamate treatment, cells were washed in warm  $1 \times$  PBS, and lysed in lysis buffer for primary neurons and brain tissue samples (Table 15) supplemented with Complete Mini Protease Inhibitor Cocktail and Phosstop Phosphatase Inhibitor Cocktail (1 tablet per 10 ml, both Roche, Mannheim, Germany). Lysis and scratching of cells was performed at  $4^\circ\text{C}$ . Protein extracts were frozen 3 times with liquid nitrogen and thawed again at room temperature before extracts were centrifuged at  $13.000 \text{ g}$  for 10 min at  $4^\circ\text{C}$ . The supernatant was placed in a new tube and stored at  $-80^\circ\text{C}$  until further use.

**Table 15: Protein Lysis Buffer for primary neurons and brain tissue; pH 7.4**

50 mM HEPES	119.15 mg
150 mM NaCl	87.66 mg
4 mM EGTA	80 µl (0.5 M EGTA-stock solution)
10 mM EDTA	100 µl (1 M EDTA-stock solution)
15 mM Na <sub>4</sub> O <sub>7</sub> P <sub>2</sub>	75 µl (2 M Na <sub>4</sub> O <sub>7</sub> P <sub>2</sub> -stock solution)
50 mM NaF	20.99 mg
5 mM Na <sub>3</sub> VO <sub>4</sub>	25 µl (2 M Na <sub>3</sub> VO <sub>4</sub> -stock solution)
1 mM DTT	100 µl (100 mM DTT-stock solution)
1 mM PMSF	100 µl (100 mM PMSF-stock solution)
0.2% NP-40	20 µl
Bidest H <sub>2</sub> O ad	10 ml

Lysis buffer was always prepared fresh before starting the experiment and stored at 4°C in the dark during use.

### 2.8.2 Protein sample preparation from cortex and hippocampal mice brain tissue

For obtaining total protein extracts from mice brain tissue, brains were isolated from untreated control C57BL/6 mice and from male C57BL/6 mice subjected to transient middle cerebral artery occlusion (MCAo, see 2.10). Cortex homogenates for immunoprecipitation and western blot analysis were generated from 4 mm sections of the ipsi- and contralateral parietal cortex (2 mm +/- bregma) respectively at 2 h, 6 h and 24 h after the onset of ischemia. Hippocampal homogenates were generated from approximately half of the hippocampus of the respective mice. After isolation of brain tissue, brain slices were separately transferred in a pre-cooled clean glas-douncer filled with 500 µl lysis buffer for brain tissue (Table 15), supplemented with Complete Mini Protease Inhibitor Cocktail and Phosstop Phosphatase Inhibitor Cocktail (1 tablet per 10 ml, both Roche, Mannheim, Germany), respectively. Each tissue sample was homogenized by douncing it 10 times followed by centrifugation at 800 x g for 5 min. at 4°C. Tissue homogenates were stored on ice until further use. For immunoprecipitation and western blot analysis, samples were used immediately without freezing at -80°C.

### 2.8.3 Determination of protein amount in cell lysates

For determination of protein amounts, the principle of the bicinchoninic acid (BCA) assay, which is well accepted for colorimetric detection and quantification of total protein, was used. This method is based on the reduction of  $\text{Cu}^{2+}$  ions to  $\text{Cu}^+$  ions by the peptide bonds in proteins in an alkaline medium (Biuret-reaction). The amount of reduced  $\text{Cu}^{2+}$  is proportional to the amount of protein present in the solution. The following purple-colored reaction product of this assay is formed by the chelation of two molecules of BCA with one cuprous ion. This water-soluble complex exhibits a strong absorbance at 562 nm that is nearly linear with increasing protein concentrations in ranges up to 2,000  $\mu\text{g}/\text{ml}$ . The macromolecular structure of the protein, the amount of peptides, and the four amino acids cysteine, cystine, tryptophan and tyrosine are reported to be responsible for the color formation with BCA. This provides a basis to monitor the reduction of alkaline  $\text{Cu}^{2+}$  by proteins and, thus determine the protein concentration in biochemical samples and cell extracts<sup>179</sup>.

Using the Pierce BCA kit (Perbio Science, Bonn, Germany) protein amounts in extracts were determined as follows: 5  $\mu\text{l}$  of each sample were diluted in 95  $\mu\text{l}$  1x PBS. A standard curve containing 0-150  $\mu\text{g}$  bovine serum albumin (Perbio Science, Bonn, Germany) per 100  $\mu\text{l}$ , 5  $\mu\text{l}$  of the respective lysis buffer and 1 x PBS add to 100  $\mu\text{l}$  was prepared. Next, 200  $\mu\text{l}$  of a 1:50 mixture of reagent B : reagent A (Perbio Science, Bonn, Germany) was added to each sample. Samples were incubated for 30 minutes at 60 °C. At this temperature, peptide bonds assist in the formation of the reaction product, so the assay sensitivity is increased since the variances caused by unequal amino acid composition are minimized. One hundred micro liter of each sample were added into a 96-well plate (Nunc, Wiesbaden, Germany). Absorption was determined at 590 nm using a plate reader (FluoStar OPTIMA, BMG Labtech, Offenburg, Germany) and protein amounts of the test samples were calculated from the standard curve.

### 2.8.4 Immunoprecipitation of Bid, VDAC1 and FLAG-VDAC1

Immunoprecipitation of Bid, VDAC1 and Flag-VDAC1 was performed by pull-down of the proteins from total protein lysates of HT-22 cells exposed to glutamate at the indicated time points 0 h to 16 h, primary mouse cortical neurons exposed to glutamate (0 h, 4 h and 22 h) and tissue homogenates of mice subjected to MCAo (see 2.8.2 and 2.10), according to the manufacturer's protocol (Invitrogen, Karlsruhe, Germany). Briefly, magnetic Dynabeads Protein A were prepared for each condition for effective binding of the respective antibodies: anti-Bid antibody (7.5  $\mu\text{g}$ , polyclonal, Cell Signaling, Danvers, Massachusetts, USA), anti-VDAC1 (N18) antibody (7.5  $\mu\text{g}$  to 10  $\mu\text{g}$ , polyclonal, Santa Cruz, Biotechnology, Santa Cruz, CA, USA) or anti-Flag antibody (7.5  $\mu\text{g}$ , polyclonal, Sigma-Aldrich, Munich, Germany). The respective antibodies were separately added to the Dynabeads Protein A for 30 min. to bind

the Dynabeads via their Fc-region. For all washing steps the tube was placed on a Dynamagnet, where the beads migrate to the side of the tube facing the magnet and allow for removal of the supernatant. A cross linking reaction with BS<sup>3</sup> was performed according to the manufacturer's protocol to avoid co-elution of the antibodies.

For each immunoprecipitation of Bid, VDAC1 or Flag-VDAC1, 2.5 mg of total protein lysate from HT-22 cells and 1-2 mg of total protein lysates from primary neurons and brain tissue samples of each treatment condition was incubated with the respective bead-bound antibodies for one hour at room temperature followed by a second hour at 4 °C. To elute the proteins with their binding partners, 70 µl of 2.5x sodium dodecyl sulfate (SDS)-sample buffer was added to each condition and the Dynabead-protein lysate-mix was boiled for 10 min. at 95 °C. Afterwards the Dynabeads were removed and the supernatant was stored at -80 °C until further use. To detect protein-interaction partners of Bid and VDAC1, 30 µl of the eluat was analyzed by electrophoresis followed by western blot analysis. The regular protein extract with 30-150 µg of total protein lysate per treatment condition was used as a control in the SDS-PAGE.

### **2.8.5 Gel electrophoresis and western blot**

Sodium dodecyl sulfate polyacrylamide gel electrophoresis (SDS-PAGE) is a well established technique to separate proteins according to their different electrophoretic mobility depending on their molecular mass. SDS is an anionic detergent that is applied to the protein sample and binds to polypeptide chain, imparting an identical protein charge per unit mass and thereby allowing a fractionation by size. Gels were prepared using a polyacrylamide separation gel with a concentration of 12.5 % and a stacking gel with 3.5 % and casting of gels was performed using BIO-RAD gel casting stands and frames. The specific buffers used for gels preparation, subsequent electrophoresis and western blot analysis are provided in Table 16 – Table 24: Stripping buffer, pH 2Table 24.

Prior to electrophoresis, an amount of 30-150 µg of each protein extract samples was mixed with 5 x SDS sample buffer and samples were filled up to an equal sample volume with bidest water. Afterwards, samples were boiled at 95°C for 10 minutes, cooled down to room temperature and loaded onto the gel. For comparative evaluation of molecular-mass, 5 µl of PageRuler™ Plus Prestained Ladder (Fermentas, St. Leon-Rot, Germany) were loaded next to the samples. Electrophoresis was performed initially at 60 V for about 30 minutes to allow for sample collection and subsequently at 125 V in electrophoresis buffer. Following electrophoretic separation, proteins were blotted on a polyvinylidenfluorid membrane (PVDF, Bio-Rad, Munich, Germany) by Semi-Dry blotting according to the Bio-Rad protocol at 15 V for 90 minutes. PVDF-membranes were first activated in methanol and then incubated for 10 minutes in 1 x transfer buffer before blotting. Meanwhile, Whatman blotting paper and the



acrylamide gel were incubated for 10 minutes in transfer buffer. Blotting was carried out by stacking one layer of Whatman paper on top of the anodic plate, followed by the PVDF membrane, the acrylamide gel as the third, and another final layer of Whatman paper on top. Blotting was carried out in a Trans-Blot SD semi-dry transfer cell (Bio-Rad, Munich, Germany) using extra thick Whatman filter paper (Bio-Rad, Munich, Germany) and 1x transfer buffer. Alternatively, proteins were blotted on a PVDF membrane by Tank-Blotting (wet-blotting) at 20 mA per Gel for approximately 20 h over night according to the Bio-Rad Tank-Blotting protocol. Therefore, a Mini-Trans-Blot Cell (Bio-Rad, Munich, Germany), in which the gel and membrane sandwich was entirely submerged under 1 x transfer buffer within a buffer tank, was used. Blotting was performed over night and temperature controlled by cooling the system with one ice pack per buffer tank.

After blotting, the PVDF-membranes were transferred directly into 5 % blocking buffer and incubated for 1 h at RT. The blots were then probed with the respective primary antibodies (2.1.3) at 4 °C overnight, followed by 1 h incubation at RT. The next day, membranes were washed three times with TBST for 5 minutes and exposed to the appropriate HRP-conjugated secondary antibody (2.1.4) in 5 % blocking solution for 1 h at RT. After washing 3 times with TBST for 15 minutes, membranes were incubated with chemiluminescence substrate solution HRP-Juice (PJK GmbH, Kleinblittersdorf, Germany) at RT in the dark. Chemiluminescence signals were recorded and quantified by densitometric analysis using the semi-automated Chemidoc-XRS Imaging System and the dedicated Quantity One software package (both, Bio-Rad, Munich, Germany). Equal protein loading and quality was controlled by re-probing the membranes with the anti-actin antibody (1:10.000, MB Biomedicals, Illkirch Cedex, France) and the respective anti-mouse HRP-conjugated secondary antibody.

For SDS gel electrophoresis following solutions were used:

**Table 16: Stacking gel 3.5 %**

0.5 M Tris-HCl solution pH 8.8	2.5 ml
Acrylamide/bisacrylamide (37.5 : 1) 30%	1.2 ml
Sodium dodecyl sulfate solution 10%	0.1 ml
Ammoniumpersulfate solution 10%	0.05 ml
Tetramethylethylenediamine TEMED	0.01 ml
Aqua demin.	ad 10 ml

**Table 17: Running gel 12.5 %**

---

1.5 M Tris-HCl solution pH 8.8	2.5 ml
Acrylamide/bisacrylamide (37,5:1) 30 %	3.34 ml
Sodium dodecyl sulfate solution 10 %	0.1 ml
Ammoniumpersulfate solution 10 %	0.05 ml
Tetramethylethylenediamine TEMED	0.01 ml
Aqua demin.	ad 10 ml

---

**Table 18: 5 x SDS-loading buffer**

---

1 M Tris-HCl pH 6.8	7 ml
Glycerol	3 ml
D,L-dithiotreitol (DTT)	0.93 g
SDS	1 g
$\beta$ -Mercaptoethanol	0.1 ml
Bromophenol blue sodium salt	1.2 mg

---

**Table 19: 1 x Electrophoresis buffer**

---

Tris base	3 g
Glycine	14.4 g
Sodium dodecyl sulfate (SDS)	1 g
Aqua demin.	ad 1,000 ml

---

For western blot analyses following buffers were used:

**Table 20: 1 x 10 % Transfer buffer (Semi-Dry-Blotting), pH 8.3**

---

Tris base	3 g
Glycine	14.4 g
Methanol	100 ml
HCl 0.1 M	q.s.
Aqua demin.	ad 1,000 ml

---

**Table 21: 1 x 20% Transfer buffer (Tank-Blotting), pH 8.3**

---

Tris base	3 g
Glycine	14.4 g
Methanol	200 ml
HCl 0.1 M	q.s.
Aqua demin.	ad 1,000 ml

---

**Table 22: 1 x TBS/Tween 20, pH 7.5**

---

Tris Base	2.4 g
Sodium chloride	29.2 g
Tween 20	0.5 ml
HCl 0.1 M	q.s.
Aqua demin.	ad 1,000 ml

---

**Table 23: 5 % Blocking buffer**

---

Skim milk powder	25 g
TBST	ad 500 ml

---

**Table 24: Stripping buffer, pH 2**

Glycine	15 g
Sodium dodecyl sulfate (SDS)	1 g
Tween 20	10 ml
HCl conc.	q.s.
Aqua demin.	ad 1,000 ml

### 2.8.6 Dot blot analysis

Dot blotting is a technique similar to the western blot technique but differing in that protein or antibody samples are not separated electrophoretically but are spotted directly onto the membrane. Therefore a grid was drawn by pencil on a PVDF membrane to indicate the region for sample point plotting. The membrane was activated in methanol and then incubated for 5 minutes in 1 x 20 % transfer buffer. Afterwards 0.5-2  $\mu$ l of the respective sample was spotted on the wet membrane at the center of the grid. The area that the solution penetrates was minimized by applying the sample slowly. The membrane was dried and then reactivated in methanol followed by 5 min. of TBST incubation. To block non-specific sites the membrane was incubated in 5 % blocking solution for 1 h at room temperature and afterwards incubated with the appropriate primary antibody in blocking solution for 1-2 h at room temperature. After washing three times with TBST for 5 min., the HRP-conjugated secondary antibody was added to the membrane for 1 h at room temperature. Detection of proteins was performed by chemiluminescence as described in 2.8.5.

### 2.8.7 Coomassie staining

To investigate the purity of recombinant proteins (2.14.1) and for determining protein-protein interactions after pull down experiments using recombinant proteins, gel electrophoresis (SDS-PAGE) was followed by staining the gels with Coomassie Blue R250, which binds nonspecific to all proteins. The detection limit is 0.3-1  $\mu$ g/protein band. For protein staining the gels were incubated for 1 h in coomassie staining solution containing 0.1 % R250, 45 % methanol, 45 % aqua bidest. and 10 % pure acetic acid. Afterwards, the gels were discolored at least 1 h - overnight in destaining solution containing 30 % methanol, 10 % pure acetic acid and 60 % aqua bidest., until single blue proteins bands were visible. Images of coomassie stained gels were taken using the semi-automated Chemidoc-XRS Imaging System (Bio-Rad, Munich, Germany) using white transmission light. The gels were stored in 7 % acetic acid.

### 2.8.8 Ponceau S staining

Ponceau S is a rapid and reversible stain for detecting proteins bands on cellulose acetate, PVDF or nitrocellulose membranes, and is especially used to check for success of transfer after western blotting. The negative stain binds to the positively charged amino groups of a protein and also non-covalently to non-polar regions in the protein. Microgram quantities of transferred protein can be detected with Ponceau S stain, which generates reddish pink protein bands with a clear background. Since staining with Ponceau S is reversible it allows further immunological detection. To detect proteins after blotting on a PVDF membrane, the blotted membranes were washed shortly in TBST and immersed in a sufficient amount of Ponceau S Staining solution (5 ml, AppliChem, Darmstadt, Deutschland) for 5-10 min. at room temperature. After staining, the membranes were washed with water until the water was clear and the reddish pink protein bands were well-defined and visible. For imaging, membranes were subsequently scanned. For further immunological detection, the membranes were discolored completely by repeated washing in water and TBST. Afterwards the membrane was re-activated with methanol and washed again in TBST before blocking in 5 % blocking solution and the following standard protocol for western blotting (2.8.5).

## 2.9 RNA analysis

For RNA extraction HT-22 cells were grown either in 24-well plates at an average density of 60,000 cells/well and 2-4 wells per condition were pooled for RNA preparation. Alternatively, cells were grown in 6 well plates at a density of 180,000 cells/well and 4 wells per condition were pooled. For RNA extraction of HT-22 cells transfected with siRNA, cells were harvest 48 h after siRNA transfection. For determination of mRNA amount in glutamate-treated cells, cells were grown in T75 flask at a density of  $1 \times 10^6$  cells/flask and harvest 15 h after glutamate treatment.

### 2.9.1 RNA preparation and determination of RNA amount

Total RNA was extracted from HT-22 cells using the NucleoSpin RNA II kit (Macherey-Nagel, Düren, Germany) according to the manufacturer's instructions. Briefly, HT-22 cells were washed with 1 x PBS and harvested in 350  $\mu$ l cell lysis buffer RA1 supplemented with 1 % 2-Mercaptoethanol. Before continuing with the extraction, all samples were shock-frozen in liquid nitrogen and left to thaw slowly on ice. Next, the raw extracts were filtered through NucleoSpin-RNA II columns to remove cellular debris. The supernatant was supplemented with ethanol, mixed carefully and loaded on a NucleoSpin RNA II column to extract nucleic acids by adsorption to the silica matrix of the column. Excessive electrolytes were removed by washing with MDB buffer (supplied with the kit). To remove possible contaminations with

genomic DNA, recombinant DNase was added. Further, purification of the column-bound RNA was achieved by subsequent purification, using RA2 and RA3 buffers. RNA was eluted in 70  $\mu$ l RNase free water supplied with the NucleoSpin Kit II. RNA-concentration was determined by UV-Vis absorption spectroscopy, using the NanoPhotometer<sup>TM</sup> (Implen, GE Healthcare Europe GmbH, Freiburg, Germany) at a wavelength of 260 nm. For intermediate storage, RNA-extracts were transferred to the -80°C freezer.

### 2.9.2 One Step reverse transcriptase polymerase chain reaction (RT-PCR)

Following RNA purification, mRNA was amplified by one-step RT-PCR using the SuperScript III One Step PCR kit with Platinum Taq (Invitrogen, Karlsruhe, Germany). Sequence specific primers were used as described in Table 1 in section 0. Sample preparation was performed according to the following scheme given in Table 25 and Table 26. For amplification of PCR products the respective cycler programs provided in Table 27 - Table 30 were used. The RT-PCR products were visualized under UV illumination after electrophoresis on a 1.5 % agarose gel containing ethidium bromide or SYBR Gold (Invitrogen Karlsruhe). The resulting gen products had a length of 400 (GAPDH), 316 (VDAC1), 289 (VDAC2), 1250 (Bid) base pairs, respectively.

**Table 25: PCR sample preparation: VDAC1, VDAC2, Bid**

2x reaction buffer	12.5 $\mu$ l
Sample (0.1 $\mu$ g)	x $\mu$ l
fwd primer (10 $\mu$ M)	0.5 $\mu$ l
rev primer (10 $\mu$ M)	0.5 $\mu$ l
SuperScript III enzyme (Platinum Taq)	0.5 $\mu$ l
Nuclease free water	ad 25 $\mu$ l

**Table 26: PCR sample preparation GAPDH**

2x reaction buffer	12.5 $\mu$ l
Sample (0.1 $\mu$ g)	x $\mu$ l
fwd primer (5 $\mu$ M)	1.0 $\mu$ l
rev primer (5 $\mu$ M)	1.0 $\mu$ l
SuperScript III enzyme (Platinum Taq)	0.5 $\mu$ l
Nuclease free water	ad 25 $\mu$ l

For amplification the following cycler programs were used:

**Table 27: RT-PCR cyclers program – murine GAPDH**

60° C 30 min	
95° C 2 min	
95° C 30 sec	} 30 cycles
57° C 1 min	
70° C 2 min	
70° C 10 min	
4° C ∞	

**Table 28: RT-PCR cyclers program – murine VDAC1**

60° C 30 min	
95° C 2 min	
95° C 30 sec	} 25 cycles
59,3° C 1 min	
70° C 2 min	
70° C 10 min	
4° C ∞	

**Table 29: RT-PCR cyclers program – murine VDAC2**

60° C 30 min	
95° C 2 min	
95° C 30 sec	} 27-28 cycles
60,4° C 1 min	
70° C 2 min	
70° C 10 min	
4° C ∞	

**Table 30: RT-PCR cyclers program – murine Bid**

60° C 30 min	
95° C 2 min	
95° C 30 sec	} 27 cycles
53° C 1 min	
70° C 2 min	
70° C 10 min	
4° C ∞	

### 2.9.3 Agarose gel electrophoresis

Analysis of PCR products were performed by agarose gel electrophoresis and subsequent fluorescence detection of ethidium bromide or SYBR Gold (Invitrogen), both intercalating agents that increase their fluorescent emission upon DNA binding. For gel preparation, 1.5 % agarose (Sigma-Aldrich) was suspended in Tris/Borate/EDTA (TBE) buffer (10 x stock, Invitrogen) and dissolved by heating up the suspension in a microwave oven. After dissolving, 2 µl of SYBR Gold or 5 µl of stock solution ethidium bromide (1 % in water) was added into 100 ml suspension, stirred carefully and the solution was filled into the gel cartridge to allow gel formation. For subsequent gel loading, a comb was inserted in the gel, to generate the pockets. Samples were loaded using 1-5 µl of PCR product, 2 µl of Blue Juice sample buffer (Sigma Aldrich) added with nuclease-free water up to a total volume of 7 µl. In addition to the samples, 4 µl of a pre-prepared 100 bp reference marker (Fermentas, St. Leon-Roth, Germany) was loaded on the gel. Electrophoresis was conducted at 100 V for about 1 hour. Stained PCR-products were detected by UV light excitation and fluorescent emission using the Chemidoc Imaging System (Bio-Rad, Munich, Germany). Pictures were taken and analyzed using Quantity One software (Bio-Rad, Munich, Germany).



## 2.10 Transient focal cerebral ischemia in mice

The middle cerebral artery occlusion (MCAo) experiments were kindly performed by Uta Mamrak (Ludwig-Maximilians-University, Munich, Germany). Male C57BL/6 mice (n = 6) (body weight, 18–22 g; Charles River Laboratories, Sulzfeld, Germany) were subjected to 60 min transient MCAo as described previously<sup>180, 181</sup>. Surgery was performed in isoflurane/N<sub>2</sub>O anesthesia (1.5% isoflurane, 68.5% N<sub>2</sub>O, 30% O<sub>2</sub>) with controlled ventilation. A silicon coated nylon monofilament was inserted into the internal carotid artery and gently pushed forward until blood flow in the MCA territory decreased to less than 20 % of baseline. Ischemia and reperfusion were verified by laser Doppler measurements. Tissue homogenates for immunoprecipitation and western blot analysis were generated from 4 mm sections of the ipsi- and contralateral parietal cortex (2 mm +/- bregma) respectively at 2 h, 6 h and 24 h after the onset of ischemia. For each experimental group, six animals were used. Statistical analysis was performed using the Kruskal-Wallis test. All procedures described are in accordance with local laws and were approved by the animal protection committee of the Government of Upper Bavaria.

## 2.11 Concentration-response curves and EC50 values

Half maximal effective concentrations (EC<sub>50</sub>) for all thiazolidindiones provided in Table 69 (Appendix) were determined based on the concentration-response curves for each compound (see also 0). To determine the concentration required to achieve maximal neuroprotective effects, initially all compounds were screened by their ability to prevent glutamate-induced cell death at concentrations of 10, 20, 30, 40 and 50 μM. Since quantification of cell viability (MTT assay) revealed maximal protective effects of the compounds in a concentration of 20 μM and higher, generation of concentration ranges for these measurements were not satisfying. Therefore compounds with an EC<sub>50</sub> < 10 μM were screened in lower concentrations of 0.1 μM up to 50 μM for maximum protection. Cell viability data were normalized between untreated control conditions (0 %) and maximum amplitude at 50 μM (100 %). Using OriginPro8.5 Software, the resulting data were fitted with a sigmoid function following the equation  $y=A1+(A2-A1)/(1+10^{((\text{LOG}x0-x)*p)})$  and EC<sub>50</sub> values for all substances were calculated.

## 2.12 Molecular docking

Molecular docking is a method used in the field of molecular modeling, to predict the preferred orientation of one molecule to another molecule when bound to each other to form a stable complex. It is frequently used to reveal the binding orientation of small-molecule drug candidates to their protein targets. Thereby, the affinity and activity of novel compounds can be predicted, and, hence docking plays an important role in the rational design of novel drugs. In this thesis, docking analyses were performed to investigate the possible binding mode of novel small-molecule inhibitors to the pro-apoptotic protein Bid.

Molecular docking analyses were kindly performed by Dr. Wegscheid-Gerlach (Pharmaceutical chemistry, Philipps-University Marburg, Marburg, Germany). According to Becattini et al.<sup>114</sup> docking studies were conducted using the NMR solution structure of mouse BID from the PDB entry 1DDB<sup>65</sup>. All compounds were converted from SMILES notation into Sybyl mol2 format using CORINA. Protein preparation and docking was performed using FlexX<sup>182</sup>, available within the LeadIT version 2.1.3 from BioSolveIT. All obtained docking solutions were re-ranked with HYDE-score<sup>183, 184</sup>. Pictures for 2D-representation of the docking solution were generated with pose view<sup>185</sup>, as implemented in LeadIT, and exported in the same way as the 3D representation, from the program.

## 2.13 Statistical analysis

All data are given as means  $\pm$  standard deviation (SD). For statistical comparison between two groups Mann-Whitney-U-test was used. Multiple comparisons were performed by analysis of variance (ANOVA) followed by Scheffé's post hoc test or Kruskal-Wallis test, as indicated. Calculations were performed with the Winstat standard statistical software package (R. Fitch Software, Bad Krozingen, Germany).

## 2.14 Molecular Biology

### 2.14.1 Recombinant proteins

Human recombinant caspase 8, mouse recombinant tBid and mouse recombinant His-Bax were kindly provided by Prof. Dr. Jean-Claude Martinou (University of Geneva, Switzerland). In addition human recombinant full-length Bax with an N-terminal GST-tag was ordered from Abnova (Heidelberg, Germany). Mouse recombinant VDAC1, VDAC1  $\Delta$ 11 and mouse recombinant VDAC2 were kindly provided by Barbara Mertins (Group of Prof. Essen, Department of Chemistry, University of Marburg). Full-length mouse Bid, truncated Bid (tBid) as well as different Bid constructs were expressed and purified in this thesis as described below.

### 2.14.2 Competent cells

For bacterial expression of recombinant proteins *Escherichia coli* Rosetta<sup>TM</sup>2 (DE3) single competent cells (Novagen/Merck Millipore, Darmstadt, Germany) were used. Rosetta<sup>TM</sup>2 host strains are BL21 derivatives designed to enhance the expression of eukaryotic proteins that contain codons rarely used in *E. coli*. The original Rosetta strains supply tRNAs for 7 rare codons (AGA, AGG, AUA, CUA, GGA, CCC, and CGG) on a compatible chloramphenicol-resistant plasmid. The tRNA genes are driven by their native promoters. DE3 indicates that the host is a lysogen of  $\lambda$ DE3, and therefore carries a chromosomal copy of the T7 RNA polymerase gene under control of the *lacUV5* promoter (see Novagen User protocol TB009). Such strains are suitable for protein production from target genes cloned in pET vectors amongst others by induction with IPTG.

### 2.14.3 Culture medium for bacteria

For bacterial growth Luria-Bertani (LB) broth medium was used, which is the most widely used medium for the growth of bacteria. For liquid LB medium 100 g Luria Broth Base powder (AppliChem, Darmstadt, Germany), containing 10 g peptone 140, 5 g yeast extract and 5 g sodium chloride per liter, was dissolved in 5 l Aqua demin. and aliquoted in 500 ml bottles. Afterwards, LB bottles were autoclaved for 21 min and stored at room temperature. For preparation of LB Agar plates, 7.5 g of agar powder (Lennox L agar, AppliChem, Darmstadt, Germany) was added to 500 ml of LB medium. After autoclaving 0.5 ml of ampicillin (100 mg/ml) and/or 0.5 ml of chloramphenicol (30 mg/ml, dissolved in ethanol) was added to 500 ml LB agar and the LB agar was poured into petri-dishes. After hardening, petri-dishes were inverted and stored at 4°C in the dark.

#### 2.14.4 Cloning and site-directed mutagenesis of Bid constructs

Different Bid constructs were expressed as GST fusion proteins. Based on the NMR structure of Bid, we reasoned that crystallization could be facilitated by removing the mobile N-terminus and loop. This was accomplished by first cloning N-terminally truncated mouse Bid constructs starting with Gly12 or Ala13 (designated  $\Delta 12$  and  $\Delta 13$ , respectively), respectively, into pGEX1 $\lambda$ T (GE Healthcare Bio-Science AB, Uppsala, Sweden) by PCR. The loop was removed in a second step by employing an endogenous HindIII site spanning Gln45 to Tyr47. The distal part of mouse Bid before Ser78 was amplified using primers encoding the HindIII site (and sometimes bases encoding for amino acids 49-52) followed by bases encoding for Ser78 and beyond. This part was then cloned into the constructs made in the first step. Detailed cloning procedure was performed as follows.

For the first step PCR samples were prepared and amplified in a Sensoquest-Cycler as described in Table 31- Table 34. Primer sequences are provided in Table 1.

**Table 31: PCR sample preparation - G12-mBid, A13-mBid**

5x Phusion HF reaction buffer	10 $\mu$ l
Template (pET15b-Bid-p22, 50 ng)	1.0 $\mu$ l
G12-mBid / A13-mBid fw primer (1 $\mu$ M)	0.5 $\mu$ l
mBid-EcoRI rev primer (1 $\mu$ M)	0.5 $\mu$ l
dNTP (10 mM)	1.0 $\mu$ l
Phusion	0.5 $\mu$ l
Nuclease free water	35.5 $\mu$ l

**Table 32: PCR sample preparation - Y47-mBid, D51-mBid**

5x Phusion HF reaction buffer	10 $\mu$ l
Template (pET15b-Bid-p22, 50 ng)	1.0 $\mu$ l
Y47-mBid / D51-mBid fw primer (1 $\mu$ M)	0.5 $\mu$ l
mBid-EcoRI rev primer (1 $\mu$ M)	0.5 $\mu$ l
dNTP (10 mM)	1.0 $\mu$ l
Phusion	0.5 $\mu$ l
Nuclease free water	35.5 $\mu$ l

**Table 33: RT-PCR Cycler program – G12-mBid and A13-mBid**

Pre-heating	
94° C 5 sec	
95° C 30 sec	} 30 cycles
66° C 30 sec	
72° C 2 min	
72° C 15 min	
4° C ∞	

**Table 34: RT-PCR Cycler program – Y47-mBid and D51-mBid**

Pre-heating	
94° C 5 sec	
95° C 30 sec	} 30 cycles
60° C 30 sec	
72° C 2 min	
72° C 15 min	
4° C ∞	

The obtained PCR products were analyzed by agarose gel electrophoresis and subsequent fluorescence detection with ethidium bromide (Promega, Mannheim, Germany) as described in 2.9.

Afterwards PCR products were purified using the QIAquick Gel Extraction Kit (Quiagen, Hilden, Germany) according to the manufacturer's protocol. Briefly, PCR samples were filled up with 3 volumes (150 µl) of QG buffer, respectively, and incubated at 50°C for 10 min. Afterwards 50 µl of isopropanol was added and samples mixed gently. Samples were transferred to a QIAquick spin column in a provided 2 ml collection tube and centrifuged for 1 min. at 13,000 rpm. After discarding the flow-through, 750 µl PE buffer was added and samples centrifuged twice at 13,000 rpm for 1 min. To elute DNA, 50 µl of Buffer EB (10 mM Tris-HCl, pH 8.5) was added to the center of the QIAquick membrane and columns centrifuged at 13,000 rpm for 1 min.

#### **Digestion and ligation of DNA products:**

The eluted G12-mBid and A13-mBid were digested with BamHI-HF and EcoRI-HF in NEB4 buffer overnight at 37°C and products were isolated by agarose gel electrophoresis followed by gel extraction with Ultra Free DNA gel extract kit (Millipore, Darmstadt, Germany)

according to the manufacturer's protocol. Products were cloned into the pGEX1 $\lambda$ T vector to obtain the pGEX- $\Delta$ 12-Bid and pGEX- $\Delta$ 13-Bid constructs by DNA ligation for 5 h at 16°C. The pGEX- $\Delta$ 12-Bid, pGEX- $\Delta$ 13-Bid, Y47-mBid and D51-mBid products were digested with HindIII-HF and EcoRI-HF in NEB4 buffer overnight at 37°C and the digestion products isolated as described above. In the last step Y47-mBid and D51-mBid were cloned into the pGEX- $\Delta$ 12-Bid and pGEX- $\Delta$ 13-Bid, respectively by DNA ligation for 2 h at 16°C. After DNA ligation all constructs were transformed into competent cells<sup>186</sup> and afterwards plated on appropriate agar plates containing ampicillin (Amp). Amplification of the obtained plasmids was performed using the Qiagen Plasmid Plus Midi kit (Qiagen, Hilden, Germany) according to the manufacturer's protocol. Plasmid DNA-concentrations were determined using the NanoPhotometer<sup>TM</sup> (Implen, Freiburg, Germany).

To confirm the successful cloning of all constructs, the plasmids were digested with PstI (Fermentas) for 1 h at 37°C and digestion products analyzed by agarose gel electrophoresis. Furthermore, all constructs were verified by sequencing. Thereby, four different Bid constructs were obtained, namely pGEX  $\Delta$ 12-Y47 (Bid1), pGEX  $\Delta$ 12-D51 (Bid2), pGEX  $\Delta$ 13-Y47 (Bid 3) and pGEX  $\Delta$ 13-D51 (Bid 4).

#### 2.14.4.1 Cloning of Bid constructs for expression in eukaryotic cells

The A13-mBid constructs were also expressed in eukaryotic cells. To this end, a KpnI site followed by a start codon was introduced in front of Ala13 by PCR using the KpnI-M13Bid primer (Table 1). mBid-EcoRI was used as the reverse primer (see Table 1). PCR conditions are described in Table 35 and Table 36. PCR products were digested with KpnI and EcoRI and ligated into pcDNA3 that had been digested with the same enzymes.

**Table 35: PCR sample preparation- A13-mBid constructs**

5x Phusion HF reaction buffer	10 $\mu$ l
Template (100 ng)	1.0 $\mu$ l
Kpn-M13Bid fw primer (100 mM)	1.0 $\mu$ l
mBid-EcoRI rev primer (100 mM)	1.0 $\mu$ l
dNTP (10 mM)	1.0 $\mu$ l
Phusion	0.5 $\mu$ l
Nuclease free water	35.5 $\mu$ l

**Table 36: RT-PCR Cycler program A13-mBid constructs**

Pre-heating	
94° C 5 sec	
95° C 30 sec	} 30 cycles
55° C 30 sec	
72° C 1 min	
72° C 15 min	
4° C ∞	

Cloning and site-directed mutagenesis were performed together with Cornelius Krasel.

### 2.14.5 Transformation of plasmids in Rosetta2 (DE3)

For the expression of the recombinant proteins full-length Bid, tBid, Bid constructs Bid1-4, Bax and caspase 8, *Escherichia coli* Rosetta2 (DE3) singles were transformed with the respective plasmids provided in 2.1.1.1. All plasmids contain an Ampicillin-resistance gene. Rosetta2 (DE3) singles carry a chloramphenicol resistance. Transformation of Rosetta2 (DE3) singles was performed according to the protocol recommended by Novagen (User protocol TB009 Rev.G0609), with an appreciated transformation efficiency of  $2 \times 10^6$  cfu/ $\mu$ g plasmid. Bacteria and plasmids were thawed on ice for 2-5 min. and gently resuspended. Afterwards, 20  $\mu$ l of Rosetta2 (DE3) were transferred to a 1.5 ml tube for each plasmid sample, respectively and 0.5-1  $\mu$ l of the purified plasmid DNA was added directly to the cells. The samples were stirred gently and the tubes incubated on ice for 5 min. to allow transformation. The mixture of DNA and cells was afterwards heated for exactly 30 s to 42°C in a water bath without shaking. After heating, the tubes were placed on ice for another 2 min. before adding 250  $\mu$ l room temperature SOC medium to each tube. The mixtures were incubated at 37°C while shaking at 250 rpm for 60 min. Before plating the bacteria on LB-Amp agar plates, the plates were treated with 50  $\mu$ l of chloramphenicol (30mg/ml in ETOH). Then 50  $\mu$ l of each transformation was spread on the LB agar plates, now containing the appropriate antibiotics, chloramphenicol and ampicillin. The agar plates were incubated at 37°C overnight until bacterial colonies were grown.

### 2.14.6 Inoculating a liquid bacterial culture

The LB agar plates prepared as described in 2.15 were frequently used to isolate individual colonies of bacteria carrying the specific plasmid. To support a higher density of bacteria a liquid culture was used to grow up sufficient numbers of bacteria necessary to isolate enough

plasmid DNA for experimental use, for generating cryo-stocks for long term storage of plasmid as well as for further expression of the recombinant proteins.

For inoculating an overnight culture of liquid LB with Rosetta2 (DE3), 2.5 ml liquid LB medium was added into a 15 ml falcon for each plasmid and each bacterial colony and supplemented with 2.5  $\mu$ l chloramphenicol (30 mg/ml in ETOH) and 2.5  $\mu$ l ampicillin (100 mg/ml in H<sub>2</sub>O), respectively. Afterwards a single bacterial colony was picked from the LB agar plate using a sterile pipette tip, transferred to the liquid LB medium containing the appropriate antibiotics and swirled gently. The bacterial culture was incubated at 37°C in a shaking incubator overnight. After incubation, bacterial growth was characterized by turbidity of the media. The liquid LB culture containing bacteria, transformed with the respective plasmids, was used for preparing cryo-stocks (2.14.7) and for further expression of specific recombinant protein (2.14.9).

#### **2.14.7 Long-term storage of plasmids via Cryo-stocks**

For long-term storage of plasmids bacterial cryo-stocks, containing the respective bacterial culture and the cryo-protectant dimethylsulfoxid (DMSO), were prepared. The optical density (OD<sub>600</sub>) of the liquid bacterial culture used for the cryo-stocks should not exceed 0.6 AU. For each stock 930  $\mu$ l of the respective bacterial overnight culture were mixed with 70  $\mu$ l sterile DMSO and transferred into sterile cryo-vials, labeled with the bacterial strain and the plasmid, respectively. Afterwards, the cryo-vials were frozen in liquid nitrogen and stored at -80°C.

#### **2.14.8 Determination of optical density of bacteria (OD<sub>600</sub>)**

Optical density was measured using the BioRad SmartSpec™ Plus spectrophotometer (BioRad laboratories, Munich, Germany) to determine the concentration of bacteria in a suspension. To measure bacteria which are in their mid-log phase of growth, the bacterial suspension was measured at a wavelength of 600 nm (OD<sub>600</sub>). All samples were measured in BioRad trUView™ cuvetts (single use). The spectrophotometer was blanked to zero using 100  $\mu$ l fresh LB medium. Afterwards, OD<sub>600</sub> of each bacterial suspension was determined using 100  $\mu$ l sample volume, respectively. Determination of OD<sub>600</sub> was repeated until an OD<sub>600</sub> of 0.6 AU was reached and protein expression was induced.

#### **2.14.9 Expression of recombinant proteins**

Recombinant proteins with a hexa-histidine tag at the N-terminus (His<sub>6</sub>-Bid, His<sub>6</sub>-tBid, His<sub>6</sub>-caspase 8) and GST-tagged Bid constructs (Bid1-Bid4) were expressed in competent *Escherichia coli* Rosetta 2 (DE3) cells (Novagen). After transformation of bacteria with the respective plasmids (2.14.5) and generation of a liquid bacterial culture (2.14.6), 5 ml of overnight culture was inoculated into 400 ml of standard LB medium containing ampicillin



(100 µg/ml) and chloramphenicol (100 µg/ml) in 1 L flasks. Three to four cultures were prepared in parallel. Bacteria were grown at 37°C in a shaking incubator for approximately 4.5 h and the optical density (OD<sub>600</sub>) was checked at regular intervals to evaluate cell growth. At an OD<sub>600</sub> of 0.6, 400 µl of isopropyl β-D-1-thiogalactopyranoside (IPTG) was added to each 400 ml culture to induce protein production. IPTG is a molecular mimic of allolactose and allows the transcription of genes in the lac-operon and is thereby commonly used as effective inducer of protein expression, where genes are under control of the lac-operator. Protein expression was induced for 4-6 h at 37 °C while shaking. Afterwards cells were harvested by centrifugation (Sorvall GSA rotor, 5000 g, 15 min, 4 °C) using the Sorvall RC 5B Plus centrifuge (Sorvall, Bad Homburg, Deutschland). All pellets of a 1.2-1.6 L culture were pooled and resuspended in 20 ml standard protein lysis buffer (Table 37). For GST-tagged proteins cells were resuspended in 20 ml protein lysis buffer provided in Table 38. Bacterial lysates were frozen in liquid nitrogen, and stored at -80 °C until further use.

#### **2.14.10 Expression tests**

Before large-scale expression of recombinant proteins, every protein construct was checked for expression efficiency and protein solubility. For this approach, 200-500 µl of the bacterial overnight culture was inoculated into 5-10 ml of standard LB medium containing ampicillin (100 µg/ml) and chloramphenicol (100 µg/ml) in a 15-100 ml flask. The bacterial culture was grown at 37°C until an OD<sub>600</sub> > 0.6 was reached and protein expression was induced by 1 M IPTG addition. Afterwards, 1 ml samples were taken at different time points from 0 h up to 19 h after IPTG induction. Samples were centrifuged at 15,300 *rpm* for 15 min. at 4°C, the supernatant discarded and the cell pellet resuspended in 20 mM Tris buffer (pH 7.5). Cells were lysed without detergent by sonication using the Sonifier Cell Disrupter S-450D (Branson Ultrasonics, Dietzenbach, Deutschland) equipped with a 3 mm micro-tip. Sonication of each sample was performed on ice for 15-20 times using 10% amplitude in pulses of 1 sec with 1 sec break between pulses. To separate soluble and membrane bound proteins, cells were centrifuged at 15,300 *rpm* for 15 min. at 4°C. The supernatant of each sample was transferred into a new sample tube and protein concentration was determined by the Bradford assay (2.20.1). All supernatant samples were acetone precipitated according to the pierce protocol (2.21). The cell pellets were resuspended in 20 mM Tris buffer (pH 7.5), respectively. Afterwards, all samples were analyzed for protein expression by gel electrophoresis followed by coomassie staining. In addition, respective protein expression was confirmed by western blot.

## 2.15 Purification of recombinant proteins

For purification bacterial cell lysates (either recently centrifuged and resuspended in lysis buffer or thawed) were subjected to sonication (Branson Sonifier Cell Disrupter S-450D, Branson Ultrasonics, Dietzenbach, Deutschland). For 20 ml bacterial cell lysate a macro-tip was used and sonication was performed at 20% maximum power (20 % amplitude). To avoid protein degradation due to heat produced by the sonicator's sound waves, samples were treated using a sonication interval of 1 sec. *puls on* and 2 sec. *puls off* for 7-10 min. total time. The solution was then centrifuged at 30,000 *rpm* for at least 30 minutes (Beckman Optima XE-90, Ti70 rotor, Beckman Coulter, Krefeld, Deutschland) at 4°C. All proteins purified in this thesis were recovered in the soluble bacteria fraction. The supernatant was subsequently filtered through a 0.45 µm filter (Whatman, Dassel, Germany) and stored on ice until further purification.

### 2.15.1 Buffers for protein purification

Buffers used for purification of recombinant proteins are provided in Table 37–Table 43.

**Table 37: Protein standard lysis buffer**

20 mM Tris base	1.21 g
250 mM NaCl	7.3 g
10 mM β-Mercaptoethanol	0.39 g (eq. 11 drops)
Aqua demin.	ad 500 ml
Complete Mini Protease Inhibitor Cocktail (Roche, Mannheim, Germany)	2 tablets per 20 ml instantaneously prior to use

**Table 38: Protein lysis buffer for GSTrap purification**

20 mM Tris base	1.21 g
100 mM NaCl	2.92 g
1 mM EDTA	0.15 g
1 mM DTT	0.5 ml DTT stock solution (1 M DTT)
Aqua demin.	ad 500 ml
Complete Mini Protease Inhibitor Cocktail (Roche, Mannheim, Germany)	2 tablets per 20 ml instantaneously prior to use

**Table 39: Buffer for His-Catcher Nickel Gravity Columns (PJK GmbH)**

<b>IMAC binding buffer, pH 7.5</b>	
20 mM Tris base	1.21 g
200 mM NaCl	5.84 g
10 mM $\beta$ -Mercaptoethanol	0.39 g (eq. 11 drops)
Aqua demin.	ad 500 ml
<b>Wash buffer, pH 7.5</b>	
20 mM Tris base	1.21 g
20 mM NaCl	0.584 g
10 mM Imidazole	0.34 g
10 mM $\beta$ -Mercaptoethanol	0.39 g (eq. 11 drops)
Aqua demin.	ad 500 ml
<b>Elution buffer, pH 7.5</b>	
20 mM Tris base	1.21 g
20 mM NaCl	0.584 g
250 mM Imidazole	8.51
10 mM $\beta$ -Mercaptoethanol	0.39 g (eq. 11 drops)
Aqua demin.	ad 500 ml

For purification of proteins by chromatography using the ÄKTAprime plus (GE Healthcare Bio-Science AB, Uppsala, Sweden) the following buffers were used:

**Table 40: Buffer for HisTrap affinity columns (HisTrap™ FF 5 ml)**

<b>Buffer A: Binding buffer, pH 7.5</b>	
20 mM Tris base	1.21 g
250 mM NaCl	7.3 g
10 mM $\beta$ -Mercaptoethanol	0.39 g (eq. 11 drops)
Aqua demin.	ad 500 ml
<b>Buffer B: Elution buffer pH 7.5</b>	
20 mM Tris base	1.21 g
20 mM NaCl	0.584 g
400 mM Imidazole	13.62 g
10 mM $\beta$ -Mercaptoethanol	0.39 g (eq. 11 drops)
Aqua demin.	ad 500 ml

**Table 41: Buffer for GSTrap affinity columns and Glutathione and HiCap Cartridges**

<b>Buffer A: Binding buffer, pH 7.5</b>	
20 mM Tris base	1.21 g
100 mM NaCl	2.92 g
1 mM EDTA	0.15 g
1 mM DTT	0.5 ml DTT stock solution (1 M DTT)
Aqua demin.	ad 500 ml
<b>Buffer B: Elution buffer pH 8.0</b>	
50 mM Tris base	3.92 g
10 mM L-Glutathione red.	1.54 g
1 mM EDTA	0.15 g
1 mM DTT	0.5 ml DTT stock solution (1 M DTT)
Aqua demin.	ad 500 ml

**Table 42: Buffer for HiTrap ion exchange columns (HiTrap Q HP, 5 ml)**

<b>Buffer A: Binding buffer, pH 8.0</b>	
20 mM Tris base	1.21 g
10 mM $\beta$ -Mercaptoethanol	0.39 g (eq. 11 drops)
Aqua demin.	ad 500 ml
<b>Buffer B: Elution buffer pH 8.0</b>	
20 mM Tris base	1.21 g
500 mM NaCl	14.61 g
10 mM $\beta$ -Mercaptoethanol	0.39 g (eq. 11 drops)
Aqua demin.	ad 500 ml

**Table 43: Buffer for HiLoad gel filtration columns (HiLoad™ 16/600 Superdex 75 pg)**

<b>Buffer A; pH 7.5</b>	
20 mM Tris base	2.42 g
50 mM NaCl	2.92 g
Aqua demin.	ad 1000 ml

To avoid bacterial growth, all buffers were supplemented with 0.03 % sodium azide. After buffer preparation, all buffers were sterile filtered through a 0.22  $\mu$ M cellulose filter and completely degassed under vacuum for at least 1-2 hours before use. All buffers were stored at 4°C.

### 2.15.2 Protein purification using the ÄKTA prime plus

ÄKTA prime plus is a compact liquid chromatography system used for one-step purification of proteins at laboratory scale. All methods applied for protein purification using the ÄKTA prime plus system were extensively established during this thesis and respectively customized for each of the purified protein constructs. The methods were programmed line-by-line using the PrimeView 5.0 software. Using this software all purification runs were monitored and results were presented by the respective chromatograms.

Prior to start of the protein purification the system was pre-equilibrated. Since the system and columns were stored in 20% ethanol, all components had to be flushed with water before working with buffers or protein. Therefore, the system, inlet tubing, sample loops and columns were purged 2-3 times with degassed aqua demin using the “system wash” program. Afterwards the system was rinsed with water for at least 2 volumes of the required column (CV) by manual run using a flow rate of 1-1.5 ml/min. For equilibrating the system for the intended purification method, it was subsequently purged with the appropriate binding buffer, followed by a manual buffer wash with 2 CV of binding buffer. The system was then ready for the following protein purification (2.15.3 and 2.15.4). The maximum pressure was fixed to 0.3 kPa for all purification methods.

At the end of the purification run, the system was rinsed with at least 2-3 CV of aqua demin. to remove all buffers in order to avoid precipitations. For storage, the system as well as sample loops and columns were rinsed with 20% ethanol. The washing procedure was performed either by manual run with a flow rate of 1-2 ml/min or by the programmed wash method provided in Table 44 overnight.

**Table 44: Programmed method for ÄKTA- wash and storage**

Action	Breakpoint	Volume [ml]	Conc Buffer B [%]	Flow rate [ml/min]	Fraction size [ml]	Inject valve position
Equilibration	1	0	0	2	0	Load
Water wash (A)	2	10	0	1	0	Load
Water wash End	3	130	0	1	0	Load
Priming B	4	130.1	100	1	0	Load
20% ETOH wash (B)	5	250	100	1	0	Load
Method end	6	260	100	1	0	Load

### 2.15.3 Purification of recombinant His<sub>6</sub>-tagged proteins

Purification of His<sub>6</sub>-tag proteins was performed by three consecutive chromatography steps as described below.

#### 2.15.3.1 Nickel-Affinity chromatography

Immobilized metal ion affinity chromatography (IMAC) is based on the specific binding properties of amino acids, particularly histidines, towards immobilized metals for purification purposes. Nickel-nitriloacetic (Ni-NTA) contains chelated nickel, which is able to specifically bind to poly-histidine in proteins and therefore used in this thesis for purification of His<sub>6</sub>-tagged proteins. For elution, an excess amount of a compound able to act as a metal ion ligand, such as Imidazole, is used and displaces the tagged protein from column resin.

Recombinant full length Bid with a hexa-histidine tag at the N-terminus was initially purified manually using His-Catcher Nickel Gravity Columns (PJK GmbH, Kleinbittersdorf, Germany) according to the manufacturer's protocol. Before starting, all buffers provided in Table 39 were prepared and the required buffer volumes as well as protein solution filtered through a 0.45 µm filter (Whatman, Dassel, Germany). The column was released from storage buffer and equilibrated twice with 3 ml aqua demin. followed by three times equilibration with 6 ml of IMAC binding buffer. Afterwards 6 ml of protein solution was applied to the column by gravity flow to allow binding of His<sub>6</sub>-tagged proteins. Sample application was repeated until the entire sample had been processed. For subsequent analysis, an unprocessed sample as well as a sample of the effluent was stored at 4°C until further use. After sample loading, the column was washed three times with 6 ml wash buffer, containing 10 mM imidazole to elute unspecifically bound proteins. Elution of the specifically bound protein was achieved by adding 4 volumes of 1.5 ml elution buffer, containing 250 mM imidazole thereby displacing the His<sub>6</sub>-tagged protein from the nickel ions. Elution fractions were collected drop-wise and stored at 4°C for further processing. All purification steps were performed on ice. Protein purity was confirmed by analyzing collected samples by SDS-PAGE.

Alternatively, affinity chromatography purification of His<sub>6</sub>-tagged full-length Bid was performed using a HisTrap<sup>TM</sup> FF column (GE Healthcare Bio-Science AB, Uppsala, Sweden) connected to the ÄKTA prime plus instrument. All buffers used for the following method are provided in Table 40. Before equilibration with binding buffer, the system was pre-equilibrated as described in 2.15.2. Depending on the protein sample size, chromatography was performed using either a 1 ml or 5 ml HisTrap<sup>TM</sup> FF column, which was likewise pre-equilibrated with binding buffer prior to sample loading. Final equilibration, sample injection, wash, sample elution as well as re-equilibration of the system were performed automatically by the applied program provided in Table 45. Protein sample was applied to the respective column by repeated injections using a 5 ml sample loop. During sample loading, flow through was collected in volumes of 8 ml. Elution of His<sub>6</sub>-tagged protein was performed using a continuous gradient of 0-300 mM imidazole followed by a wash out step up to concentrations of 400 mM imidazole. Elution fractions were collected in volumes of 1-5 ml and stored at 4°C until further use. The respective purification run was monitored using PrimeView5.0 and the resulting chromatogram was analyzed for elution peaks. Elution fractions collected within peak areas were analyzed by SDS- gel electrophoresis followed by coomassie staining. Afterwards, Bid-containing fractions were pooled and stored at 4°C until further purification by ion exchange.

**Table 45: Programmed method for ÄKTA - IMAC- Ni-Affinity chromatography**

(1 ml HiTrap column, 5 ml sample loop, &lt; 25 ml sample volume)

Action	Breakpoint	Volume [ml]	Conc Buffer B [%]	Flow rate [ml/min]	Fraction size [ml]	Inject valve position
Equilibration	1	0	0	1	0	Load
Sample injection 1	2	5	0	1	8	Inject
Equilibration/Buffer A wash	3	13	0	1	0	Load
Sample injection 2	4	15	0	1	8	Inject
Equilibration/Buffer A wash	5	23	0	1	0	Load
Sample injection 3	6	25	0	1	8	Inject
Equilibration/Buffer A wash	7	33	0	1	0	Load
Sample injection 4	8	35	0	1	8	Inject
Equilibration/Buffer A wash	9	43	0	1	0	Load
Sample injection 5	10	55	0	1	8	Inject
Wash 7% imidazole	11	63	0	1	5	Load
Elution	12	73	5	1	1	Load
Elution wash out	13	93	75	1	1	Load
End wash	14	103	75	1	5	Load
Re-equilibration	15	113	100	1	5	Load
End method	16	123	0	1	0	Waste

### 2.15.3.2 Ion exchange chromatography

Ion exchange chromatography is based on electrostatic properties of proteins, which can bind to the charged groups exposed on the surface of the exchanger. In this thesis anion exchange chromatography was performed by using HiTrap columns containing Q-Sepharose, which is composed of cross-linked 6% agarose beads with quaternary ammonium (Q) strong anion exchange groups. Q-Sepharose is commonly used for separation of proteins during purification.

Ion exchange chromatography was performed using pre-packed 5 ml HiTrap Q HP columns (GE Healthcare Bio-Science AB, Uppsala, Sweden) and the ÄKTA prime plus system. The appropriate buffers are provided in Table 42. To ensure ionic binding of full-length Bid, the total ionic strength of the protein buffer (Table 39; Buffer B, Table 40) needed to be reduced. Therefore, the Bid-containing fractions achieved by Ni-affinity chromatography were pooled and either four-times diluted with binding buffer A or desalted using Zeba™ Spin Desalting columns (Thermo Scientific, Langensfeld, Germany). After equilibrating the system (2.15.2) and connection of the column to the ÄKTA, ion exchange was started by applying the programmed method depicted in Table 46. During the process, the protein sample was applied to a 5 ml sample loop and sample injection was repeated 3-5 times depending on the particular sample volume. Throughout purification, elution fractions were collected in 2-5 ml



sizes and stored at 4°C until further use. Elution fractions collected within peak areas were analyzed by SDS- gel electrophoresis followed by coomassie staining. Bid-containing fractions were pooled and stored at 4°C.

**Table 46: Programmed method for ÄKTA – Ion Exchange Gradient elution**

(5 ml HiTrap column, 5 ml sample loop, < 25 ml sample volume)

Action	Breakpoint	Volume [ml]	Conc Buffer B [%]	Flow rate [ml/min]	Fraction size [ml]	Inject valve position
Equilibration	1	0	0	5	0	Load
Sample injection 1	2	25	0	5	5	Inject
Equilibration/Buffer A wash	3	30	0	5	2	Load
Sample injection 2	4	32	0	5	5	Inject
Equilibration/Buffer A wash	5	37	0	5	2	Load
Sample injection 3	6	39	0	5	5	Inject
Equilibration/Buffer A wash	7	44	0	5	2	Load
Sample injection 4	8	46	0	5	5	Inject
Equilibration/Buffer A wash	9	51	0	5	2	Load
Sample injection 5	10	53	0	5	5	Inject
Buffer A wash	11	58	0	5	5	Load
Elution	12	85	0	5	2.5	Load
Elution wash out	13	185	100	5	2.5	Load
End wash	14	205	100	5	2.5	Load
Re-equilibration	15	210	0	5	0	Waste
End method	16	215	0	5	0	Waste

When indicated, the Bid-containing fractions were subjected to proteolytic cleavage of the His<sub>6</sub>-tag (see 2.16) and in either case concentrated prior to the subsequent size exclusion chromatography.

### 2.15.3.3 Gel filtration

Gel filtration (size exclusion chromatography, SEC) is used for fractionation of proteins by their size and/or molecular weight. The macromolecule solution is separated by flowing through porous, inert matrices which are characterized by an exclusion limit indicating the molecular weight of the largest protein that is still delayed in the column.

In this thesis a HiLoad 16/600 column (GE Healthcare Bio-Science AB, Uppsala, Sweden) was used with a Superdex 75 prep grade matrix composed of dextran and highly cross-linked agarose. Due to different pore sizes within the matrix, molecules of different sizes elute through the stationary phase at different rates. The column allows for separation of proteins in the molecular weight range of 3,000 up to 70,000 Da.

Since separation efficiency increases with smaller sample volumes, the pooled Bid-containing fractions were concentrated using 3-kDa cut-off Amicon filters (Millipore, Schwalbach, Germany) up to a sample volume < 2 ml (2.18) and filtered through a 0.45 µm filter. Afterwards, gel filtration was performed using the ÄKTA prime plus system. After pre-equilibrating the system and column (2.15.2) with aqua demin. followed by gel filtration buffer (Table 43), the sample was applied to a 2 ml sample loop and the programmed method depicted in Table 47 was started. Elution fractions were collected in volumes of 2 ml. Due to gel filtration, highly pure Bid protein was yielded as shown by gel electrophoresis and coomassie staining. The protein was finally concentrated with 3-kDa cut-off Amicon filters (Millipore, Schwalbach, Germany) up to concentrations required for respective functional experiments or crystallization studies. Protein samples were stored at 4°C until use, or supplemented with 30% glycerol for long-term storage.

**Table 47: Programmed method for ÄKTA – Gel filtration (full-length Bid)**

(HiLoad 16/600 Superdex 75 pg column, 2 ml sample loop, < 2 ml sample volume)

Action	Breakpoint	Volume [ml]	Conc Buffer B [%]	Flow rate [ml/min]	Fraction size [ml]	Inject valve position
Equilibration	1	0	0	1	0	Load
Sample injection	2	10	0	1	0	Inject
Buffer wash	3	12	0	1	0	Load
Elution	4	35	0	1	2	Load
Re-equilibration	5	140	0	1	2	Load

## 2.15.4 Purification of recombinant GST-tagged proteins

### 2.15.4.1 GSH-Affinity chromatography

Glutathione S-transferase (GST) is a 26 kDa protein, which is used as N-terminal tag of target proteins to allow simple purification by affinity chromatography based on the high affinity of GST for immobilized glutathione. When applied to the affinity medium, GST-tagged proteins bind to the glutathione ligand, and impurities can be removed by washing with binding buffer. Elution of tagged proteins from chromatography medium is performed under mild, non-denaturing conditions that preserve both protein structure and function. Due to the positive influence of the GST-tag on protein solubility, expression efficiency and detection especially of small proteins, GST-tags are commonly used to generate proteins for crystallization and molecular immunology studies involving protein-protein interactions. Therefore, in this thesis, all truncated Bid constructs were fused to GST to allow highly pure

protein purification. To avoid interference of the GST-tag during crystallization, the tag was removed after affinity purification by proteolytic (thrombin) cleavage (2.16).

GSH-affinity chromatography was performed with the ÄKTA prime plus system using pre-packed 5 ml columns containing a matrix composed of highly cross-linked 4-6% agarose beads and a glutathione ligand. Depending on the protein amount, either GSTrap™ FF columns (GE Healthcare Bio-Science AB, Uppsala, Sweden) with a binding capacity of approximately 11 mg GST-tagged protein/ml, or Glutathione HiCap Cartridges (Quiagen, Hilden, Germany) with a binding capacity up to 100 mg GST-tagged protein were used.

To increase binding capacity, usually two 5 ml HiCap Cartridges were connected on after another. All buffers used for this method are provided in Table 41. After pre-equilibration of columns and the ÄKTA system (2.15.2), protein sample was loaded to the column through tube B using the programmed method provided in Table 48. Afterwards GSH-affinity chromatography was performed using the ÄKTA installed application template “GST-tag purification GSTrap”, as provided in Table 49. Elution was performed with buffer containing 10 mM glutathione and fractions were collected and stored at 4°C until SDS-gel electrophoresis. Fractions containing the respective Bid construct were pooled and subjected to further cut-off concentration and buffer exchange followed by proteolytic cleavage of the GST-tag.

Alternatively, sample application and purification of Bid construct 4 was performed in a one-step process by applying the programmed method in Table 50 to the ÄKTA system. Using this method, application of 25 ml sample volume was performed by repeated injection steps using a 5 ml sample loop. Fractions were collected in volumes of 2-5 ml. Elution and fraction analysis was performed as outlined above.

**Table 48: Programmed method for ÄKTA – sample application**

Action	Breakpoint	Volume [ml]	Sample tube B [%]	Flow rate [ml/min]	Fraction size [ml]	Inject valve position
Equilibration	1	0	0	1	0	Load
Sample injection	2	2	100	1	5	Load
Buffer wash	3	44	100	1	0	Load
Re-equilibration	4	50	0	1	0	Load
End method	5	65	0	0	0	Load

**Table 49: ÄKTA installed method – GST-tagged purification GSTrap**  
(5 ml GSTrap™ column)

Action	Breakpoint	Volume [ml]	Conc Buffer B [%]	Flow rate [ml/min]	Fraction size [ml]	Inject valve position
Priming A1	0	0	0	40	0	Waste
Equilibration	1	35	0	1	0	Load
Autozero	2	45				
Sample injection	2	45	0	0.3	0	Inject
Buffer wash	3	50	0	1	0	Load
End wash	4	60	0	1	0	Load
Priming B	5	60.1	100	40	0	Waste
Elution	6	95	100	1	1	Load
End elution	7	105	100	1	0	Load
Priming A1	8	105.1	0	40	0	Waste
Re-equilibration	9	120	0	1	0	Load
End method	10	125	0	0	0	Load

**Table 50: Programmed method for ÄKTA – GST-affinity chromatography**  
(2 x 5 ml HiCap Cartridge, 5 ml sample loop, < 25 ml sample volume)

Action	Breakpoint	Volume [ml]	Conc Buffer B [%]	Flow rate [ml/min]	Fraction size [ml]	Inject valve position
Pre-equilibration	1	0	0	1	0	Load
Equilibration	2	10	0	1	0	Load
Sample injection 1	3	12	0	1	5	Inject
Equilibration/Buffer A wash	4	17	0	1	2	Load
Sample injection 2	5	19	0	1	5	Inject
Equilibration/Buffer A wash	6	24	0	1	2	Load
Sample injection 3	7	26	0	1	5	Inject
Equilibration/Buffer A wash	8	31	0	1	2	Load
Sample injection 4	9	33	0	1	5	Inject
Equilibration/Buffer A wash	10	38	0	1	2	Load
Sample injection 5	11	40	0	1	5	Inject
Equilibration/Buffer A wash	12	45	0	1	2	Load
Sample injection 6	13	47	0	1	5	Inject
Buffer A wash	14	52	0	1	2	Load
Pre-elution	15	72	0	1	2	Load
Elution	16	74	100	1	2	Load
Elution wash out	17	104	100	1	2	Load
Reequilibration	18	110	0	1	2	Load
Method end	19	120	0	1	0	Load

### 2.15.4.2 Gel filtration

To achieve highly pure recombinant Bid constructs suitable for further crystallization studies, Bid construct-containing fractions were finally purified by gel filtration. After buffer exchange to gel filtration buffer, provided in Table 43, and cleavage of the GST-tag (2.16), protein samples were concentrated using 3-kDa cut-off Amicon filters (Millipore, Schwalbach, Germany) up to a sample volume < 5 ml and filtered through a 0.45 µm filter. Gel filtration was performed as described above following the programmed methods provided in Table 47 and Table 51, depending on the particular sample volume. Purity of the elution fractions was confirmed by SDS- gel electrophoresis and Bid construct-containing fractions were pooled, concentrated and subjected to further crystallization studies.

**Table 51: Programmed method for ÄKTA – Gel filtration (Bid constructs)**

(HiLoad 16/600 Superdex 75 pg column, 5 ml sample loop, ≤ 5 ml sample volume)

Action	Breakpoint	Volume [ml]	Conc Buffer B [%]	Flow rate [ml/min]	Fraction size [ml]	Inject valve position
Equilibration	1	0	0	1	0	Load
Sample injection	2	10	0	1	0	Inject
Buffer wash	3	16	0	1	5	Load
Elution	4	20	0	1	2	Load
Elution wash out	5	45	0	1	2	Load
Re-equilibration	6	160	0	1	2	Load

### 2.16 Thrombin cleavage of His<sub>6</sub>- and GST-fusion proteins

Thrombin is a protease used to digest fusion proteins prepared from pGEX or pET15b vectors, which include the thrombin recognition sequence (LeuValProArg<sup>↓</sup>GlySer). By cleaving the peptide bond between Arg and Gly, thrombin enables site-specific cleavage of recombinant fusion proteins and the removal of the purification His<sub>6</sub>- and GST-tag.

After purifying the recombinant proteins by affinity and ion exchange chromatography, protein concentration was determined by photometry to calculate the required volume of thrombin (GE Healthcare, Bio-Science AB, Uppsala, Sweden). According to the manufacturer's protocol, the lyophilized thrombin was solved in 1 x PBS to final solutions of 1 U/µl or 0.1 U/µl. In order to preserve thrombin activity, aliquots were stored at -80°C. Generally, one unit thrombin will cleave ≥ 90 % of 100 µg GST-protein and cleavage should be complete following overnight treatment at 22°C with ≤ 10 units/mg fusion protein. For cleavage of His<sub>6</sub>-tagged full-length Bid one unit thrombin was used to cleave 50 µg of His<sub>6</sub>-protein. After addition of thrombin, the mixture was incubated at 37°C for 16 h and the

digestion was stopped by adding 1 mM of the serine protease inhibitor phenylmethylsulfonyl fluoride (PMSF). The cutting efficiency was controlled by SDS- gel electrophoresis followed by coomassie staining. In addition, MALDI-TOF analyses were performed by Jörg Kahnt at the Max-Planck-Institute of Terrestrial Microbiology, Marburg, Germany to confirm the cutting efficiency and to exclude further cleavage within the Bid protein sequence. For MALDI-TOF analysis, a buffer exchange of protein samples was performed prior to thrombin cleavage. Protein desalting was performed using Zeba<sup>TM</sup> Spin Desalting columns (Thermo Scientific, Langenselbold, Germany) according to the manufacturer's protocol.

GST- tagged Bid constructs (Bid1-Bid4) were cleaved after affinity chromatography in GST-elution buffer (Table 41). For effective removal of the GST-tag, a thrombin concentration of 3.5 U/ml was used, and to enhance thrombin activity, the digestion was carried out in the presence of 10-12 mM calcium chloride for 16 h at 37°C. Afterwards, thrombin activity was inhibited by addition of 1 mM PMSF. Alternatively, removal of GST-tag from GST-fused Bid constructs was performed using the thrombin protease provided from Novagen<sup>®</sup>, with the unit definition of 1U/mg protein. Cleavage efficiency was controlled by SDS- electrophoresis.

## 2.17 Dialysis of recombinant proteins

Dialysis is a process used to separate molecules in solution by the differences in their rates of diffusion through a semi permeable membrane. Due to the pore size of the membrane large molecules in the sample, such as proteins, cannot pass through the membrane, thereby restricting their diffusion from the sample chamber. In contrast, small molecules, such as salt molecules, will freely diffuse across the membrane and obtain equilibrium across the entire solution volume. In this study dialysis was used to decrease the salt concentration and to remove the imidazole content of the protein samples after purification by Ni-affinity chromatography.

For dialysis a flexible Spectra/Por<sup>®</sup> cellulose membrane tube with a molecular weight cut-off of 7kDa (Serva electrophoresis, Mannheim, Germany) was used. Prior to sample dialysis, the dialysis tube was cut to a size dependent on the respective sample volume. Afterwards the membrane was incubated in the dialysis buffer (20 mM Tris pH 8, 10 mM  $\beta$ -Mercaptoethanol) for 1-2 hours prior to sample addition. The tubing was closed at the end by a locking clamp and loaded with the protein solution and closed with a second locking clamp. The sample-filled tubing was placed into a chamber containing 5 liter of dialysis buffer and incubated at 4°C overnight with gentle stirring of the buffer. The day after the sample was transferred to a new sample tube and protein concentration was determined by Bradford assay or UV photometry before concentration of the protein when indicated.

## 2.18 Cut-off concentration of recombinant proteins

To achieve the final concentration of recombinant proteins required for the respective experiments and to reach high concentration of pure protein for crystallographic studies 3-kDa cut-off ultra-filtration was used. Therefore the respective samples were filled into 3-kDa cut-off Amicon concentrators (Amicon<sup>®</sup> Ultra-4/ Amicon Ultra-15, Millipore, Schwalbach, Germany) for volumes up to 4 ml or up to 15 ml, respectively. Afterwards the samples were centrifuged at 4,000 *rpm* at 4°C until the required protein concentration was reached. In the meantime of centrifugation, protein concentration was determined by absorption at 280 nm with the NanoPhotometer<sup>™</sup> (Implen, Munich, Germany).

## 2.19 Cleavage of full length Bid with Caspase 8

Cleavage of full-length Bid with recombinant caspase 8 was performed as previously described<sup>69</sup>. Therefore, 200 µl of pure recombinant Bid in 20 mM Tris (pH 7.4), 50 mM NaCl, was 1:1 diluted with 200 µl of caspase-cutting buffer (50 mM HEPES, 100 mM NaCl, 10 mM DTT, 1 mM EDTA, 10% sucrose, pH 7.5) and incubated with 1 µl of recombinant caspase 8 (7.6 mg/ml) for 2-4 h at room temperature. The cutting efficiency was estimated to be over 95% by SDS-polyacrylamide gel electrophoresis and coomassie staining and additionally by western blot. After 1h, Bid was cleaved providing the insoluble C- and N-terminal fragment. For functional analysis of tBid, the mixture was applied to fluorescence liposomes (2.22.1.2). For thermophoresis measurements and analyzing the effect of tBid on VDAC1 channels the cleaved Bid fractions were separated from excess of caspase 8. Therefore, the solution was diluted 1:1 with SEC-buffer (25 mM HEPES/NaOH pH 7.5, 300 mM NaCl, 0.2 mM DTT, 2% OG) to resolve tBid and applied onto a Superdex 200 (GE Healthcare Bio-Science AB, Uppsala, Sweden) column, yielding both fragments of cleaved Bid protein as shown by SDS-PAGE. tBid was concentrated with a 3-kDa cut-off Amicon concentrator (Amicon Ultra-15, Millipore, Darmstadt, Deutschland). The protein concentration was measured by absorption at 280 nm with the NanoPhotometer<sup>™</sup> (Implen, Munich, Germany). The samples were stored at 4 °C until use.

## 2.20 Determination of protein concentration

The concentration of recombinant proteins was determined either by the Bradford assay or by UV spectroscopy using the NanoPhotometer™ (Implen, GE Healthcare Europe GmbH, Freiburg, Germany).

### 2.20.1 Bradford assay

Total protein concentrations of expressed recombinant full-length Bid and different Bid constructs, were determined by the Bradford assay according to the manufacturers protocol (AppliChem, Darmstadt, Germany). The Bradford method is a fast procedure for determination of protein concentrations in solutions that depends on quantifying the binding of a dye, Coomassie Brilliant Blue G-250, to an unknown protein. The Coomassie blue G250 binds most readily to arginyl and lysyl residues of the respective proteins and the binding is proportional to the protein amount present. When binding to a protein occurs, the absorbance maximum for the acidic solution of Coomassie Brilliant Blue-G250 shifts from 465 nm to 595 nm, causing a visible color change in a linear range of the assay from 5 to 25 µg/ml protein amount. The protein concentration of a test sample was determined by comparison to that of a standard protein, bovine serum albumin (BSA).

For standard, a serial dilution of a BSA stock (10 mg/ml) was prepared by diluting the stock with protein buffer (20 mM Tris base, pH 7.4, 50 mM NaCl) to final concentrations of 0, 2, 4, 6, 8, 10 µg BSA. To each sample 1 ml of Bradford reagent (AppliChem, Darmstadt, Germany) was added and mixed gently by vortexing. The reagent blank (0 µg BSA) was used to zero the spectrophotometer (BioRad laboratories, Munich, Germany). After transferring the samples to disposable trUView™ cuvetts (BioRad laboratories, Munich, Germany) the absorbance of each sample was measured at 595 nm using the Lambda 595 nm assay. For sample preparation, 10 µl of each sample was filled up with protein buffer to a final volume of 100 µl. After adding 1 ml of Bradford reagent, samples were mixed gently by vortexing and transferred to cuvetts. Using the BSA standard curve, the protein concentration of each sample was determined. Since samples were diluted 1:10 before measuring, the calculated protein concentration was multiplied by 10 to get the amount of protein in 100 µl.

### 2.20.2 Nanodrop photometry

For determining the protein amount of recombinant protein samples after chromatography purification, the absorbance of protein samples was measured using the NanoPhotometer™ (Implen, GE Healthcare Europe GmbH, Freiburg, Germany). The protein concentration was determined at 280 nm due to absorption by tyrosine, tryptophan and phenylalanine amino acids. Since the Abs 280 varies greatly for different proteins due to their amino acid content,



the specific absorption value for a particular protein must be determined. Therefore, a specific A280 factor was determined for each protein, according to the Implen NanoPhotometer™ User manual. The A280 factor is based on the extinction coefficient of the respective protein [molecular weight/molar extinction coefficient]. The molar extinction coefficients for each protein were determined based on the amino acid sequence data as described by Gill et al.<sup>187</sup>. Molar extinction coefficients were calculated as provided in Table 52. Before measuring the protein concentration of each sample, A260 Factor was set to zero for direct  $\lambda$ 280 UV protein measurement and A280 factor was set to the value calculated for the respective protein construct (Table 52). Afterwards the system was blanked using protein buffer (20 mM Tris base, pH 7.4, 50 mM NaCl) and each sample was measured using a sample volume of 4  $\mu$ l. The respective protein concentrations were calculated as mean of at least three measurements.

**Table 52: Molar extinction coefficients and A280 factors**

Protein	Molecular weight	Molar extinction coefficient	A280 Factor
Full-length His <sub>6</sub> -Bid	24,114.75 g/mol	8250 mol/l*cm-1	2,923
Full-length Bid	22,232.04 g/mol	8250 mol/l*cm-1	2,695
Bid construct 1	17,626.22 g/mol	2560 mol/l*cm-1	6,885
Bid construct 2	18,127.72 g/mol	8250 mol/l*cm-1	2,197
Bid construct 3	17,569.17 g/mol	2560 mol/l*cm-1	6,863
Bid construct 4	18.070,67 g/mol	8250 mol/l*cm-1	2,190

## 2.21 Acetone precipitation

To increase the concentration of soluble protein fractions after bacterial expression and pull-downed proteins from protein-protein interaction studies, the protein samples were acetone precipitated according to the pierce protocol for acetone precipitation (Thermo Fisher Scientific, Schwerte, Germany). Briefly, samples were gently mixed with the 4-fold amount of cold acetone (Roth, Karlsruhe, Germany), and incubated at -20°C for at least 120 min. or overnight. Afterwards, the solution was centrifuged at 15,300 *rpm*, 4°C for 15-30 minutes. After removing the supernatant the acetone was evaporated from the uncapped tube at room temperature for 30 minutes without over-drying the pellet. The pellet was then resuspended in the respective protein buffer and supplemented with 5 x SDS buffer to control the samples by gel electrophoresis followed by coomassie staining or western blot analysis.

## 2.22 Functional analysis of recombinant proteins

In order to investigate the functional activity of recombinant proteins, recombinant full-length Bid and its truncated form tBid were applied to *in vitro* assays addressing the effect of the proteins on lipid membranes and to investigate protein-protein interactions.

### 2.22.1 Models of membrane permeabilization

To explore the effect of full-length Bid, tBid and Bax on artificial lipid bilayer structures, which mimic the mitochondrial membrane, two *in vitro* assays for membrane permeabilization were established in this thesis.

All lipids used for liposome and planar lipid bilayer preparations were derived from Avanti Polar lipids (Avanti Polar lipids, Alabaster, AL, USA) and provided in Table 53.

**Table 53: Lipids (Avanti Polar lipids)**

Lipid	Origin	Concentration	Physical state
L- $\alpha$ -Phosphatidylcholine (PC)	Egg, Chicken	25 mg/ml	Chloroform
L- $\alpha$ -Phosphatidylethanolamine (PE)	Egg, Chicken	25 mg/ml	Chloroform
Cardiolipin (CL)	Heart, Bovine-Disodium Salt	25 mg/ml	Chloroform

#### 2.22.1.1 Preparation of liposomes

5,6-carboxyfluorescein (CF) containing liposomes, with a lipid composition reflecting that of the mitochondrial outer membrane (MOM), were prepared by extrusion using the Avanti-Mini-Extruder (Avanti Polar lipids, Alabaster, AL, USA). Lipids used for liposome preparation are provided in Table 53. For cardiolipin-containing liposomes (PC/PE/CL: 54/20/26), 66.67  $\mu$ l phosphatidylcholin (PC), 23.82  $\mu$ l phosphatidylethanolamine (PE) and 62.16  $\mu$ l cardiolipin in chloroform were mixed. For comparison, liposomes without cardiolipin (PC/PE: 80/20) were prepared using a mixture of 98.76  $\mu$ l PC and 23.82  $\mu$ l PE in chloroform. For purification purposes, both liposome mixtures were supplemented with 1 % of rhodamine DHPE (Lissamine<sup>TM</sup> rhodamine B 1,2-Dihexadecanoyl-*sn*-Glycero-3-Phosphoethanolamine, Triethylammonium Salt, Invitrogen, Karlsruhe, Germany). After stirring the liposome mixtures, the organic solvent was removed by evaporation under a nitrogen stream for 15 min. at room temperature or for 5-10 min. at 30°C using the EVA-EC1-24 evaporator (VLM GmbH, Bielefeld, Germany). Subsequently, lipid samples were incubated in an exsiccator under vacuum for 1-2 h at room temperature for complete removal of the chloroform. To avoid

drying out of the lipid film, samples were consistently inspected in between. Dry lipid films were resuspended in 1 ml 1 x PBS, pH7.4 containing 20 mM 5,6-carboxyfluorescein (CF, Invitrogen), respectively. Large multi-lamellar vesicles (LMV), obtained by hydration, were further downsized by subjection to several freeze/thaw (F/T) cycles followed by extrusion. For preparation of large uni-lamellar vesicles (LUV), samples were frozen in liquid nitrogen for 1 min. and thawed at 37°C in a water bath. After 20 F/T cycles, liposomes were extruded 15 times through two polycarbonate filters with pores of 200 nm diameters using the Avanti-Mini-Extruder. Prior to sample application, the extruder was prepared according to the manufacturer's protocol. After extrusion, samples were stored at 4°C until all liposome samples were prepared. Liposomes were isolated and untrapped CF was removed by gel filtration using a pre-packed Sephadex-G25 column (PD MidiTrap G-25, GE Healthcare Europe GmbH, Freiburg, Germany). According to the manufacturer's gravity protocol, the columns were three-times equilibrated with 15 ml of 1 x PBS. Afterwards 1 ml liposome sample was applied to the column and finally eluted with 1.5 ml 1 x PBS. Untrapped CF appeared as yellow band whereas rhodamine-stained liposomes were visualized as pink-colored band in the gel-packed bed.

Since the phase transition temperature ( $T_m$ ) of all required phospholipids was approximately 2°C, the whole procedure could be performed at room temperature.

#### **2.22.1.2 Liposome channel activity assay**

The liposome channel activity assay was performed in black 96-well plates (Greiner, Frickenhausen, Germany) on a fluorescence plate reader (FluoStar OPTIMA, BMG Labtech, Offenburg, Germany). Fluorescence was recorded as a function of time with excitation at 485 nm and emission at 520 nm and fluorescence values were given every 5 seconds. Twenty  $\mu$ l of purified 5,6-carboxyfluorescein-containing liposomes were diluted in 80  $\mu$ l PBS to give a suitable fluorescence value. For baseline fluorescence, liposomes were initially measured at room temperature without addition of proteins every 5 seconds for at least 3 minutes. Afterwards, recombinant proteins were added and the change in fluorescence was monitored every 5 seconds for at least 20 min. up to 1 hour. If proteins were able to induce channel formation or disruption of the liposome membrane, 5,6-carboxyfluorescein was released as indicated as an increase in fluorescence over time. In detail, caspase 8- cleaved Bid (tBid) was added at final concentrations of 10 nM up to 6  $\mu$ M for dose-dependence studies. Recombinant Bax was used in final concentrations of 100 nM and 500 nM when applied to liposomes alone. For investigation of the pore-forming activities of both proteins in combination, 100-500 nM Bax was mixed with 50 nM-6  $\mu$ M tBid and the protein mixture was incubated 3 min. prior to adding the mixture to the liposomes. Addition of the appropriate protein buffer to the liposomes was used as negative control.

For comparison of fluorescence release, 20 µl of aqua demin. was added to the liposomes and the recorded fluorescence was set to 0 % release of CF. To reach 100 % release of CF, liposomes were incubated with 3-4% of TritonX-100.

To establish the liposome channel activity assay as an *in vitro* assay to screen novel small-molecules for their ability to inhibit Bid-channel activity, recombinant Bid/tBid, in presence or absence of recombinant Bax, was pre-incubated with different concentrations of the Bid inhibitor BI6c9 at room temperature for 1-3 min. The mixture was afterwards added to the CF-containing liposomes and change in fluorescence (excitation 485 nm and emission 520 nm) was recorded every 5 seconds for at least 20 min. up to 1 h.

## 2.22.2 Analysis of protein-protein interactions

### 2.22.2.1 *In vitro* Bid/tBid – VDAC1 binding assay

Binding of VDAC1 to purified His<sub>6</sub>-tagged Bid or tBid was assayed by His-tag pull-down using Ni-NTA resin (Quiagen, Hilden, Germany). Therefore, 50 µg of recombinant full-length His<sub>6</sub>-Bid (His-rBid) and 50 µg of caspase 8-cleaved Bid (His-rtBid) were mixed separately with 50 µg of recombinant mVDAC1 (rVDAC1) or with 50 µg of a VDAC1 deletion mutant (rVDAC1 Δ11). Afterwards protein mixture were incubated with 150 µl of nickel-nitrilotriacetic acid-agarose (Ni-NTA) in binding buffer (10 mM Tris HCl pH 8.0, 100 mM NaCl, 0.05 % LDAO) at 4 °C with gentle rotation for 1-2 h, respectively. His-rBid without incubation with mVDAC1 and sample containing only mVDAC1 or rVDAC1 Δ11 were used as negative controls. The protein-Ni-NTA suspensions were loaded on a Poly-Prep<sup>®</sup> Chromatography column (BioRad Laboratories, Munich, Germany) and washed 2-3 times with 2 ml wash buffer (10 mM Tris HCl pH 8.0, 100 mM NaCl, 0.05 % LDAO, 20 mM imidazole) to remove unbound protein amounts. His-rBid and His-rtBid together with their binding partners bound to Ni-NTA, were finally eluted with 0.5 ml elution buffer containing 200 mM imidazole (10 mM Tris HCl pH 8.0, 100 mM NaCl, 0.05 % LDAO, 200 mM imidazole). The washing fractions (W) and elution fractions (E) for each sample were collected and acetone precipitated following the pierce manufacturer's protocol for acetone precipitation. To determine protein-protein interactions, the protein samples were analyzed by SDS-PAGE followed by coomassie staining. Alternatively, the SDS-PAGE was followed by western blot and proteins detected using specific antibodies as described before. Samples containing only one protein served as controls for non-specific binding.

### 2.22.2.2 Thermophoresis measurements

Microscale thermophoresis is based on the direct movement of biomolecules in a microscopic temperature gradient and is used to determine binding affinities or surface modifications of molecules. The method enables the quantitative analysis of molecular interactions in solution at a microliter scale. Changes of the hydration shell of small molecules or proteins due to structural or conformational alterations result in a relative change of movement along the temperature gradient. To study protein-protein interaction one protein is fluorescently labeled and used under constant concentration and buffer condition, while the binding partner is titrated in serial dilution experiments. Thermophoresis of the fluorescently labeled protein differs significantly from the protein-target complex due to changes in size, charge and solvation entropy. Therefore protein-protein interactions can be measured and sigmoid binding curves are obtained using different concentrations of the dilution series, resulting in dissociation constants  $K_D$ .

Thermophoresis experiments were performed by Barbara Mertins from the group of Prof. Essen (Philipps-University Marburg, Department of Chemistry, Marburg, Germany). For thermophoresis measurements of mVDAC1 and Bid/tBid, mVDAC1 was labeled using Alexa Fluor® 532 C5-maleimide (Invitrogen). 1 mM TCEP (AppliChem) were added to 100  $\mu$ M protein solution and incubated for 30 min at 4°C. After incubation 1 mM label was added and incubated over night at 4°C and 350 rpm in a Thermomixer (Eppendorf). Excess label was removed by using a Sephadex G25 column (GE Healthcare Bio-Science AB, Uppsala, Sweden). Protein concentration and label efficiency were measured at 280 nm and 532 nm with a Nanodrop ND-1000 (peqLab). Microscale thermophoresis (MST) measurements were performed using the Monolith NT.115 instrument (NANO TEMPER). mVDAC1 concentration was kept constant at 50 nM and Bid / tBid were added to the solution ranging from 15 nM to 500  $\mu$ M. Protein solution was incubated in the dark for 20 min at RT and centrifuged (25402 g, 5 min) to remove precipitated proteins. Standard capillaries (NANO TEMPER) were filled with 8-10  $\mu$ L of the protein solution and MST curves were recorded.  $K_D$  values were calculated using the NT-Analysis software. Fluorescently labeled OmpG was used to rule out unspecific interactions of Bid/tBid with  $\beta$ -barrels.

### 2.22.2.3 Single channel conductance recordings of mVDAC1 ion channels

Single channel conductance recordings were performed using the black lipid membrane (BLM) technique<sup>188</sup>. The planar lipid membranes were prepared by painting or rising the solution surface over a 200  $\mu\text{m}$  hole in a two chamber apparatus (polystyrene cuvette: CP2A, bilayer chamber: BCH-22A, Warner Instruments) filled equally with BLM buffer (10 mM Tris/HCl, pH 7.4, 1 M KCl, 5 mM  $\text{CaCl}_2$ ). As membrane mixture a solution of diphytanoylphosphatidylcholin (Avanti Polar Lipids, No.341601) in *n*-decane (25 mg/mL) was used. The porin was added beside the BLM, the bilayer was reconstituted and a voltage-gradient was imposed across the membrane while waiting for insertion of single channels. Once a stable single VDAC1 channel was inserted, recombinant Bid or tBid were added to the *cis* side, respectively. For current detection voltages from +40 mV to -40 mV were applied and current was detected using the Multipatch 700B patch-clamp amplifier combined with a Digidata 1440A A/D converter with pClamp 10.2 software (Axon Instruments). The data were collected at 5 kHz and sampled at 200 Hz for further analysis. For each measurement the differences from the baseline to the stable high conductance state (S0) and the low conductance states (S1, S2, S2') were determined with the software. Each data point of the *I/V*-curve was taken in account to determine the conductivity via the slope derived by linear regression. The BLM measurements were performed by Philip Reiß (Philipps-University of Marburg, Department of Chemistry, Marburg, Germany).

## 2.23 Crystallographic methods

### 2.23.1 Protein crystallization

To provide a basis for the structural understanding of molecular functions of Bid in cell death signaling and to allow the determination of protein-ligand complexes, the purified recombinant Bid constructs were subjected to extensive crystallization screening. Crystal structure analysis was performed using X-ray diffraction, which is the most advanced method available for obtaining high-resolution structural information about biological macromolecules.

Crystallographic studies were performed at the MarXtal crystallization lab (SYNMICRO, University of Marburg, Germany) with the support of Ralf Pöschke.

The integrity of Bid constructs was verified by MALDI-TOF analysis, which was kindly performed by Jörg Kahnt at the Max-Planck-Institute of Terrestrial Microbiology, Marburg (MPI, Marburg, Germany).

Beside various crystallization screens using purified full-length Bid, slightly modified truncated Bid constructs were subjected to the described crystallization procedures

#### 2.23.1.1 Protein sample preparation

For X-ray crystallization, the protein sample should be as pure as practically possible (>95%) and free of amorphous and particulate material. Highly pure protein has to be obtained in concentrations of 5-25 mg/ml, commonly approximately 10 mg/ml. Such high protein concentrations enable a faster crystal growth than less concentrations of protein.

Therefore, recombinant full-length Bid as well as recombinant Bid constructs (Bid1- Bid4) were purified as outlined above. After gel-filtration, purity of the proteins was confirmed by SDS-PAGE and estimated about 98%. Proteins were concentrated using 3-kDa cut-off Amicon concentrators (Amicon<sup>®</sup> Ultra-4/ Amicon Ultra-15, Millipore, Schwalbach, Germany) to concentrations as high as possible. Notably, a concentration of 10 mg/ml could not always be reached due to limitations in protein sample amount and protein absorption on filter membranes. Therefore, protein concentrations of 4.5 mg/ml up to 15 mg/ml were subjected to the following crystallographic methods. To avoid bacterial growth during crystallization all proteins samples were sterile-filtered using a 0.2 µm filter (Whatman Puradisc<sup>™</sup> 4 mm Syringe filter, Whatman, Dassel, Germany). All proteins were subjected to crystallization screens in buffer containing 20 mM Tris, pH 7.4, 50 mM NaCl, and 0.03% Na-azide.

### 2.23.1.2 Crystal growth techniques

In this study, crystallization screens were performed utilizing the vapor-diffusion technique, which is the most common used crystallization technique, due in part to the simplicity of the experiments and the diversity of variables that can be manipulated. Vapor-diffusion experiments undergo a dynamic equilibration process. At the beginning of the crystallization experiment a crystallization drop is sealed into an airtight chamber with a reservoir solution. The difference in concentration between the drop and the reservoir drives the system towards the equilibrium by diffusion through the vapor phase. Thereby the experiment drop dehydrates and reduces its volume, driving the protein toward a state of supersaturation where crystallization may occur<sup>189</sup>.

Using this technique, a small droplet of the respective Bid protein (1  $\mu$ l using 24 well-plates, 0.3  $\mu$ l using 96-well plates), was mixed with an equal volume of the appropriate precipitating solution. For all initial crystallization screens the sitting-drop technique was performed (Figure 11A), thus sitting drops are more mechanically stable and more resistant to temperature changes than hanging drops. However, it can be hard to mount crystals from sitting drops. Therefore, some optimization screens were performed in 24-well plates using hanging-drop vapor-diffusion by placing a small droplet of sample mixed with crystallization reagent on a screw cap (EasyXtal tool, Qiagen, Hilden Germany) inverted over the reservoir in vapor equilibration with the reagent (Figure 11B).

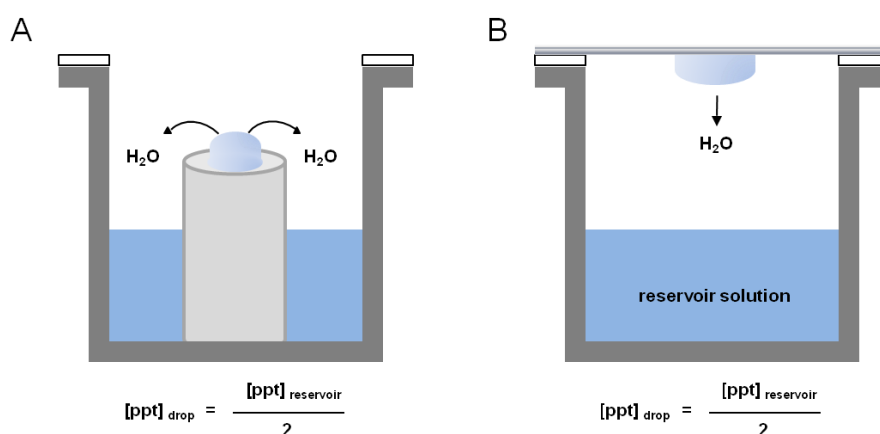


Figure 11: Vapor-diffusion techniques: A) sitting-drop, B) hanging-drop.



### 2.23.1.3 Crystallization screens

To obtain crystals for determination the three-dimensional structure of a protein, a wide array of crystallization conditions has to be screened. Since many factors, such as protein concentration, precipitant concentration, pH value, buffer composition, presence of salt anions and/or additives, influences the crystallization of a protein, initial screening was performed using the Quiagen NeXtal-screening suites (Quiagen, Hilden, Germany). These screening suites utilize the sparse matrix screening strategy that typically maps a wide sector of the chemical space using many different reagents selected from known and published crystallization conditions. Each screening suite consists of a set of 96 precisely defined chemical solutions and differs in pH, buffer material, salt and precipitant. Starting with different sets of initial screening conditions, the search for a suitable condition can be narrowed down by further developing conditions surrounding a promising “hit” condition that provides crystalline forms (see 2.23.2).

All initial trials were performed by “automated sitting-drop crystallization in 96-well plates” using the MarXtal crystallization equipment. Prior to protein sample application, each of the 96 screening suite solutions was transferred automatically into a 2.2 ml 96-deep-well plate (Abgene, Thermo Fischer Scientific, Schwerte, Germany) using the Lissy-system (Zinsser Analytic GmbH, Frankfurt, Germany). Afterwards 80 µl of each of the reservoir solutions was pipetted into the corresponding reservoir of a MRC2 2-drop-chamber 96-well crystallization plate (Jena Bioscience, Jena, Germany), which was then loaded on the Cartesian Microsys™ SQ4000 crystallization robot (Genomic Solutions, Huntingdon, UK, USA). Using this robot, 300 nl drops of the respective reservoir were transferred into each of the two corresponding wells on the plate. Afterwards, 300 nl of either protein or buffer solution were pipetted into the freshly prepared reservoir drops. Finally, the setup was isolated by sealing the plates with ViewSeal™ (Greiner Bio-one, Frickenhausen, Germany) adhesive transparent plastic sheets.

The procedure was repeated for each screening suite and the finished crystallization plates were stored at 18°C or 4°C in the Formulatrix Rock Imager™ (MarXtal, Department of Chemistry, University of Marburg), which is a fully automated documentation system for crystallization experiments. Within this Rock Imager, each well of the respective screening plates was automatically monitored by microscopy and images were taken in continuous time-lags. Screening results were scored by analyzing the taken photomicrographs using the Rock Maker Web provided by MarXtal (Department of Chemistry, University of Marburg). Using this setup, the respective recombinant Bid constructs, expressed and purified in this thesis, were initially subjected to 13 different screenings suites, respectively. Since temperature does affect crystal growth most of the screens were duplicated at 4°C and

18°C. Table 54 predicts the initial standard setup for the different Bid constructs tested for crystallization during this work.

**Table 54: Initial screens and set ups tested for the different Bid constructs**

Parameter	His <sub>6</sub> -Bid	Bid-22	Bid 1 (12-47)	Bid 2 (12-51)	Bid 4 (13-51)
Drop 1	Protein	Protein	Protein	Protein	Protein
Drop 2	Buffer	Buffer	Buffer	Buffer	Buffer
Protein concentration (mg/ml)	4.5 mg/ml	9.9 mg/ml	9.5 mg/ml	8.5 mg/ml	10.0 mg/ml
Protein buffer	Tris 20 mM, 50 mM NaCl, pH 7.4				
Screening temperature	18°C	18°C	18°C	18°C	4°C + 18°C
Screening Suites tested	1-13*	1, 3, 5, 7-9, 11, 13*	1-13*	1-13*	1-13*
* Screening Suites (Qiagen)	1. AmSO4 Suite, 2. Anions Suite, 3. Classics Suite, 4. Classics Lite Suite, 5. Cryos Suite, 6. JCSG+ Suite, 7. JCSG Core Suite I, 8. JCSG Core Suite II, 9. JCSG Core Suite III, 10. JCSG Core Suite IV, 11. MBClass I Suite, 12. MBClass II Suite and 13. PACT Suite				

Following this strategy, Bid construct 4 was additionally applied to screening suites Classic, Cryos, JCSG+, JCSG Core suite I-IV and PACT suite in concentrations of 15.2 mg/ml at 18°C. Initial screens were repeated at 18°C and 4°C using the Bid construct 1 in concentrations of 10.5 mg/ml. In duplicate screens, Bid1-containing protein drops were supplemented with nanoparticles. Hit conditions found during initial screening were optimized as described below. Additionally, co-crystallization of Bid1 with the Bid inhibitor BI-6c9 was attempted using the screening suites JCSG Core I-IV, PACT and JCSG+.

### 2.23.2 Optimizing and reproducing crystallization

Optimization of crystallization aims to enlarge the crystal size and to enhance the occurrence of single crystals obtained in the initial crystallization screen. Conditions where initial crystallization was observed, referred to as “hit” conditions, were manually set up and adjusted in a grid screen. In contrast to the sparse matrix screen, in a grid screen the precipitant type of the “hit” condition is screened systematically in a separate tray, varying pH and precipitant concentration. Optimization of hit conditions was initially performed using the hanging-drop technique in 24-well plates with a screw cap (EasyXtal tool, Qiagen, Hilden Germany). Protein solution was added in volumes of 2 µl to an equal volume of the respective reservoir solution. Optimizations of Bid 22 crystals were performed in 24-VDX

plates by sitting-drop vapor diffusion. To initialize crystal growth some optimization grids were additionally supplemented by heterogeneous or homogeneous seeding (2.23.2.2). Since small differences in drop and reservoir volumes can affect crystal growth, optimizations performed in 24-well plates were additionally transferred to 96-well crystallization plates. Reservoir conditions in 24-well plates were prepared using customized buffers and reagents, while 96-well optimizations were mostly performed with the original NeXtal stock solutions (Quiagen, Hilden, Germany). Final buffer compositions were manually pipetted and transferred into 96-deep well plates. Pipetting of 0.3  $\mu$ l protein solution and 0.3  $\mu$ l reservoir solution was performed either manually or using the Cartesian Microsys<sup>TM</sup> SQ4000 crystallization robot. Table 55 et sqq. show the optimization steps of most promising hit conditions performed for the different Bid constructs, respectively.

### 24-well plate optimization grids:

**Table 55: Optimization of Bid 22 crystals I, 4°C + 18°C**

*(based on condition 21 from the Classic Suite)*

Composition	Original	Optimization steps
0.1 M Tris (pH)	8.5	7.5/8.0/8.5
2-Methyl-2,4 pentanediol (% in v/v)	50	50/55/60/65
Ammonium di-hydrogenphosphat (M)	0.2	0.2

**Table 56: Optimization of Bid 22 crystals II, 4°C + 18°C**

*(based on condition 12 from JCSG Core I Suite)*

Composition	Original	Optimization steps
Polyethyleneglycol (PEG) 3,350 (% in v/v)	20	20/23/26/29
0.2 M Magnesiumacetat (pH)	--	7.5/8.0/8.5

**Table 57: Optimization of Bid construct 1 I, 21°C***(based on condition 5 from Cryos Suite)*

Composition	Original	Optimization steps
0.085 M Hepes sodium salt (pH)	7.5	7.0/7.25/7.5/8.0
PEG 4,000 (% in v/v)	17	13/15/17/19/21/23
Isopropanol (% in v/v)	8.5	8.5
Glycerol (% in v/v)	15	15
Heterogenous seeding		5% nanoparticles

**Table 58: Optimization of Bid construct 1 II, 21°C***(based on condition 79 from JCSG+ Suite )*

Composition	Original	Optimization steps
0.1 M succinic acid (pH)	7.0	6.5/7.0/7.5/8.0
PEG 3,3500 (% in v/v)	15	11/13/15/17/19/21
Homogenous micro-seeding	--	After 3 days

**96-well plate optimization grids:****Table 59: Opti-Grid 96 of Bid construct 1 I, 4°C + 18°C***(based on condition 5 from Cryos Suite)*

Composition	Original	Optimization steps
0.085 M Hepes sodium salt (pH)	7.5	6.5/7.0/7.5/8.0
PEG 4,000 (% in v/v)	17	9/11/13/15/17/19/21/23/25
Isopropanol (% in v/v)	8.5	8.0/8.5/9.0/9.5/10
Glycerol (% in v/v)	15	13/15/17/19/21

**Table 60: Opti-Grid 96 of Bid construct 1 II, 4°C + 18°C***(based on condition 79 from JCSG+ Suite)*

Composition	Original	Optimization steps
0.1 M succinic acid (pH)	7.0	6.5/7.0/7.5/8.0/8.5
PEG 3,3500 (% in v/v)	15	11/13/15/17/19/21/23/25

Screens with both opti-grids 96 were performed under three conditions: once without any addition, once with seeding of nanoparticles and once with seeding from old crystal stocks. Optimizations were performed with two batches of Bid1 protein (9.5 mg/ml and 10.5 mg/ml) and screens were always duplicated for crystal growth at 4°C and 18°C.

### 2.23.2.1 Additive screen

Another strategy for crystal fine-tuning used in during this work was the application of additives to the most promising screening conditions yielding crystals in the initial and optimization screens. A number of additives have been identified as useful for enhancing crystallization. According to their chemical properties, additives are divided into different classes. For example, salts, co-factors, multivalent cations, linker, amino acids, reducing agents, polymers, detergents and non-detergents as well as chelators and organics are common.

To investigate a wide array of additives, the commercial Additive Screen HT™ (Hampton Research, Aliso Viejo, CA, USA) was used to fine-tune the hits based on condition 5 from cryos suite and condition 79 from the JSCG+ suite. The Additive Screen HT™ consists of 96 unique additives pre-formulated in deionized water and sterile filtered. Additive screens were performed in 96-well sitting-drop crystallization plates. First, 90 µl of the respective hit condition was transferred into each of the 96 reservoir wells. Afterwards 10 µl of the appropriate additive was pipetted into the corresponding reservoir and mixed gently. For drop setup, 0.3 µl of Bid 1 protein (10.5 mg/ml) was mixed with 0.3 µl of crystallization reagent/additive mixture from the reservoir. The procedure was repeated for each of the remaining additives. After finishing for all 96 additives, the plates was sealed with ViewSeal™ (Greiner Bio-one, Frickenhausen, Germany) and stored in the Rock Imager. In addition to the additive applications, the protein solution was supplemented with nanoparticles prior to pipetting. Additive screens for cryos condition 5 and JSCG+ condition 79 were duplicated and the crystallization plates stored and imaged at 18°C and 4°C, respectively.

### **2.23.2.2 Seeding**

Crystals obtained in initial screens that did not have the desired diffraction properties, because they were too small or grew together, were used as seeds in new experiments to optimize the original growth conditions or to explore other crystallization conditions. Two seeding procedures were performed, streak seeding and modified micro-seeding. For streak seeding, a 24-well crystallization plate was prepared with the respective reservoir conditions for reproducing crystal growth or optimization of hit conditions. Before seeding, the protein/crystallization reagent drop was prepared as described above and the sealed plate was stored for at least 12 h to allow drop equilibration and first drop concentration. Afterwards, the plate was resealed for the seeding procedure. A cat whisker was used as a seeding tool to touch and stroke the surface of the parent crystal in the old mother liquor. Thereby small, not visible seeds of the old crystal adhered at the surface of the whisker. The whisker was then transferred into the fresh crystallization drops by drawing the tip along the surface of each drop in a straight line. Four to six drops were seeded sequentially without redipping the whisker on the old crystal. The procedure was repeated until all 24 drops were seeded. The plate was sealed again and stored at 21°C or 4°C. Crystal growth was observed along the streak line within a few days.

For seeding of 96-well crystallization plates, modified micro-seeding was performed. Therefore, a micro-seed stock was prepared by breaking a parent crystal with a thorn. A previously obtained crystal was transferred into a tube containing a small volume of mother liquor solution (respective reservoir solution) and broken as much as possible using the thorn. The generated microcrystal solution was then diluted 1:10 in reservoir solution. 1-2 µl of the seeding solution was mixed with 50 µl of fresh protein solution. The protein/seeding solution was used for preparation of 96-well crystallization plates using the Cartesian Microsys™ SQ4000 crystallization robot as outlined above.

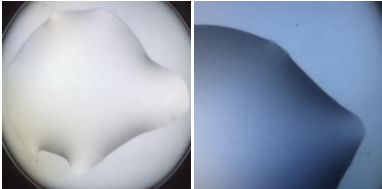
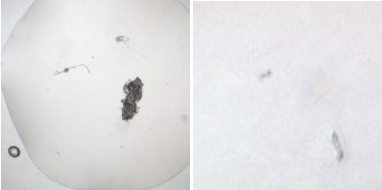
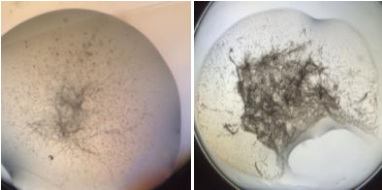
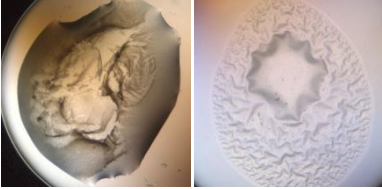
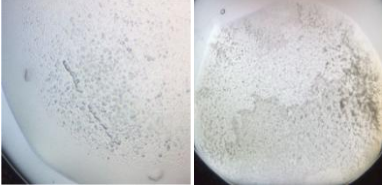

### **2.23.3 Scoring and interpretation of crystallization drop results**

For scoring of crystallization conditions and crystal growth, the screening plates were monitored by microscopy. 96-well crystallization plates were automatically imaged in the Formulatrix Rock Imager™ (MarXtal, Department of Chemistry, University of Marburg) and photomicrography analyzed using the Rock Maker Web. After initialization of the screening plates, pictures of every well were taken every day during the first week, then once every week and finally at exponentially increasing times after dispensing. 24-well crystallization plates were analyzed manually by microscopy.

For interpretation of drop results, a non-Q scoring system was used, as recommended by Bergfors T.M.<sup>189</sup>. Table 61 shows the scoring system used for interpretation of crystallization drop results. Pictures reveal examples of drop results that were obtained in the crystallization screens performed during this work.

**Table 61: Scoring system used for interpretation of crystallization drop results**

(Modified by Bergfors T.M.<sup>189</sup>, pictures were obtained from crystallization screens performed within this work)

Score	Phenomenon	Drop example
<b>Protein is not precipitated</b>		
0	clear drop	
1	artifacts (dust, fiber)	
<b>Precipitate shows no birefringence and has no edges</b>		
2	partial precipitation	
3	heavy precipitates, skin	
4	Gelatinous and white precipitants	
5	phase separation	

Precipitate shows birefringence and has edges		
6	spherulites, microcrystals	
Crystals		
7	needles	
8	plates (2D crystals)	
9	3D crystals	

#### 2.23.4 Differentiation between of protein and salt crystals

Observing a crystal in an initial or optimization screen does not necessarily indicate a protein crystal. Many of the typical components in the crystallization mother liquor, besides the protein, can crystallize, such as salts and detergents. Although, the only definitive test to distinguish between salt and protein is to put the crystal into the X-ray beam, it is not always possible, since crystals could be too small for mounting. During this thesis, three methods for distinguishing salt and protein crystals were performed prior to X-ray diffraction. In addition, all crystallization screens were controlled by comparing protein drops and buffer solution drops on the 2-drop chamber crystallization plate.

##### 2.23.4.1 Polarized light

During storage of the crystallization plates in the Rock Imager, imaging was additionally performed using polarized light. Anisotropic protein crystals show a double refraction that causes color effects while viewed with polarized light. The obtained color of a crystal is different to that of the background and i.e. different from the color reflection from the plastic tray in phase separation. Notably, most crystals obtained from salt or detergent have also



strong optical properties and show extensive birefringence under a cross polarizer. In general, protein crystals have a weaker birefringence than salt and detergent crystals.

#### **2.23.4.2 Dye-test**

Protein crystals can be stained using different dyes, such as IZIT (methylene blue) or coomassie blue dye. Protein, peptide and nucleic acid crystals typically have large solvent channels which will accommodate the small molecule dye, and thereby color the crystal. In contrast, inorganic crystals do not possess such solvent channels and will not absorb the dye thereby remaining uncolored. Notably, some screening conditions in a high relative supersaturation can precipitate or even crystallize the dye. Crystallized dyes typically appear as dark colored needles or whiskers within a few minutes after adding the dye.

To differentiate between protein and salt crystal, methylene blue solution (IZIT Crystal Dye™, Hampton Research, Aliso Viejo, CA, USA) was used. Methylene blue is a cationic organic dye that binds to negative charges on the protein. The crystals were transferred into a 4-10 µl mother liquid drop on a cover slide. Afterwards 0.5-1 µl IZIT was pipetted into the drop containing the crystals. For purposes of comparison, 0.5-1 µl IZIT was pipetted into a 4-10 µl reservoir solution drop containing salt crystals. The uptake of the dye was observed with the microscope immediately, after few hours and then overnight. Protein crystals appeared blue, whereas salt crystals did not become blue. The blue color of the protein crystals was typically intensified within the crystal over time.

#### **2.23.4.3 Snap-test**

Physical manipulation of crystals can be used to differ between protein and salt crystals, since a biological crystal behaves more like an ordered gel than a hard crystal. Because of the high solvent content of protein crystals, they are soft, and powder, crumble or break easily when touched with a micro tool or a needle. In contrast, salt crystals are very hard and require more force to break apart. Typically one can hear a snap or crunching sound when inorganic crystals breaking apart under the force of a micro tool. For the Snap-test, crystals were transferred to a cover slide and crashed using a micro tool (Hampton Research, Aliso Viejo, CA, USA). The hardness of the crystals and the sound while breaking apart were analyzed subjectively. Once a crystal is broken, it cannot be used for X-ray diffraction anymore. Therefore, the snap-test was only performed with small crystals that were not mountable, or when many crystals were grown in the respective screening condition.

### **2.23.5 Mounting crystals and diffractometric measurements**

For collecting X-ray data on the obtained crystals, cryo-crystallography was performed. Protein crystals were measured at very low temperatures, such as that of liquid nitrogen (boiling point -196°C) to avoid radiation damage during the diffraction experiment. However, freezing crystals might result in damage of crystals due to formation of ice crystals. For cryo-protection, the crystals were placed into mother liquor containing a cryo-protectant such as PEG 400, glycerol or MPD for 5-30 seconds. Crystals that were already grown in cryo-conditions, as crystals obtained from the cryo suite or from optimization screens containing MPD or glycerol, were native frozen and mounted directly. For sample preparation, the crystals were picked out of the mother liquor using a Cryo-loop (Hampton Research, Aliso Viejo, CA, USA) with the required loop size. If necessarily, the loop containing the crystal was transferred into the cryo-solution for 10-15 seconds. Afterwards, the crystals were flash frozen by dipping the loop into liquid nitrogen. Crystals were stored in a dewar container filled with liquid nitrogen until X-ray data collection.

### **2.23.6 Data collection and processing**

Data were collected by Synchrotron measurements of the respective protein crystals either at the Helmholtz-Zentrum Berlin using the MX Beamline 14.1, BESSY II (Berliner Elektronenspeicherring-Gesellschaft für Synchrotronstrahlung, Berlin, Germany)<sup>190</sup> or at the DESY Hamburg, using the EMBL MX1 and MX2 beamline at the PETRA III ring (Deutsches Elektronen Synchrotron, Hamburg, Germany). Data processing was performed by Holger Steuber (Core Facility Structural Biology, LOEWE Center of Synthetic Microbiology (SYNMIKRO)) using XDS<sup>191</sup> as implemented in XDSAPP<sup>192</sup>. Molecular replacement (MR) trials were attempted using Phaser<sup>193</sup> with search models from various sources (e.g. Bid NMR structures obtained from the PDB, poly-Ala models)

## 3 Results

### 3.1 Targeting Bid for mitoprotection

The first anti-apoptotic small molecules targeting Bid were developed by Becattini et al. and inhibited tBid-induced Smac/DIABLO release, caspase-3 activation and cell death<sup>99, 114</sup>, suggesting that pharmacological Bid inhibition could provide a protective benefit against several disorders, such as neurodegenerative diseases, mood disorders, liver inflammation and other pathologies, where Bid has been implicated as a major trigger of the underlying cell death<sup>63, 98, 99, 194-196</sup>.

In order to confirm that pharmacological inhibition of Bid is sufficient to provide mitoprotection, the specific Bid inhibitor BI-6c9 (**5**) was used to validate the model of glutamate-induced cell death in the HT-22 cell-line as suitable model for the initial screening of novel Bid-targeting molecules. In line with previous studies<sup>97, 116</sup>, Bid inhibition by BI-6c9 resulted not only in the preservation of cell morphology and cell viability of glutamate-treated HT-22 cells but also prevented several hallmarks of Bid-mediated mitochondrial dysfunction. Recent studies supposed Bid as an upstream mediator of mitochondrial impairments and the associated neuronal death signaling<sup>63, 197, 198</sup>, and further revealed a pivotal role of Bid in the balance of mitochondrial fission and fusion and a Bid-mediated permeabilization of the outer mitochondrial membrane<sup>24, 97, 199, 200</sup>. As shown previously, pharmacological Bid inhibition using BI-6c9 was sufficient to prevent the glutamate-induced Bid translocation to mitochondria<sup>97</sup> as well as mitochondrial demise downstream of Bid activation. Further, Bid-mediated mitochondrial fission, the associated accelerated production of highly detrimental ROS as well as the breakdown of  $\Delta\psi_m$  and impairments in mitochondrial ATP production and oxygen consumption were significantly prevented by BI-6c9, as shown below (see 3.1.3 et seq.), confirming the pivotal role of the pro-apoptotic protein Bid in the regulation of mitochondrial integrity and function.

#### 3.1.1 Neuroprotective potency of BI-6c9

In order to achieve a better classification of the neuroprotective potency of BI-6c9, the Bid inhibitor was titrated in HT-22 cells at concentration ranges from 0.1  $\mu\text{M}$  up to 10  $\mu\text{M}$  and cell viability was analyzed by MTT assay 14 h after exposure to glutamate (3 mM) (Figure 12 A). Notably, slightly protective effects against glutamate-induced cell death were already achieved by BI-6c9 at low concentrations of 1  $\mu\text{M}$ , while cell viability was completely restored at concentrations of 2.5  $\mu\text{M}$  and higher (Figure 12 A). To calculate the half maximal effective concentration ( $\text{EC}_{50}$ ) of BI-6c9 at the applied concentration ranges, cell viability data were normalized between 0 % for glutamate only treated cells (vehicle) to 100 % protection at 10  $\mu\text{M}$  and a concentration-response curve was fitted with a sigmoid function (dose response

fit). Revealing an  $EC_{50}$  of 2.5  $\mu\text{M}$ , BI-6c9 emerges as a potential Bid-targeting molecule, suitable for further structure optimizations and investigations of Bid-dependent cell death features.

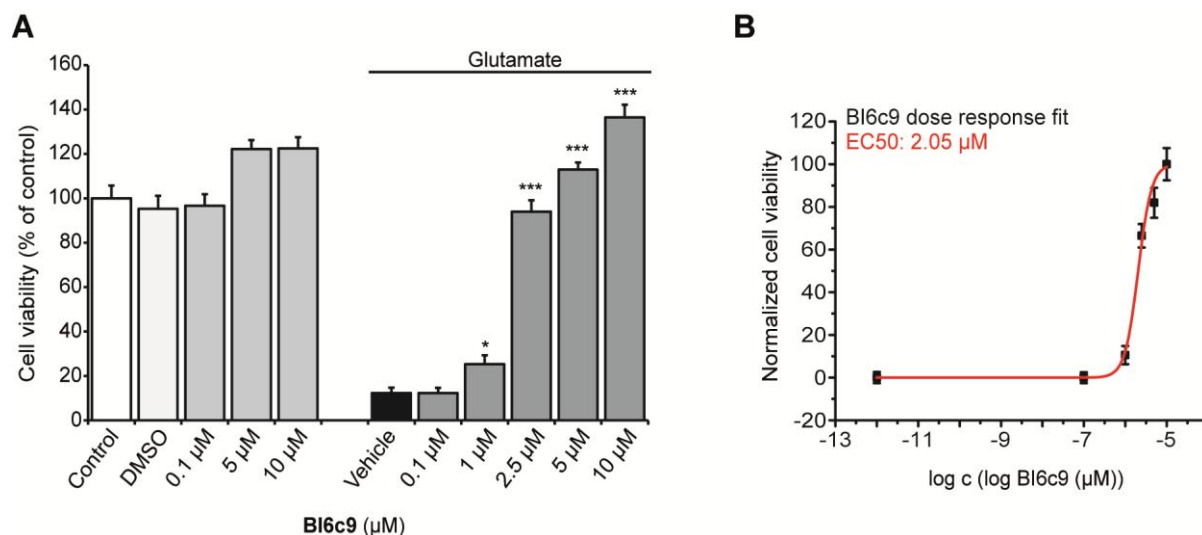


**Figure 12: Neuroprotective potency of BI-6c9 – half maximal effective concentration.**

**A**, Determination of cell viability 14 h after co-treatment with glutamate (3 mM) and BI-6c9 in a concentration-range of 0.1  $\mu\text{M}$  up to 10  $\mu\text{M}$ . BI-6c9 prevents glutamate-induced toxicity in a concentration-dependent manner. Cell viability is completely preserved by BI-6c9 in concentrations of 2.5  $\mu\text{M}$  and higher. The experiment was independently repeated three times with an  $n = 8$  per treatment condition. Results are presented as mean  $\pm$  SD (\*\* $p < 0.001$  compared to glutamate treated vehicle controls, ANOVA, Scheffé's test). **B**, Based on this data, a concentration-response curve and an  $EC_{50}$  value was calculated for BI-6c9. Cell viability data were normalized between un-treated control conditions (0%) and maximum amplitude at 10  $\mu\text{M}$  (100%). Using OriginPro8.5 Software, the resulting data were fitted with a sigmoid function following the equation  $y = A1 + (A2 - A1) / (1 + 10^{-(\text{LOG}x - x) * p})$  and  $EC_{50}$  values were generated from three independent experiments.

### 3.1.2 tBid-induced cell death in HT-22 cells

The abovementioned data confirmed the important role of Bid in glutamate-induced cell death, indicating its apparent direct action at the level of mitochondria to regulate the control point of life and death. To further confirm, that the cleaved and active protein tBid is the main mediator downstream of glutathione depletion and the activation of lipoxygenases<sup>116</sup> and sufficient to induce cell death in the present neuronal cell line, a model of tBid-induced cell death was validated in order to examine the specific Bid-targeting of novel small-molecules that were screened within this thesis. Therefore, HT-22 cells were transfected with a tBid-expression vector (pIRES-tBid) and cell morphology as well as cell viability were addressed 17-24 h after tBid-transfection. Over-expression of tBid resulted in excessive alterations in cell morphology, similar to the glutamate-induced phenotype of cell death. tBid transfected cells clearly appear shrunken, rounded up and detached from the bottom of the culture plate (Figure 13 A). To exclude that these cytotoxic effects were a result of the transfection

process itself, control cells were transfected with an empty control vector (pcDNA3.1+) or only treated with the transfection reagent attractene (vehicle), revealing the normal spindle-like cell morphology (Figure 13 A). It is important to note, that the sensitivity of HT-22 to tBid-induced toxicity is highly dependent on the cell density (Figure 13), even more than the sensitivity to glutamate toxicity. While cells seeded at a density of 40,000 to 50,000 cells per well (24-well plate) respond with severe damage to tBid over-expression, seeding densities of 60,000 to 70,000 cells per well results in a resistance of cells to tBid-induced cell death, indicating that confluent cell growth prohibits either the efficient transfection of the cells with the tBid-encoding plasmid or permits protective strategies via cell-cell contacts (Figure 13). Quantification of cell viability by MTT assay confirmed, that over-expression of tBid reduces cell viability by approximately 75 % depending on the respective cell density (Figure 13 B). It should be noted, that the mechanisms of Bid-mediated cell death signaling might only be partly reflected in the model of tBid over-expression as Bid truncation to tBid was not detectable in glutamate-exposed HT-22 cells by western blot analysis. However, in consideration of the fact that tBid is well accepted to be the active death promoting form of Bid, the model system is appropriate to mimic mechanisms that occur downstream of Bid activation and further provides a suitable screening model to examine the effect of novel compounds on tBid-mediated neurotoxicity.

In order to confirm that tBid-induced toxicity is accompanied by detrimental effects on mitochondria, mitochondrial membrane potential of tBid over-expressing HT-22 cells was investigated. TMRE-FACS recordings revealed that tBid over-expression causes a remarkable drop in red fluorescence by approximately 40 % of control cells, indicating a tBid-induced loss of mitochondrial membrane permeability, which was clearly prevented by pharmacological Bid inhibition (Figure 14 A). Notably, tBid-toxicity was similarly effective as CCCP treatment (Figure 14 B), while pre-treatment of cells with BI-6c9 significantly restored  $\Delta\psi_m$  almost to control levels (Figure 14 B).

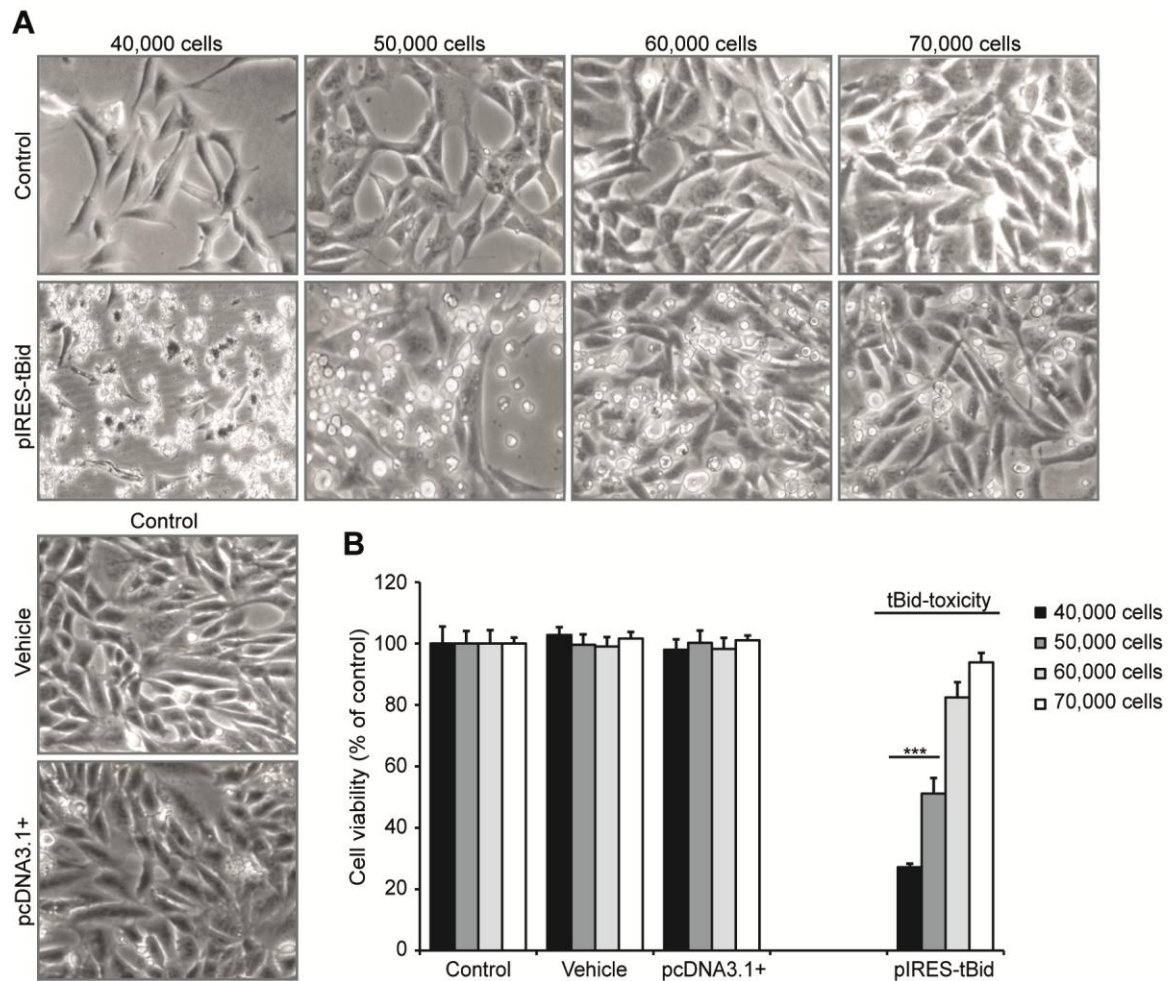


**Figure 13: tBid-induced cell death in HT-22 cells.**

HT-22 cells were cultured in 24-well plates at densities of 40,000; 50,000; 60,000 and 70,000 cells per well and transfected with a tBid-encoding plasmid (pIRES-tBid) 24 h after seeding. Transfection of cells with an empty vector (pcDNA3.1+) was used as control. Vehicle cells were treated only with the transfection reagent attractene. 20-24 h after plasmid transfection, tBid-induced toxicity was determined by microscopy (**A**) and measurements of cell viability using the MTT assay (**B**). **A**, tBid-induced cell death is detectable by typical alterations in cell morphology of HT-22 cells, indicated by rounded and shrunken cells detached from the bottom of the cell culture plate, as shown by photomicrographs (10 x 0.25 NA objective). Of note, sensitivity of HT-22 cells to tBid-induced toxicity depends on the cell density. Cells seeded at density of 40,000 cells per well are more sensitive against tBid-over-expression than cultures of  $\geq 50,000$  cells. Cells seeded at a density of 70,000 cells per well show almost complete confluent growth and are not responding to tBid-over-expression. **B**, MTT assay reveals, that tBid over-expression reduces cell viability of HT-22 cells up to 74 % compared to control cells depending on the cell density. The experiments were repeated three times with  $n = 4$  per treatment condition and the results provided as mean  $\pm$  SD, (\*\*\*)  $p < 0.001$  compared to vehicle controls, ANOVA, Scheffé's test).

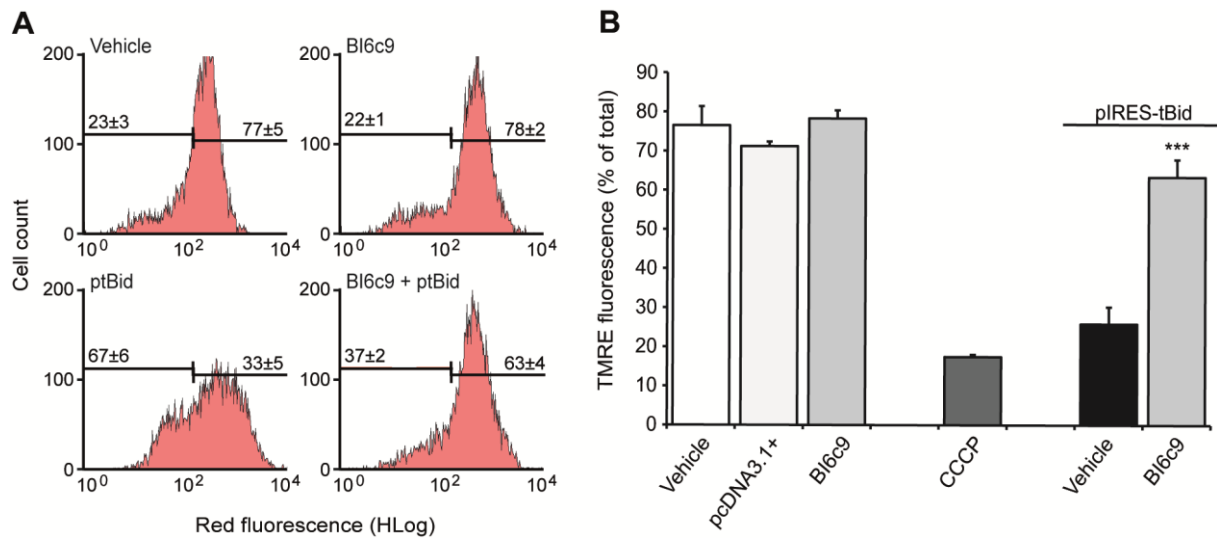


**Figure 14: tBid-induced loss of  $\Delta\psi_m$  is prevented by BI-6c9**

Mitochondrial membrane potential was analyzed by FACS recordings of HT-cells stained with MitoPT™ TMRE dye and transfected with a tBid-encoding plasmid. **A**, Eighteen hours after tBid over-expression a remarkable breakdown of mitochondrial membrane potential ( $\Delta\psi_m$ ) was detectable, indicated by a significant drop of red fluorescence up to 40 % of control cells. Pre-treatment (1 h before tBid transfection) of cells with BI-6c9 (10  $\mu$ M) prevents tBid-induced loss of  $\Delta\psi_m$ . Numbers are mean percentages  $\pm$  SD with  $n = 4$  per treatment group, indicating loss of  $\Delta\psi_m$  (left side) or intact  $\Delta\psi_m$  (right side). Pictures are representatives of at least three independent experiments. **B**, Quantification of TMRE fluorescence confirms, that tBid over-expression decreases mitochondrial membrane potential, which was restored by BI-6c9 (10  $\mu$ M) pretreatment. tBid over-expression was almost as effective as the positive damage-control CCCP, which causes a fast breakdown of the mitochondrial membrane potential. The experiments were repeated at least three times with  $n = 4$  and data presented as mean  $\pm$  SD (\*\*\*)  $p < 0.001$  compared to tBid-transfected vehicle, ANOVA, Scheffé's test).

The presented data fortify the current model of glutamate- and tBid-induced cell death in the HT-22 cell line as suitable model systems to screen newly-synthesized compounds for their ability to prevent Bid-mediated cell death. Since BI-6c9 was shown to target and inhibit Bid and provided a sustained protection against several hallmarks of neuronal intrinsic cell death pathways, the Bid inhibitor was used as a positive control for neuroprotection throughout the following experiments and was always applied at a concentration of 10  $\mu$ M as shown before to provide 100 % protection (Figure 12).

### 3.1.3 Synthesis strategy for development of novel small Bid inhibitors

The data above point to the pivotal role of Bid in the regulation of intrinsic neuronal cell death pathways that are relevant also in brain injury caused by acute brain damage and neurodegenerative diseases<sup>63, 97, 114</sup>. Major roles of Bid-dependent mitochondrial cell death mechanisms were also substantiated in models of cerebral ischemia and traumatic brain injury *in vivo*, thereby encouraging to focus on Bid as a molecular drug target for the development of novel small molecule Bid inhibitors that are needed for treatment of pathologies associated with mitochondrial demise and neuronal dysfunction.

As mentioned before, the Bid inhibitor BI-6c9 was discovered as one of the first small Bid-targeting molecules. The structure of BI-6c9 (**5**) was derived by Becattini et al. through combinations of the Bid-binding fragments BI-2A7 (**1**) and BI-2A1 (**3**) and described as the compound with the most active binding to Bid (Figure 4)<sup>99, 114</sup>. Despite the promising neuroprotective properties of this available Bid inhibitor BI-6c9 *in vitro*, it failed, however, in model systems of neuronal degeneration *in vivo*. Possible reasons for the lack of efficacy *in vivo* are limited affinity to the target and/or a poor bioavailability. It should be noted, that a major disadvantage of BI-6c9 is based on the poor solubility limiting its application to cell culture models, as it is only soluble in serum-containing medium or in high DMSO concentrations. Therefore BI-6c9 was chosen as a template for further development of structurally novel small-molecules aiming to provide protection against neurotoxic insults by targeting the pro-apoptotic protein Bid. Key structural elements of BI-6c9 were identified by the chemical department using ligand-based virtual screening and are depicted in Figure 15 (marked in red). Chemical modifications based on the structure of BI-6c9 resulted in three structurally diverse classes of small-molecule compounds, namely *N*-aryl substituted phenoxyanilines, *N*-phenyl substituted thiazolidine-2,4-diones and *N*-aryl substituted pyrazolopyrimidindiones (Figure 15). The former two chemical structure classes were synthetically optimized, yielding in approximately 120 small chemical compounds that were screened in this thesis for their ability to provide neuroprotection, with the aim to identify novel highly potent Bid inhibitors suitable for applications in model systems of brain damage *in vivo*.



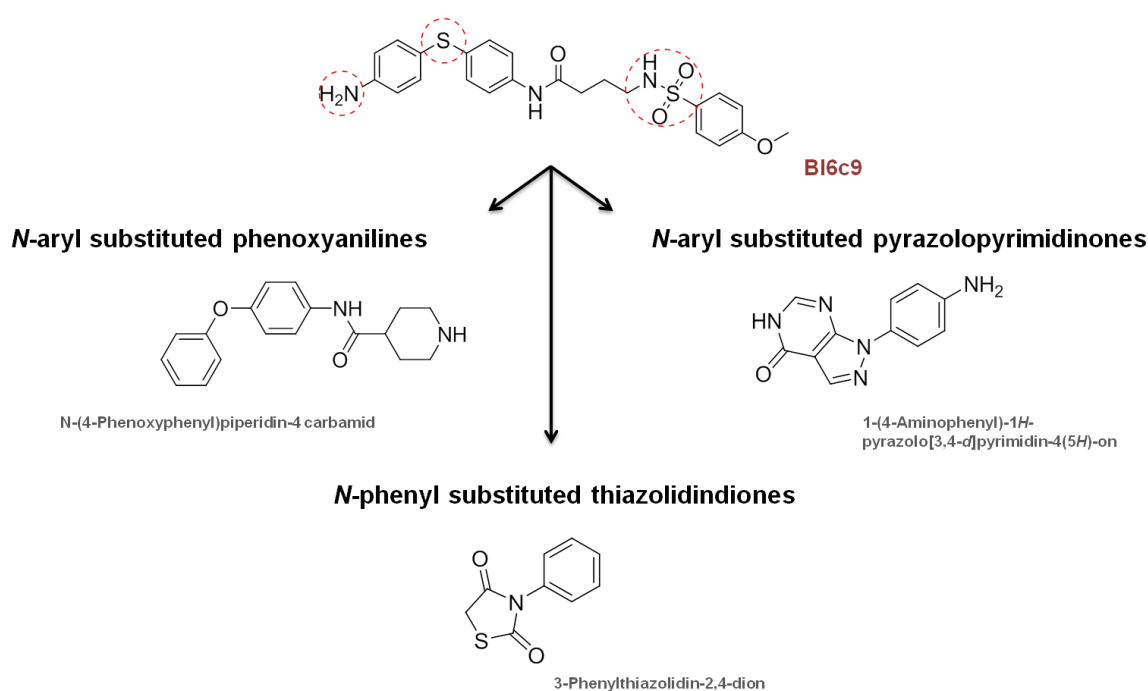


**Figure 15: Synthesis strategy for development of novel Bid inhibitors**

Key structural elements of the available Bid inhibitor BI-6c9, marked in red, were identified by ligand-based virtual screening, which was performed by S. Glinca (Pharmaceutical Chemistry, University of Marburg, Marburg, Germany). By replacement of pharmacophors and reduction of the molecular structure of BI-6c9, three structurally diverse classes of compounds were developed, one of which was synthetically optimized. Syntheses of novel compounds were performed by the group of Prof. Schlitzer (Pharmaceutical Chemistry, University of Marburg, Marburg, Germany).

The following chapters reveal the development of the most promising compounds and focus on their protective properties in the respective screening assays. Depicted results of functional analysis of the compounds effects on cell viability, proliferation and mitochondrial function are only a few examples and represent the most potent compounds for the respective class.

In general, all newly synthesized structures were initially screened for their protective effects in the model of glutamate-toxicity in HT-22 cells. Therefore, the compounds were applied to the cells in concentration ranges of 1  $\mu\text{M}$  up to 100  $\mu\text{M}$  and analyzed in the presence and absence of toxic glutamate levels (3-5 mM). After 14-16 h treatment, cell viability of HT-22 cells was determined by the MTT assay. The neuroprotective properties of the most promising compounds were additionally confirmed by real-time analysis of cell impedance using the xCELLigence system (Roche). In order to investigate the intended interference of the synthesized compounds with the pro-apoptotic activities of Bid, the protective efficiency of the target molecules was further examined in the described model of Bid-induced toxicity in the present neuronal cell line. Most potent compounds were further analyzed for their ability to prevent glutamate-induced Bid-mediated impairments in mitochondrial integrity

and function. Results of the initial screening (MTT assay) of all synthesized and tested compounds as well as their chemical structures are provided in Table 67-Table 70 (appendix).

Chemical syntheses of all novel compounds were performed by the group of Prof. Schlitzer (Dept. Pharmaceutical Chemistry, University of Marburg, Marburg, Germany). MTT assays of the first screening in the glutamate-toxicity model were kindly supported by Katharina Elsässer.

### 3.1.4 *N*-acyl derivatives of 4-phenoxyaniline as neuroprotective agents

The development of alternative Bid-inhibitors was based on the structure of BI-6c9 (**5**) identified above as the potential Bid-targeting compound. Since structural analogues of BI-6c9 (**5**), having a similar molecular size, revealed no protective activities in the model of glutamate toxicity, further structure modifications were based on a fragment similar to BI-2A7 (**1**). This fragment (**1**) was shown to reduce Bid-mediated Smac/DIABLO release and chosen by Becattini et al. as a scaffold for their inhibitors<sup>99, 114</sup>. The first synthetic modification of BI-2A7 (**1**) was the replacement of the metabolically unstable 4-(4-aminophenyl)sulfanylaniline substructure by simple 4-phenoxyaniline (**6**) (Figure 16).

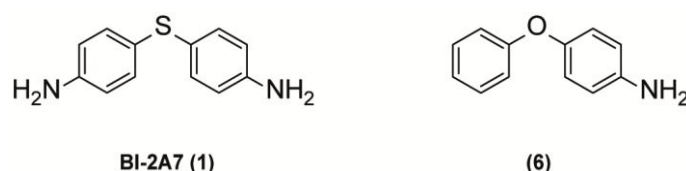


**Figure 16: Structures of fragment BI-2A7 and the replacement 4-phenoxyaniline.**

Based on the fragment BI-2A7<sup>99</sup> (**1**), the metabolically unstable 4-(4-aminophenyl)sulfanylaniline substructure was replaced by simple 4-phenoxyaniline (**6**). Synthesis of compound **6** was performed by the group of Prof Schlitzer (Pharmaceutical Chemistry, University of Marburg, Marburg, Germany).

Further modifications were aimed at avoiding structure toxicity. Therefore the second amino group of compound **6** was omitted since 4-(4-aminophenoxy)aniline is known to be highly toxic<sup>201</sup>. Thus, the subsequent development included the enlargement of compound **6** by acylation of the aromatic amino group of the 4-phenoxyaniline with small acyl residues addressing the remaining areas of the presumed inhibitor binding site. Following this synthesis strategy 32 *N*-acyl-4-phenoxyaniline derivatives were generated by the chemistry department (group of Prof Dr Schlitzer) and screened in this thesis to prevent Bid-mediated neuronal cell death.

Table 62 depicts the chemical structure and the neuroprotective activities of representative compounds obtained within this development. Further derivatives and their screening results are provided in appendix Table 67 and Table 68.

Compound ID	Compound name	Structure	Neuroprotective activity					Cytotoxicity ( $\mu\text{M}$ , $p < 0.001$ )
			compound concentration ( $\mu\text{M}$ )					
			1	10	25	50	100	
6	SCHL 28001		*	**	***	***	***	N/A <sup>a</sup>
7	SCHL 24396		---	---	---	---	---	$\geq 100$
8	SCHL 24519		***	***	***	***	***	$\geq 100$
9	SCHL 24543		---	***	***	***	***	$\geq 100$
10	SCHL 24381		---	---	---	***	***	$\geq 100$
11	SCHL 24521		***	***	***	***	***	$\geq 100$

**Table 62: Neuroprotective properties of *N*-acyl phenoxyanilines.**

Chemical structures and neuroprotective activities of representative *N*-acyl 4-phenoxyanilines against glutamate-induced toxicity as achieved by the first screening and determined by MTT assay. Results are representatives of 3-8 independent experiments each with  $n = 8$  (\* $p < 0.05$ ; \*\* $p < 0.01$ ; \*\*\* $p < 0.001$  compared to glutamate treated controls, ANOVA Scheffé's test; N/A<sup>a</sup>, not active: compound revealed no toxic effects in HT-22 cells at concentrations from 1  $\mu\text{M}$  up to 100  $\mu\text{M}$ ).

### 3.1.4.1 Neuroprotective activity of *N*-acyl phenoxyanilines in the model of glutamate-induced cell death

The first screening of compound **6** in the model of glutamate-induced toxicity affirmed the hypothesis that the 4-phenoxyanilin is a potent scaffold for further structure optimizations. Photomicrographs of HT-22 cells treated with 20  $\mu\text{M}$  of compound **6** in the presence and absence of toxic glutamate solution revealed its ability to prevent the phenotype of glutamate-induced cytotoxicity (Figure 17 A). MTT assay confirmed the considerable neuroprotective activity of compound **6** against glutamate-induced toxicity (Figure 17 B). Cell

viability of glutamate-treated HT-22 cells was significantly reduced up to 20% compared to un-treated control cells, whereas co-treatment of cells with compound **6** in concentration ranges of 10  $\mu\text{M}$  up to 50  $\mu\text{M}$  preserved cell viability 15 h after glutamate exposure (Figure 17 B).

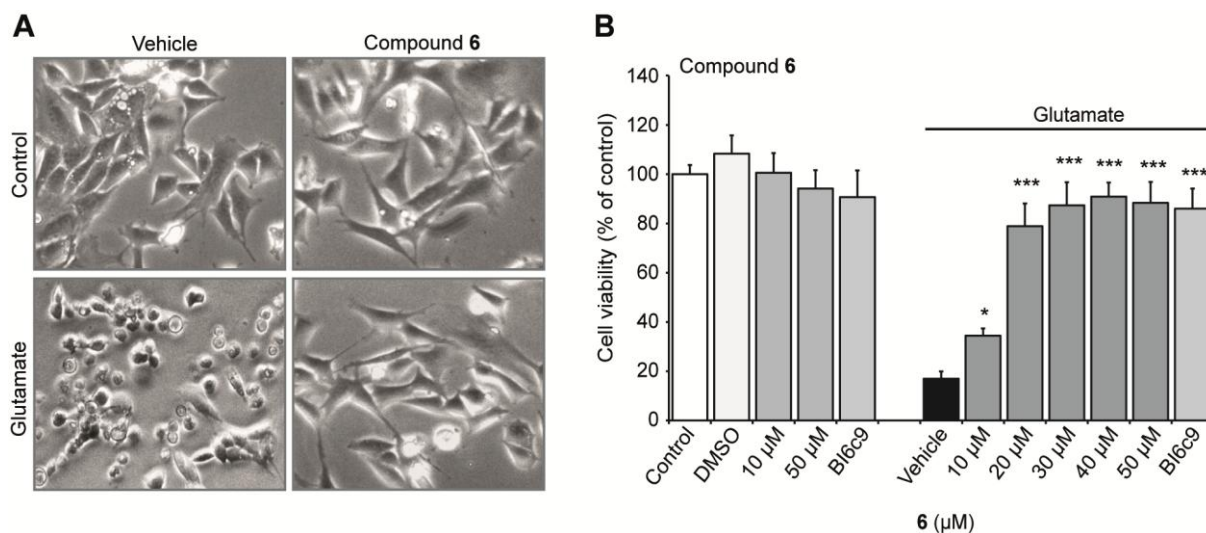


**Figure 17: Neuroprotective activity of compound 6 in HT-22 cells exposed to glutamate.**

HT-22 cells were co-treated with SCHL 28001 (**6**) in application ranges of 10  $\mu\text{M}$  up to 50  $\mu\text{M}$  and toxic glutamate solution (3 mM). BI-6C9 was applied at 10  $\mu\text{M}$  and used as a positive control for neuroprotection. DMSO was applied to cells as a solvent control. **A**, Photomicrographs (10 x 0.25 NA objective) show protective effects of compound **6** (20  $\mu\text{M}$ ) against glutamate-induced morphological changes of HT-22 cells. **B**, 16 h after treatment, cell viability of HT-22 cells was determined by MTT assay. Compound **6** significantly prevents glutamate-induced cell death in concentrations of 20  $\mu\text{M}$  to 50  $\mu\text{M}$ . Data are normalized to untreated control (100% cell viability). The experiment was independently repeated at least three times with  $n = 8$  per treatment condition. Data are predicted as mean  $\pm$  SD (\* $p < 0.05$ , \*\*\* $p < 0.001$  compared to glutamate treated vehicle, ANOVA, Scheffé's test).

To investigate the compound's ability to provide neuroprotection in low concentrations and additionally to examine if large doses cause toxic effects, all substances were further screened in concentration ranges from 1  $\mu\text{M}$  up to 100  $\mu\text{M}$ . Structure-activity relationships that were derived from the first screening results suggested that high structure flexibility, accompanied for example with long side chains (compound **7**), might hamper the binding of the compounds to the target protein Bid. Therefore, more rigid 4-phenoxyanilines derivatives, with a terminal nitrogen incorporated in a cyclic system, were investigated in the following. The most potent compounds emerged from these developments were compound **8** and **9**, which significantly prevented glutamate-induced toxicity of HT-22 cells. While compound **8** revealed significant protective effects at concentrations as low as 1  $\mu\text{M}$ , sufficient protection by compound **9** was achieved at concentrations of 10  $\mu\text{M}$  and higher as determined by MTT assay (Figure 18 A, B). Of note, both compounds caused slightly toxic effects under control conditions, when applied at high concentrations of 100  $\mu\text{M}$ , although a protection against glutamate-toxicity was still detectable (Figure 18 A, B).

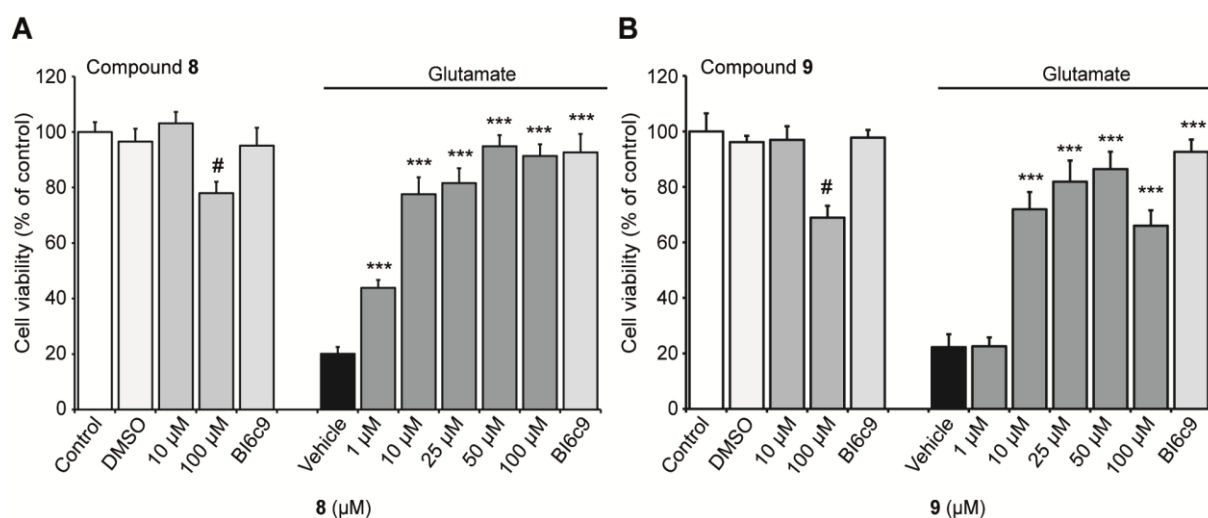


**Figure 18: Neuroprotective activities of compounds 8 and 9 against glutamate-induced cell death.**

MTT assay reveals neuroprotective properties of the SCHL 24519 (**8**) (**A**) and SCHL 24543 (**9**) (**B**) against glutamate-induced cell death in a concentration-dependent manner and predicts slightly toxic effect of compounds in applications of 100  $\mu$ M. HT-22 cells were treated with compound **8** and **9** in concentrations of 1  $\mu$ M up to 100  $\mu$ M as indicated, or BI-6C9 (10  $\mu$ M) in the presence or absence of glutamate (3 mM). A DMSO treatment was used as solvent control. Cell viability was analyzed by MTT assay 14.5 h after glutamate exposure. The presented data are normalized to untreated control. For statistical analysis, the experiments were repeated at least 6 times with  $n = 8$  and results presented as mean  $\pm$  SD ( $\#p < 0.05$  compared to untreated controls,  $***p < 0.001$  compared to glutamate treated vehicle, ANOVA, Scheffé's test).

Based on these results, compound **8** was used for further investigations resulting in a series of 4-piperidin carboxylic acid derivatives and identifying an important role of the terminal amino moiety and the rigidity of the piperidin as critically involved in the positioning and interaction with the Bid protein (Table 67). In a last series, *N*-alkylated substances were synthesized, revealing the apparent trend that neuroprotective activity is increased by short hydrophilic chains, possibly due to specific interactions via hydrogen bonds with the terminal Asp195 of Bid.

For example, compound **11**, containing a terminal hydrophilic chain, significantly provided protection against glutamate-induced cell death at concentrations of 1  $\mu$ M up to 100  $\mu$ M, although slightly toxic effects were observed at concentrations of 100  $\mu$ M (Figure 19).

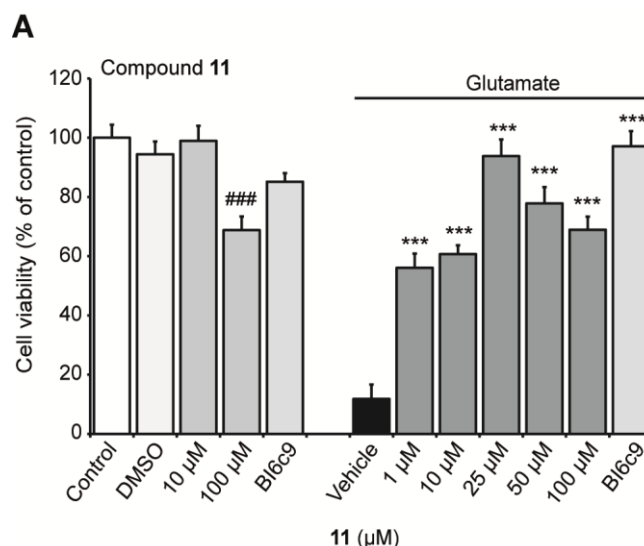


**Figure 19: Compound 11 provides neuroprotection against glutamate-induced cell death.**

SCHL 24521 (**11**) was screened for its ability to prevent glutamate-induced cell death in HT-22 cells. Cell viability of HT-22 cells was determined by MTT assay 14.5 h after treatment of cells with compound **11** in application ranges of 1 μM up to 100 μM as indicated. The Bid inhibitor BI-6C9 (10 μM) was used as positive control for neuroprotection. Compound **11** provides strongest protection against glutamate-induced cell death at concentrations of 25 μM. The experiment was independently repeated at least 4 times and data are provided as mean ± SD (###*p* < 0.001 compared to untreated controls, \*\*\**p* < 0.001 compared to glutamate treated vehicle, ANOVA, Scheffé's test).

As compound **8**, **9** and **11** were identified as the most potent structures obtained from the series of *N*-acyl-phenoxyanilines, they were subjected to further analyses in order to gain more insight into their neuroprotective effects and their ability to specifically target Bid.

Therefore, molecular docking analyses of the compounds into the three-dimensional structure of Bid (PDB code 1DDB) were kindly performed by Dr Wegscheid-Gerlach (Pharmaceutical Chemistry, University of Marburg, Marburg, Germany). Virtual docking solutions of compound **8** (Figure 20 A) and compound **11** (Figure 20 C) into a deeply buried pocket of the Bid protein show that the inhibitors fit nicely into the presumed binding site (Figure 20) and reveal for both compounds a possible interaction between the C-terminal Asp195 of Bid and the terminal basic amino function of compound **8** and accordingly the terminal hydroxyl group of compound **11**, possibly by forming a salt bridge (Figure 20 B, D).



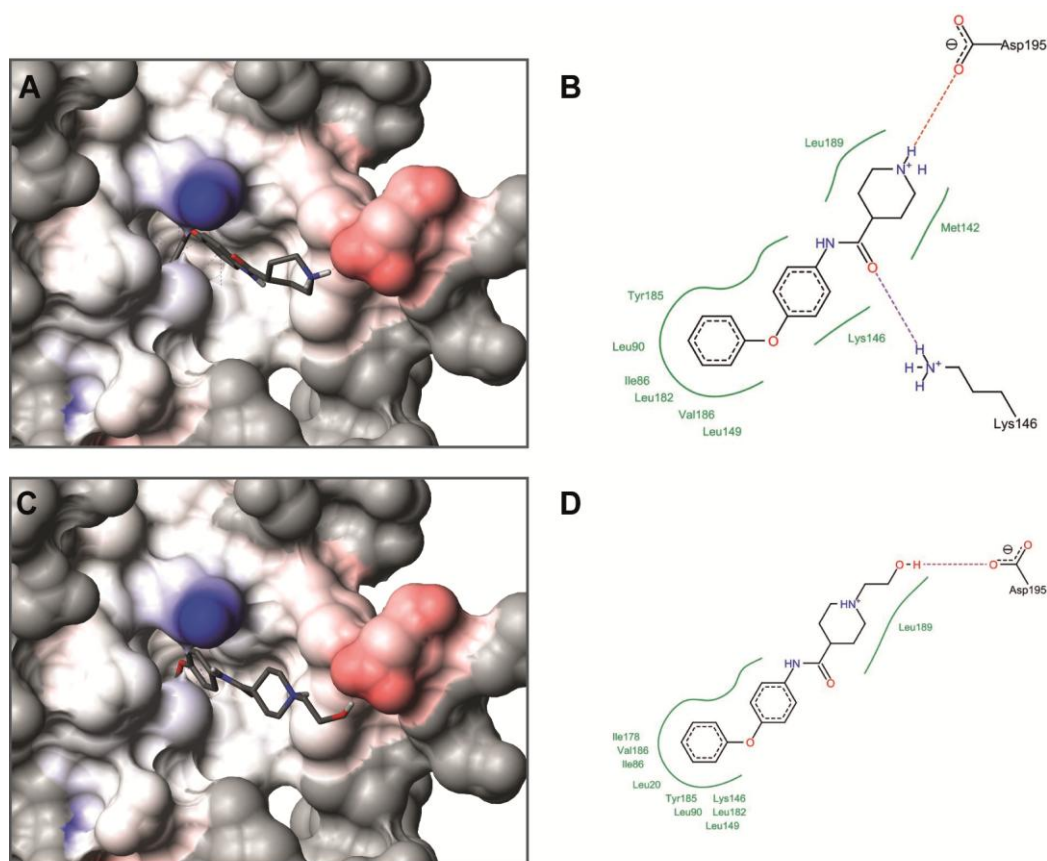


**Figure 20: Molecular docking of compounds 8 and 11 into the 3D-structure of Bid.**

**A, C,** Molecular docking of compound **8** (**A**) and compound **11** (**C**) into the three-dimensional structure of Bid (PDB code 1DDB). The compounds fit into the hydrophobic crevice on the surface of Bid. The solvent-accessible surface of Bid is represented with formal charges (red negative; blue positive). For the inhibitor compounds the carbon atoms are shown in grey, oxygen in red and nitrogen in blue. **B, D,** 2D-representation of the docking solutions of compound **8** (**B**) and compound **11** (**D**) and the suggested interactions with amino acids of Bid shown in green. Docking analyses were kindly performed by Dr. Wegscheid-Gerlach (Pharmaceutical Chemistry, University of Marburg, Marburg, Germany).

For a better evaluation of the compounds' potency to achieve neuroprotection and to distinguish between transient and persistent effects of the individual structures, the most potent compounds **8** and **11** were investigated by real-time analysis of cell impedance using the xCELLigence system. In accordance with our findings determined by MTT assay, treatment of cells with compound **8** or compound **11** restored cell proliferation and viability in a concentration-dependent manner, indicated by the prevention of the glutamate-induced decline of NCI (Figure 21 A, B). While both compounds provided only transient protective effects at concentrations of 1  $\mu\text{M}$  and 10  $\mu\text{M}$ , a sustained protection over approximately 10 h was achieved by adding compound **8** at concentrations of 50  $\mu\text{M}$  (Figure 21 A). In comparison, compound **11** provided almost persistent protection even at lower concentrations of 25  $\mu\text{M}$ , while higher concentrations of 50  $\mu\text{M}$  decreased cell proliferation even though a complete breakdown of NCI was still prevented (Figure 21 B). These data

confirm that the glutamate-induced loss of NCI and cell death can be prevented by *N*-acyl-phenoxyanilines derivatives in a concentration-dependent manner, and further accentuate real-time monitoring of the glutamate-induced cytotoxicity as a useful tool to generate compound-specific profiles allowing to modulate the effective time window of the neuroprotective compounds.

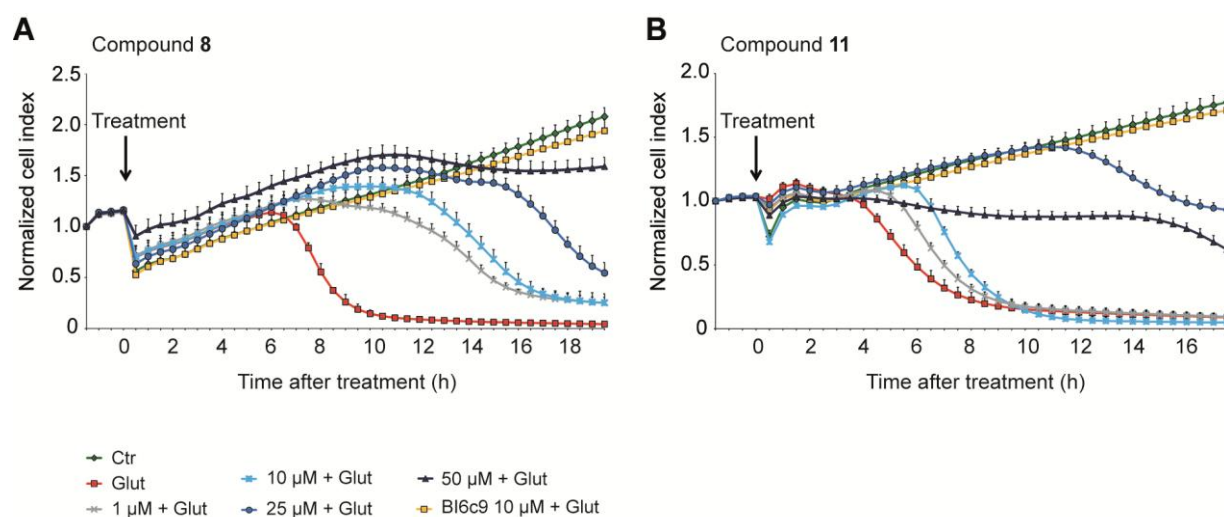


**Figure 21: Real-time detection of cellular impedance confirms neuroprotective properties of *N*-acyl-phenoxyanilines.**

Cell proliferation of HT-22 cells was monitored for 24 h before treatment (0 h). Compound **8** (A) and **11** (B) were applied to cells at concentrations of 1  $\mu\text{M}$  up to 50  $\mu\text{M}$ , as indicated, in the presence and absence of 3 mM glutamate. BI-6C9 was applied at 10  $\mu\text{M}$  and used as positive control for persistent protection. Cellular impedance was continuously monitored using the xCELLigence system (Roche) for another 16-18 h after treatment. Cell index was normalized at 0 h (treatment-time). NCI of HT-22 cells revealed reduction of cell viability around 4-6 h after glutamate treatment. Compounds **8** and **11** provided a dose-dependent transient protection against glutamate-induced toxicity. Results are predicted as mean  $\pm$  SD with  $n = 8$  per treatment group. The experiments were independently repeated at least three times.

### 3.1.4.2 Specificity of 4-phenoxyaniline scaffolds against tBid-induced toxicity

Although the glutamate-induced oxidative cell death has been linked to Bid transactivation to mitochondria, Bid-mediated breakdown of  $\Delta\psi_m$  and subsequent release of AIF and Smac/DIABLO<sup>97, 99, 202</sup> as described above, and the delayed neuronal cell death, occurring in a constant and small time window as shown by the xCELLigence measurements (Figure 21), is well correlated with time frames of glutamate-induced Bid translocation to mitochondria<sup>97</sup>, it is not mandatory, that the protective effects of compounds in this glutamate-toxicity model are mediated by the specific inhibition of the pro-apoptotic protein Bid. Even though the targeting of Bid was suggested by the docking analysis (Figure 20), the specificity of the *N*-acyl-phenoxyanilines to inhibit Bid, had to be confirmed in a further study.



Therefore, the molecules were further screened in HT-22 cells transfected with a tBid-encoding plasmid (Figure 22). As shown above (Figure 13), over-expression of Bid resulted in characteristic alterations in cell morphology (Figure 22, pIRES-tBid). In contrast, application of compound **8** (10  $\mu$ M), compound **9** (10  $\mu$ M) or compound **11** (10  $\mu$ M) 1 h before tBid-transfection clearly preserved the spindle shaped morphology of cells comparable to control conditions (Figure 22 A). In addition, MTT assay confirmed that cells pre-treated with the compounds **8**, **9** or **11** at concentrations of 10  $\mu$ M were significantly protected from tBid-induced cell death (Figure 22 B, C, D).

Furthermore, the model of tBid-induced toxicity was used for cellular dose-response studies. Pre-treatment of cells with the compounds at concentrations as low as 1  $\mu$ M attenuated tBid-induced cell death to a slightly lesser extent as revealed for concentrations of 10  $\mu$ M (Figure 23), while at concentrations higher than 40  $\mu$ M the compounds showed toxic effects in this cell death model. Figure 24 represents an example of the toxic effect of compound **8**, **9** and **11** obtained in application ranges of 50  $\mu$ M. Applying high doses of the compounds under control conditions caused a severe cytotoxic damage of HT-22 cells as shown by photomicrographs (Figure 24 A) and thereby a reduction of cell viability as determined by MTT assay (Figure 24 B). Similar toxic results were detected for all three compounds applied in doses ranges from 40  $\mu$ M up to 100  $\mu$ M. Overall, the protective activities of the *N*-acyl-phenoxyanilines against tBid-mediated toxicity at concentrations lower than 10  $\mu$ M strongly indicate the compounds specific mode of action and confirm their ability to target and inhibit Bid

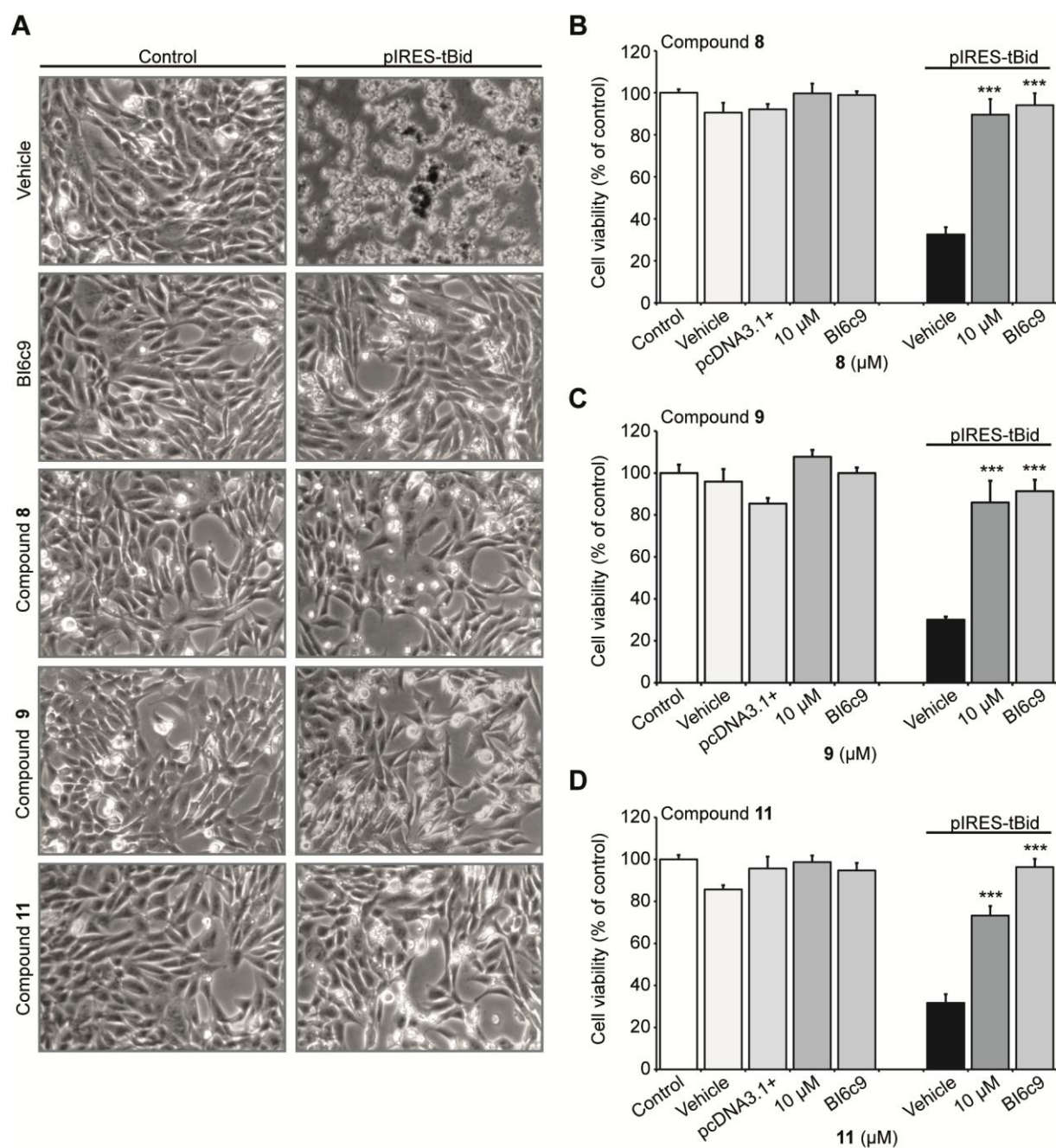


**Figure 22: Neuroprotective activities of *N*-acyl-phenoxanilines against tBid-induced neuronal cell death.**

HT-22 cells were pre-treated with novel compounds 1 h before transfection with a tBid-encoding plasmid (pIRES-tBid). 20-22 h after tBid over-expression cell morphology (**A**) was analyzed by microscopy and cell viability (**B**, **C**, **D**) was determined by MTT assay. Novel compounds were applied at concentrations of 10  $\mu$ M and BI-6C9 (10  $\mu$ M) was used as a positive control for prevention of tBid-induced toxicity. **A**, tBid over-expression induces typical changes in cell morphology, while compounds **8**, **9**, **11** preserved spindle shaped cell morphology as shown by photomicrographs (10 x 0.25 NA objective). **B**, **C**, **D**, Cell viability was quantified by MTT assay, confirming the compounds ability to prevent tBid-induced toxicity (**B**; SCHL 24519 (**8**), **C**; SCHL 24543 (**9**), **D**; SCHL 24521 (**11**)). The presented data are normalized to un-transfected controls (100% cell viability). The experiments were independently repeated at least three times with  $n = 3$  per treatment condition. Results are predicted as mean  $\pm$  SD (\*\*\*)  $p < 0.001$  compared to tBid-transfected vehicle, ANOVA, Scheffé's test).

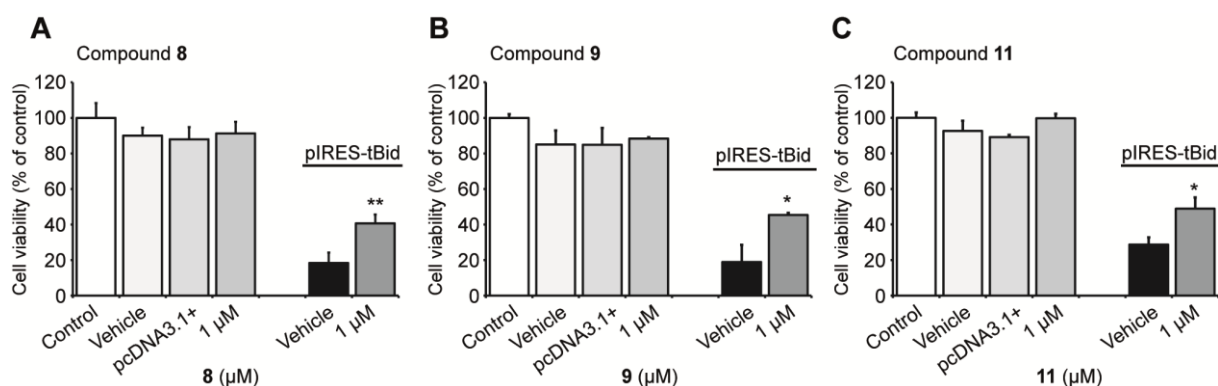


**Figure 23: *N*-acyl-phenoxyanilines provide slightly protective effects against tBid-induced toxicity in low concentrations as 1  $\mu$ M.**

MTT assay was used to determine protective effects of compound **8**, **9** and compound **11** at low concentrations of 1  $\mu$ M. HT-22 cells were pre-treated with 1  $\mu$ M of each compounds 1 h prior to tBid transfection. Cell viability was analyzed 20-24 h after tBid over-expression. All compounds show moderate protection against tBid-induced cell death. The experiments are representatives of 3-6 experiments with  $n = 3$  per treatment condition. Data are presented as mean  $\pm$  SD (\*\* $p < 0.001$  compared to tBid-transfected vehicle, ANOVA, Scheffé's test).

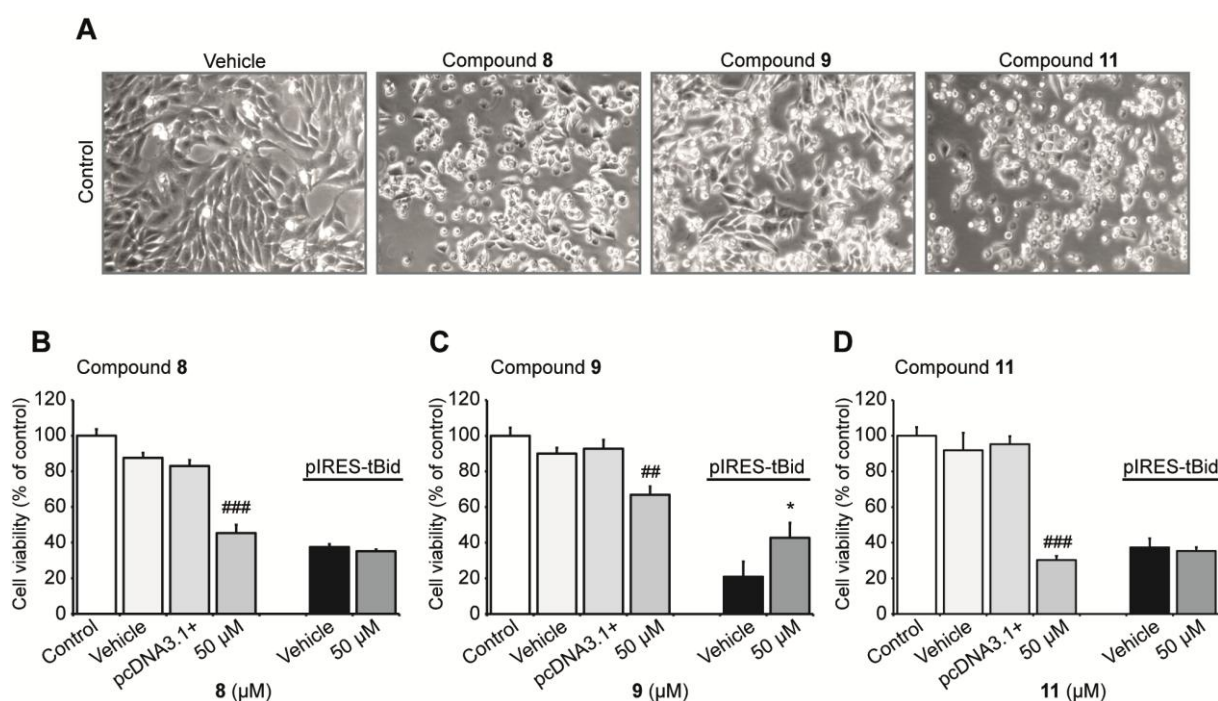


**Figure 24: Concentration-dependent toxic effects of *N*-acyl-phenoxyanilines**

HT-22 cells were pre-treated with novel compounds 1 h before transfection with a tBid-encoding plasmid (pIRES-tBid). 20-22 h after tBid over-expression cell morphology (**A**) was analyzed by microscopy and cell viability (**B**, **C**, **D**) was determined by MTT assay. For analysis of doses limitations, novel compounds were applied at concentrations of 50  $\mu$ M. **A**, Photomicrographs (10 x 0.25 NA objective) reveal cytotoxic effects of the compounds **8**, **9**, **11** when applied to HT-22 cells at concentrations of 50  $\mu$ M compared to un-treated control cells. Cells treated with high doses of the compounds show already typical cell death features without tBid over-expression. **B**, **C**, **D**, Cell viability was quantified by MTT assay, which confirms the concentration-dependent toxicity, thereby doses limitations of the applied compounds (**B**; SCHL 24519 (**8**), **C**; SCHL 24543 (**9**), **D**; SCHL 24521 (**11**)). Compound **9** was still slightly protective against tBid-induced toxicity, while compound **8** and compound **11** reveal no protective activity in concentrations of 50  $\mu$ M. Similar results were obtained by compound treatment in concentrations of 40  $\mu$ M and 100  $\mu$ M. The presented data are representatives for compound-toxicity studies. The

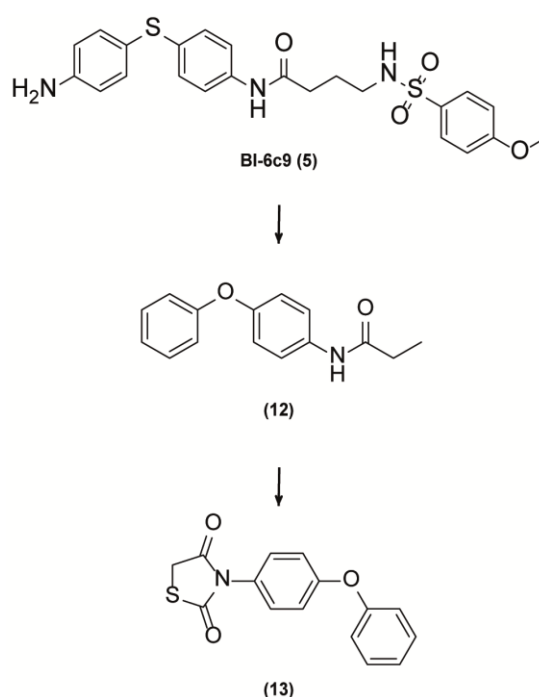
experiments were independently repeated at least three times with  $n = 3$  per treatment condition (\* $p < 0.05$  compared to tBid-transfected vehicle, ### $p < 0.001$  compared to un-transfected control, ANOVA, Scheffé's test).

In conclusion, these data predict a novel type of neuroprotective agents based on a 4-phenoxyaniline scaffold, and displayed significant neuroprotective activities of the compounds at concentrations as low as  $1 \mu\text{M}$ . The results, obtained from the docking of the molecules into the three-dimensional structure of Bid, and more considerable the findings emerged from the compound-screening in the model of tBid-induced toxicity indicated that these small-molecule agents indeed target the Bid protein and represent a significant step in the ongoing development of therapeutically useful neuroprotective agents.

### 3.1.5 *N*-phenyl substituted thiazolidindiones provide protection against tBid-mediated cell death pathways

Upon the basis of the promising neuroprotective effects achieved by the *N*-aryl substituted phenoxyanilines, presented above, structural optimizations were continued resulting in a series of *N*-phenyl substituted thiazolidinedions, which are presented in the following.

These optimizations were again accorded to the lead compound BI-6c9 (**5**) and further advanced based on the *N*-propionyl-derivative of *p*-phenoxyaniline (**12**). In order to reduce the conformational flexibility and thereby to enhance the binding affinity to the target Bid, the acylamid partial structure of **12** was incorporated into a thiazolidine-2,4-dione (**13**) (Figure 25), giving the core structure of about 36 novel compounds depicted in Table 69.

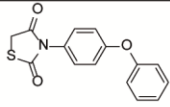
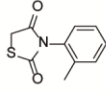
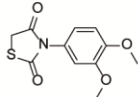
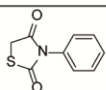
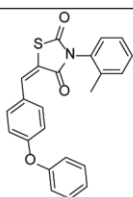
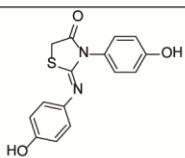


**Figure 25: Development of thiazolidine-2,4-dione structure 13 based on the structure of BI-6C9 (5).**

Based on the structure of BI-6c9 (**5**), the *N*-propionyl-derivate of 4-phenoxyaniline (**12**) was synthesized. The acrylamide partial structure of compound **12** was incorporated into a thiazolidine-2,4-dione (**13**), concurrently reducing the conformational flexibility. Structure syntheses and estimation of structure-activity relationships were performed by the group of Prof Schlitzer (Pharmaceutical Chemistry, University of Marburg, Marburg, Germany).

### 3.1.5.1 *N*-phenyl substituted thiazolidinediones provide neuroprotection against glutamate-induced toxicity

To investigate the protective and toxic properties of this compound class, the thiazolidine-2,4-diones were subjected to the first screening approach using the present model of glutamate-induced toxicity. All substances were applied in concentration ranges of 0.1  $\mu\text{M}$  up to 50  $\mu\text{M}$  and cell viability of HT-22 cells was determined 14 h after co-treatment with 3 mM glutamate solution. Table 63 depicts the results of representative structures of the *N*-phenyl substituted thiazolidinediones (all provided in appendix Table 69), which will be characterized more in detail in this chapter.

Compound ID	Compound name	Structure	EC <sub>50</sub> ( $\mu\text{M}$ )	Neuroprotective activity					Cytotoxicity ( $\mu\text{M}$ , $p < 0.001$ )
				compound concentration ( $\mu\text{M}$ )					
				0.1	1	5	10	50	
13	SCHL 24270		13.27	---	---	---	***	***	$\geq 100$
14	SCHL 24277		6.78	---	---	***	***	***	N/A <sup>a</sup>
15	SCHL 24213		9.39	---	---	***	***	***	N/A <sup>a</sup>
16	SCHL 24292		9.87	---	---	***	***	***	N/A <sup>a</sup>
17	SCHL 30008		N/D <sup>b</sup>	---	---	---	---	---	$\geq 100$
18	SCHL 24100		N/D <sup>b</sup>	---	---	---	---	---	N/A <sup>a</sup>

**Table 63: Neuroprotective properties of *N*-phenyl substituted thiazolidinediones.**

Chemical structures of newly synthesized compounds are shown. Neuroprotective activity of the compounds against glutamate-toxicity in HT-22 cells was determined within the first screening approach by MTT assay. EC<sub>50</sub> are given as the mean drug concentration required for inhibiting cell death by 50 % compared to controls. Toxicity values indicate toxic drug concentrations found to induce cell death without co-treatment with glutamate. (\*\*\*)  $p < 0.001$  compared to glutamate treated control, ANOVA Scheffé's test; N/A<sup>a</sup>, not active – substance revealed no toxic properties at concentrations of 0.1  $\mu\text{M}$  up to 100  $\mu\text{M}$ ; N/D<sup>b</sup>, not determinable – EC<sub>50</sub> values could not be

calculated due to lack of protective effects. The results presented are representatives of 4-6 independent experiments (MTT assay).

Notably, the first screening set up, examining substance concentrations between 10  $\mu\text{M}$  and 50  $\mu\text{M}$ , revealed maximal neuroprotection for most of the compounds at a concentration of 20  $\mu\text{M}$ , while concentrations higher than 30  $\mu\text{M}$  and up to 50  $\mu\text{M}$  could not further increase the protective properties (Figure 26)

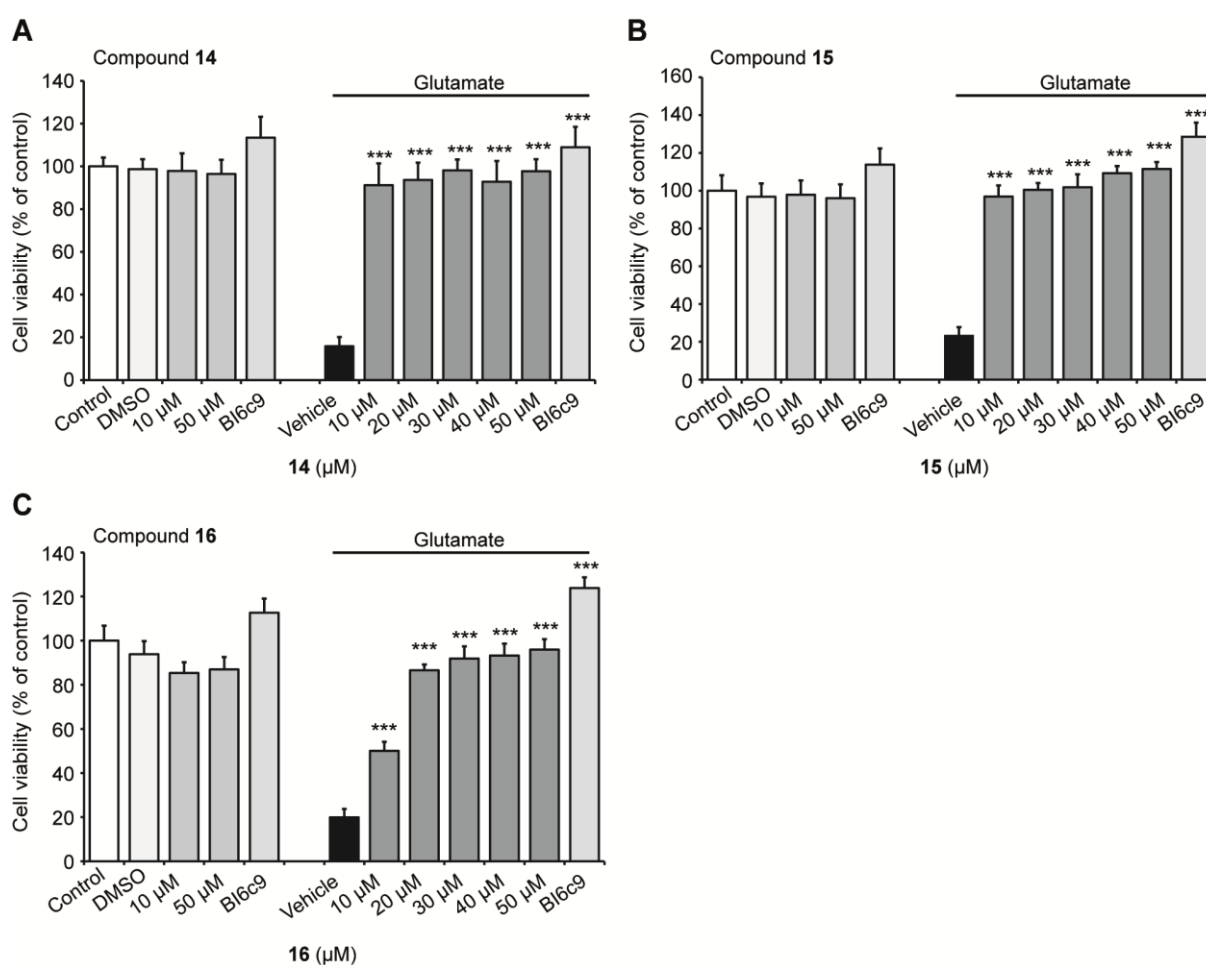


**Figure 26: *N*-phenyl substituted thiazolidinediones provide maximal neuroprotection at concentrations of 20  $\mu\text{M}$  and higher.**

Initially all thiazolidindiones were analyzed by their ability to prevent glutamate-induced cell death in concentrations of 10  $\mu\text{M}$  up to 50  $\mu\text{M}$ . HT-22 cells were cultured in 96-well plates with 10.000 cells per well and cell viability was determined 14 h after co-treatment with glutamate (3 mM) and novel compounds. BI-6C9 (10  $\mu\text{M}$ ) was used as a positive control for neuroprotection. SCHL 24277 (**14**) (A), SCHL 24213 (**15**) (B) as well as SCHL 24292 (**16**) (C) reveal maximum protective effects against glutamate-induced toxicity at concentrations of 20  $\mu\text{M}$  and higher. The presented data are normalized to un-treated controls. For statistical analysis, the experiments were independently repeated at least three times with an  $n = 8$  per treatment condition. Results are presented as mean  $\pm$  SD (\*\*\*)  $p < 0.001$  compared to glutamate-treated control (vehicle), ANOVA, Scheffé's test).

In order to examine the doses required to achieve maximal protection, thiazolidine-2,4-diones were further tested in concentration ranges between 0.1  $\mu\text{M}$  and up to 10  $\mu\text{M}$ , and the concentration of 50  $\mu\text{M}$  was set as steady state dose providing 100 % protection. Figure 27 shows the protective effects of three representative 3-aryl substituted thiazolidinedione derivatives, which significantly preserved cell viability of glutamate-treated HT-22 neurons in a concentration-dependent manner between 5  $\mu\text{M}$  up to 50  $\mu\text{M}$  (Figure 27 A, C, E). Impressively, the compounds **14**, **15** and **16** achieved full protection against glutamate-induced toxicity at concentrations higher than 20  $\mu\text{M}$  (Figure 27 A, C, E). This pronounced protective effect was comparable to the protective effect of the available Bid inhibitor BI-6C9 (10  $\mu\text{M}$ ) that was always applied in the screening experiments as a reference for maximal protection in this cell death model. Importantly, treatment of cells with the newly synthesized substances alone revealed no toxic effects in concentrations up to 50  $\mu\text{M}$  (Figure 26 A, B, C and Figure 27 A, C, E). Similar results were obtained for further synthesized thiazolidin-2,4-diones depicted in appendix Table 69.

To further compare the neuroprotective potency of all tested compounds, half maximal effective concentrations ( $\text{EC}_{50}$ ) were calculated from the cell viability data at the applied concentration ranges. Since the MTT data revealed full protective effects of the compounds at concentrations of 50  $\mu\text{M}$  (positive control for highest protection), cell viability data were normalized between 0 % for glutamate only treated cells (vehicle) to 100 % protection at 50  $\mu\text{M}$  and concentration-response curves were fitted with a sigmoid function (Dose Response Fit). Concentration-response curves for compound **14**, **15** and **16**, which represent highest therapeutic potency within the series of thiazolidin-2,4-diones, are shown in Figure 27 (Figure 27 B, D, F) and calculated  $\text{EC}_{50}$  values of all structures are provided in Table 63 and Table 69. The  $\text{EC}_{50}$  values calculated for the newly synthesized thiazolidinediones were almost as good as the  $\text{EC}_{50}$  value obtained for BI-6c9 (Figure 12).



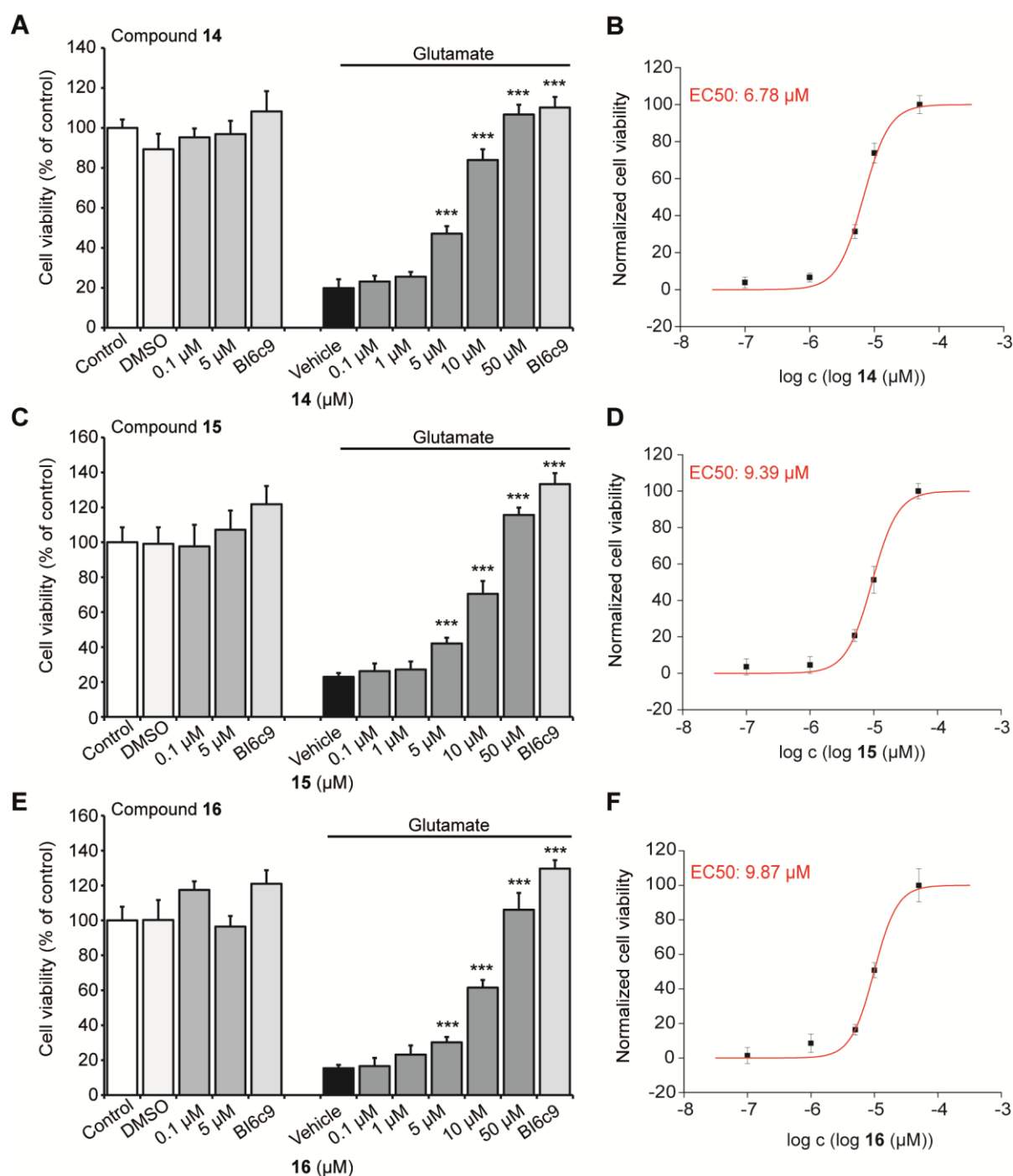


**Figure 27: N-Phenyl substituted thiazolidinediones provide neuroprotection against glutamate-induced toxicity.**

MTT assay was used to determine cell viability of HT-22 cells 14 h after co-treatment with glutamate (3 mM) and respective small molecules in different concentrations from 0.1  $\mu\text{M}$  to 50  $\mu\text{M}$ . BI-6C9 (10  $\mu\text{M}$ ) was used as a positive control for neuroprotection. SCHL24277 (**14**) (**A**), SCHL 24213 (**15**) (**C**) and SCHL 24292 (**16**) (**E**) attenuates glutamate-induced toxicity in a concentration-dependent manner. For statistical analyses, experiments were independently repeated at least three times with an  $n = 8$  per treatment condition. Results are presented as mean  $\pm$  SD (\*\* $p < 0.001$  compared to glutamate-treated control (vehicle), ANOVA, Scheffé's test). **B**, **D**, **F**, Based on this data concentration-response curves and EC50 values were calculated for each substance. Cell viability data were fitted from 0 for glutamate-treated control (vehicle) to 100 for highest protection at 50  $\mu\text{M}$  and dose response fits for compound **14** (**B**), **15** (**D**) and **16** (**F**) are shown.

As described for the *N*-aryl substituted phenoxyanilines above, real time analysis of cell impedance (xCELLigence) were reapplied in order to substantiate the neuroprotective properties of the *N*-phenyl substituted thiazolidinediones that were determined by MTT assay (Figure 28). While cellular impedance significantly decreased in cell populations exposed to glutamate (3 mM) 5 h to 8 h after treatment, NCI was fully preserved to control levels by co-treating the cells with glutamate (3 mM) and compounds **16**, **14**, or **15** at a concentration of 50  $\mu$ M, respectively (Figure 28 A-C). Compound **16** and **15** revealed transient neuroprotection at concentrations of 5  $\mu$ M, 10  $\mu$ M and 25  $\mu$ M (**15**) while a sustained protection over time was revealed at concentrations of 50  $\mu$ M (Figure 28 B, C). Similarly, compound (**14**) was only transiently protective at concentrations lower than 5  $\mu$ M, but attenuated the complete decline of NCI already at concentrations of 10  $\mu$ M, although not to levels of control cells. However, persistent neuroprotection against glutamate-induced toxicity was achieved at a concentration of 50  $\mu$ M (Figure 28 A). Concluded, these RTCA-measurements could not only confirm the findings detected by MTT assay, but further provided a better estimation of the protective potential of the novel small-molecules.

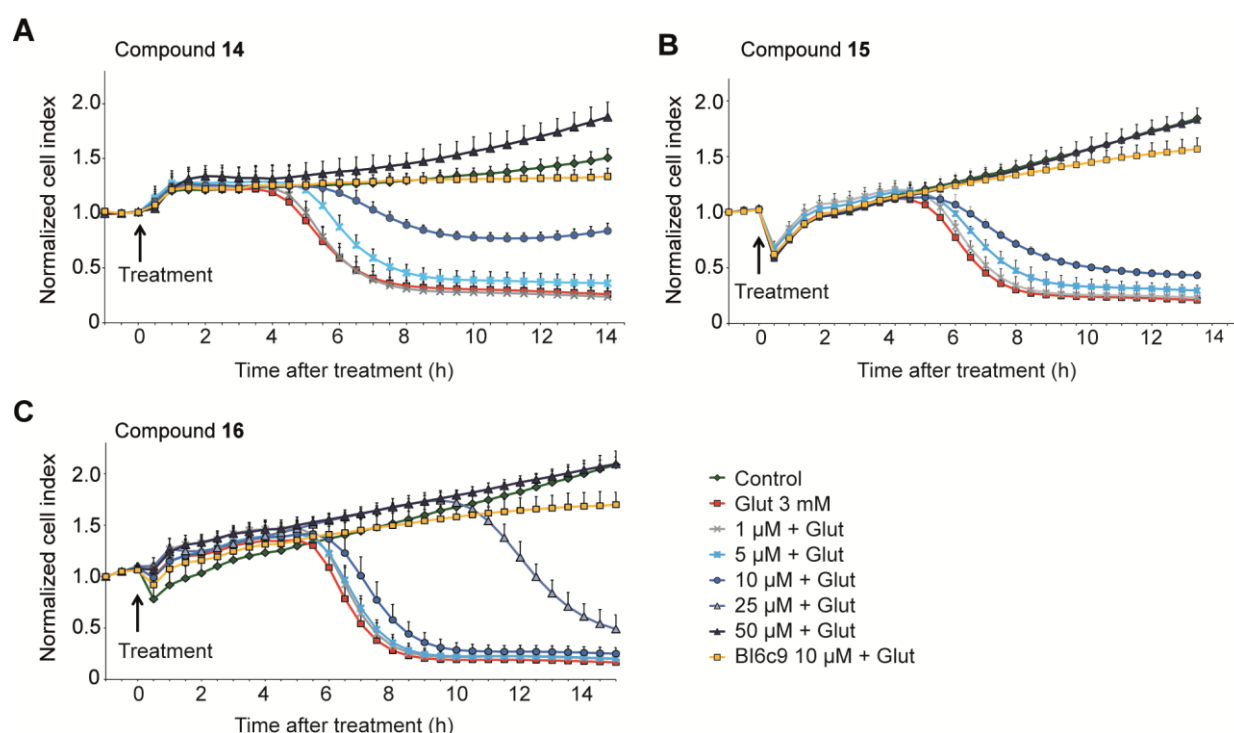


**Figure 28: Real time monitoring of cell impedance confirms concentration-dependent neuroprotection mediated by thiazolidindiones.**

The indicated cell groups were co-treated with glutamate (3 mM) and the novel compounds SCHL24277 (**14**) (A), SCHL 24213 (**15**) (B) and SCHL 24292 (**16**) (C) in concentrations of 1  $\mu$ M to 50  $\mu$ M. Cellular impedance was continuously monitored by the xCELLigence system (Roche) and cell index was normalized at 0 h (treatment time-point). Co-treatment with glutamate and BI-6C9 (10  $\mu$ M) was used as a positive control for persistent

protection. Each compound revealed a dose-dependent transient protection at concentrations from 10  $\mu\text{M}$  to 25  $\mu\text{M}$  yet a sustained protection over time at 50  $\mu\text{M}$ . Results are provided as mean  $\pm$  SD with  $n = 8$  per treatment group. All experiments were independently repeated three times.

### 3.1.5.2 Specificity of the thiazolidinediones

#### 3.1.5.2.1 *N*-phenyl substituted thiazolidinediones target Bid to prevent cell death in HT-22 cells

To investigate the compound's ability to target Bid, the role of the newly developed *N*-phenyl substituted thiazolidinediones was examined in the current tBid-mediated cell death model (see 3.3.5).

Compound **14**, compound **15** and compound **16**, as representatives of the thiazolidinediones, clearly attenuated tBid-induced cell damage and morphologic shape changes already at low concentrations of 1  $\mu\text{M}$  (Figure 29 A), and significantly prevented the tBid-induced reduction in cell viability of HT-22 cells assessed by the MTT assay (Figure 29 B, C, D). Similar results were observed pre-treating the cells with the indicated compounds at higher concentrations of 10  $\mu\text{M}$  and 50  $\mu\text{M}$ , while, in contrast to the *N*-aryl phenoxyanilines, no toxic effects of the thiazolidine-2,4-diones were detected when applied under control conditions (data not shown). These findings show that the new *N*-phenyl substituted thiazolidinedione compounds are able to rescue HT-22 cells after tBid-over-expression thereby providing strong evidence that the newly synthesized compounds indeed provided neuroprotection by targeting the pro-apoptotic protein Bid.

The compound's ability to specifically inhibit Bid was further confirmed by virtual docking analysis into the three-dimensional structure of Bid, kindly performed by Dr Wegscheid-Gerlach (Pharmaceutical Chemistry, University of Marburg, Marburg, Germany) (Figure 30). Thereby a possible binding mode of compound (**14**), which revealed the highest protective potency ( $\text{EC}_{50} = 6.78$ ), was derived: the thiazolidinedione moiety points into a deeply buried pocket on the surface of Bid, like BI-6C9, and allows interactions with the amino acids VAL 186 and ILE86 of Bid. Further, a hydrophobic interaction between the aromatic ring of compound **14** with the side chain of TYR 185 of Bid is suggested (Figure 30 B) and substantiate the intended specific targeting of the Bid protein.

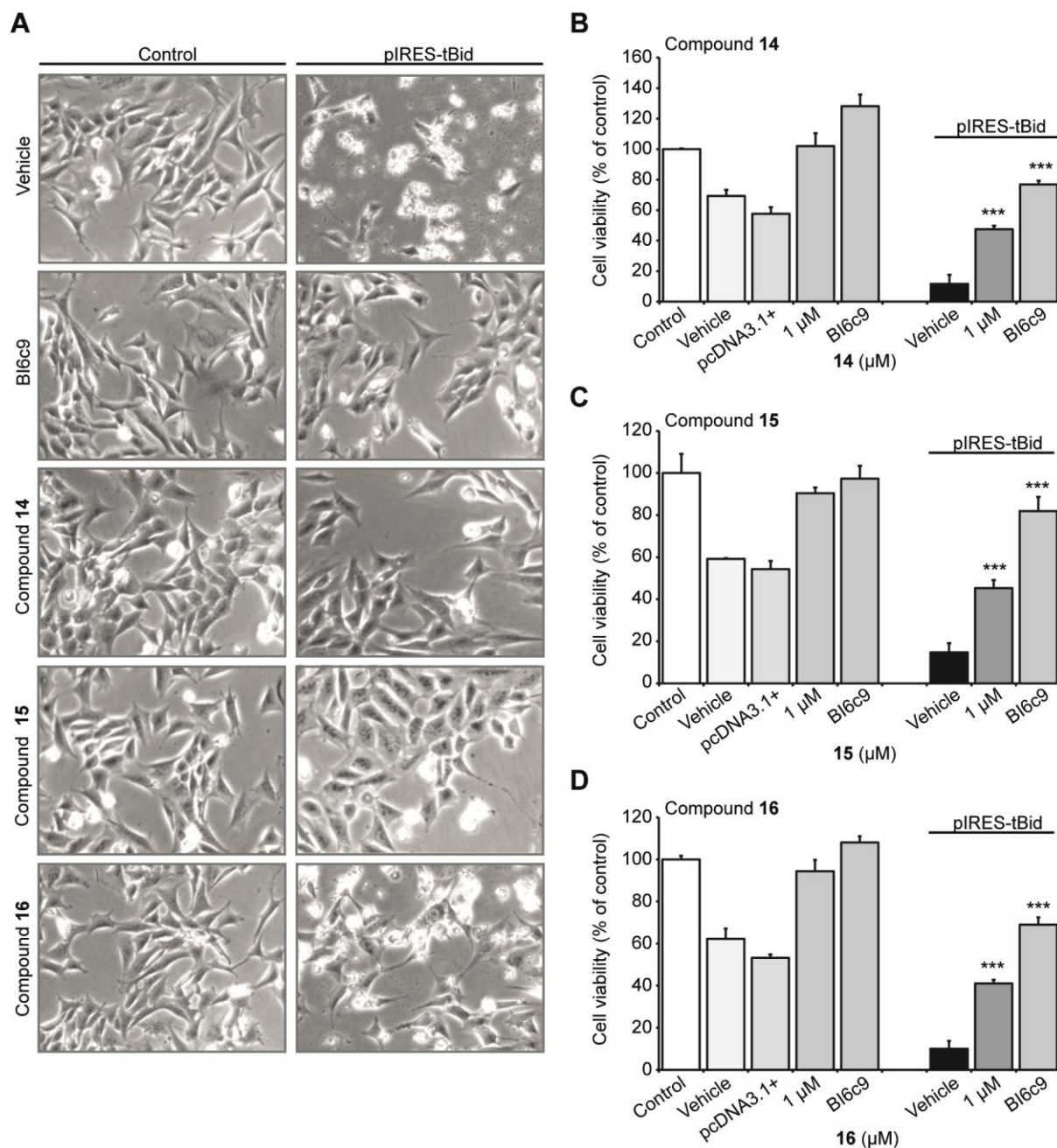


**Figure 29: N-Phenyl substituted thiazolidinediones attenuate tBid-induced neuronal cell death.**

tBid-induced toxicity was determined 21-23 h after transfection of HT-22 cells with a tBid-encoding plasmid (pIRES-tBid). Cell morphology was analyzed by microscopy (**A**) and cell viability was determined by MTT assay (**B, C, D**). Pre-treatment with the novel compounds SCHL 24277 (**14**), SCHL 24213 (**15**) and SCHL 24292 (**16**) (1  $\mu$ M) was performed 1 h before tBid-transfection. **A**, Photomicrographs (10 x 0.25 NA objective) show typical alterations in cell morphology of HT-22 cells 20 h after tBid over-expression (pIRES-tBid, control). Compound **14**, **15** and **16** preserves cell morphology of HT-22 cells. **B, C, D**, Quantification of cell viability confirms significant protective effects against tBid-induced toxicity mediated by compound **14** (**B**), compound **15** (**C**) and compound **16** (**D**). The presented data are representatives of concentration-dependent studies. Similar protective effects were obtained when compounds were applied in concentrations of 10  $\mu$ M and 50  $\mu$ M. No toxic effects were observed. The presented data are normalized to un-transfected control (100% cell viability). For statistical analysis, experiments were independently repeated at least three times with  $n = 3$  per treatment condition and results are reported as mean  $\pm$  SD (\*\*\*)  $p < 0.001$  compared to t-Bid treated control cells, ANOVA, Scheffé's-test).

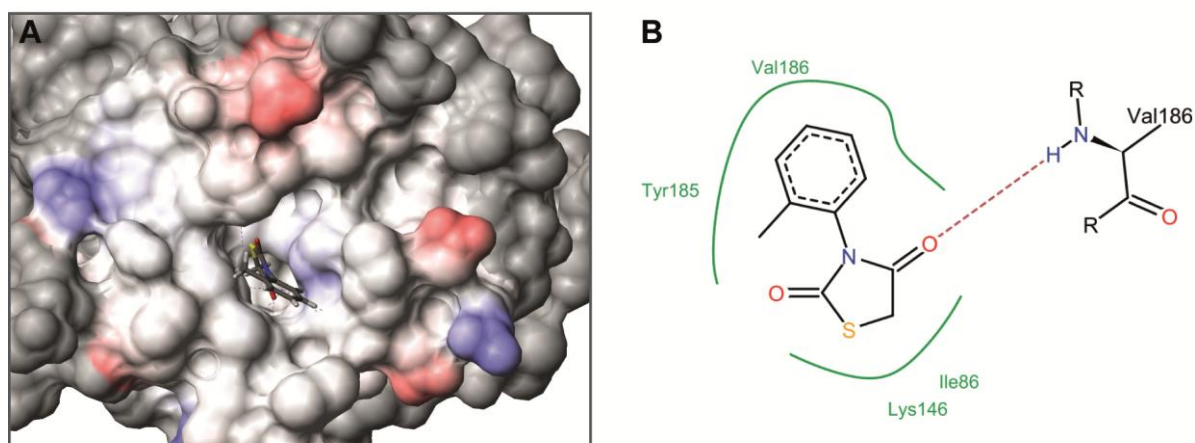


**Figure 30: 2D and 3D-representation of the binding mode of compound 13 for inhibition of Bid.**

**A**, 3D-Docking of SCHL 24277 (**14**) in the hydrophobic groove of Bid. **B**, 2D-representation of the docking solution of **A** reveals interaction of compound **14** with VAL186 and ILE86 and TYR185 of Bid. **A**, **B**, For the inhibitor compound the carbon atoms are shown in gray, oxygen in red, nitrogen blue and sulphur in yellow. The solvent-accessible surface of Bid is represented with formal charges (red- negative; blue positive). Docking analyses were kindly performed by Dr. Wegscheid-Gerlach (Pharmaceutical Chemistry, University of Marburg, Marburg, Germany).

### 3.1.5.3 Thiazolidine-2,4-diones prevent glutamate-induced Bid-mediated mitochondrial impairments

As the protective effects of the *N*-phenyl substituted thiazolidinediones in the models of glutamate- and tBid-induced toxicity were convincing, it should be further investigated whether these compounds are also able to prevent impairments in mitochondrial integrity and function that are shown to be Bid-dependent and precede the final execution of intrinsic caspase-independent cell death<sup>24, 58, 63, 97, 98</sup>.

Therefore, the effect of compound **14**, **15** and **16** on mitochondrial membrane potential ( $\Delta\psi_m$ ) was investigated. As described above, glutamate causes a significant drop in red TMRE fluorescence, indicating a glutamate-induced loss of  $\Delta\psi_m$  (Figure 31 A, B). In contrast, the application of 20  $\mu$ M of the compounds **14**, **15** or **16** did not affect  $\Delta\psi_m$  under control conditions, but almost completely attenuated the pronounced breakdown of  $\Delta\psi_m$  after glutamate challenge (Figure 31 A, B). The protective effects mediated by the novel compounds were comparable to that of the available Bid inhibitor BI-6C9, suggesting that the thiazolidinediones preserve Bid translocation to mitochondria thereby maintaining  $\Delta\psi_m$ . To further address whether the *N*-phenyl thiazolidinediones are also able to prevent the functional integrity of mitochondria, ATP levels of compound-treated HT-22 cells were examined in the presence and absence of glutamate (Figure 31 C). Indeed, the rapid depletion in cytoplasmic ATP caused by glutamate-induced cell injury, was completely



attenuated by compound **14**, **16** and **15**, whereas ATP levels of control cells were not altered (Figure 31 C). Therefore, these data confirmed at a functional level that the predicted *N*-phenyl substituted thiazolidinedione derivatives preserve mitochondrial integrity and energy production of glutamate-treated HT-22 cells.

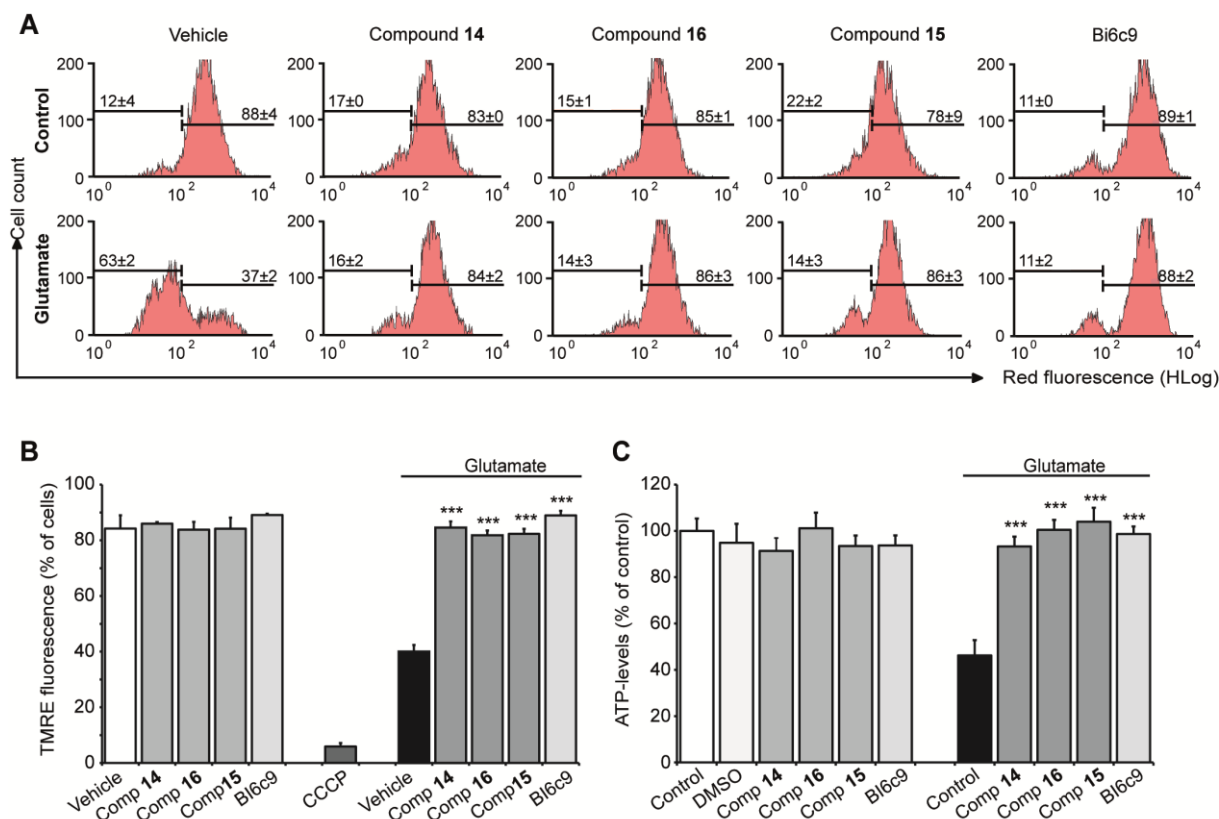


**Figure 31: *N*-Phenyl substituted thiazolidinediones preserve mitochondrial integrity and function.**

**A**, Mitochondrial membrane potential ( $\Delta\psi_m$ ) was determined by TMRE-FACS recordings. HT-22 cells were treated with glutamate (5 mM) alone or co-treated with glutamate (5 mM) and thiazolidinedione derivatives (20  $\mu$ M). Twenty hours after treatment, cells were stained with MitoTM<sup>TM</sup> TMRE dye and red fluorescence of 10,000 cells per treatment condition was analyzed. Glutamate-treated cells (vehicle) show significant reduction of red fluorescence (loss of  $\Delta\psi_m$ ) compared to control vehicle, while SCHL 24277(**14**), SCHL 24292 (**16**) and SCHL 24213 (**15**) prevent breakdown of  $\Delta\psi_m$ . Numbers are mean percentages  $\pm$  SD of TMRE fluorescence of the indicated cell groups with  $n = 3$ . High red fluorescence indicates intact mitochondria (right side), drop of red fluorescence depicts loss of  $\Delta\psi_m$  (left side). Pictures are representatives of three independent experiments. **B**, Quantification of TMRE fluorescence (**A**) confirms the breakdown of  $\Delta\psi_m$  in glutamate exposed vehicle cells, which is significantly prevented by the compounds **14**, **16** and **15**. The uncoupler CCCP, which causes a fast breakdown of the mitochondrial membrane potential, was used as a positive damage-control. The experiment was independently repeated four times with  $n = 3$  and data are presented as mean  $\pm$  SD. **C**, ATP-levels of HT-22 cells, treated with 20  $\mu$ M of the compounds **14**, **16** or **15** as indicated, were analyzed in the presence or absence of glutamate (5 mM, 20 h) by ATP-luminescence measurements. Compound treatment does not affect basal ATP levels, but significantly prevents ATP depletion after glutamate exposure. Experiment was repeated three times with  $n = 8$  per treatment condition and results are provided as mean  $\pm$  SD (\*\* $p < 0.001$  compared to glutamate-treated vehicle, ANOVA, Scheffé test (**B**, **C**)).

Broader insights into the compounds ability to rescue metabolic functions were derived from from measurements of oxygen consumption rate (OCR) of intact HT-22 cells, enabling the evaluation of mitochondrial bioenergetics and metabolism under conditions that are more physiologically realistic compared to isolated mitochondria<sup>203</sup>. O<sub>2</sub>-consumption of HT-22 cells was analyzed in the presence and absence of glutamate using the Extracellular Flux Analyzer (Seahorse Bioscience) designed for the exposure of mitochondria to defined substrates and inhibitors to modulate mitochondrial respiration in adherent cells<sup>204</sup>. In accordance with previous studies reporting that glutamate-induced mitochondrial dysfunction involves changes in mitochondrial acidification and oxygen consumption<sup>205</sup>, glutamate exposure of HT-22 cells decreased oxygen consumption rate (OCR) indicating a glutamate-induced reduction in mitochondrial respiration (Figure 32). After recording the basal mitochondrial respiration, the ATP synthase inhibitor oligomycin was added to uncouple mitochondrial respiration from ATP production. While OCR of control cells was decreased after oligomycin injection, glutamate-treated cells responded less to oligomycin, (Figure 32). This indicates a glutamate-induced decrease in ATP production, which is in line with the ATP luminescence measurements described above. In comparison, OCR measurements similarly confirmed the preservation of ATP-generation by the compound **14**, **16** and **15** at concentrations of 20 μM, respectively and BI-6c9 at concentrations of 10 μM (Figure 32 A *till* B). The further application of the protonophor FCCP increased OCR to a maximum extent allowing the examination of the maximum oxygen flux (MOF) and mitochondrial respiratory capacity (MRC) of cells. After glutamate treatment both, MOF and MRC were significantly decreased, but notably restored by co-treatment of cells with compound **14**, **16** and **15** or BI-6c9 (Figure 32). Finally, the mitochondrial respiratory chain was inhibited by the application of the complexes I and III inhibitors, rotenone and antimycin A. While rotenone/antimycin A-sensitive OCR specifically indicates respiration in mitochondria, rotenone/antimycin A-non-resistant rate identifies non-mitochondrial respiration<sup>203</sup> and allows for calculation of mitochondrial maximum respiration. The remarkable reduction in mitochondrial maximum respiration in glutamate-treated HT-22 cells was significantly prevented by the compounds **14**, **16** and **15** and the Bid inhibitor BI-6c9 (Figure xx A, B). The ability of BI-6c9 and the newly synthesized compounds to prevent the glutamate-induced reduction in mitochondrial respiratory capacity and maximum respiration provides additional evidence that inhibition of Bid emerges as potential strategy for maintaining mitochondrial metabolic functions.

In conclusion, the N-phenyl substituted thiazolidinediones rescued metabolic functions and maintained energy metabolism in mitochondria of HT-22 cells challenged with glutamate. Of note, the fact that the compounds do not affect mitochondrial maximum respiration, providing a full protection against respiratory dysfunctions, presumes that all three molecules

(compound **14**, **15** and **16**) act upstream of mitochondria, thereby supporting the hypothesis that the protective effects are mediated by inhibiting Bid.

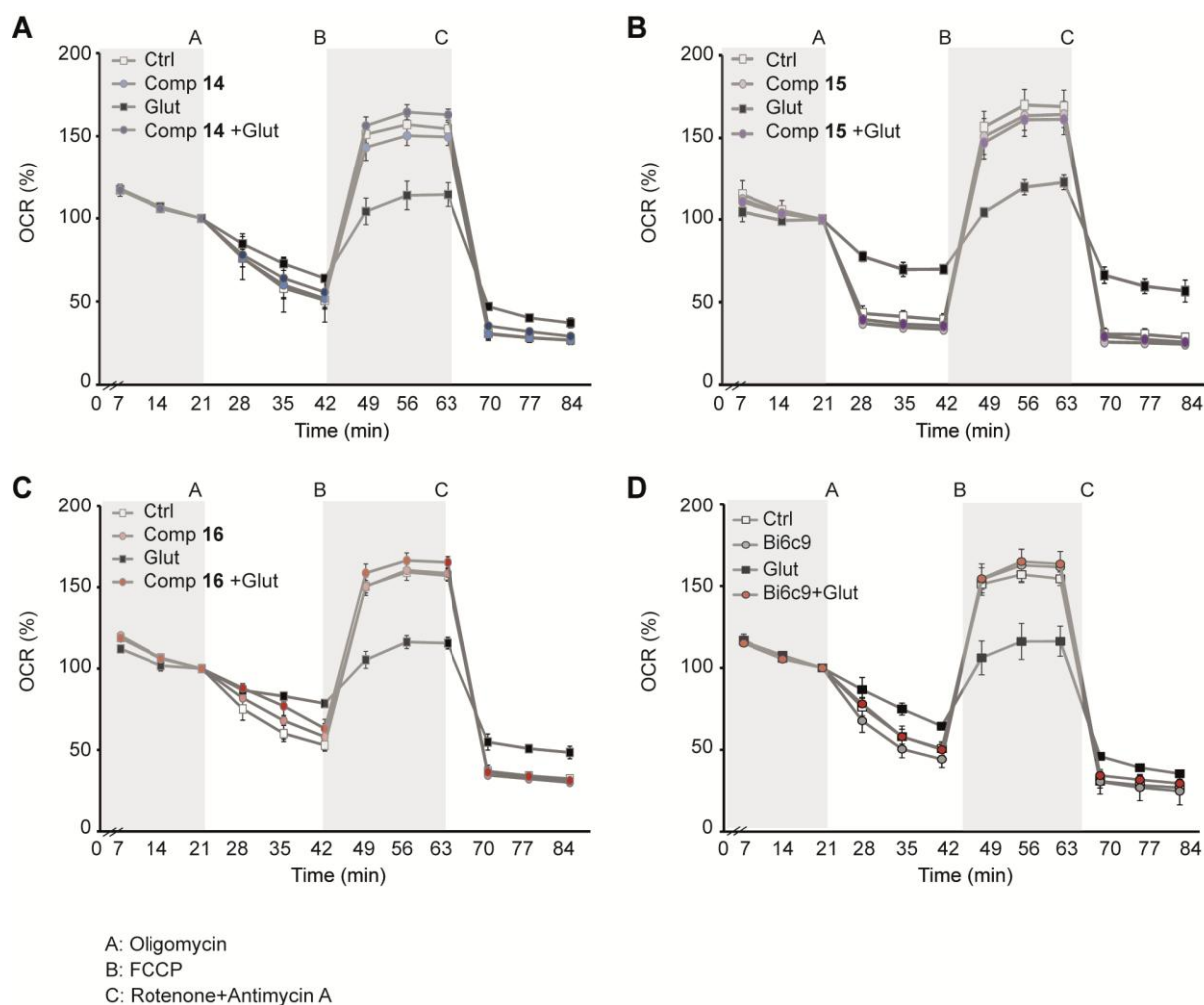


**Figure 32: *N*-Phenyl substituted thiazolidinediones preserve mitochondrial respiration**

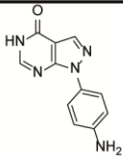
**A-C**, Time course of oxygen consumption rate (OCR) in HT-22 cells in the presence and absence of glutamate. HT-22 cells were seeded in XF96-well micro plates (Seahorse Bioscience) at a density of 10,000 cells per well and treated with glutamate (5 mM) and/ or the indicated thiazolidindiones SCHL 24277 (**14**) (**A**), SCHL 24213 (**15**) (**B**), SCHL 24292 (**16**) (**C**), or the Bid inhibitor BI-6c9 (**D**), respectively. Twenty hours after treatment, mitochondrial respiration was analyzed using the XF Mito Stress kit and recorded as the rate of OCR by the Extracellular Flux Analyzer (Seahorse Bioscience). As controls, Oligomycin (3  $\mu$ M) was used to inhibit ATP-linked OCR, FCCP (0.4  $\mu$ M) to measure uncoupled respiration and Rotenone/Antimycin (1  $\mu$ M) to inhibit complex I/III-dependent respiration. Glutamate exposure of HT-22 cells decreases oxygen consumption rate and thereby mitochondrial respiration. Co-treatment of cells with the indicated thiazolidindiones in concentrations of 20  $\mu$ M respectively, restores mitochondrial maximum respiration as well as respiratory capacity. Data were depicted as normalized OCR (% baseline rate) for each individual populations of cells and representative of four independent experiments, each with  $n = 8$  for all treatment groups, respectively.

In summary, these data demonstrate, that the screened *N*-phenyl substituted thiazolidindiones, showed a pronounced potency against glutamate toxicity and indicate the specific inhibition of Bid as the underlying key mechanism of their protective properties.



### 3.1.6 *N*-aryl substituted pyrazolopyrimidinones promise a novel class of neuroprotectants

Several other small-molecules differing in their chemical structure, size and solubility were screened within this thesis revealing variable efficiency in protecting the cells against glutamate- and tBid-induced toxicity (appendix Table 70).

Compound ID	Compound name	Structure	Neuroprotective activity					Cytotoxicity ( $\mu\text{M}$ , $p < 0.001$ )
			compound concentration ( $\mu\text{M}$ )					
			1	10	25	50	100	
19	SCHL 24394		---	---	***	***	***	N/A <sup>a</sup>

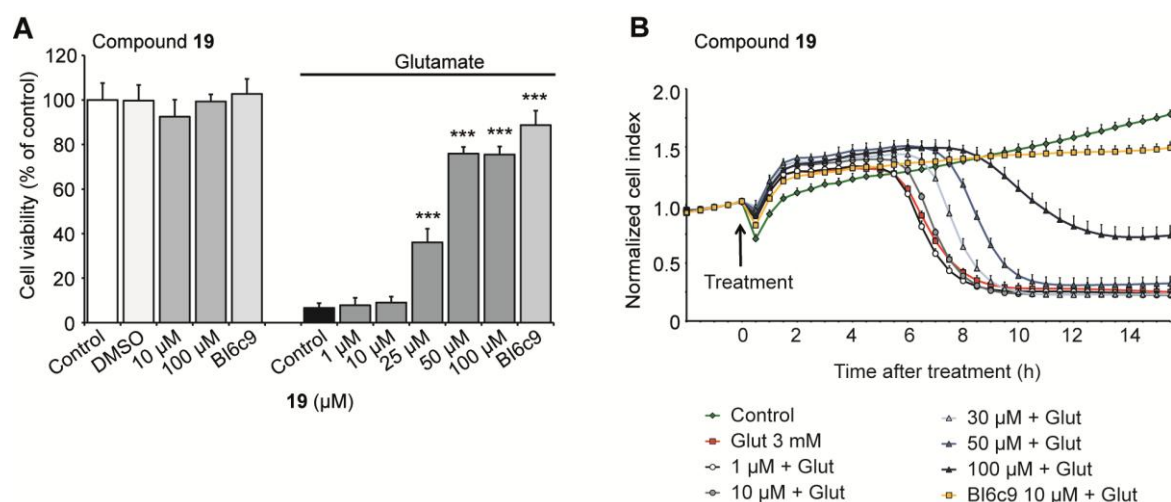
**Table 64: Neuroprotective properties of *N*-aryl substituted pyrazolopyrimidinone (19)**

Chemical structure of the 1-(4-Aminophenyl)-1*H*-pyrazolo[3,4-*d*]pyrimidin-4(5*H*)-on is shown. The pyrazolopyrimidinone provided significant protection against glutamate-toxicity in HT-22 cells at concentrations of 25  $\mu\text{M}$  up to 100  $\mu\text{M}$  and revealed no toxic effects as determined by MTT assay (\*\* $p < 0.001$  compared to glutamate treated control, ANOVA Scheffé's test; N/A<sup>a</sup>, not active – substance revealed no toxic properties at concentrations of 1  $\mu\text{M}$  up to 100  $\mu\text{M}$ ). The result presented is a representative of 5 experiments (MTT assay).

It is noteworthy that one compound (**19**) (Table 64) representing the chemical class of *N*-aryl substituted pyrazolopyrimidinones emerged as potent neuroprotectant and indicates this structure type as promising scaffold for the ongoing development of neuroprotective compounds..

This compound **19** attenuated glutamate-induced cell death of HT-22 cells in a concentration-dependent manner from 25  $\mu\text{M}$  up to 100  $\mu\text{M}$  as revealed by MTT assay (Figure 33 A) and further confirmed by the RTCA-measurements, showing a transient protective effect of compound **19** in concentrations of 30  $\mu\text{M}$  up to 100  $\mu\text{M}$  (Figure 33 B).

Interestingly, despite this moderate protection against glutamate-toxicity, the compound **19** was highly potent against tBid-mediated cell injury and provided significant protection already at low concentrations of 1  $\mu\text{M}$  (Figure 34). Noteworthy, compound **19** did not reveal toxic effects in any of the applied model systems at concentrations up to 100  $\mu\text{M}$ , which is an advance of this structure type compared to the *N*-aryl phenoxyanilines described above.

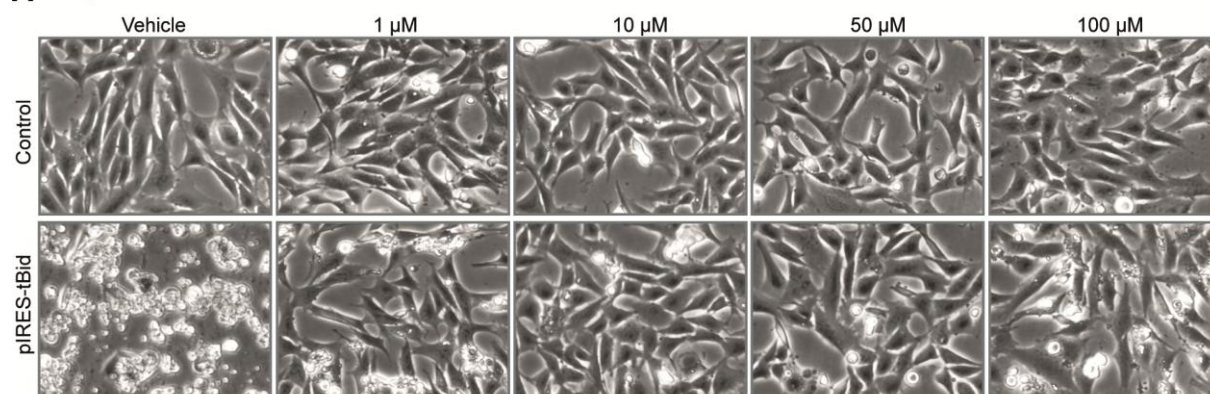
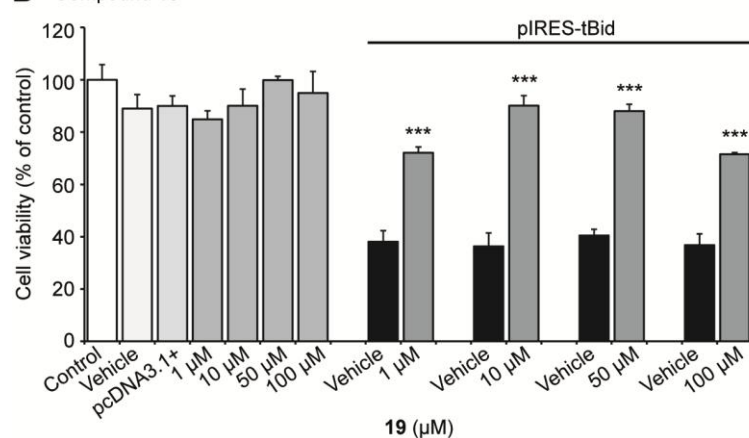


**Figure 33: N-aryl substituted pyrazolopyrimidinone protects against glutamate-induced toxicity in a concentration dependent manner.**

SCHL 24394 (**19**) reveals protective effects against glutamate-induced toxicity in a concentration dependent in from 1 μM up to 100 μM. **A**, Cell viability of HT-22 cells was determined by MTT assay 16 h after co-treatment with glutamate (3 mM) and compound **19**. BI-6C9 (10 μM) was used as a positive control for neuroprotection. Substance treatment alone shows no toxic effects and attenuates against glutamate toxicity at concentration of 25 μM and higher. Results are presented as mean ± SD (\*\*p < 0.01 compared to glutamate-treated control, ANOVA, Scheffé's test). **B**, Real-time analysis of cellular impedance with the xCELLigence system (Roche) confirms the concentration-dependent protective effect of compound **19**. While concentrations of 30 μM and 50 μM obtained only slightly protection, a more pronounced protection is revealed at concentrations of 100 μM. Cell index was normalized at 0 h (treatment time-point). Results are provided as mean ± SD with n = 8 per treatment group. All experiments were independently repeated three times.

As this compound represents the first structure of the class of N-aryl substituted pyrazolopyrimidinones, further chemical modifications are warranted in order to further explore structure-activity relationships of this structure for developing highly potent and specific Bid inhibitors that may provide neuroprotection in a low and *in vivo* applicable concentration range.

In summary, these studies revealed the development and screening of a series of novel small-molecules designed to inhibit the pro-apoptotic molecule Bid in neurons. Based on the structure of the available Bid inhibitor BI-6c9, three diverse compound classes were developed and structurally optimized by the chemistry department (group of Prof Dr Schlitzer) in order to explore the structure-activity relationships of the small-molecules targeting Bid. Seven compounds, belonging to the class of N-acyl substituted 4-phenoxyanilines, N-phenyl substituted thiazolidindiones and accordingly N-aryl substituted pyrazolopyrimidinones, were identified as novel small-molecules with promising potential for neuroprotection in a range of cellular model systems, including glutamate- as well as tBid-induced cell injury. Therefore, the compounds presented in this work are not only potent scaffolds for future structure optimization resulting in compounds with favorable pharmaceutical properties, but might indicate already promising drug candidates for first trials in model systems of brain damage *in vivo*.

**A** Compound 19**B** Compound 19**Figure 34: Compound 19 prevents tBid-induced neuronal cell death.**

tBid-induced toxicity was determined 18-20 h after transfection of HT-22 cells with a tBid-encoding plasmid (pIRES-tBid). Compound 19 was applied to cells 1 h before pIRES-tBid-transfection. **A**, Photomicrographs (10 x 0.25 NA objective) reveal the preservation of the spindle-like morphology of HT-22 cells after tBid over-expression by the application of compound 19 at concentrations of 1 μM up to 100 μM. **B**, Quantification of cell viability by the MTT assay confirms significant protective effects of SCHL 24394 (19) against tBid-induced toxicity, while no toxic effects of the compound 19 was observed. For statistical analysis, experiments were independently repeated at least three times with n = 3 per treatment condition and results are reported as mean ± SD (\*\*\*p < 0.001 compared to t-Bid treated control cells, ANOVA, Scheffé's-test).

## 3.2 Expression, purification and crystallization of recombinant Bid constructs

The molecular mechanism by which the pro-apoptotic protein Bid regulates mitochondrial cell death pathways, and in particular how Bid mediates impairments in mitochondrial membrane integrity and function is still far from being explained. Structural and functional studies are required for a more thorough understanding of Bid action, and thereby for the development of target-directed perspectives of therapies for neuronal diseases.

While the first part of this work could already demonstrate promising Bid-targeting compounds that provide protection in various approaches of cell death models, the exact mechanism of their inhibitory activity remains to be clarified, and further structural optimization is required to improve their binding affinities to low nanomolar concentrations. The determination of protein-ligand structures and the facilitation of a rational and structure-guided design of novel compounds that selectively target the protein of interest, Bid, is a challenge. The three-dimensional structures of biological macromolecules are not only often the key to gaining a deep understanding in the proteins function, but, beyond doubt, they are the necessary tool for target-specific drug development. While crystal structures of other Bcl-2 family proteins, such as Bcl-xl, Mcl-1 or Bax<sup>68, 105, 109, 121, 122</sup>, provided the basis for the design of selective inhibitors, up to now there is no report on a crystal structure determination of Bid from any species. In an effort to gain more insights in the structural properties of Bid and to explore the binding affinities of novel compounds, the further part of this work includes the establishment of a suitable pipeline from construct design and cloning to expression and purification of recombinant Bid required for the first Bid crystallization set up.

The approach of recombinant proteins further aimed at the development and validation of *in vitro* assay systems suitable to address the physical action of Bid on artificial membranes (3.3) and to generate a basis for primary screening of small-molecule Bid inhibitors. Lastly, purified Bid protein should be used for determining its functional interactions with other proteins involved in the mechanisms of intrinsic cell death.

### 3.2.1 Expression of recombinant full-length Bid and its active form tBid

The first step towards crystallization is the high-yield expression and purification of the target protein. Therefore, full-length mouse Bid as well as its truncated, active form tBid were cloned as fusion proteins with a hexa-histidin-tag into the pET15b vector and tested for effective expression in *Escherichia coli* Rosetta2 (DE3).

### 3.2.1.1 High-yield expression of full-length Bid

To investigate the expression efficiency and solubility of His<sub>6</sub>-tag full-length Bid, Rosetta2 (DE3) singles were transformed with the pET15b-Bid 22 vector and grown at 37°C in LB medium. When bacterial growth reached an optical density (OD<sub>600</sub>) of 0.6 AU, protein expression was induced by addition of 1 M IPTG solution. Gel-electrophoresis and western blot analysis confirmed the effective expression of full-length Bid in *E.coli* and its recovery in the soluble protein fraction (Figure 35 A, B). An increasing 22 kDa Bid-band was detected 2 h to 6 h after IPTG induction, while no Bid protein appeared at time point 0 and in the bacterial overnight culture (control) (Figure 35 B). Notably, large amounts of Bid were already produced 2 h after IPTG induction, indicating the protein is suitable for large-scale production. In addition, full-length Bid was also found in the membrane-bound protein fractions 2 h after expression induction, but in a less amount compared to the soluble fractions (Figure 35 C).

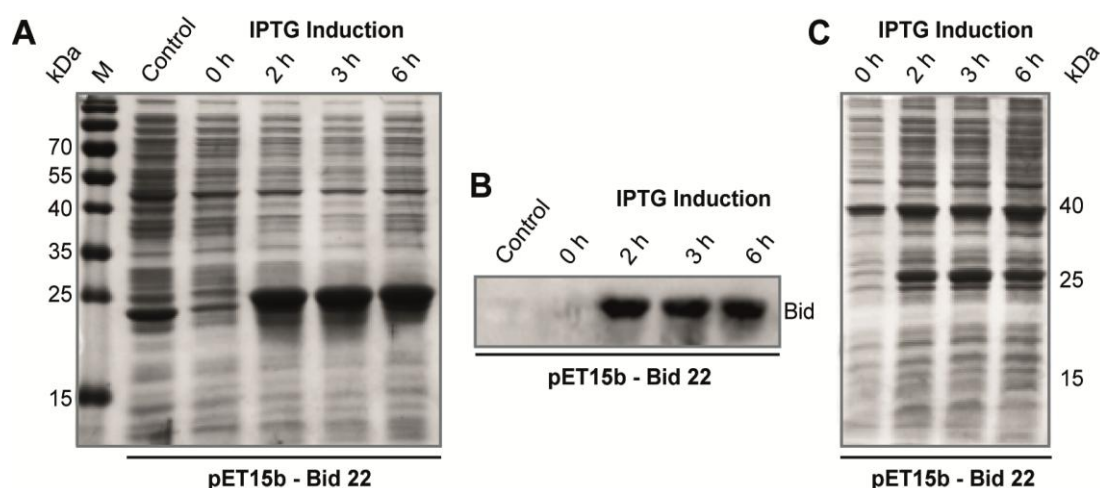


**Figure 35: Effective expression of full length Bid.**

Expression efficiency and solubility of His<sub>6</sub>-tag full length Bid was analyzed by expression tests in Rosetta2 (DE3). **A**, Coomassie stained SDS-PAGE predicts soluble protein fractions after expression of His<sub>6</sub>-tag full length Bid in Rosetta2 (DE3). Full length Bid is efficiently expressed and recovered in a high amount in the soluble fraction 2 h after IPTG expression. **B**, Western blot analysis confirms the successful expression of full length Bid recovered in the soluble fraction after cell lysis. **C**, Coomassie stained SDS-PAGE of the membrane-bound proteins after expression of His<sub>6</sub>-tag full length Bid in Rosetta2 (DE3). Bid is predicted after 2 h IPTG induction. Note that the amount of Bid protein in the soluble protein fractions is much more pronounced than in the membrane-protein fractions.

As Bid is described as a soluble and cytosolic protein in healthy cells<sup>61</sup>, the detection of Bid in the bacterial membrane fractions (Figure 35 C) might be due to adsorbance of the soluble protein to bacterial membranes. Notably, in contrast to the highly effective expression of full-length Bid, no expression could be detected for the truncated and active form tBid, indicating that *E. coli* strains avoid the expression of the toxic construct.

### 3.2.2 Purification of full length Bid yields reasonable protein amounts

For large-scale production and purification of full-length Bid, the His<sub>6</sub>-tagged protein was expressed in *E. coli*. Rosetta2 (DE3) as described above. The determination of an exponential growth curve for *E. coli*. indicated that the bacterial culture reached an OD<sub>600</sub> of 0.6 AU 4-5 h after growth induction. Therefore, Bid expression was mostly induced 4.5 h after inoculating the bacterial overnight culture to fresh LB medium for large-scale protein production.

His<sub>6</sub>-tagged full-length Bid could be readily purified from raw cell lysates following expression and three chromatography steps. The initial purification step was performed manually by nickel-affinity chromatography yielding a protein recovery from the initial purification set of 7.2 mg per liter bacterial culture, or by Ni-affinity chromatography using the Äkta prime plus system, allowing for large-scale purification of volumes up to 25 ml bacterial lysate within one purification run (Figure 36). His<sub>6</sub>-tagged Bid was sufficiently eluted between 200 mM and 250 mM imidazole (Figure 36 A). Gel-electrophoresis of the elution fractions revealed the highest amount of Bid in fraction E10 and E11 (Figure 36 B). Of note, the elution profile was almost constant for all further affinity purifications of novel protein batches. The Bid-containing fractions were subjected to the second purification step performed by ion exchange chromatography (Figure 36 C, B). Within a continuous NaCl gradient, the elution of Bid was observed at approximately 250 mM NaCl, as shown in the ion exchange chromatogram (Figure 36 C). Gel-electrophoresis confirmed the purity of the eluted protein in the fractions E42-E48 (Figure 36 D). Although the chromatogram revealed two peaks, SDS-PAGE confirmed that both peaks (E40-44 and E48) belong to the full-length Bid protein and no degradation products were detected (Figure 36 D). Notably, protein-containing fractions could be stored at 4°C over several weeks until further use.

SDS-PAGE followed by western blot (Figure 37 A, B) confirmed the identity of the purified Bid protein. Even though high amounts of Bid achieved by affinity chromatography were decreased after ion exchange, probably due to exceeding the column binding affinity, the highly pure Bid was finally recovered in amounts of about 15-20 mg per liter bacterial culture. Since the purity of the His<sub>6</sub>-tagged Bid was already approximately 90-95 % after ion exchange chromatography (Figure 37 A), protein samples were suitable for functional analysis as described below.

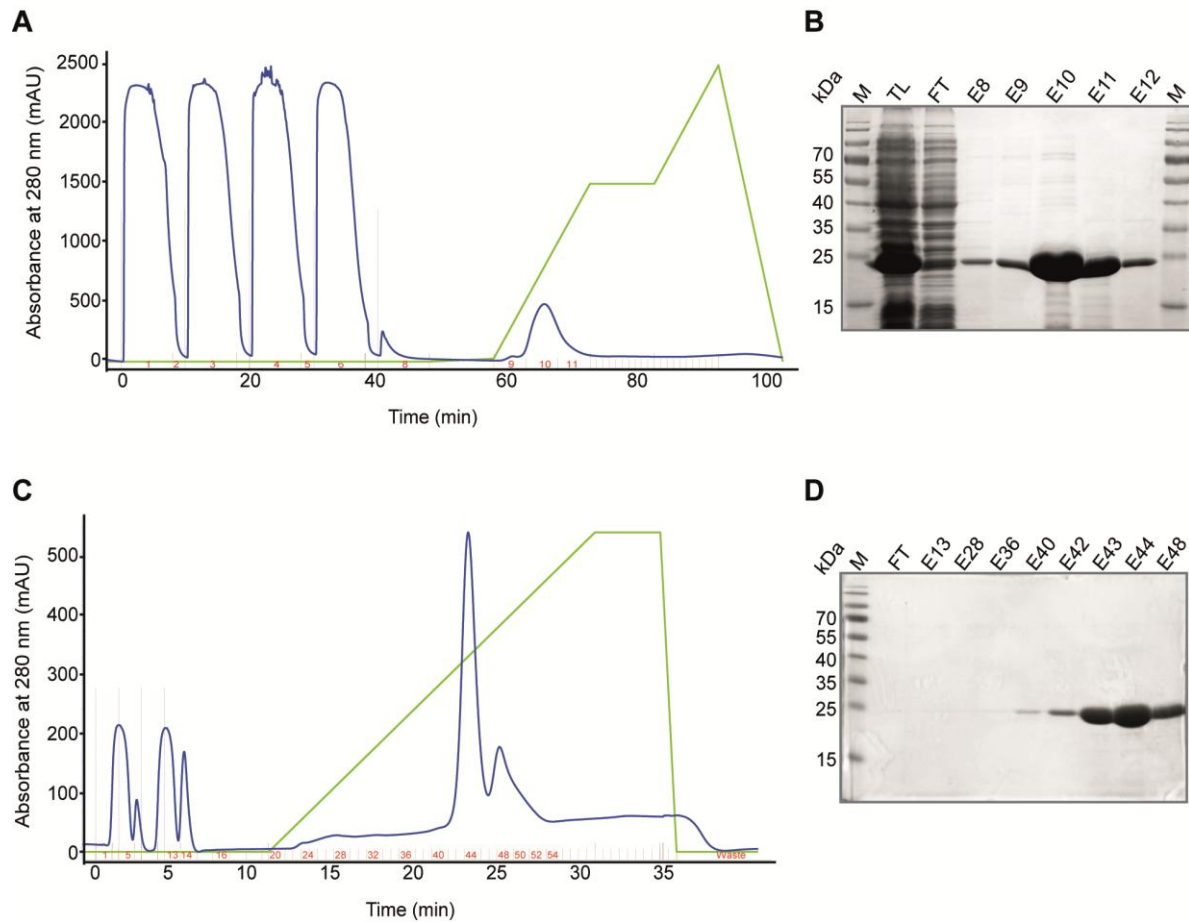


### Figure 36: Purification of full length Bid by Äkta-chromatography.

Successful purification of one of full length Bid by chromatography using the Äkta prime plus. **A**, Elution profil of Nickel-affinity chromatography is shown. **B**, The elution-fractions within the peak area were analyzed by SDS-PAGE followed by coomassie staining. Fraktions E8 – E12 were pooled for further purification by ion exchange (TL=cellular lysate, FT= Flow through). **C**, Second step purification: Ion exchange chromatography. The protein was eluted at 250 mM NaCl. **D**, Confirmation of high purified Bid protein by gel electrophoresis and coomassie staining. M = protein size ladder, FT = Flow through, E13-E48 = elution fractions within the peak area of C.

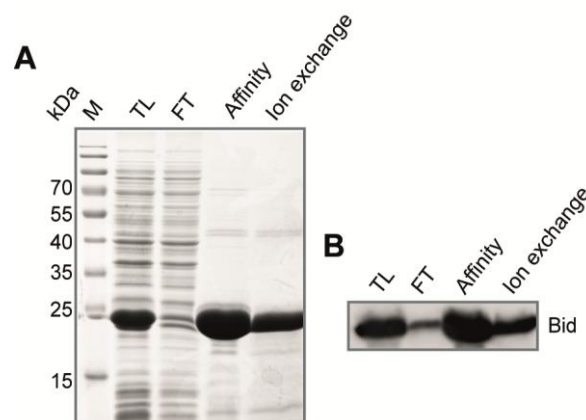


### Figure 37: Purified His<sub>6</sub>-Bid.

**A**, Coomassie-stained SDS-PAGE reveals purity of recombinant His<sub>6</sub>-Bid after Affinity chromatography (Affinity) and ion exchange. TL = Total lysate, soluble protein fractions; FT = Flow through; M = protein size ladder. **B**, Western blot analysis confirms the identity of Bid. Final recovery of Bid was 15-20 mg/ml bacterial culture.



Since X-ray crystallization requires the highest purity and homogeneity of the protein as practically possible ( $\geq 95\text{-}98\%$ )<sup>189</sup>, the final purification step of all recombinant proteins was performed by gel filtration. Highly pure Bid was eluted in 20 mM Tris (pH 7.4), 50 mM NaCl as confirmed by the gel filtration chromatogram (Figure 38 A). The second peak was confirmed as the Bid absorbance peak as gel-electrophoresis revealed high yields of Bid protein in the elution fractions E17 and E18 (Figure 38 B), revealing a purity of about 98 %.

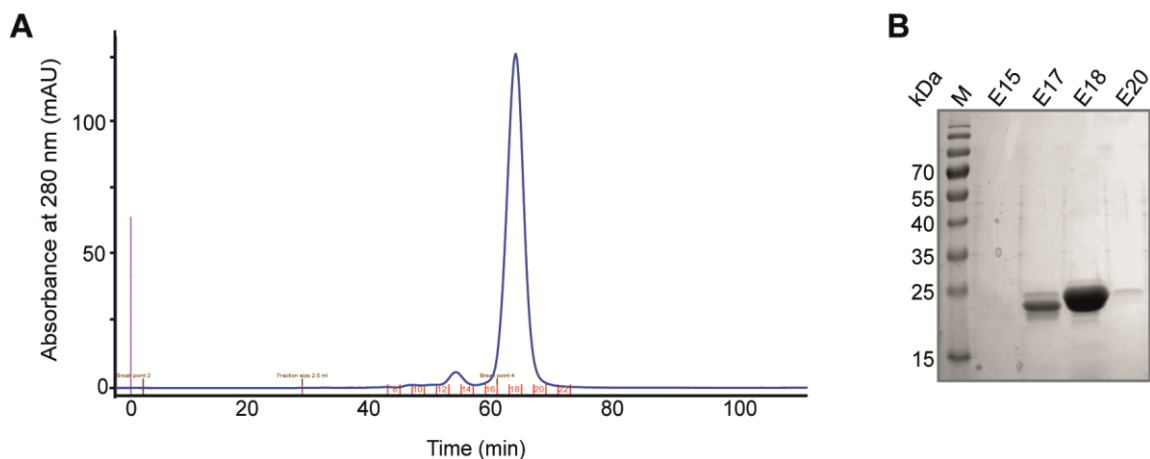


**Figure 38: Gel filtration of full length His<sub>6</sub>-Bid.**

**A**, Gel filtration chromatogram of full-length His<sub>6</sub>-Bid. Bid was eluted in 20 mM Tris (pH 7.4), 50 mM NaCl in the fractions E17-E19. **B**, Coomassie-stained SDS-PAGE confirms the purity of Bid (> 98 %).

Crystallization requires to bring the macromolecule to supersaturation<sup>189, 206</sup>. Therefore, pure protein batches were concentrated to the highest possible concentration without causing aggregation or precipitation of the macromolecule<sup>206</sup>. Concentrations between 5-25 mg/ml, sometimes even up to 100 mg/ml are recommended with the commonly used concentration of 10 mg/ml. Notably, the required concentration for obtaining crystals that diffract to high resolution always depends on the behavior of each individual protein and has to be established during the initial crystallization screens.

Even though high yields of protein were obtained after gel filtration (~10-15 mg protein per liter culture), concentration of His<sub>6</sub>-tagged full-length Bid was limited to a concentration of 4.5-5 mg/ml. In an effort to improve the concentration of full-length Bid and due to the fact, that purification-tags might interfere with the crystallization of proteins, an alternative purification set up for full-length Bid was scaled up, including the proteolytic cleavage of the His-tag. Initial purification was performed by Nickel-affinity chromatography followed by ion exchange as described above. Separation of the thrombin-cleaved His-tag and full-length Bid was finally achieved using gel filtration.



The high recovery and purity of full-length Bid was confirmed by determining the respective yields of protein after the particular purification runs within one SDS-PAGE (Figure 39 A). Notably, affinity chromatography provided yields of 65 % compared to the total lysate (TL), which was retained by ion exchange without loss of protein. The final gel filtration step achieved the highest purity of the Bid protein, up to 99%, but in fewer yields (50 % compared to affinity chromatography, Figure 39 A). The successful cleavage of the His-tag and integrity of full-length Bid was finally confirmed by MALDI-TOF analysis, which was kindly performed by Jörg Kahnt at the Max-Planck-Institute of Terrestrial Microbiology, Marburg, Germany (Figure 39 B).

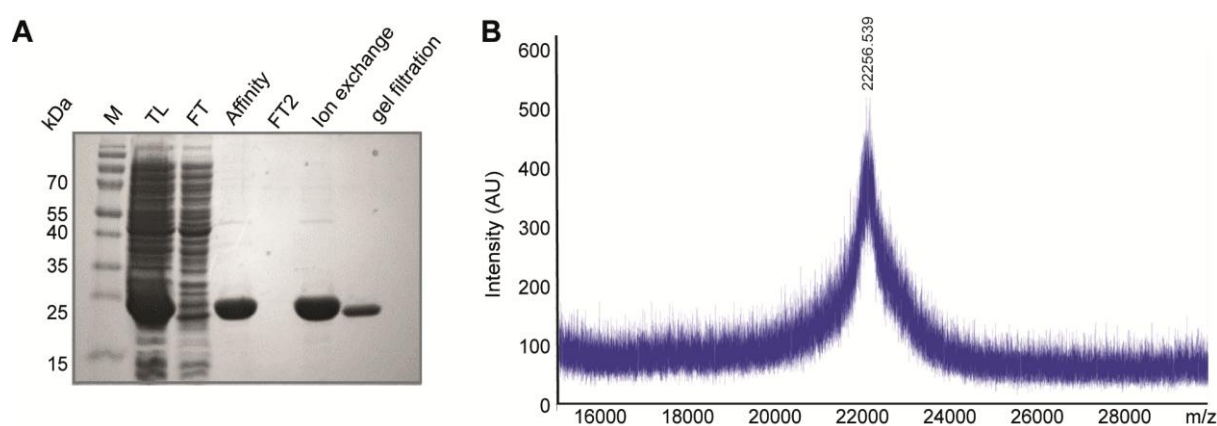


**Figure 39: Recovery of full-length Bid during chromatography purification and MALDI-TOF analysis.**

**A**, 12.5 % coomassie stained SDS-Page predicts the results from each purification step. Pooled fractions which contained the purified Bid protein after Ni-affinity chromatography (affinity), Ion exchange and gel filtration, respectively were analyzed to estimate the protein recovery and purity. Cleavage of the His<sub>6</sub>-tag was performed after ion exchange and separation of the purification tag and full-length Bid was achieved by gel filtration. The final yield was 10-15 mg protein per liter bacterial culture. M = protein size ladder, TL = Total lysat before purification, FT = Flow through during affinity chromatography, FT2 = Flow through during ion exchange. **B**, Maldi analysis of the produced recombinant full length Bid after Thrombin- cleavage of the His-tag, confirms the production of Bid with a molecular weight of 22.256 kDa.

Notably, cleavage of the His<sub>6</sub>-tag benefitted the final concentration step of full-length Bid resulting in concentrations of up to 9.5-10.0 mg/ml compared to 4.5-5 mg/ml for full-length Bid containing the His<sub>6</sub>-tag.

### 3.2.3 Crystallization of full-length Bid

Crystal structure determination is regarded as the preferred method to obtain insights into the structural understanding of the molecular function of proteins as well as into the interaction geometry of protein-ligand complexes. To date, 86 % of the Protein Data bank (rcsb-PDB) entries are macromolecular structures that were determined using X-ray crystallography. The successful determination of the crystal structure of a protein requires the preparation of crystals suitable for X-ray analysis, usually single crystals characterized by a high degree of homogeneity, long-range order and suitable size with an optimum between  $10^{-4}$  and  $10^{-3}$  mm<sup>3</sup><sup>189, 206-209</sup>, causing the process of obtaining crystals as cumbersome and not trivial.

As the purity, homogeneity and monodispersity of the respective Bid protein sample was evaluated at the purification stage, the protein was introduced to precipitating agents that can promote the nucleation of protein crystals in the solution. All crystallization screens throughout this thesis were performed using the vapor-diffusion technique as the main commonly used method for obtaining crystals. Initial crystallization screenings for the respective Bid protein constructs were performed using typical protein crystallization screens purchased from Qiagen (see Table 54) thereby testing about 1300 different conditions at two different temperatures (4°C and 18°C) respectively, as temperature can influence protein solubility and thereby crystallization. The crystallization screens were carried out at the Core Facility Structural Biology, LOEWE Center of Synthetic Microbiology (SYNMICRO), University of Marburg, using a HoneyBee crystallization robot and 96-well plates with 600 nL mother liquor and protein (1:1) and 80 µl reservoir volume incubated, and continuously imaged using a Formulatrix RockImager (see methods for detail). For scoring and interpretation of crystallization drop results, a non-Q scoring system was used<sup>189</sup>, which is shown in Table 61 (2.23.3).

#### 3.2.3.1 Highly flexible regions eliminate crystallization of full-length Bid

Purified His<sub>6</sub>-tagged full-length Bid was subjected to crystallization screening at a concentration of 4.5 mg/ml. Despite of 1300 crystallization conditions, the first crystallization screens failed to yield Bid crystals, although some tendencies for initial crystal nucleation and micro-crystallization could be observed. The formation of heavy precipitates (score 2-3) was often observed in the presence of cadmium, nickel or zinc ions, while microcrystals and needles (score 6-7) could be obtained in the presence of cryoprotectants, such as 2-Methyl-2,4 pentanedion (50% MPD) or different polyethyleneglycols (PEG 3350, PEG 4000). However, reproduction and optimization failed to identify a clear “hit”-condition for the crystallization of His<sub>6</sub>-tagged full-length Bid.

Full-length Bid lacking the His<sub>6</sub>-tag was subjected to a selection of 8 screening suites (Table 54) at higher concentrations of 9.9 mg/ml and monitored at 18°C which was found to be the more promising temperature. Two conditions are worth mentioning, condition 21 from the classic suite and condition 12 from JCSG Core I suite, revealing small micro-crystals (score 6) approximately 25-30 days upon drop incubation. Both conditions were optimized as presented in Table 55 and Table 56. Although, crystal growth could be slightly improved, the obtained microcrystals were still too small for mounting and appeared to be overlapping each other, forming small and amorphous crystal clusters.

As these observations demonstrated that crystallization screening of full-length Bid failed to yield crystals suitable for diffraction measurements, further work included the design of novel Bid constructs which should facilitate the crystallization procedure.

### **3.2.4 Design of modified truncated Bid constructs promise successful crystallization**

Structures of mouse and human Bid proteins generated so far by nuclear magnetic resonance (NMR) techniques provide insights into the structural mobility of Bid: consisting of 20 NMR solutions differing in their energy (PDB entry, 1DDB)<sup>65</sup>, the three-dimensional solution structure of Bid predicts the arrangement of the eight  $\alpha$  helices, building the core of Bid, and two strongly disordered regions with a high conformational mobility (Figure 40, marked in red). The conformation of the unstructured N-terminal region and the highly flexible loop located between  $\alpha$ 2 and  $\alpha$ 3 predicted in Figure 40 A are only two of many that satisfy the NMR-derived restraints. Thus, the presence of these highly mobile regions might explain the failure of obtaining crystals using full-length Bid as a conformational mobility interfere with the generation of severe ordered crystal packages. As shown in Figure 40 B revealing an overlay of the NMR structure of mouse Bid (1DDB)<sup>65</sup> and the X-ray structure of mouse Bcl-xl (1MAZ)<sup>68</sup>, the overall tertiary fold derived for Bid is similar as that observed for the Bcl-xl structure<sup>68, 113</sup>. Therefore, further strategies for Bid crystallization were based on previous experiences collected for the construct design and crystallization of Bcl-xl and other related proteins such as Bcl-2 and Mcl-1<sup>68, 122, 210</sup>, indicating that crystallization of Bid could be facilitated by removing the mobile N-terminus and loop.

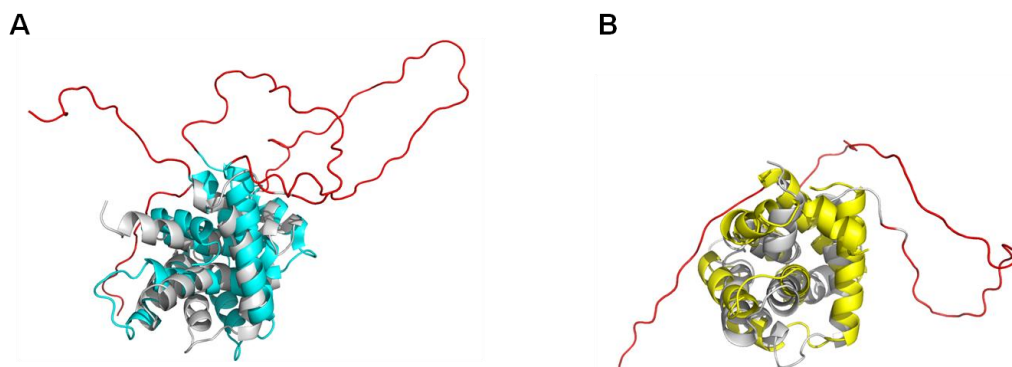


**Figure 40: Highly flexible regions of full-length Bid**

**A**, Overlay of two NMR structure of full-length mouse Bid (PDB entry, 1DDB)<sup>65</sup>. Ribbon depiction reveals, that the protein Bid consists of a eight-helix core shown in grey and turquoise, respectively and two strongly disordered regions located at the N-terminus and between helices  $\alpha 2$  and  $\alpha 3$  (both marked in red). The schematic drawing illustrates the size and two possible conformations of the flexible N-terminus and the loop. As the 1DDB structure solution of full-length mouse Bid consist of 20 NMR solutions<sup>65</sup>, the predicted orientations of the loop are only two of many that satisfy the NMR-derived restraints. In contrast, the core conformation is almost consistent. **B**, Overlay of one NMR structure solution of mouse full-length Bid in grey (PDB entry, 1DDB) and x-Ray structure of mouse Bcl-xl (PDB entry, 1MAZ)<sup>68</sup> in yellow. The Bcl-xl protein consists of two central hydrophobic  $\alpha$ -helices surrounded by amphipathic helices and a highly flexible 60-residue loop connecting helices  $\alpha 1$  and  $\alpha 2$ . Since the removal of this loop was essential for obtaining crystals, it is not predicted in the yellow Bcl-xl structure.

Based on these considerations<sup>211</sup>, four different Bid constructs lacking the highly flexible regions of mouse Bid were designed as GST-fusion proteins following the strategy predicted in Figure 41 A, namely pGEX  $\Delta 12$ -Y47 (Bid 1), pGEX  $\Delta 12$ -D51 (Bid 2), pGEX  $\Delta 13$ -Y47 (Bid 3) and pGEX  $\Delta 13$ -D51 (Bid 4).

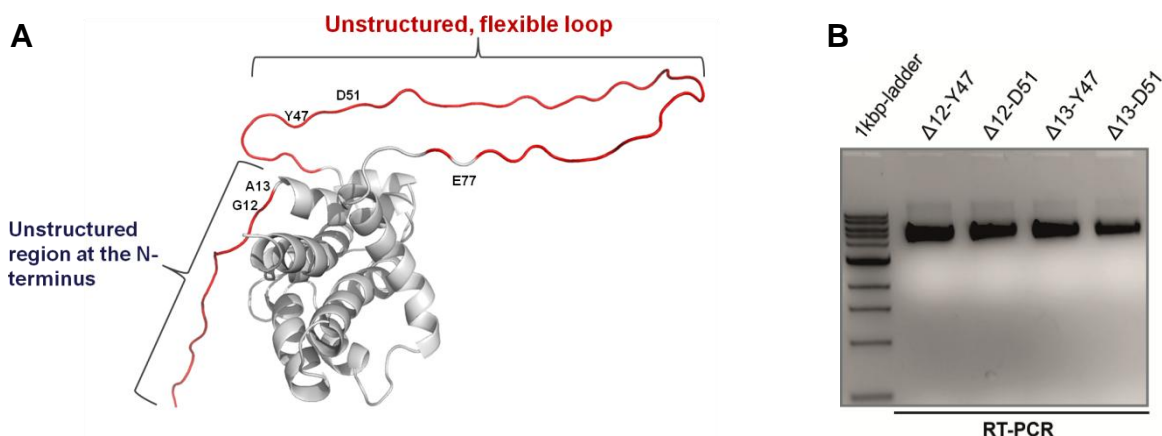


**Figure 41: Strategy for design of novel truncated Bid constructs.**

**A**, Schematic drawing of the NMR solution structure of mouse full-length Bid (PDB entry, 1DDB)<sup>65</sup>, revealing the structure core of Bid in grey and unstructured regions in red. Highlighted amino acids (black) predict the cleavage points for generation of four Bid construct. First cleavage was performed at the N-terminus at either Glycin 12 (G12) or Alanin 13 (A13). Secondly, the loop was cleaved from either Thyrosin 47 (Y47) or Aspartat 51 (D51) up to Glutamate 77 (E77). The combination of both cleavages resulted in four truncated Bid constructs. **B**, PCR analysis confirms successful cloning of the truncated Bid constructs: pGEX  $\Delta 12$ -Y41 (Bid 1), pGEX  $\Delta 12$ -D51 (Bid 2), pGEX  $\Delta 13$ -Y47 (Bid 3) and pGEX  $\Delta 13$ -D51 (Bid 4).

The successful cloning of the N-terminal truncated Bid constructs starting with Glycin 12 or Alanin 13 (designated  $\Delta 12$  and  $\Delta 13$ , respectively) into the pGEX1 $\lambda$ T vector and the removal of the unstructured loop from either Thyrosin Y47 or Aspartat D51 to glutamate 77, was analyzed by PCR (Figure 41 B) and finally confirmed by multiple alignment of the four generated Bid constructs and mouse full-length Bid (Table 65).

**Table 65: Gene alignment of novel Bid constructs and mouse full-length Bid**

Multiple Alignment of Bid constructs		
12	GAEHITDLLVFGFLQSSGCTRQELEVLGRELPVQAYWEADLEDELQTDGSQAS	64
„12-47“	GSGAEHITDLLVFGFLQSSGCTRQELEVLGRELPVQAY-----	
„12-51“	GSGAEHITDLLVFGFLQSSGCTRQELEVLGRELPVQAYWEAD-----	
„13-47“	GS-AEHITDLLVFGFLQSSGCTRQELEVLGRELPVQAY-----	
„13-51“	GS-AEHITDLLVFGFLQSSGCTRQELEVLGRELPVQAYWEAD-----	
65	RSFNQGRIEPDSSESQEEIIHNIARHLAQIGDEMDHNIQPTLVRQLAAQFMNGSLSEEDKR	124
„12-47“	-----SQEEIIHNIARHLAQIGDEMDHNIQPTLVRQLAAQFMNGSLSEEDKR	
„12-51“	-----SQEEIIHNIARHLAQIGDEMDHNIQPTLVRQLAAQFMNGSLSEEDKR	
„13-47“	-----SQEEIIHNIARHLAQIGDEMDHNIQPTLVRQLAAQFMNGSLSEEDKR	
„13-51“	-----SQEEIIHNIARHLAQIGDEMDHNIQPTLVRQLAAQFMNGSLSEEDKR	
125	NCLAKALDEVKTAFFPRDMENDKAMLIMTMLLAKKVASHAPSLLRDVFHTTVNFINQNLFS	184
„12-47“	NCLAKALDEVKTAFFPRDMENDKAMLIMTMLLAKKVASHAPSLLRDVFHTTVNFINQNLFS	
„12-51“	NCLAKALDEVKTAFFPRDMENDKAMLIMTMLLAKKVASHAPSLLRDVFHTTVNFINQNLFS	
„13-47“	NCLAKALDEVKTAFFPRDMENDKAMLIMTMLLAKKVASHAPSLLRDVFHTTVNFINQNLFS	
„13-51“	NCLAKALDEVKTAFFPRDMENDKAMLIMTMLLAKKVASHAPSLLRDVFHTTVNFINQNLFS	
185	YVRNLVRNEMD	195
„12-47“	YVRNLVRNEMD	
„12-51“	YVRNLVRNEMD	
„13-47“	YVRNLVRNEMD	
„13-51“	YVRNLVRNEMD	

### 3.2.5 Effective expression of GST-tagged Bid constructs

As GST-tags positively influence protein solubility and expression efficiency of small proteins, the designed Bid constructs were expressed in *E. coli* as GST-fusion proteins. For evaluation of gene expression, Rosetta2 (DE3) singles were transformed with the respective designed plasmids and protein expression was succeeded 5 h to 19 h after IPTG induction (Figure 42 A, B). Expression tests revealed an increased protein expression from 2 h up to 5 h, while the amount of protein decreased again 19 h after expression induction (Figure 42 A, B). Notably, all four Bid constructs were easily expressed in high amounts, as confirmed by gel-electrophoresis revealing just soluble extracts without purification (Figure 42 A, B). To ensure the maximal yield of protein expression, protocols for expression of the respective Bid constructs were scaled up and bacteria were harvested 4.5-6 h after IPTG induction to avoid deficiencies due to protein degradation.

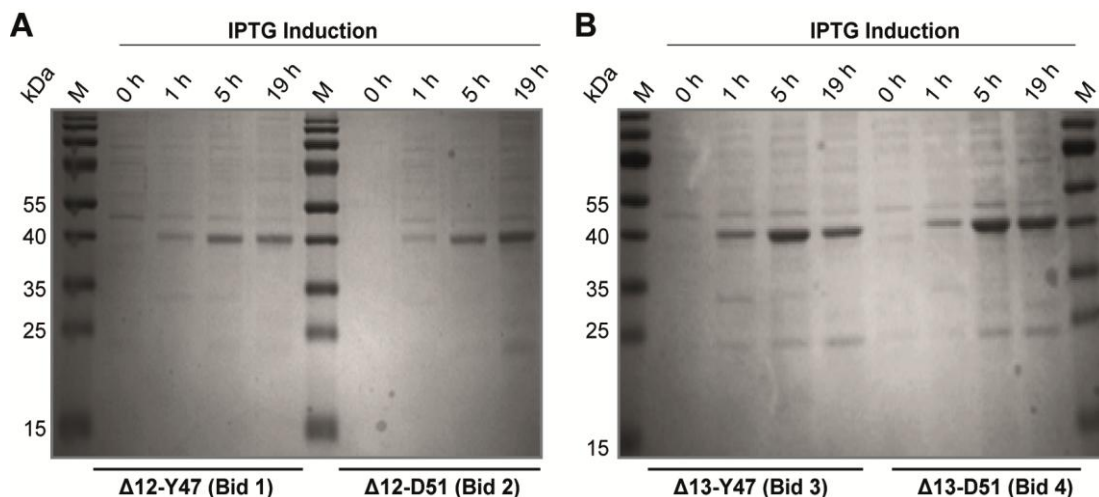


**Figure 42: Effective expression of truncated Bid constructs.**

Effective expression of the truncated Bid constructs was analyzed by expression tests in Rosetta 2 (DE3). *E. coli* were transformed with the respective pGEX-1 $\lambda$ T vector encoding the truncated Bid construct as GST-fusion protein. Samples were taken after 0 h – 19 h after induction of protein expression by 1 M IPTG. Soluble protein fractions were analyzed by gel-electrophoresis followed by coomassie staining. Protein expression of all four Bid constructs was significantly increased from 2 h up to 5 h, while slightly less protein was detected after 19 h bacterial growth. The molecular weight of the GST- tagged constructs is about 40 kDa. Note that the gels show just soluble extracts without purification.

### 3.2.6 Purification of the Bid construct pGEX $\Delta$ 12-Y47 (Bid 1)

The GST-fusion protein pGEX  $\Delta$ 12-Y47 (Bid 1) was highly expressed in Rosetta2 (DE3) and recovered in the soluble protein fraction (TL) 4.5-6 h after IPTG induction, as confirmed by gel-electrophoresis followed by coomassie staining (Figure 43 B (TL)). Purification of pGEX  $\Delta$ 12-Y47 was performed by two chromatography steps using the Äkta prime plus system. GSH-affinity chromatography yielded high amounts of GST-Bid 1, eluted with 10 mM glutathione in the fractions E7-E9 (Figure 43 A, B). Notably, the chromatogram revealed only one clear absorbance peak for Bid 1, already indicating a high purity of the recovered protein (Figure 43 A), which was confirmed by the related SDS-PAGE which estimated a purity of 90-95% (Figure 43 B). Due to this high purity after affinity chromatography the Bid construct was directly subjected to further gel filtration without ion exchange in between. To avoid interference of the relatively large GST-tag (24 kDa) during crystallization, the GST-tag was effectively cleaved using thrombin (3.5 U/ml) as confirmed by gel-electrophoresis revealing the GST-tag at 24 kDa and the pure Bid 1 below (Figure 43 C). The following gel filtration successfully separated the purification-tag from the cleaved Bid 1, as shown by the diverse peaks in the purification run profile (Figure 43 D). Notably, compared to high absorbance up to 500-800 AU for the GST-tagged protein, the Bid 1 absorbance peak shown in the chromatogram (second peak) is relatively small as only a few aromatic amino acids are present in the Bid 1 sequence (Table 65). The related coomassie stained SDS-PAGE confirmed a purity of >98%, enabling the subjection of the batch to crystallization screenings. A final yield of 15-20 mg Bid 1 per liter culture could be obtained (Figure 43 E).

Based on the sequence of the pGEX  $\Delta$ 12-Y47 (Bid 1) construct a molecular mass of 18 kDa (17.626 kDa) was calculated. However, purification SDS-PAGEs revealed the eluted protein between 11 and 15 kDa (Figure 43 C, E). In order to investigate the identity of the construct, the final purification batch was subjected to MALDI-TOF analysis (Figure 44), confirming the actual mass of  $\approx$  18 kDa (17.645 kDa). Markedly, the sample subjected to MALDI-TOF had been stored for a couple of weeks, explaining the appearance of additional peaks that might be due to protein aggregations or reagent adsorptions during purification.

For crystallization studies, the purified Bid 1 construct was concentrated up to concentrations of 9.5-10.5 mg/ml. In particular, the removal of the flexible N-terminus and loop benefitted the concentration procedure, which was more effective compared to the concentrations performed for full-length Bid.

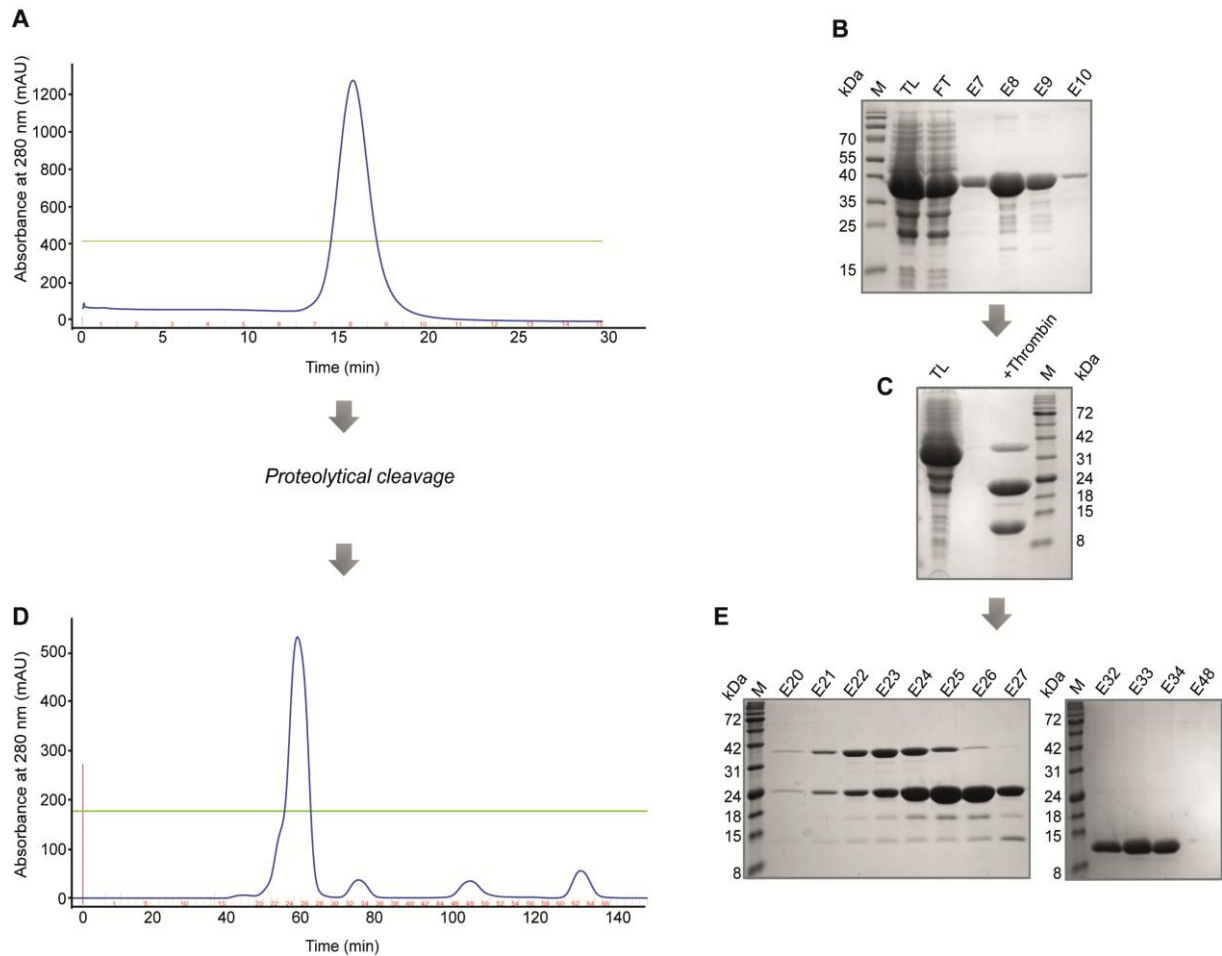


**Figure 43: Purification of Bid 1 (pGEX-Δ12-Y47).**

Bid 1 was expressed as a GST-fusion protein in *E. coli* (Rosetta 2 (DE3)) and recovered in the soluble protein fraction. **A**, GSH-affinity chromatography using the Äkta prime plus system connected to a GSTrap FF column (GE Healthcare). Protein elution was performed with buffer containing 10 mM glutathione. **B**, Coomassie stained 12.5 % SDS-PAGE revealing the analyzed elution fractions within the peak area shown in A (TL = total lysate before purification, FT = flow through, E7-E10 = elution fractions). Fractions E7 to E19 were pooled and subjected to the following thrombin cleavage. **C**, The GST-tagged Bid 1 construct was digested with thrombin (3.5 U/ml) for 16 h at 37°C. The successful removal of the GST-tag was confirmed by 12.5 % gel-electrophoresis and coomassie staining. **D**, Separation of GST-tag and Bid1 by gel filtration. The chromatogram shows 5 peaks, predicting GST-Bid1 fusion protein at 40-50 min. and cleaved GST-tag at 60 min. The cleaved Bid 1 was eluted between 70 min. and 80 min. Other peaks indicate thrombin and PMSF. **E**, Highly pure Bid 1 protein was recovered in elution fractions E32-E34 (second chromatogram peak) as confirmed by 12.5 % coomassie stained SDS-PAGE. Fractions E20-E26 were recovered from the first chromatogram peak predicting GST-Bid1, fractions E26 and E27 show the GST-tag.



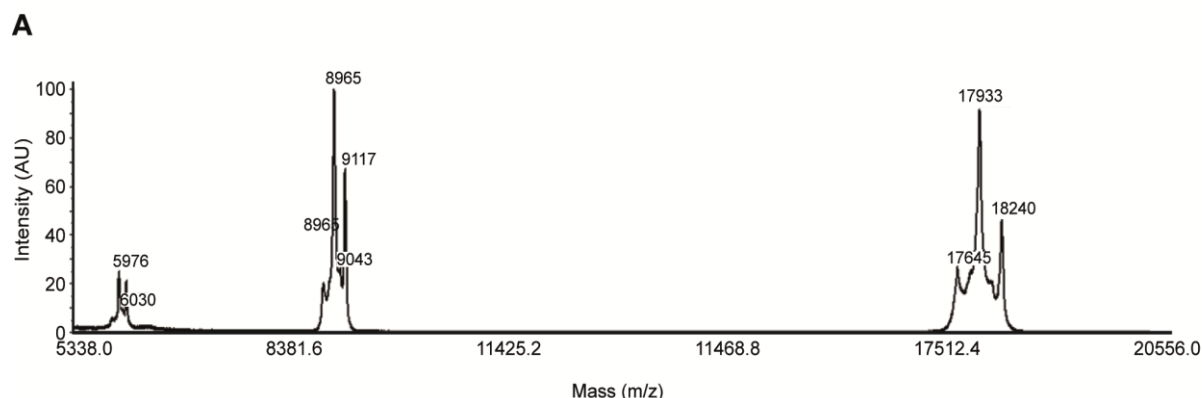


**Figure 44: MALDI-TOF analysis of Bid1 (pGEX- $\Delta$ 12-Y47).**

**A**, Purified Bid 1 was subjected to MALDI-TOF analysis, performed by Jörg Kahnt at the Max-Planck-Institute of Terrestrial Microbiology, Marburg, Germany. The molecular mass of Bid 1 represents 17645 Da in the predicted MALDI-TOF spectrum and fits to the theoretically calculated mass of 17626 Da. Additional peaks in the mass spectrum might be due to storage or glutathione adsorption during purification.

### 3.2.7 Crystallization screening of pGEX $\Delta$ 12-Y47 (Bid 1)

The purified Bid 1 construct was subjected to an extensive crystallization screening at concentrations of 9.5 mg/ml as well as at concentrations of 10.5 mg/ml. Initial crystallization screens were performed as described above (0). As crystallization from solution generally occurs via the sequential steps of nucleation of the phase, destined by the compositions of the solution, followed by growth of the nuclei to larger sizes by incorporation of the solution material<sup>189, 209</sup>, a common method for promoting nucleation is to supplement the protein-reservoir drops with nanoparticles. Therefore, duplicate crystallization screens of Bid 1 were performed in the presence of 2 % nanoparticles. The first crystals of pGEX  $\Delta$ 12-Y47 (Bid 1) were finally obtained upon drop incubation at 277 K after mixing 300 nL protein solution with 300 nL reservoir solution of two different conditions: (a) Cryo suite condition 5, containing 90 mM HEPES pH 7.5, 15 % (V/V) glycerol, 8.5 % (V/V) 2-propanol and 17 % (V/V) PEG 4000 (Figure 45 A), and (b) JCSG+ suite condition 79, consisting of 0.1 M di-sodium succinat pH 7.0 and 15 % (V/V) PEG 3350. (Figure 45 B). While first crystals obtained from condition (a) were observed 20 days after drop incubation showing an increasing growth up to day 35, crystals yielded from condition (b) were debuted on day 9 with an increasing growth up to day 23. Figure 45 shows the continuous growth of crystals obtained from the respective conditions.

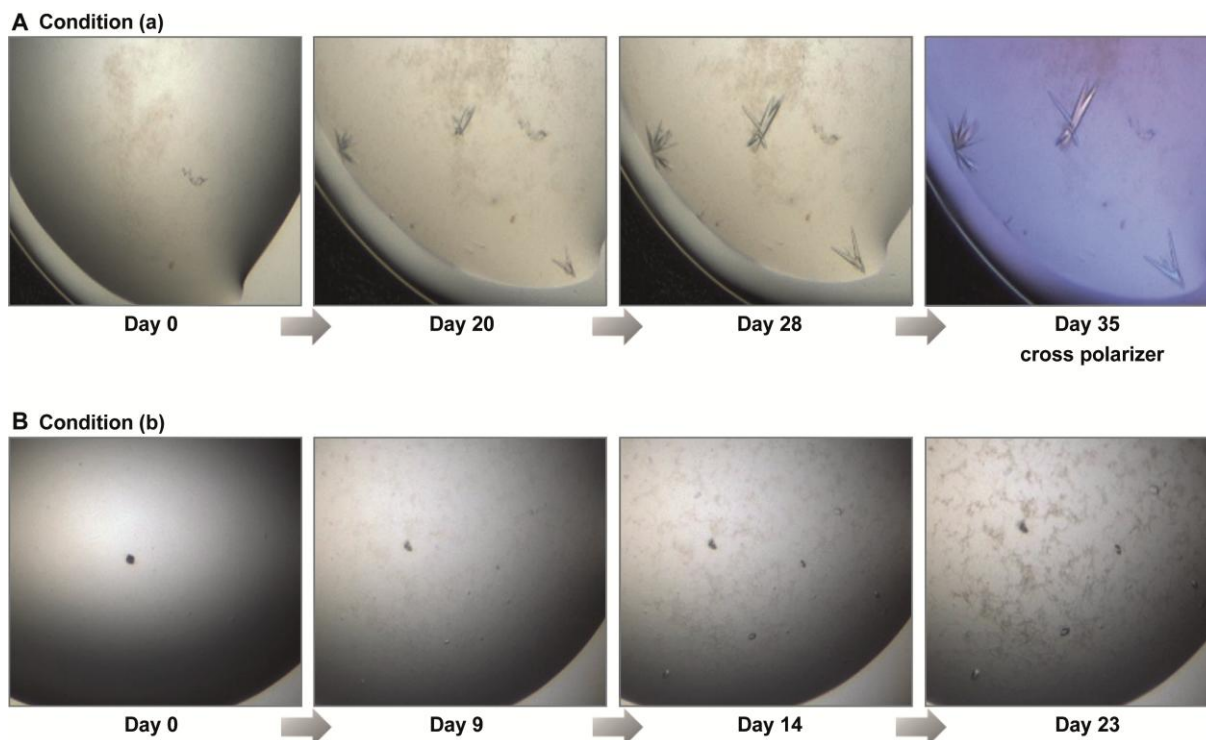


**Figure 45: Successful result of Bid 1 crystallization.**

Highly pure Bid 1 protein (construct  $\Delta 12$ -Y47) was subjected to extensive crystallization screening using the Quiagen NeXtal screening suites. **A**, Successful crystallization was obtained using the cryo suite condition 5, containing. First crystal growth was obtained 90 mM HEPES (pH 7.5), 15 % Glycerol, 8.5 % 2-propanol and 17 % PEG 400020 days after screening start and mounted after 38 days. Cross polarized light was used on day 35 to confirm that the crystal is a protein crystal. **B**, Successful crystallization was obtained using the JCSG+ condition 79, containing 0.1 M di-Sodium succinat (pH 7.5), 15 % PEG 3350. First crystal growth was obtained at day 9 after initial screening set up and a continuous growth was observed up to day 23. Crystals were frozen at day 26.

The relatively slow growth of the crystals as well as their three-dimensional shape strongly indicated protein crystals rather than salt crystals. This was further suggested as the buffer control, always performed in drop 2 (Table 54), obtained no crystal growth. However, as many compounds, not just the protein, can crystallize in the crystallization drop<sup>189</sup>, further tests to distinguish between protein and salt crystals were performed. Both crystals were stainable with methylene blue and physical manipulation using a micro tool indicated a soft and easy breaking behavior of both crystals. These results strongly indicated the presence of a protein crystal as a salt crystal would not be stainable with dyes and would break apart with a snap or crunching sound under the force of a micro tool (2.23.4.3). Additional evidence for the presence of protein crystals was derived from viewing the crystals with polarized light which revealed color effects due to a double refraction of the anisotropic protein crystal as shown for crystal\_11 of the cryo suite condition 5 (Figure 45 A, cross polarizer). However, the only definitive test to confirm the identity as a protein crystal is the X-ray diffraction pattern, which was finally obtained by synchrotron measurements described below for crystals obtained from both conditions (a) and (b).

### 3.2.8 Optimization strategies of Bid 1 crystals

Several optimizations rounds were performed in order to optimize the respective crystallization hit conditions (a) and (b) as described in Table 57 et sqq.. It is worth mentioning that in protein crystal growth, the formation of crystals is often hard to reproduce even by scrupulously following the original conditions<sup>207</sup>. Therefore, optimization experiments were also used to improve the reproducibility of crystal growth in the abovementioned hit conditions. Notably, reproduction and optimization of condition (a) was even more cumbersome than optimizations of condition (b). Figure 46 A predicts a representative result obtained from the cryo suite condition 5 opti-grids, revealing crystals which are larger in length compared to the original hit crystals (Figure 46 A), but with a shape of thin needles (score 7) rather than 3D crystals (score 9). In contrast, optimizations of hit condition (b) succeeded in producing several crystals that were grown in conditions consisting of 0.1 M di-sodium succinat and different concentrations of PEG 3350 in a range of 11 % up to 21 % (V/V), respectively. Although crystal growth was observed in conditions with low pH of 6.5 (Figure 46 B), the preferred pH for crystal growth within these conditions was obviously pH 8.0 revealing the most crystals during optimization (Table 56 et sqq.). In addition to seeding strategies, the abovementioned hit conditions were supplemented with additives using the commercial Additive Screen HT<sup>TM</sup> (Hampton Research) performed in the 96-well format at both temperatures of 4°C and 18°C. Using this approach, crystals were obtained from condition (b) supplemented with 5 % (W/V) n-dodecyl- $\beta$ -D-maltoside (Additive screen condition 72 (F12)), 40 % (V/V) 2,5-hexanediol (mixture of isomers, Additive screen condition 78 (G6)) and 40 % (V/V) formamide (Additive screen condition 89 (H5)).

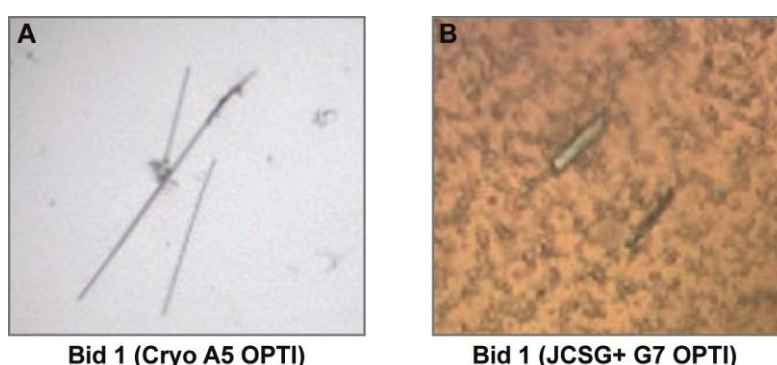


**Figure 46: Bid 1 crystals obtained from opti grid conditions.**

Bid 1 (10.5 mg/ml) was subjected to optimization grids of condition cryo A5 and condition JCSG+ G7. To examples of the obtained crystals are shown. **A**, Bid 1 crystal obtained from cryo opti-grid condition A9 consisting of 90 mM HEPES (pH 7.5), 30 % Glycerol, 21 % 2-propanol and 17 % PEG 4000 at 18°C. **B**, Bid 1 crystal obtained from JCSG+ opti-grid condition A3, consisting of 0.1 M di-Sodium succinat (pH 6.5), 15 % PEG 3350 at 4°C. Of note, further crystals were obtained during optimization of the JCSG+ G7 condition at pH 8 and a range of 11 % to 21 % PEG 3350.

### 3.2.9 Data collection and processing

Crystals obtained for the indicated hit conditions, as well as crystals obtained from the respective optimization grids and additive screens were harvested from mother liquor, frozen in liquid nitrogen in the presence of a cryoprotectant if necessary, and transferred to the synchrotron. Data were collected at 100 K at BESSY II (Helmholtz-Zentrum Berlin, Germany), Beamline 14.1<sup>190</sup> or at PETRA III (DESY, Hamburg, Germany) and processed using XDS<sup>191</sup> as implemented in XDSAPP<sup>192</sup>. From all crystals measured, the best results were recorded for crystals obtained from the original hit conditions (a) and (b). Figure 47 reveals the typical diffraction pattern obtained throughout data collection on the respective Bid 1 crystals shown above and recorded at BESSY II under cryoconditions. Although crystals obtained from condition (a) were the larger and better-looking crystals, best data were produced from the smaller and 'uglier' crystals of condition (b) as in line with plenty of reports mentioning that the best data are often derived from the most unimpressive crystal shapes<sup>189, 207, 209</sup>. Table 66 depicts the results of data processing for the most promising data collection that was obtained for Bid 1 crystal\_11 derived from the abovementioned condition (b). Indexing of the initial diffraction data revealed unit cell constants as expected for crystals of this protein size. Data processing suggests a crystal form in space group C222<sub>1</sub> with two monomers per asymmetric unit, as indicated by the Matthews coefficient of 2.2 Å<sup>3</sup>/Da and an estimated solvent content of 44.1%.

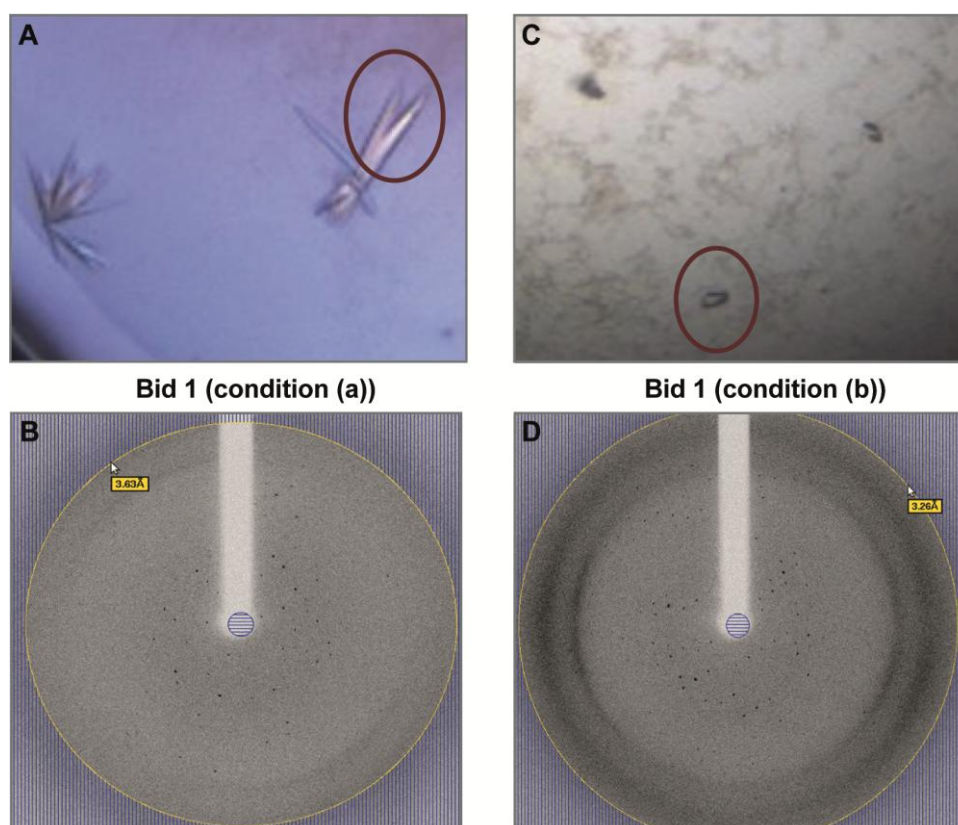


**Figure 47: Bid 1 crystals used for data collection and typical diffraction pattern**

The Bid 1 crystals, obtained by initial crystal screening for Bid 1 (10 mg/ml) and grown in condition 5 from cryo suite (A) an appropriate 79 from JCSG+ suite (B) were frozen in liquid nitrogen and transferred to the synchrotron. B, D, Typical diffraction pattern obtained throughout data collection on the respective Bid 1 crystals shown above and recorded at BESSY II. Crystal A: 3.63 Å, Crystal B: 3.28Å.

Despite extensive molecular replacement (MR) trials using Phaser<sup>193</sup> with search models from various sources, such as Bid NMR structures obtained from the PDB (PDB entry, 1DDB, 2BID), homology models and poly-Ala models with different domain boundaries, no unique MR solution could be identified so far, implying a preliminary status to the space group assignments given in Table 66. Data indexing and molecular replacement trials were performed by Holger Steuber (LOEWE Center of Synthetic Microbiology (SYNMICRO), University of Marburg).

**Table 66: Statistics for data collection and processing for Bid 1.**

Crystal Bid\_11 was obtained from JCSG+ suite, condition 79

Data collection and processing	Crystal Bid_11
Radiation Source	Bessy MX 14.1
No. of crystals used	1
Wavelength [Å]	0.91841
possible Space group	C222/C222(1)
Unit cell parameters	
a, b, c [Å]	63.4; 128.2; 78.0
$\alpha$ , $\beta$ , $\gamma$ [°]	90 ; 90 ; 90
Matthews coefficient [Å <sup>3</sup> /Da]	2.2
Solvent content [%]	44.1
Diffraction data	
Resolution range [Å]	22.0 – 3.75 (3.95-3.75)
Unique reflections	3 442 (487)
R(I) <sub>sym</sub> [%]	15.9 (61.3)
Completeness [%]	99.4 (100.0)
Redundancy	6.3 (6.5)
I/σ(I)	12.7 (3.5)



### 3.2.10 Purification and crystallization of pGEX $\Delta$ 12-D51 (Bid 2) and pGEX $\Delta$ 13-D51 (Bid 4)

The Bid constructs pGEX  $\Delta$ 12-D51 (Bid 2) and pGEX  $\Delta$ 13-D51 (Bid 4) were analogously expressed as GST-fusion proteins in Rosetta2 (DE3) and purified using the optimized and scaled up expression and purification protocol for construct pGEX  $\Delta$ 12-Y41 (Bid 1), with minor changes. Figure 48 reveals the purification profiles and related SDS-PAGEs for purification of the Bid 2 construct. Gel-electrophoresis of the bacterial total lysate (TL, Figure 48 B) confirmed the recovery of Bid 2 in the soluble protein fraction and the high purity of the construct achieved by elution during GSH-affinity purification (Figure 48 B (E)). The subsequent cleavage of the GST-tag was further improved by the use of 1 U thrombin (Novagen) per mg protein succeeding in a complete removal of the purification-tag (Figure 48 B, (+thrombin)). The final gel filtration yielded large quantities of Bid 2 (20 mg protein per liter culture) with a high purity of > 98 % (Figure 48 C, D). Bid 2 containing fractions were pooled, concentration and subjected to the crystallization approach.

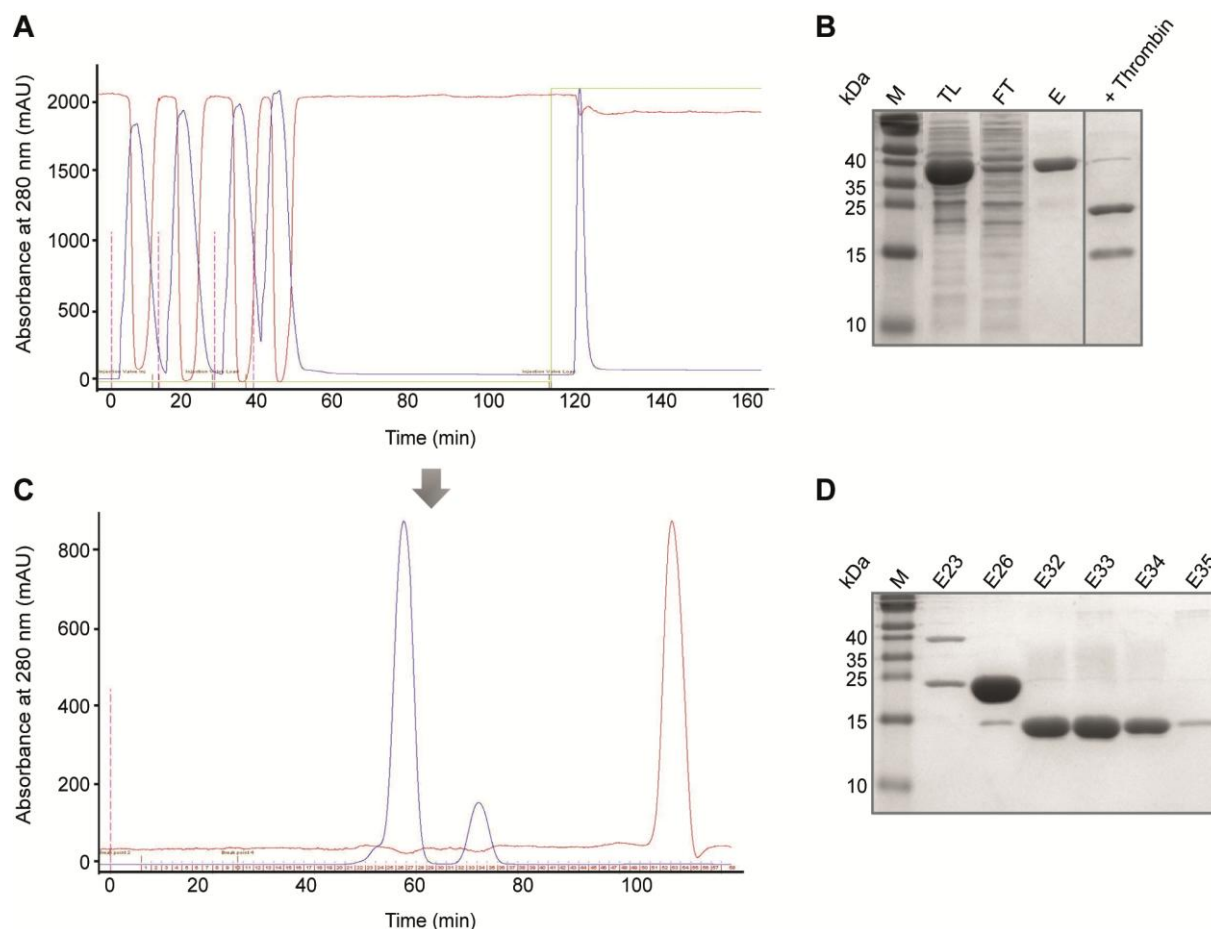


**Figure 48: Purification of Bid 2 (pGEX- $\Delta$ 12-D51).**

The fusion protein GST-Bid 2 was successfully expressed in *E. coli* (Rosetta 2 (DE3)) after IPTG induction for 4.5 h. **A**, GSH-Affinity chromatography of Bid 2 was performed using a glutathione HiCap Cartridge. 20 ml of Bid 2 protein lysate was injected four times via a 5 ml sample loop. Elution of the protein was performed with buffer

containing 10 mM glutathione. **B**, The purity of the elution fraction (peak area) was confirmed by 12.5 % gel-electrophoresis and coomassie staining. Note that the elution fraction reveals already pure protein compared to the total lysate (TL) before purification and flow through (FT). For removal of the GST-tag, the recovered elution fraction, containing 22 mg protein, was supplemented with 22 U thrombin (+ Thrombin) and incubated for 16 h at 37°C. Notably, the cleavage of the GST-tag was almost completely. **C**, To separate the cleaved GST and to yield highly pure protein, gel filtration was performed and the pure protein eluted in 20 mM Tris, 50 mM NaCl buffer (pH 7.4). **D**, The elution fractions within the peak area predicted in the gel filtration chromatogram (C) were analyzed by 12.5 % SDS-PAGE. While elution fraction 26 (E26) contains the GST-tag, pure Bid 2 protein was recovered in the fractions E32-E35.

The high purity and integrity of pGEX  $\Delta$ 12-D51 (Bid 2) indicated by the clear and improved chromatography profile (Figure 48), was further confirmed by MALDI-TOF analysis, revealing only one peak at the expected molecular mass of 18 kDa (Figure 49).

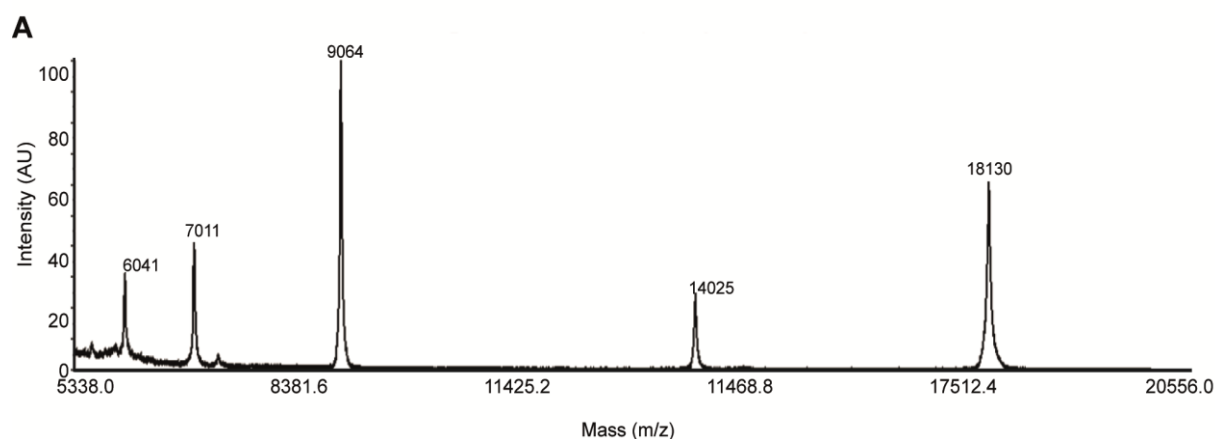


**Figure 49: MALDI-TOF analysis of purified Bid 2 (pGEX- $\Delta$ 12-D51).**

Purified Bid 2 was subjected to MALDI-TOF analysis, performed by Jörg Kahnt at the Max-Planck-Institute of Terrestrial Microbiology, Marburg, Germany. The molecular mass of Bid 2 represents 18130 Da in the predicted MALDI-TOF spectrum as expected by theoretically calculated mass of 18127 Da. Note, that the well defined peak, indicating highly pure and intact Bid 2 protein.

Finally, the pGEX  $\Delta$ 13-D51 (Bid 4) construct was subjected to the described purification procedure, as shown in Figure 50. Notably, gel electrophoresis after GSH-affinity chromatography revealed a relatively high amount of Bid 4 in the flow through fractions (FT, FT2, Figure 50 B), indicating an even more pronounced high-yield expression of this construct compared to construct Bid 2. This was confirmed by determining the protein amount after the first purification step, predicting a mentionable yield of 86 mg protein per 1.2 liter bacterial culture. Admittedly, cleavage of the GST-tag was probably not completely due to undercharged amounts of thrombin (Figure 50 C). Nevertheless, the fractions that revealed Bid 4 completely separated from the GST-tag (E31-E35, Figure 50 D) contained high amounts of pure Bid 4 protein (> 98%), that could be concentrated up to values of

15.2 mg/ml. The following MALDI-TOF analysis confirmed the molecular mass of 18 kDa for Bid 4, although additional peaks at higher values (18.381 kDa and 18.689 kDa) were observed and might indicate a contamination with remains of GST-Bid 4 fusion protein (Figure 51).

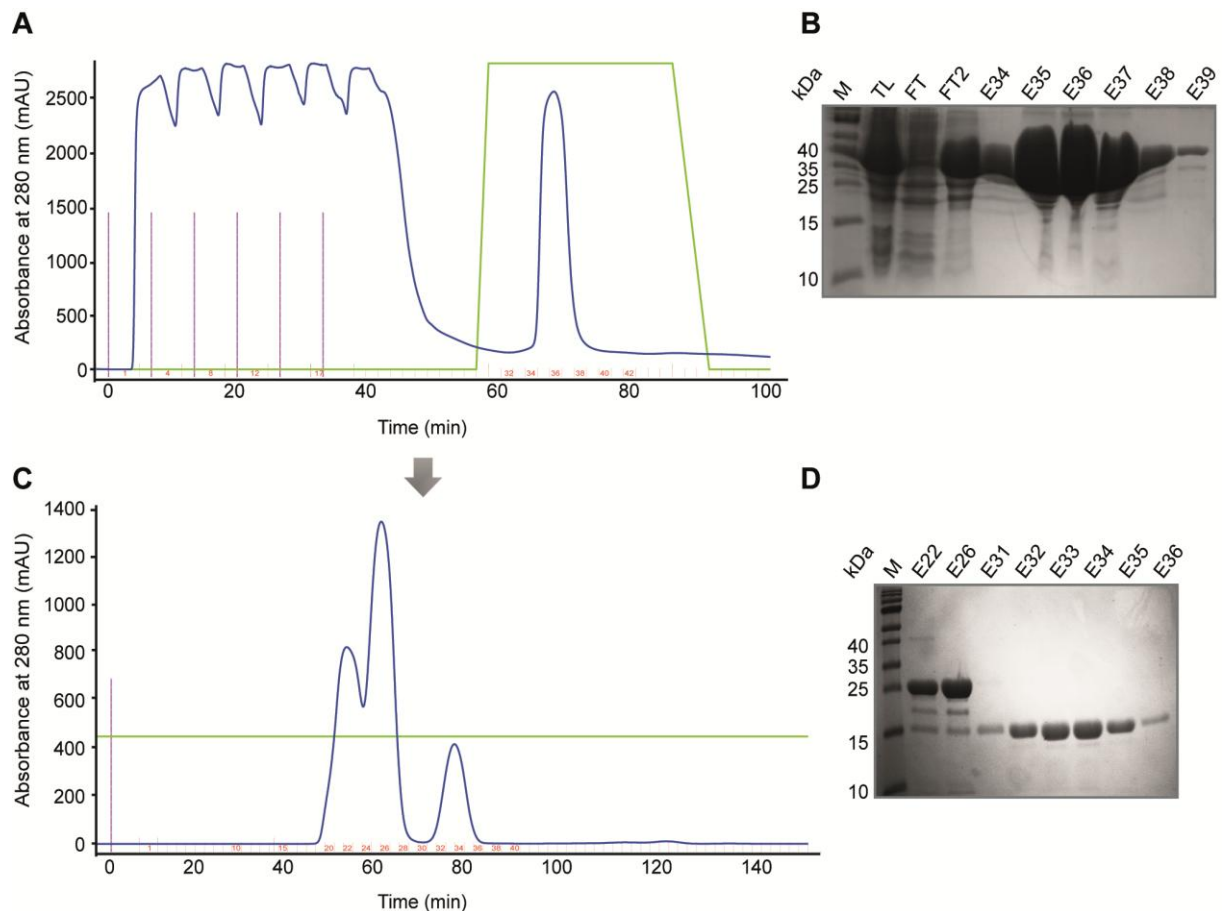


**Figure 50: Purification of highly pure Bid 4 protein (pGEX-Δ13-D51).**

Bid 4 was expressed as a GST-fusion protein in *E. coli* (Rosetta 2 (DE3)) and recovered in the soluble protein fraction. **A**, GSH-affinity chromatography. 25 ml of protein solution was loaded and protein elution was performed with buffer containing 10 mM glutathione. **B**, Coomassie stained 12.5 % SDS-PAGE (TL = total lysate before purification, FT = flow through, flow through end method, E34-E39 = elution fractions). The fractions E34-E39 were pooled, containing 7.2 mg/ml pure protein (total amount 86 mg). Note that FT2 contains high amounts of Bid 4, indicating that the binding capacity of the column was exceeded. **C**, The GST-tagged Bid 2 construct was digested with thrombin (Novagen) for 16 h at 37°C. Separation of GST-tag and Bid 4 was achieved by gel filtration. The chromatogram shows 3 peaks, predicting GST-Bid 4 fusion protein at 50-60 min. and cleaved GST-tag at 60 min. The cleaved Bid 4 was recovered in the elution fractions E31-E36. **D**, Gel-electrophoresis confirms the purity of Bid 4 in elution fractions E31-E36. Fractions E22 and E26 were recovered from the first chromatogram peak predicting the GST-tag.



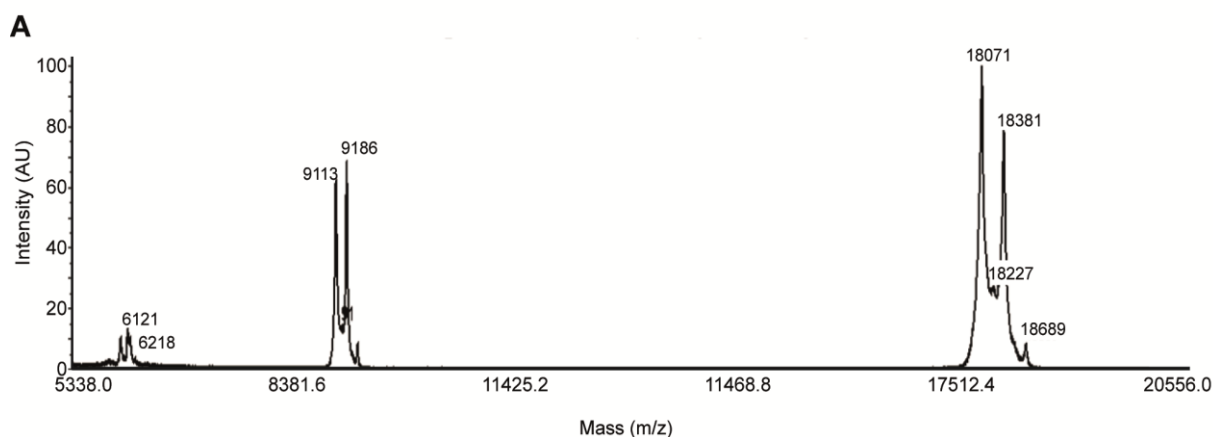


**Figure 51: MALDI-TOF analysis of purified Bid 4 (pGEX- $\Delta$ 13-D51).**

Purified Bid 4 was subjected to MALDI-TOF analysis, performed by Jörg Kahnt at the Max-Planck-Institute of Terrestrial Microbiology, Marburg, Germany. The molecular mass of Bid 4 represents 18071 Da in the predicted MALDI-TOF spectrum as expected by theoretically calculated mass of 18070 Da. The protein sample might contain remains of GST-Bid 4 fusion protein as indicated by the peak with the mass 18381 Da.

Constructs pGEX  $\Delta$ 12-D51 (Bid 2) and pGEX  $\Delta$ 13-D51 (Bid 4) were analogously subjected to the abovementioned crystallization screenings at a concentration of 8.5 mg/ml for Bid 2 and at concentrations of 10.0 mg/ml and 15.5 mg/ml for Bid 4. The tested screening suites are quoted in Table 54. So far no crystals suitable for X-ray diffraction were obtained for any of the construct Bid 2 and Bid 4. As crystallization screenings are still ongoing only some tendencies can be mentioned up to date. Both constructs immediately precipitate if ions such as cadmium or zinc are present in the crystallization screening conditions, as it was similarly observed for full-length Bid and construct Bid 1. Promising conditions observed for Bid 2 were conditions 14, 38 and 58 from the JCSG+ suite and conditions 38, 39 and 61 from the JSCG core I suite. Crystallization screens performed for Bid 4 obtained similar results, but with a more pronounced tendency for precipitations and phase separations. In general, more promising results were observed when crystallization screening was performed at 18°C compared to the drop results obtained at 4°C. Further screenings and optimizations have to be conducted to improve the crystallization of both constructs.

### 3.2.11 Functional analysis of Bid constructs in HT-22 cells

It is well accepted, that the pro-apoptotic activity of Bid is mainly mediated by its truncated active form tBid<sup>61, 66, 173</sup>, rapidly accumulating at the mitochondrial membrane and initiating cytochrome c release and cell death. As described above, beside the caspase-8 mediated cleavage of full-length Bid, cleavage can also be mediated by granzyme B, calpains or cathepsins that all cleave Bid in the unstructured loop region between helices  $\alpha 1$  and  $\alpha 2$ <sup>60, 61, 74, 76, 212</sup>. Since the Bid constructs Bid 1-Bid 4 lack the flexible loop region, a cleavage mediated by any of the abovementioned proteases is unlikely and thereby a pro-apoptotic function of the novel Bid constructs is not expected. However, a death-promoting nature of full-length Bid was also reported by previous studies, showing that apoptosis could be induced by over-expression of full-length Bid<sup>55</sup> or a Bid mutant lacking the caspase-8 cleavage site<sup>213</sup>. Furthermore, it has been described that the N-terminal sequence of Bid ensures its cytoplasmic localization and negatively regulates the binding of Bid to membranes thereby inhibiting the exposure of the BH3 region and its apoptotic function<sup>61</sup>. To investigate, if the designed Bid constructs, that lack the first 12 and accordingly 13 amino acids of the N-terminus, procure a pro-apoptotic activity in cellular systems, over-expression of the respective constructs was examined in the present HT-22 cell line. To this aim, the constructs were cloned into the pcDNA3.1 vector suitable for expression in eukaryotic cells (2.14.4.1). In accordance to the tBid-toxicity assay, HT-22 cells were transfected with the plasmids encoding the sequence of the truncated Bid construct 3 and 4, respectively, and cell viability was analyzed 24 h to 48 h after over-expression. To compare the toxic or non-toxic activity of Bid 3 and Bid 4 with the tBid-induced cell death features, controls were transfected with the tBid-encoding plasmid as outlined above. Photomicrographs revealed that any of the truncated Bid constructs induced alterations in cell morphology, as they were observed in tBid-over-expressing HT-22 cells (Figure 52 A). Cells over-expressing  $\Delta 13$ -Y47 and  $\Delta 13$ -D51, respectively, retained the normal spindle-shaped morphology comparable to pcDNA3.1 transfected cells (Figure 52 A). Quantification of cell viability determined by MTT assay, confirmed that none of the both constructs induced cell death in HT-22 cells, indicating a “full-length Bid like behavior” of  $\Delta 13$ -Y47 and  $\Delta 13$ -D51 rather than a tBid-like function when over-expressed in HT-22 cells.

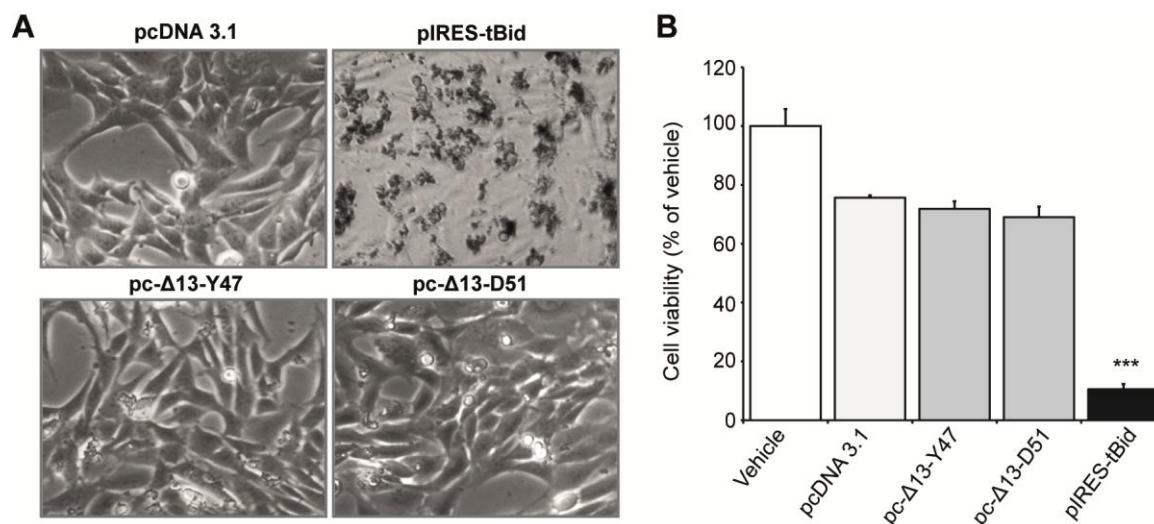


**Figure 52: Functional analysis of Bid constructs.**

HT-22 cells were transfected with a plasmid containing either Bid 3 sequence (pc-Δ13-Y47) or the Bid 4 sequence (pc-Δ13-D51). Controls were treated with attractene only (vehicle) or transfected with an empty control vector (pcDNA3.1). Transfection of cells with the tBid-encoding plasmid (pIRES-tBid) was used as positive control for tBid-induced toxicity. **A**, Cell morphology was analyzed by microscopy. Photomicrographs show the typical phenotype of tBid-induced cell death in cells transfected with the pIRES-tBid vector, but no alterations in cells transfected with the truncated Bid constructs, comparable to control pc-DNA3.1. **B**, Cell viability was analyzed by MTT assay 48 h after over-expression of the respective Bid constructs. Note that cell viability is not affected by any of the novel truncated Bid constructs (Bid 3 and Bid 4), yet significantly decreased by over-expression of tBid.

To summarize, the work above provides the basis for a suitable pipeline for Bid construct design, cloning, expression up to protein purification and first Bid crystallization approaches. Protocols for recombinant expression and purification were optimized and scaled up not only for full-length Bid, but also for diverse truncated Bid constructs, yielding high amounts of 15-50 mg Bid variant per liter culture, depending on the respective Bid variant. The pure protein batches were subjected to extensive crystallization screenings, including initial screens using 1300 different crystallization conditions at two temperatures respectively, as well as several optimization strategies such as opti-grids, seeding or additive screenings. The construct Δ12-Y47 (Bid 1) was successfully crystallized and yielded diffraction data of 3.75 to 3.95 Å resolution under X-ray exposure at the BESSY II synchrotron. In addition, constructs Δ12-D51 (Bid 2) and Δ13-D51 (Bid 4) also promise successful crystallization, although further optimizations have to be performed with both Bid variants. Lastly, the constructs were over-expressed in the HT-22 cell line confirming the non-apoptotic function of the truncated variants as expected from the structural modifications. Further optimizations of crystallization and diffraction properties of the Bid crystals, which were obtained during this work, promise a successful structure determination of Bid as an indispensable tool for a deeper understanding of the molecular mechanisms of Bid and the further structure-guided development of Bid-targeting compounds.

### **3.3 Functional analysis of recombinant Bid and Bax – a model system for membrane permeabilization**

Although previous studies demonstrated that Bid mediates apoptotic cell death via detrimental effects at the mitochondrial membranes<sup>24, 63, 97</sup>, the precise mechanism by which Bid or tBid trigger MOMP is still not fully understood. Several studies point to the caspase 8 cleaved C-terminal fragment t<sup>c</sup>Bid as the pro-apoptotic form with activity for membrane binding and permeabilization<sup>69, 214</sup> and suggest a tBid-mediated Bax activation and subsequent MOMP<sup>69, 71, 77, 82, 215-219</sup>. A well accepted tool for investigating the pore-forming abilities of diverse proteins is the use of artificial lipid bilayer structures which mimic the mitochondrial membrane<sup>69, 72, 77, 82, 218, 219</sup>. To investigate the effect of the newly synthesized recombinant Bid and caspase-8 cleaved cBid on lipid membranes, in the presence and absence of recombinant Bax, continuing work included the validation of a model systems for membrane permeabilization, namely the liposome channel activity assay (3.3.1). The system was further used to examine the role of cardiolipin (CL) in Bid-mediated membrane permeabilization as many previous reports suggest CL as mitochondrial receptor for Bid<sup>77, 220-225</sup>.

#### **3.3.1 Liposome channel activity demonstrates cBid- and Bax-mediated membrane permeabilization to be dependent on the presence of cardiolipin**

To investigate the effect of Bid and Bax on artificial membranes, 5,6-carboxyfluorescence-containing liposomes were prepared using phosphatidylcholin (PC) and phosphatidylethanolamine (PE) as the most abundant lipids of the mitochondrial outer membrane (MOM). For investigation of the role of cardiolipin, PC/PE liposomes were compared to liposomes containing CL in addition. For baseline fluorescence, liposomes were initially measured at RT without the addition of proteins for 3-5 min. To rule out unspecific destabilization effects caused by protein buffer compositions, buffer containing 20 mM Tris (ph 7.4), 50 mM NaCl was added to act as a 0 % CF-release control (Figure 53 A), while the addition of Triton X-100 was used to induce 100 % CF release (Figure 53 B). Liposome stability as well as permeabilization ability was further investigated over a period of 60 min. (Figure 53 C), revealing that no CF was released in the absence of Triton X or when liposomes were just measured in PBS without compound addition, indicating that the system is suitable for investigating the pore-forming abilities of the recombinant proteins Bid and Bax.

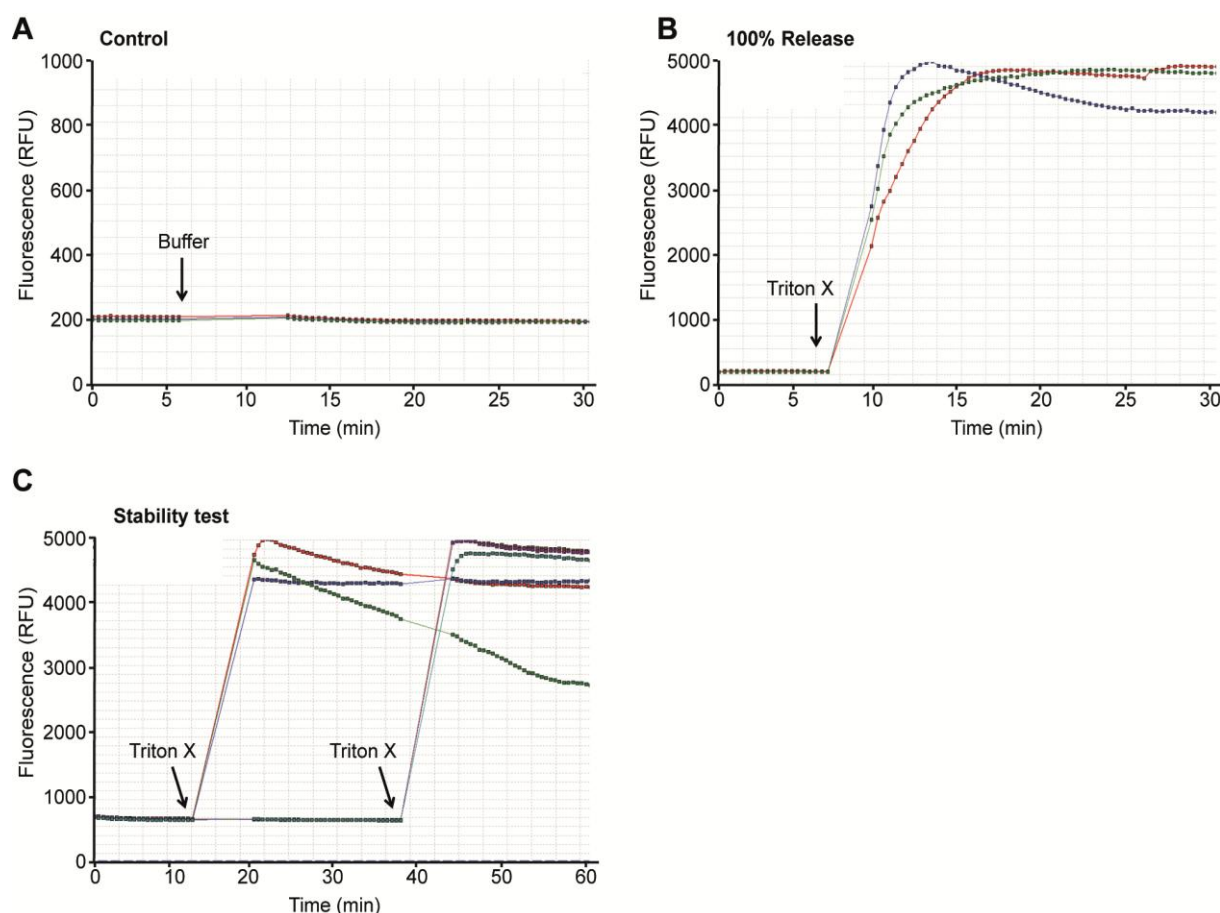


**Figure 53: Liposome channel activity assay as model system for membrane permeabilization.**

Liposomes with a lipid composition of phosphatidylcholin (PC), phosphatidylethanolamin (PE) and cardiolipin (CL) (PC/PE/CL: 54/20/26) stained with 1 % rhodamine DHPE and containing 20 mM 5,6 carboxyfluorescein (CF) were incubated in PBS and measured at RT without proteins. **A**, **B**, Change in fluorescence was measured over time after addition of H<sub>2</sub>O as negative control (**A**) or addition of 4% Triton-X as positive control for 100 % CF-release (**B**). **C**, Stability of liposomes was determined over 60 min and 4 % Triton-X was added 12 min and 40 min after initial measurement, respectively, revealing 100 % CF-release in both cases. Note the stability of liposomes after addition of H<sub>2</sub>O (**A**) and without any addition of Triton-X (**C**). Experiments show a measurement with n=3 (blue, green, red line, respectively) as a representative series of five independent measurements.

As mentioned above, cleavage of full-length Bid is necessary for induction of its apoptotic function. In order to simulate the activation of Bid by caspase 8 and thereby to compare the pore-forming or membrane destabilizing abilities of full-length Bid and cleaved Bid, purified full-length Bid was modified through proteolysis by recombinant caspase 8 (Figure 53 A-C). Full-length Bid was already efficiently cleaved 0.5 h after caspase 8 incubation, as confirmed by gel-electrophoresis followed by coomassie staining (Figure 53 A) and western blot analysis (Figure 53 B), revealing the C-terminal fragment ( $t^c$  Bid) and the 6.5 kDa N-terminal fragment ( $t^n$  Bid). As both,  $c$ Bid and  $t$ Bid are described to be pro-apoptotic and have been used in recently published mechanistic studies<sup>72, 77, 221</sup>, the following experiments were performed using  $c$ Bid, without octylglucoside-mediated dissociation of the  $t^c$ Bid and  $t^n$ Bid fragment. The purity and integrity of the cleaved Bid samples S1 and S2 used for these studies was confirmed by gel-electrophoresis as shown in Figure 53 C.

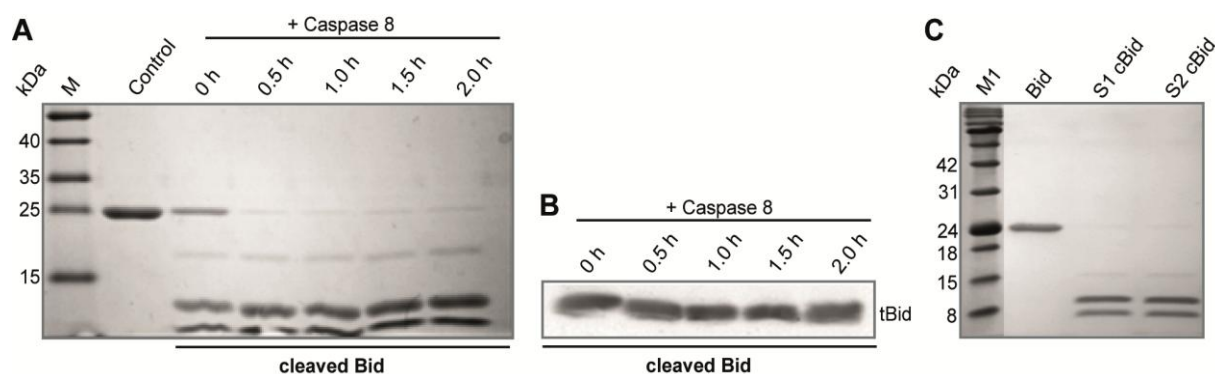


**Figure 54: Cleavage of full-length Bid with caspase 8.**

Purified recombinant full-length was cleaved with recombinant caspase 8 to obtain cleaved Bid (cBid). **A**, Recombinant Bid in 20 mM TRis (pH 7.4), 50 mM NaCl was diluted 1:1 with caspase-cutting buffer (50 mM HEPES (pH 7.5), 100 mM NaCl, 1 mM EDTA, 10 mM DTT, 10 % sucrose) and incubated with caspase 8 (7.6 mg/ml) at RT. To determine the cutting efficiency, samples were taken at the indicated time points between 0 h and 2 h after caspase 8 incubation and analyzed by 12.5 % SDS-PAGE followed by coomassie staining. Complete cleavage was obtained already after 0.5 h. Control predicts full-length Bid without caspase 8 addition. **B**, western blot analysis confirms the successful production of tBid. **C**, Coomassie stained 12.5 % SDS-PAGE confirms the complete cleavage of full-length Bid 1.5 h after caspase 8 incubation. S1 and S2 indicate two different samples of cleaved Bid (cBid) that were used for membrane permeabilization assays.

As cleaved Bid has been described as the protein with the more pronounced permeabilizing properties especially in the presence of CL, the effect of cBid was initially analyzed by adding increasing concentrations of cBid to cardiolipin-containing liposomes filled with 20 mM of CF. Upon protein addition, a clear concentration dependence of permeabilization rates for cBid could be detected (Figure 55 A). While no release of CF was observed using 10 nM of cBid, high concentrations of 6  $\mu$ M increased the fluorescence values even though in slow kinetics (Figure 55 A). Of note, the cBid mediated fluorescence release did not reach 100 % compared to the Triton X release (Figure 55 B), resulting in an undervaluation of the liposome permeabilization. Experiments performed in parallel revealed a further increase in CF-release due to post-treatment of liposomes with Triton X. This is in line with recent reports observing similar results, when comparing the tBid- and cBid-induced fluorescence release to detergent-solubilization of liposomes<sup>72</sup>. As these results revealed the dose-dependent membrane permeabilization mediated by cBid, the next step was to examine if the pore-forming ability of cBid is dependent on the presence of cardiolipin. In contrast to the reproducible CF-releasing effect of cBid on liposomes containing cardiolipin (Figure 55 C), no change in fluorescence was recorded when cBid was added to CF-incorporated liposomes lacking cardiolipin (Figure 55 B), confirming the previous reported importance of the phospholipid for Bid-mediated liposome permeabilization<sup>77, 91, 219</sup>. While these results revealed that cleaved Bid itself was able to induce CF release of liposomes at a concentration above 100 nM, full-length Bid showed no membrane destabilizing properties



as no change in fluorescence could be recorded after subjection of full-length Bid to the liposome channel activity assay (Figure 55 D, E). Notably, the absence of CF-release after Bid addition was independent of the presence or absence of cardiolipin (Figure 55 D, E).

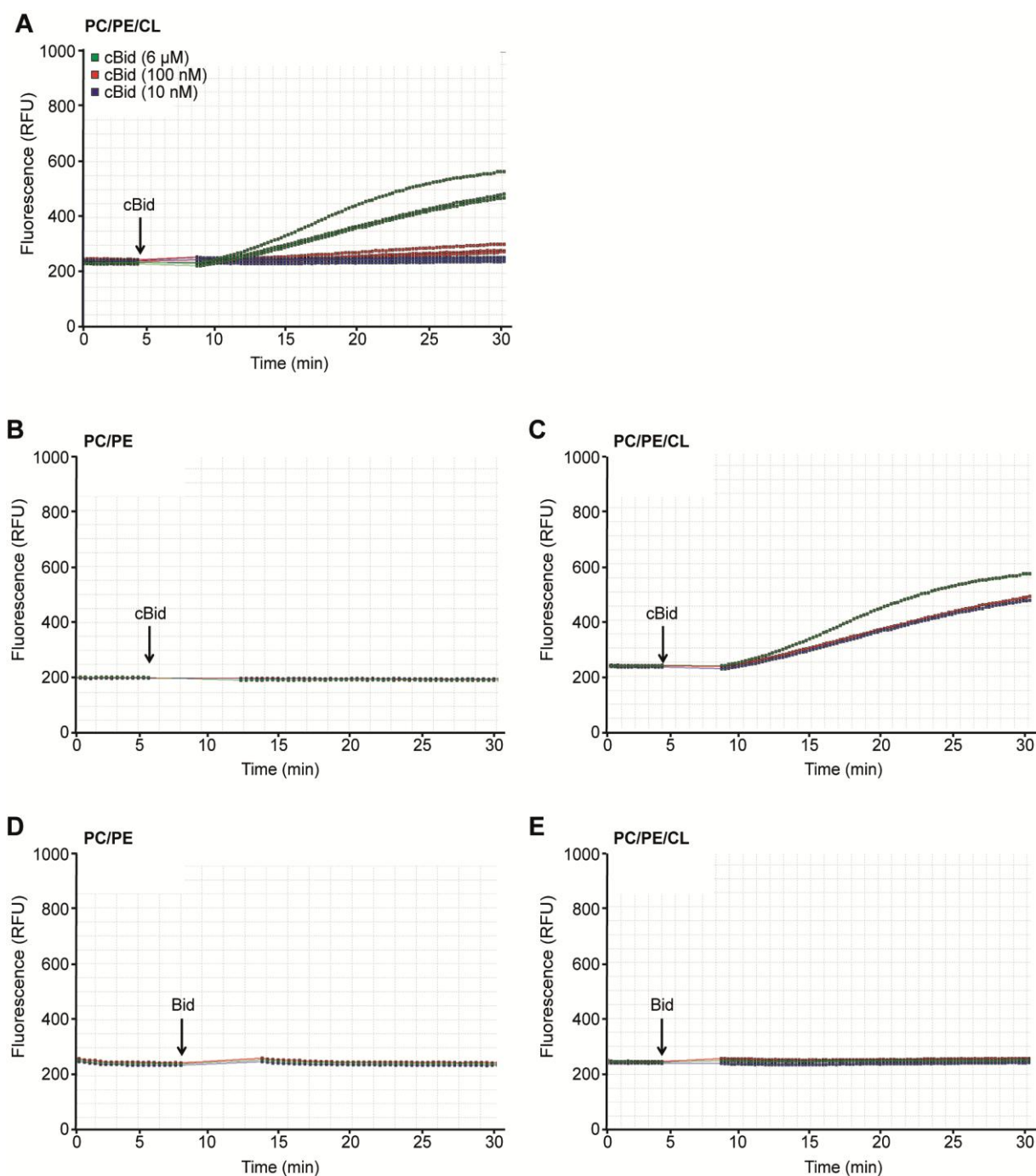


**Figure 55: Permeabilization of cardiolipin-containing liposomes is induced by Bid in a concentration dependent manner, but not by full-length Bid.**

CF-containing liposomes with a lipid composition of PC/PE/CL: 54/20/26 were compared to liposomes lacking cardiolipin (CL) with a composition of PC/PE of 80/20. Both liposomes were stained with 1 % rhodamine DHPE, diluted in PBS and measured at RT for 3-5 min prior to protein addition. **A**, After addition of caspase 8 cleaved cBid in concentrations of 10 nM, 100 nM and 6  $\mu$ M, change in fluorescence was measured over time. While 10 nM of cBid was not sufficient to release CF and 100 nM showed slight increases in fluorescence, high concentrations of 6  $\mu$ M increased fluorescence up to 600 RFU. **B**, cBid (6 $\mu$ M) was added to PC/PE liposomes lacking cardiolipin and fluorescence was measured at RT for further 25 min. No release of CF was detected. **C**,

Addition of cBid (6 $\mu$ M) to cardiolipin-containing induced the release of CF as indicated by increase in fluorescence. **D, E**, Addition of full-length Bid (6 $\mu$ M) to CF-liposomes containing PC and PE (**D**) and CF-liposomes containing cardiolipin in addition (**E**) did not induce release of CF as indicated by stable values of fluorescence. All experiments were performed with n=3 independent prepared liposome (green, blue, red line, respectively) samples and present a representative series of measurements from three independent experiments. cBid, caspase 8 cleaved Bid without dissociation of the t<sup>c</sup>Bid and t<sup>o</sup>Bid fragment.

Since several previous reports described a Bax-induced lipidic pore formation that is accelerated by tBid<sup>71, 72, 77, 82, 91, 217-219, 225</sup>, the effect of recombinant Bax was examined on both, PC/PE- and PC/PE/CL-liposomes. In line with the abovementioned reports, no CF release was observed when Bax (100-500 nM) was added alone to the liposomes (Figure 56 A, B). Intriguingly, post-addition of cBid to the Bax-liposome mixture had no effect on the liposome stability (Figure 56 A, B), while fluorescence release was clearly increased when both proteins, Bax and cBid, were pre-incubated prior to co-addition to the liposomes (Figure 56 C). These results indicate that either both proteins have to interact before recruitment to membranes, or that the sequential arrangement of cBid- and Bax- membrane association is essential for the subsequent permeabilization. The effects of the recombinant proteins Bid, cBid and Bax on lipid membranes obtained by the fluorescent liposome preparations were confirmed by preliminary data revealing the pore forming properties of cBid and Bax on CL-containing black lipid membranes (BLMs) produced by the Ionovation Compact system and measured by the Ionovation GmbH, Osnabrück, Germany.

In order to examine, if the established liposome channel activity assay is a suitable system for testing the direct inhibitory effects of the Bid inhibitors, preliminary experiments were performed using the available Bid inhibitor BI-6c9 (Figure 56 D). As the cBid/Bax mixture induced the most prominent CF release of cardiolipin-containing liposomes, this set up was chosen to test the effect of BI-6c9 (10  $\mu$ M). Although BI-6c9 is well established to sufficiently inhibit Bid, addition of this inhibitor to the cBid/Bax mixture prior to co-addition to the CF-containing liposomes resulted in only one of three measurements in a decrease of the cBid/Bax-induced fluorescence release (Figure 56 D). However, it should be noted, that the addition of BI-6c9 to the protein buffer immediately caused the partial precipitation of the compound, so that its effective concentration in solution cannot be estimated. Therefore, the failure of BI-6c9 to completely inhibit the cBid/Bax-induced fluorescence release might be due to undercharged concentration rather than to its failure to inhibit. Nevertheless, the results indicate that the CF-liposome channel activity assay is a well validated model system for mitochondrial membrane permeabilization and in general suitable as a primary *in vitro* screen for examining the effects of novel Bid inhibitors.



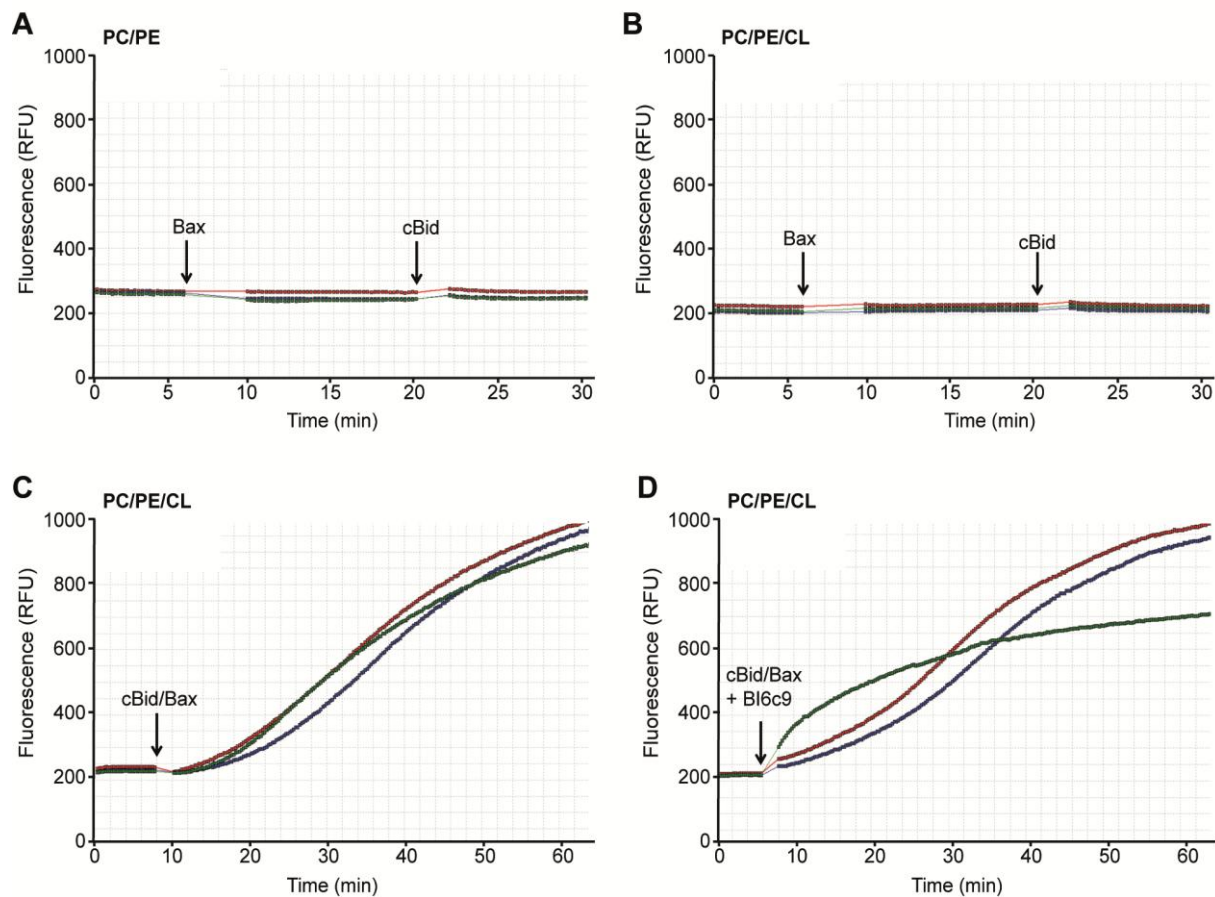


**Figure 56: cBid-mediated permeabilization of cardiolipin-containing liposomes is increased by pre-incubation with Bax, and slightly reduced by the Bid inhibitor BI6c9.**

**A, B**, CF release of PC/PE- and PC/PE/C-containing liposomes was measured prior and after addition of Bax (100 nM) and cBid (10 nM), respectively. Bax alone was not able to permeabilize both types of liposomes and post-incubation with cBid did not increase the fluorescence values. **C**, Bax (500 nM) and cBid (6  $\mu$ M) were pre-incubated 5 min. prior to addition to cardiolipin-containing CF-liposomes. Changes in fluorescence were measured for 60 min after protein incubation. cBid-mediated permeabilization was increased in presence of Bax up to 1000 RFU. **D**, Cardiolipin-containing CF-liposomes were incubated with the cBid/Bax mixture in presence of the Bid inhibitor BI6c9 (10  $\mu$ M). Only one of three samples revealed a decrease in fluorescence release (green line). Experiments reveal representative series of 2-3 measurements with  $n=3$  (green, blue, red line). cBid, caspase 8 cleaved Bid without dissociation of the  $t^c$ Bid and  $t^N$ Bid fragment.

### 3.4 Role of VDAC1 in Bid-mediated mitochondrial demise and cell death

In conditions of lethal stress increasing evidence points to a crucial role of mitochondrial dynamics and integrity for the decision between cellular life and death<sup>20, 24</sup>. The widely accepted role of the pro-apoptotic protein Bid in mediating mitochondrial injury and subsequent cell death<sup>24, 116</sup>, was elaborately substantiated in the abovementioned part of this thesis. While the sequences of Bid transactivation to mitochondria and the subsequent Bid-dependent cell death pathways are well established, the precise mechanism by which Bid mediates MOMP and mitochondrial dysfunction is unknown. An alternative model to the Bcl-2 family involvement in MOMP, is the opening of the mitochondrial permeability transition pore (mPTP) consisting of the voltage-dependent anion channel (VDAC), the adenine nucleotide transporter (ANT) and the matrix protein cyclophilin D, among other proteins<sup>23, 40</sup>. VDAC1 is proposed as the main channel-forming protein of the mPTP and it is reported to be involved in the regulation of mitochondrial apoptosis participating in the release of death promoting factors and interacting with anti-apoptotic proteins<sup>21, 125, 126, 131, 132, 157, 161</sup>. However, how these different mechanisms lead to MOMP and in particular whether Bcl-2 family proteins and VDAC are related to each other is widely discussed<sup>126, 130, 131, 151</sup>.

Therefore, the next part of the present thesis addressed the question, whether the voltage-dependent anion channel VDAC1 might serve as a rational target for Bid or its active form tBid to mediate MOMP and mitochondrial impairments in *in vitro* and *in vivo* paradigms of intrinsic cell death.

#### 3.4.1 Expression of VDAC1 and VDAC2 in HT-22 cells

In mammals, three homologous genes encode three VDAC isoforms, namely VDAC1, VDAC2 and VDAC3<sup>132</sup>. The three proteins have similar molecular weights (30-35 kDa), each shares approximately 70 % identity, and all are highly conserved across species and can be found in most tissues<sup>125, 132</sup>, albeit in different amounts. VDAC1 is reported as the most abundant isoform in most cells, being ten times more prevalent than VDAC2 and 100 times more abundant than VDAC3 in HeLa cells<sup>226</sup>. Since a pore-forming activity and thereby a possible involvement in apoptosis has been discussed for VDAC1 and VDAC2, but not for VDAC3, further work focused on these two isoforms. To confirm, that both proteins are expressed in the neuronal HT-22 cell line, and to further determine the more prominent isoform, mRNA levels of VDAC1 and VDAC2 were verified by RT-PCR (Figure 57). Compared to the high and equable expression levels of VDAC1 in control and glutamate exposed HT-22 cells, VDAC2 is expressed in a less amount, confirming VDAC1 as the most abundant sub-type in this cell line (Figure 57). Notably, mRNA levels of VDAC2 apparently

decreased after glutamate exposure of HT-22 cells as determined by RT-PCR (Figure 57). However, this decrease could not be confirmed on the protein level by western blot.

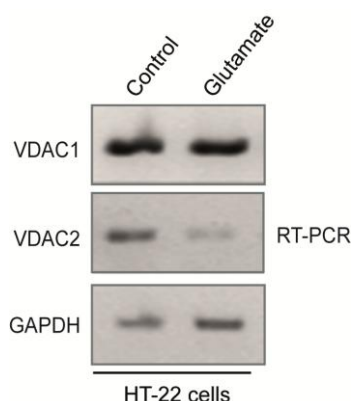


**Figure 57: Expression levels of VDAC1 and VDAC2 in HT-22 cells.**

Expression levels of VDAC1 and VDAC2 in HT-22 cells in the absence and presence of glutamate exposure were examined by RT-PCR using specific primers for VDAC1 and VDAC2, respectively. RT-PCR with primers specific for glyceraldehyde-3-phosphate-dehydrogenase (GAPDH) was used as control. Note, that the isoform VDAC1 is much more higher expressed than VDAC2, indicating VDAC1 as the most abundant isoform in HT-22 cells. VDAC1 levels in HT-22 control cells are not altered after glutamate-induced cell death of cells.

Since these data confirmed the expression of VDACs in HT-22 neurons, revealing VDAC1 as the most prominent voltage-dependent anion channel, further study addressed the role of VDACs in glutamate- and Bid-mediated neuronal cell death pathways.

### 3.4.2 The anion channel blocker DIDS provides neuroprotection in HT-22 cells

The anion channel blocker DIDS was used in order to gain an initial insight to the question of whether VDAC1 plays a relevant role in Bid-dependent mechanisms of neuronal cell death. Due to the lack of specific inhibitors for the subunit VDAC1, the existence of several side effects of the abused VDAC inhibitor König's polyanion<sup>227-229</sup>, and the apoptosis-inducing ability of the VDAC targeting phosphorothioate (PS) oligonucleotide G3139<sup>230</sup>, the anion channel blocker and well accepted VDAC inhibitor 4,4'-diisothio-cyanatostilbene-2,2'-disulfonic acid (DIDS)<sup>148, 158, 231</sup> was subjected to the following experiments.

#### 3.4.2.1 DIDS protects against glutamate-induced toxicity

According to other studies reporting a protective role of DIDS against neuronal injury, particularly preventing penumbral cell death<sup>232</sup> and accordingly delayed neuronal death in hippocampal neurons after transient forebrain ischemia<sup>233</sup>, a significant neuroprotective effect of DIDS could be revealed in the model of glutamate-induced toxicity in HT-22 cells.

The morphological phenotype of glutamate-induced injury was clearly prevented by DIDS in applications of 500  $\mu\text{M}$  up to 1 mM, respectively, preventing the retraction of cellular processes and shrinking of glutamate-exposed HT-22 cells (Figure 58 A). In addition, DIDS was able to enhance cell viability in glutamate-treated cells (3 mM, 17 h) in a concentration-dependent manner as detected by the MTT assay (Figure 58 B, C). Real-time impedance measurements (Figure 58 D) confirmed a transient protective effect of DIDS in concentration ranges from 250  $\mu\text{M}$  up to 750  $\mu\text{M}$ , yet a persistent protection at 1 mM (Figure 58 C, D). Notably, low micromolar concentrations of DIDS revealed no protective properties against glutamate-induced reduction in cell viability and proliferation (Figure 58 B, C). This is in line with other studies, using DIDS mostly in the upper micromolar range<sup>231, 232, 234</sup>, presumably due to the high polar structure of DIDS possibly hampering its passage through hydrophobic cell membranes. Therefore, further examinations were mostly performed using 500  $\mu\text{M}$  and 1 mM of DIDS in parallel.

Although increasing evidence has suggested that DIDS provides protection in a variety of experimental preparations, including the inhibition of neuronal cell death induced by several apoptotic factors<sup>235-238</sup>, it was reported in contrast that DIDS acts as an apoptotic inducer in hippocampal HT-22 neurons<sup>234</sup>. To address this confounding finding, FACS analysis of apoptotic cells after annexin-V/propidium iodide-staining of HT-22 neurons were performed. Therefore, HT-22 cells were treated with DIDS at concentrations of 500  $\mu\text{M}$  and 1 mM in the absence and presence of glutamate (3 mM) and cell death was detected 16-18 h after treatment. In contrast to the reports of Pamerter et al.<sup>234</sup>, a DIDS-induced apoptosis was not detectable in any concentration (Figure 59 A, B). DIDS treatment of HT-22 neurons neither increased annexin V binding to cells, which would indicate apoptosis induction, nor induced the uptake of propidium iodide in necrotic cells. In fact, both concentrations of DIDS were sufficient to significantly abolish the glutamate-induced cell death ( $63 \pm 3\%$ ) up to control levels ( $6 \pm 1\%$ ) (Figure 59 A, B). Thus, these data confirm the neuroprotective effects of DIDS in HT-22 cells and might indicate a critical involvement of VDACs in the mechanisms of glutamate-induced intrinsic cell death.

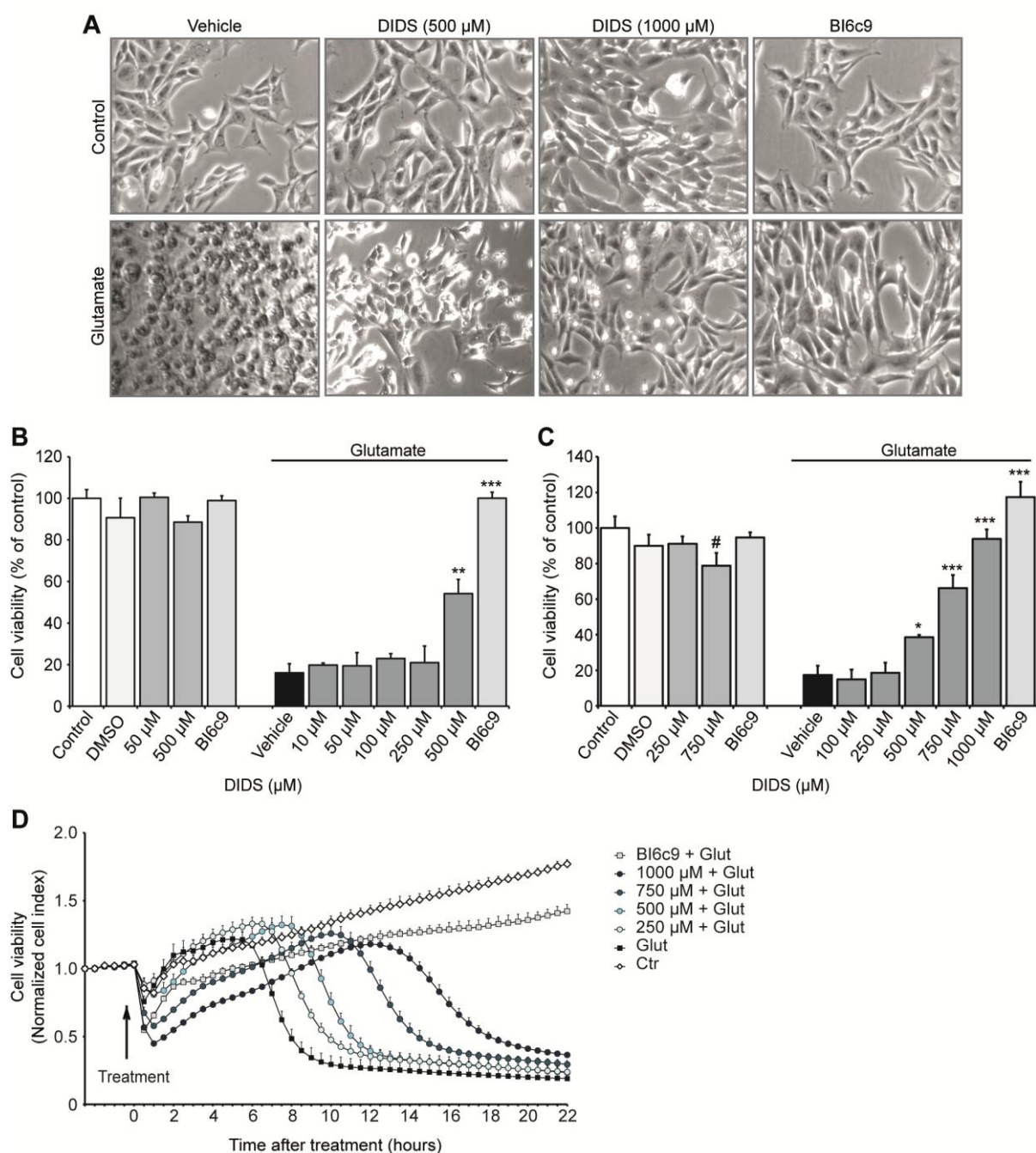


**Figure 58: DIDS protects against glutamate-induced toxicity.**

**A**, Photomicrographs (10  $\times$  0.25 NA objective) of HT-22 cells. The anion channel blocker DIDS (500, 1000  $\mu\text{M}$ ) preserves the spindle-like cell morphology of HT-22 cells after glutamate treatment (3 mM, 17 h). **B**, **C**, Cell viability of HT-22 cells was analyzed by MTT assay 17 h after glutamate exposure (3 mM). DIDS provides significant protection against glutamate-induced cell death in a concentration-dependent manner. **D**, Real-time analysis of cell impedance for 22 h after glutamate treatment (3 mM) confirmed the transient protection of DIDS against glutamate toxicity. While concentrations of 250  $\mu\text{M}$  reveal only slightly protective effects, high concentrations of 1 mM prohibit cell injury about 10 h after glutamate challenge. The Bid inhibitor BI-6c9 (10  $\mu\text{M}$ ) is used as positive control for protection against glutamate-induced toxicity. All experiments were independently repeated at least three times with  $n = 8$  per treatment condition. Data are presented as mean  $\pm$  SD (\* $p < 0.05$ , \*\*\* $p < 0.001$  compared to glutamate treated vehicle, ANOVA Scheffé's test).

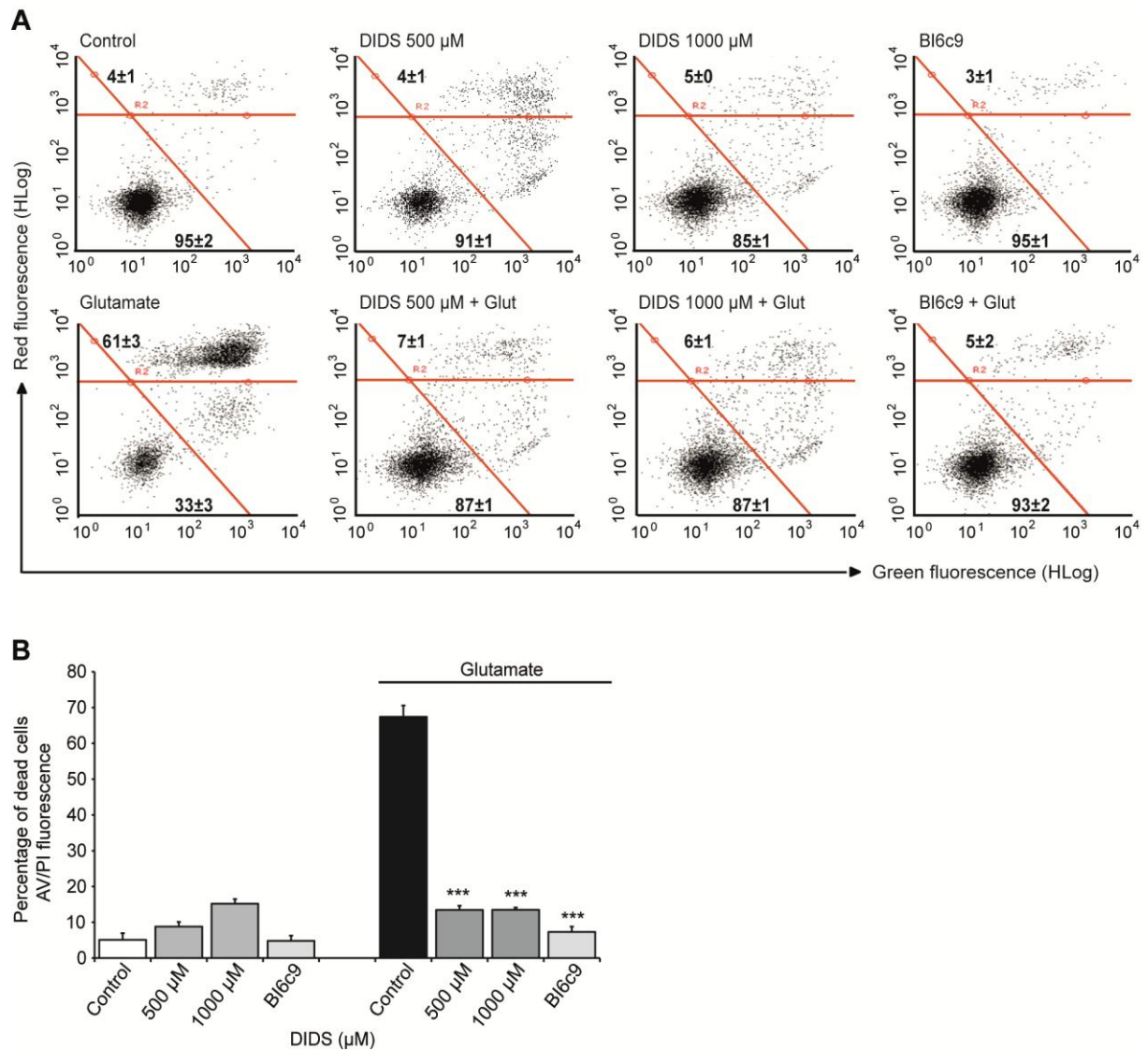


**Figure 59: DIDS attenuates apoptotic and necrotic cell death.**

**A, B,** HT-22 cells were co-treated with DIDS and 3 mM toxic glutamate solution. **A,** FACS analysis of annexin-V/propidium iodide-stained HT-22 cells depicts dead cells in the upper right corner and healthy cells in the lower left corner. Note that glutamate-induced cell death ( $61 \pm 3\%$ ) is completely prevented by DIDS in a concentration of 500  $\mu\text{M}$  and 1000  $\mu\text{M}$ . Numbers are mean percentages  $\pm$  SD for three cell groups treated as indicated in the corresponding quadrants. Glut, Glutamate, 3 mM. **B,** Quantification of AV<sup>+</sup>/PI<sup>-</sup> cells (**A**), indicated as percentage of dead cells. The Bid inhibitor BI-6c9 (10  $\mu\text{M}$ ) is used as positive control for neuroprotection. All Experiments were independently repeated at least three times. (\*\*\*)  $p < 0.001$  compared to glutamate treated vehicle and control, (#)  $p < 0.05$  compared to control,  $n=8$ , ANOVA, Scheffe test).

### 3.4.2.2 DIDS preserves mitochondrial integrity and function

In order to investigate the potential mechanisms behind the protection mediated by DIDS, mitochondrial integrity and function was assessed.

#### 3.4.2.2.1 Mitochondrial energy metabolism and respiratory activity is maintained by the anion channel blocker DIDS

Mitochondrial dysfunction, with the resulting compromise of cellular ATP supply and impairments in the respiratory chain, is an essential event described to ultimately trigger cell death<sup>6</sup>. As an important role of VDAC1 in the exchange of ATP/ADP and other metabolites into and out of the mitochondria as well as its involvement in oxidative phosphorylation has been described previously<sup>39, 138, 141</sup>, the effect DIDS on mitochondrial energy metabolism and respiratory activity was investigated to determine if DIDS might act on mitochondrial VDAC1.

Notably, high doses of DIDS (750  $\mu$ M and 1 mM) decreased basal cellular ATP levels of HT-22 cells, but significantly restored the further rapid ATP decline after the onset of glutamate exposure (Figure 60 A), indicating that VDAC inhibition by DIDS is sufficient to rescue metabolic functions in mitochondria. These findings were further substantiated by measurements of oxygen consumption rate (OCR). In accordance to previous experiments using this method, glutamate induced a remarkable reduction in mitochondrial maximum respiration and respiratory capacity (Figure 60 B, C). Concentrations of 500  $\mu$ M DIDS preserved both impairments (Figure 60 B), though high concentrations of 1 mM DIDS affected mitochondrial respiration already under control conditions (Figure 60 C).

These data accentuate VDAC inhibition as a suitable tool for further investigations of mechanisms that trigger mitochondrial demise and point to VDAC as a possible target for neuroprotection against glutamate-induced cell injury.



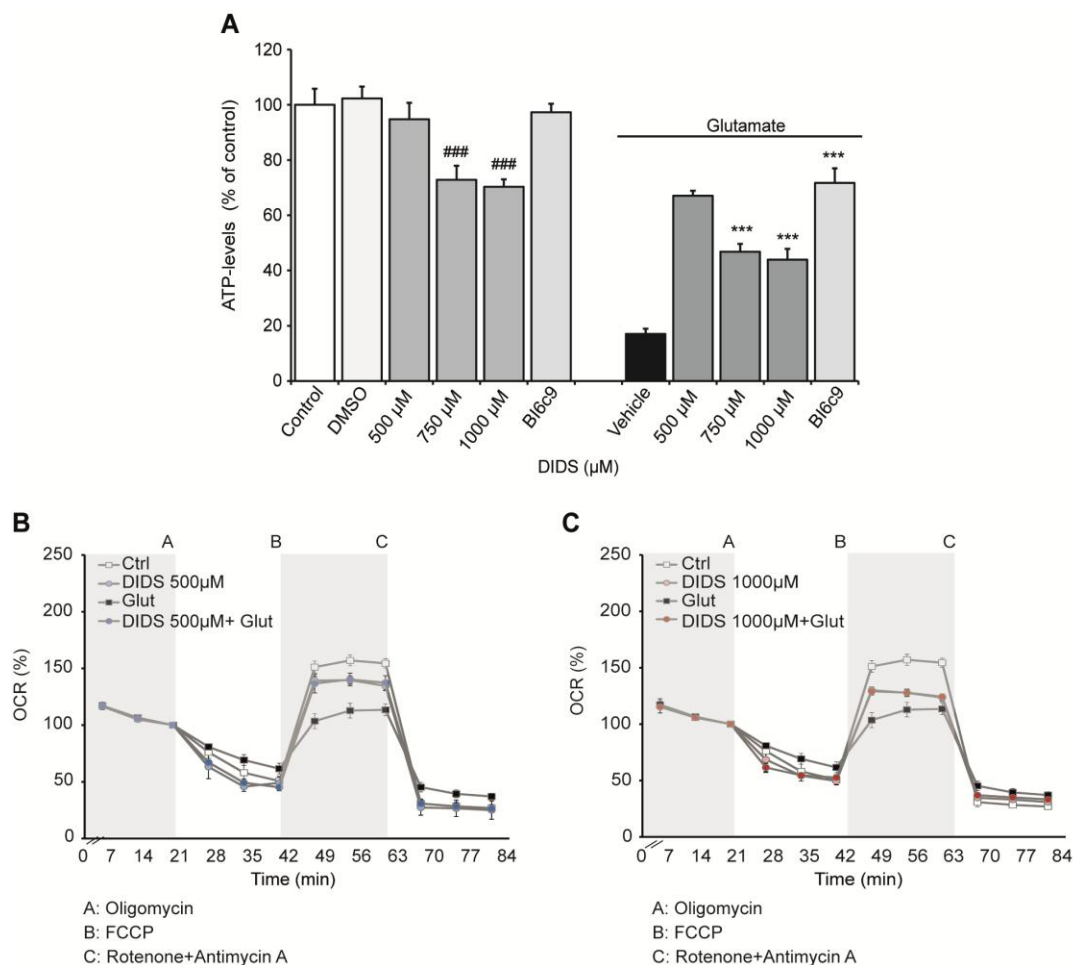


**Figure 60: The anion channel blocker DIDS maintains mitochondrial energy metabolism and respiratory activity.**

HT-22 cells were co-treated with glutamate (4-5 mM) and DIDS (500  $\mu$ M or 1000  $\mu$ M) or BI-6c9 (10  $\mu$ M). Seventeen to twenty hours after the onset of glutamate mitochondrial integrity was analyzed. **A**, ATP-luminescence measurements of HT-22 cells. High concentrations of DIDS (750  $\mu$ M and 1000  $\mu$ M) reduced basal ATP level, but prevented glutamate-induced ATP-depletion. The Bid inhibitor BI-6c9 was used as a positive control for restored ATP level after glutamate challenge (###  $p < 0.001$  compared to control, \*\*\*  $p < 0.001$  compared to glutamate treated vehicle (ANOVA, Scheffé's test). Experiments were independently repeated 3 to 5 times. **B**, Oxygen consumption rate (OCR) of HT-22 cells, treated as indicated, was measured by using the Seahorse Bioscience system. Glutamate-induced reduction in mitochondrial maximum respiration and respiratory capacity was prevented by co-treatment with DIDS (500  $\mu$ M). Treatment of cells with high concentrations of 1 mM DIDS were less protective against impairments in mitochondrial respiration. The results are representatives of 3-4 experiments.

### 3.4.2.2.2 DIDS is sufficient to prevent lipid peroxidation, mitochondrial fission and permeabilization of the mitochondrial outer membrane of HT-22 cells

The suspicion that plays a crucial role in the mechanisms of glutamate-induced Bid-mediated mitochondrial demise was substantiated as a pronounced protection against increases in detrimental ROS formation was achieved by DIDS (Figure 61 A, B). BODIPY-FACS analysis revealed a significant production of lipid peroxides in HT-22 cells 18 h after glutamate exposure, indicated by increases in green fluorescence (Figure 61 A). This late and



secondary boost in lipid peroxides, previously shown to be caused by Bid-mediated mitochondrial dysfunction<sup>116</sup>, was not affected by DIDS in concentrations of 500  $\mu$ M, but completely blocked when applied at concentrations of 1 mM (Figure 61 A, B).

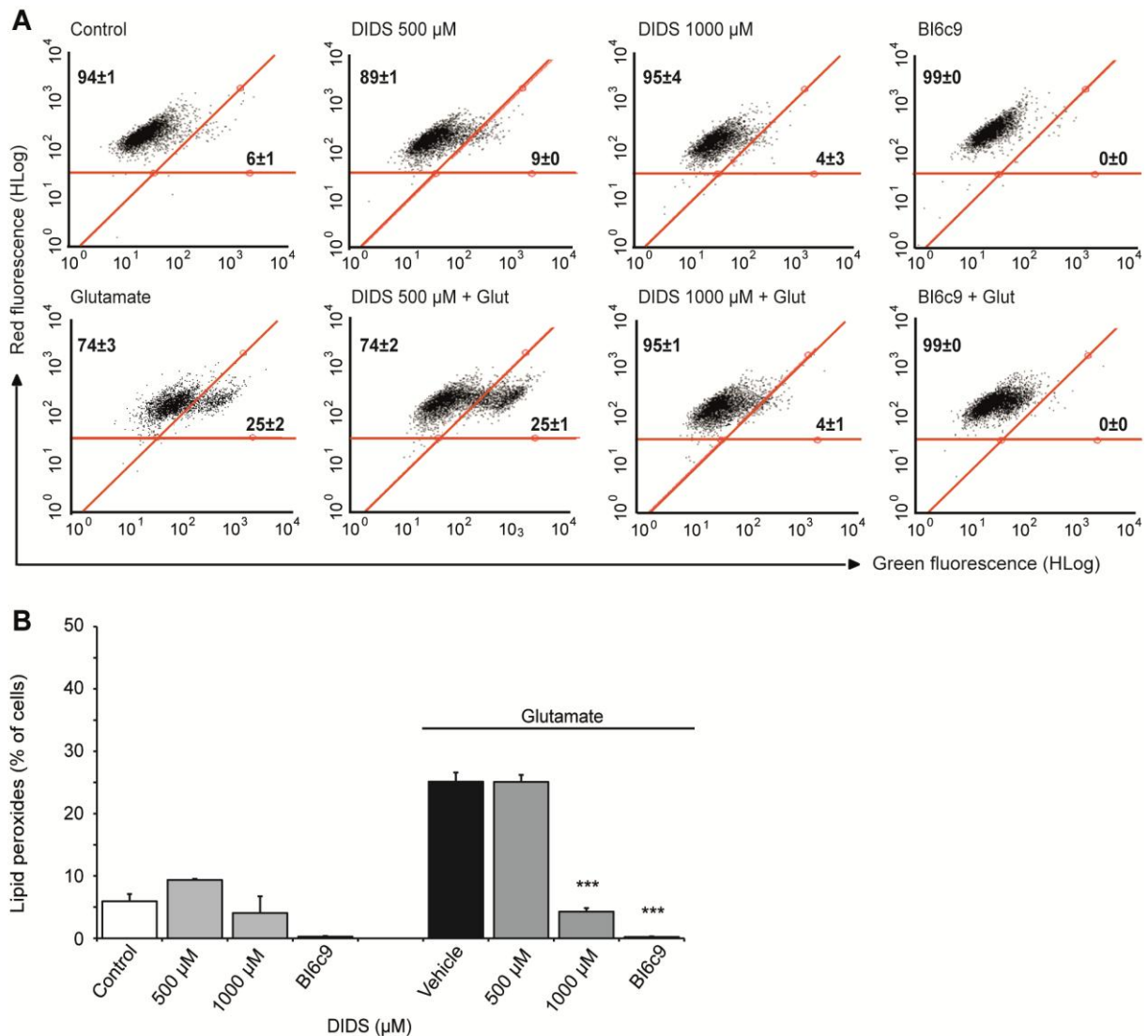


**Figure 61: DIDS prevents glutamate-induced ROS formation.**

**A,B**, BODIPY-FACS analysis of lipid peroxides. HT-22 cells were treated with DIDS (500  $\mu$ M or 1000  $\mu$ M) or BI-6c9 (10  $\mu$ M) 24 h after seeding. Lipid peroxide formation was determined 17 h after the onset of glutamate (4 mM). **A**, Values in the corresponding quadrants predict mean percentages  $\pm$  SD for three indicated treatment groups. Note, that formation of lipid peroxides is completely preserved by DIDS (1000  $\mu$ M) and comparable to the preservation of ROS by Bid inhibition (BI-6c9). **B**, Quantification of lipid peroxides in HT-22 cells after glutamate and DIDS co-treatment. The experiment was repeated four times with  $n = 3-4$  and results provided as mean  $\pm$  SD (\*\*\*)  $p < 0.001$  compared to glutamate treated vehicle, ANOVA, Scheffé test).

Analyses of mitochondrial morphology confirmed the protective potential of DIDS in the model of glutamate-induced toxicity. Application of DIDS (500  $\mu$ M and 1 mM) preserved the tubular mitochondrial morphology and completely rescued HT-22 cells from glutamate-induced mitochondrial fission (Figure 62 A, B). Quantification of mitochondrial morphology substantiated the potent effect of DIDS, revealing that the anion channel blocker increased the overall mitochondrial length thereby shifting the majority of mitochondria into category I in glutamate-treated HT-22 cells (Figure 62 B).

Previous reports described a VDAC1 mediated breakdown of the mitochondrial membrane barrier and the subsequent cell death through mitochondrial dysfunction<sup>143, 144</sup>. Since the loss of mitochondrial membrane potential ( $\Delta\psi_m$ ) is a major feature of glutamate-induced cell death that is associated with mitochondrial fragmentation<sup>24, 97</sup>, the further experiments addressed the impact of DIDS, as a tool for VDAC inhibition, on the functional integrity of mitochondrial membranes. TMRE-FACS staining of HT-22 neurons revealed a glutamate-induced reduction in red fluorescence in glutamate-treated cells (Figure 62 C) indicating a decrease in  $\Delta\psi_m$  17 h after glutamate challenge. In contrast, DIDS prevented the pronounced depolarization of the mitochondrial membrane and showed significantly higher  $\Delta\psi_m$  than glutamate exposed control cells (Figure 62 C, D).

Notably, the pronounced protection against various hallmarks of glutamate-induced toxicity achieved by DIDS was similar to the protective effects of the Bid inhibitor BI-6c9, which was always applied in the experiments as a positive control for neuroprotection (Figure 58 - Figure 62). This finding strongly assumes a close relationship between the mechanisms behind both protective effects, mediated by Bid inhibition or DIDS, and might indicate a close interrelationship among mitochondrial anion channels and the BH3-only protein Bid.

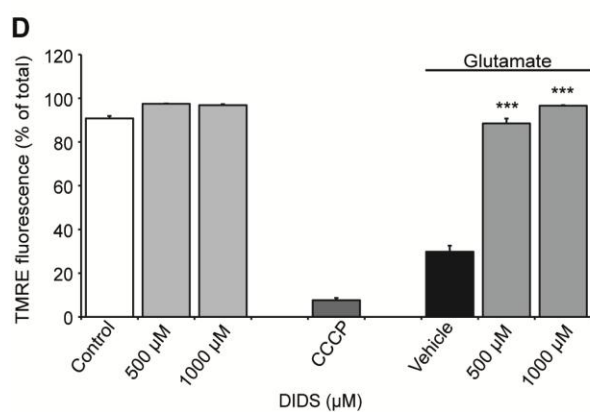
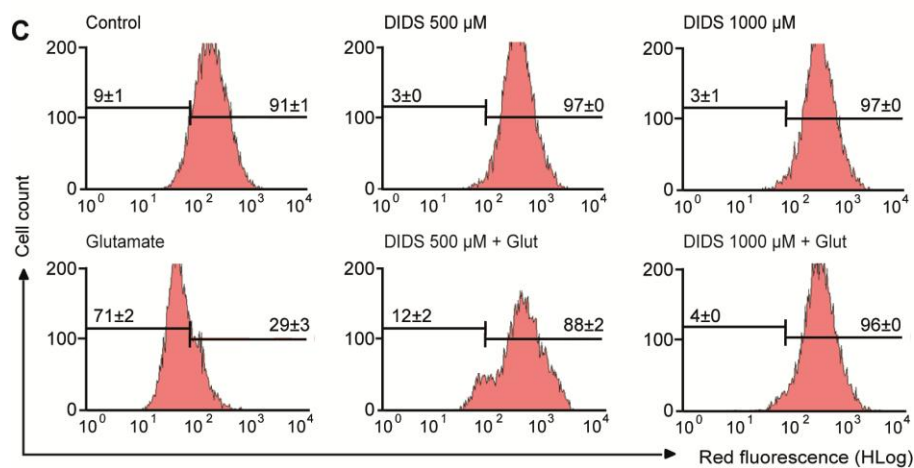
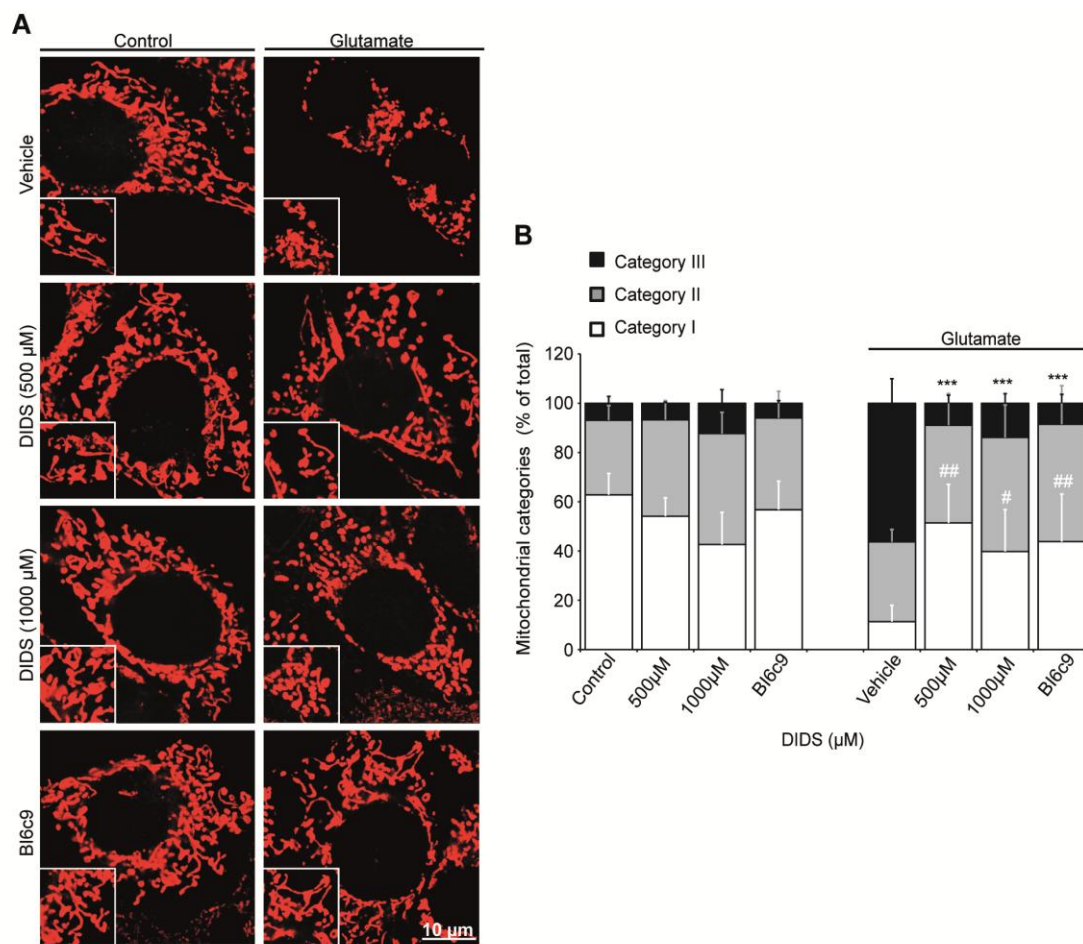


**Figure 62: DIDS prevents mitochondrial fission and loss of  $\Delta\psi_m$ .**

**A**, HT-22 cells were stained with Mitotracker red and co-treated with glutamate (4 mM) and DIDS (500  $\mu$ M) or BI6c9 (10  $\mu$ M). Confocal fluorescence photomicrographs reveal mitochondrial fission 17 h after glutamate challenge, which is preserved by DIDS and BI-6c9. **B**, Quantification of mitochondrial morphology: Category I: elongated, category II: intermediate, category III: fragmented mitochondria. Data represent the mean  $\pm$  SD of three independent experiments, each with 500 cells per treatment condition (### $p < 0.001$  compared to category I, \*\*\* $p < 0.001$  compared to category III in glutamate treated vehicle, ANOVA, Scheffé test). **C**, Mitochondrial membrane potential ( $\Delta\psi_m$ ) of HT-22 cells treated with DIDS (500  $\mu$ M and 1000  $\mu$ M) was analyzed by TMRE-FACS recordings 17 h after glutamate treatment (4 mM). Numbers are mean percentages  $\pm$  SD of TMRE fluorescence for  $n = 3$  indicated treatment groups. Glutamate treated HT-22 cells showed significantly reduced red fluorescence compared to controls, whereas DIDS treatment prevented the breakdown of the mitochondrial membrane potential as indicated by preservation of the red TMRE-fluorescence. **D**, Quantification of TMRE fluorescence of HT-22 cells co-treated with DIDS (500  $\mu$ M or 1000  $\mu$ M) in the presence and absence of glutamate. The experiment was independently repeated three times with  $n = 3$  per treatment group, data are provided as mean  $\pm$  SD (\*\* $p < 0.001$  compared to glutamate treated vehicle, ANOVA, Scheffé test).

**3.4.2.3 DIDS prevents tBid-induced mitochondrial depolarization and cell death**

To further clarify whether DIDS provides protection downstream of Bid activation, the anion channel blocker was applied to the model of tBid-induced toxicity (3.1.2). As described above, over-expression of tBid induced characteristic alterations in cell morphology indicating cytotoxicity, such as retraction of cell processes, rounding up and detaching from the culture dish (Figure 63 A). These morphological changes were clearly preserved in cells pre-treated with DIDS (500  $\mu$ M and 1 mM). The tBid-induced toxicity in HT-22 cells was further detected by FACS analysis of tBid-expressing cells after annexin V/propidium iodide staining (Figure 63 B, C) and cell viability measurements by MTT assay (Figure 63 D). DIDS was sufficient to prevent both, the tBid-induced increases in AV/PI positive cells (ptBid, Figure 63 B, C) as well as tBid-induced reduction in cell viability (Figure 63 D). Notably, application of DIDS was as effective against tBid toxicity as Bid inhibition by the Bid inhibitor BI-6c9 (Figure 63 A, C, D), confirming DIDS' action downstream of tBid activation. The fact, that DIDS achieved an even more pronounced protection than BI-6c9 might be allegeable through additional unspecific effects of DIDS on the level of mitochondria (Figure 63 B-D).

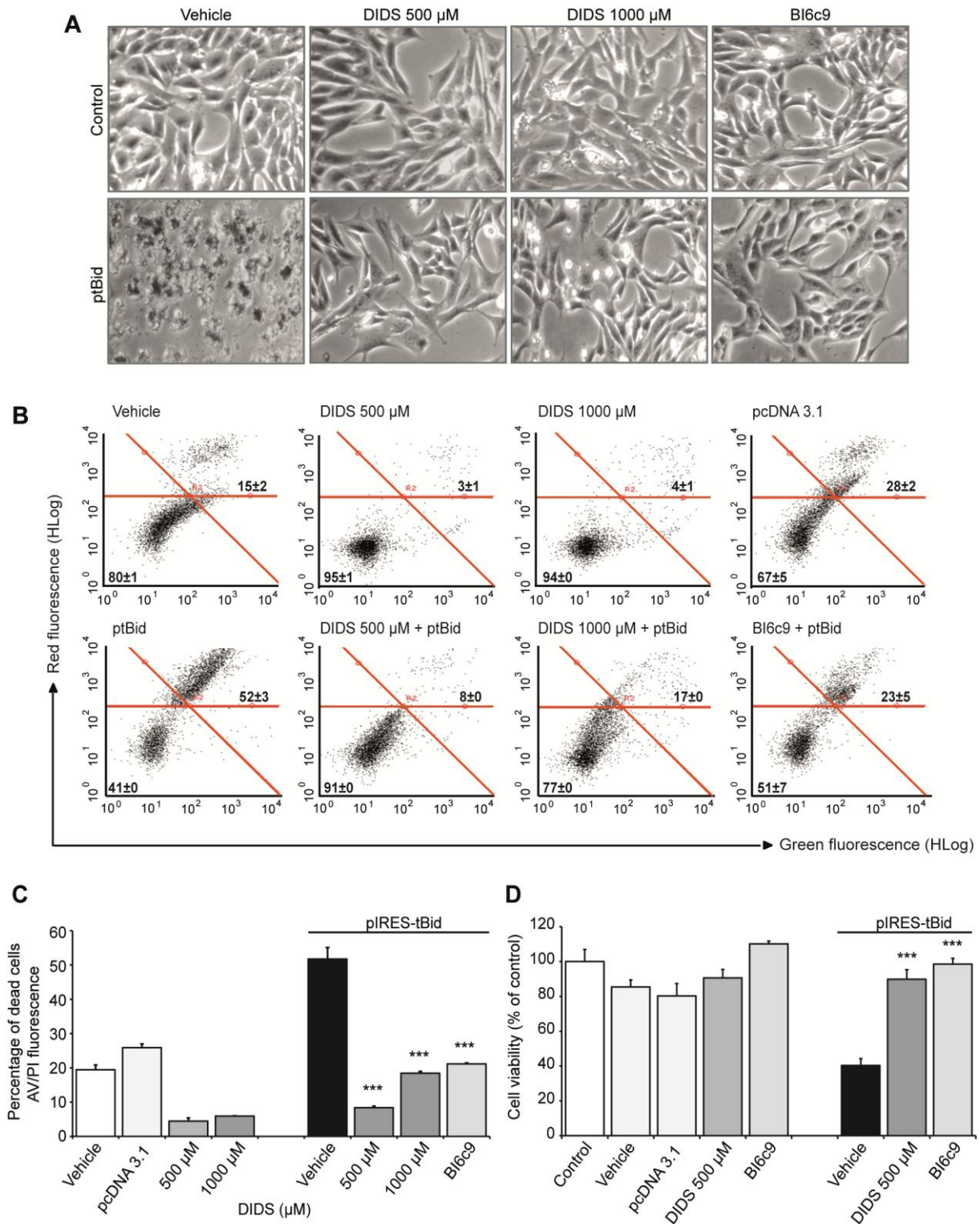


**Figure 63: tBid-induced toxicity in HT-22 cells is prevented by DIDS.**

HT-22 cells were pre-treated with the anion channel blocker DIDS (500  $\mu$ M and 1000  $\mu$ M) or the Bid inhibitor BI6c9 (10  $\mu$ M, positive control for protection) 1 h before transfection with a tBid-encoding plasmid (ptBid/pIRES-tBid). **A**, Photomicrographs (10 x 0.25 NA objective) show morphological changes of HT-22 cells 18 h after tBid over-expression. **B**, **C**, Annexin-V/propidium iodide-FACS analysis of tBid-over-expressing cells. Numbers are mean percentages  $\pm$  SD for three cell groups treated as indicated in the corresponding quadrants. **C**, Quantification of AV<sup>+</sup>/PI<sup>+</sup> cells (**b**), indicated as percentage of dead cells. **D**, tBid-induced reduction in cell viability was significantly prevented by DIDS (500  $\mu$ M) as determined by MTT assay. (\*\*\*)  $p < 0.001$  compared to tBid over-expressing vehicle) Experiments were independently repeated 3 to 5 times with  $n = 4$  per treatment group. Results are predicted as mean  $\pm$  SD.



Final evidence that DIDS attenuates tBid-mediated mitochondrial dysfunction was achieved from TMRE-FACS measurements (Figure 64 A, B). tBid over-expression induced a reduction in red TMRE fluorescence up to approximately 50 % of control cells, which was fully restored by pre-treatment of cells with DIDS (500  $\mu$ M and 1 mM, Figure 64 A, B). As these data reveal that tBid-induced loss of  $\Delta\psi_m$  and cell death was significantly attenuated by DIDS-mediated VDAC inhibition, they do not only substantiate the hypothesis that VDACs are involved in glutamate- and tBid-induced cell death pathways, but also leads to the assumption that VDAC- and Bid-associated MOMP mechanisms are related to each other.

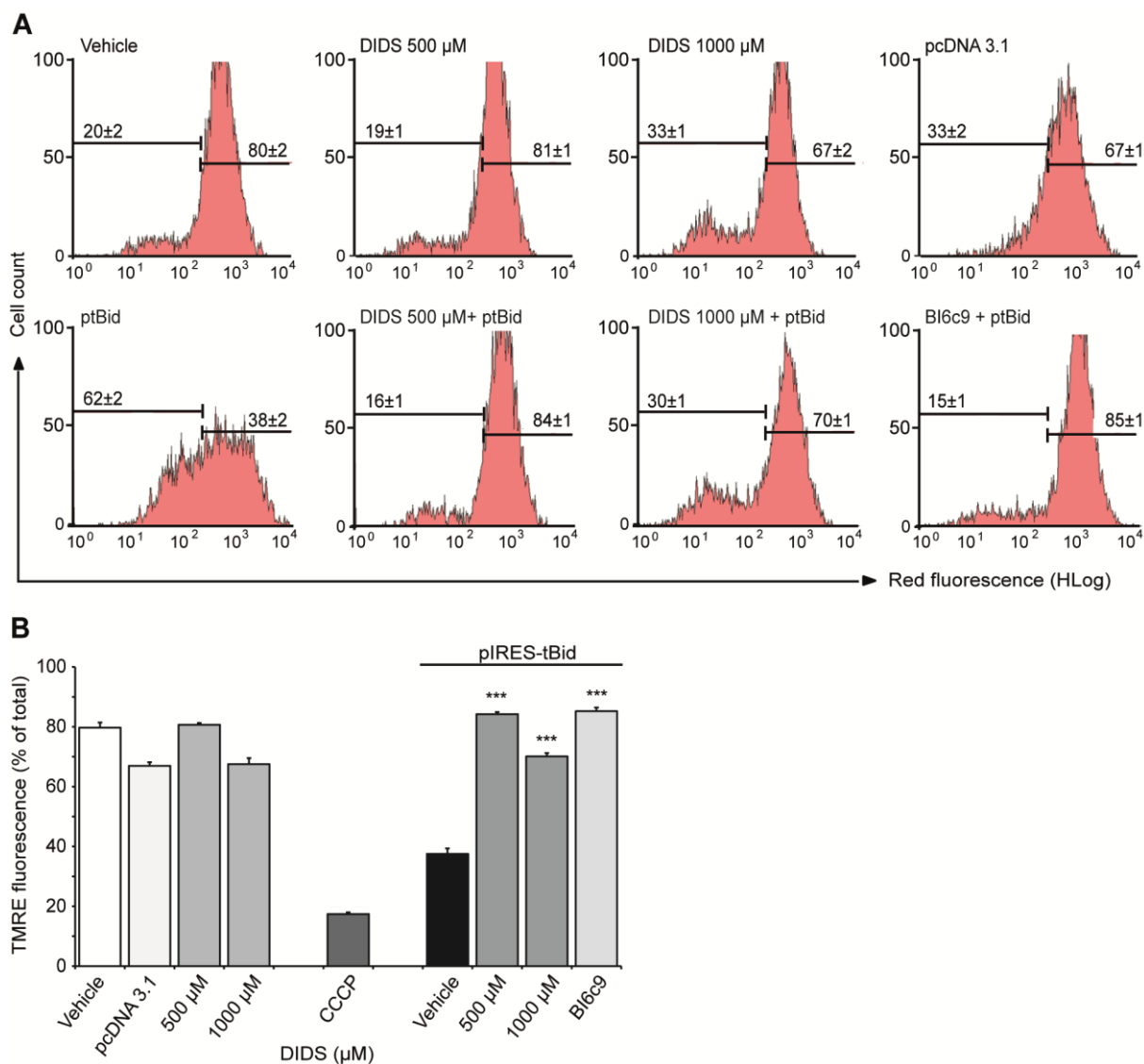


**Figure 64: DIDS prevents tBid-induced loss of  $\Delta\psi_m$ .**

HT-22 cells were pre-treated with the anion channel blocker DIDS in concentrations of 500  $\mu$ M and 1000  $\mu$ M 1 h before tBid-transfection. **A**, TMRE-FACS analyses reveal a tBid-induced loss of  $\Delta\psi_m$ , which is prevented by DIDS. Drop in red TMRE fluorescence indicates loss of  $\Delta\psi_m$  (left side), high red fluorescences indicate intact mitochondria (right side). Numbers are mean percentages  $\pm$  SD of TMRE fluorescence of three indicated treatment groups. **B**, Quantification of TMRE fluorescence confirmed the protective effects of DIDS against tBid-induced breakdown of  $\Delta\psi_m$ . (\*\*\*)  $p < 0.001$  compared to tBid over-expressing vehicle) Experiments were independently repeated five times and data presented as mean  $\pm$  SD.

### 3.4.3 Direct and functional interaction between Bid/tBid and VDAC1

Based on the data above, a close interplay between Bid and mitochondrial anion channels, likely VDACs, relating to intrinsic mitochondrial cell death pathways was suggested. This implication was supported by previous reports suggesting that Bid reduces metabolic exchanges between mitochondria and the cytosol through interactions with VDACs thereby leading to impaired mitochondrial function<sup>161</sup>. Although a close interplay of VDAC with Bcl-2 family proteins such as Bcl-xl, Bax or Bid has been proposed<sup>157, 159, 161, 162</sup>, a direct interaction of VDAC1 with any of these Bcl-2 family members had not yet been demonstrated on the cellular level. Therefore, the further effort of this thesis was to prove the assumed interaction between both proteins and to scrutinize whether a disturbance of the Bid-VDAC interplay might be the underlying mechanism of the protective effects achieved by VDAC inhibition.

Since determining protein-protein interactions within living cells is challenging as the detection might depend on several circumstances, including cell type, cell death stimuli as well as buffer and reagents used for the different binding studies, a possible interplay between Bid and VDAC1 was first examined *in vitro* using recombinant proteins.

#### 3.4.3.1 *In vitro* Bid-VDAC1 binding assays confirm the direct interaction of both proteins

The first evidence of a direct interaction of Bid and its active form tBid with VDAC1 was derived from *in vitro* Bid-VDAC pull down assays. (Figure 65 A, B) Purified recombinant VDAC1 (mVDAC1) bound to recombinant His<sub>6</sub>-tagged Bid (His-rBid) as well as to recombinant truncated Bid ((His)-rtBid) as shown by SDS-PAGE and western blot analysis (Figure 65 A, B).

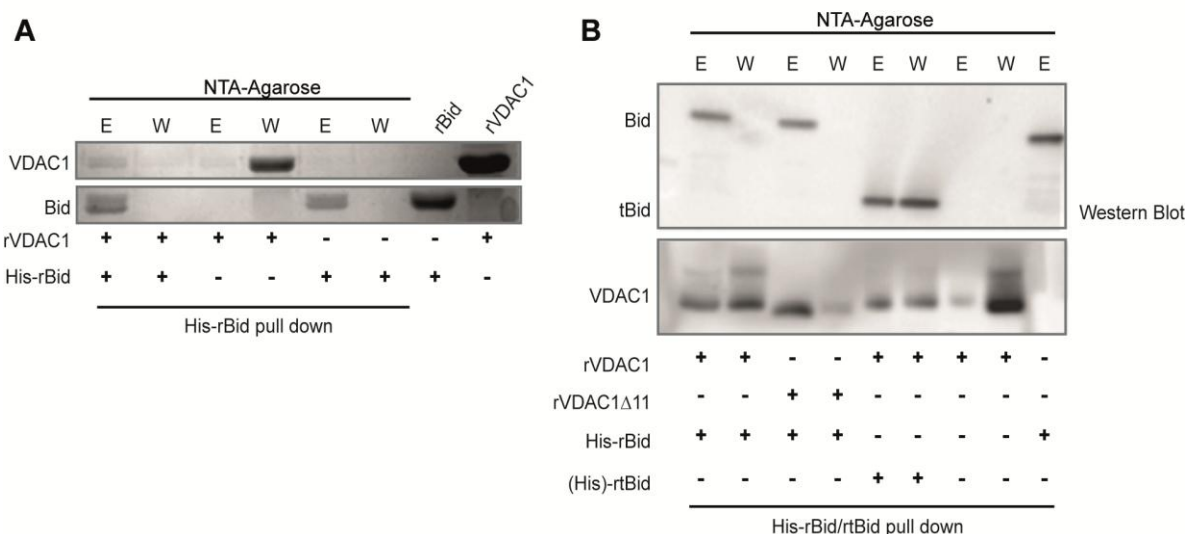


**Figure 65: Direct interaction between recombinant Bid/tBid and VDAC1.**

Direct interaction between rVDAC1 and rBid was confirmed by *in vitro* Bid/tBid-VDAC1 binding assays. **A**, Purified recombinant His-rBid and rVDAC1 were incubated for 2 h before incubation with NTA- Agarose (2 h) on a poly-prep® chromatography column. Elution fractions (E) and wash fractions (W) were acetone precipitated and analyzed by SDS-Page and coomassie staining. Recombinant rBid and rVDAC1 were used as protein size controls. E: Elution fractions, W: wash fractions. **B**, The direct interaction between purified rBid and rVDAC1 was confirmed by western blot analysis. For generation of tBid, recombinant full-length Bid was incubated with recombinant caspase 8 for 2 h at RT. Pull down of His-rBid and His-rtBid was done as described in **A**. Elution-fractions (E) and wash-fractions (W) were analyzed by SDS-PAGE followed by western blot. Anti-Bid antibody was used to detect full-length Bid as well as tBid (upper panel). Direct binding of VDAC1 to full-length Bid and tBid was indicated by clear VDAC1 bands in His-rBid and His-rtBid elution-fractions. For comparison, deletion of the N-terminal helix of VDAC1 (rVDAC1  $\Delta$ 11) did not affect co-IP with Bid.

### 3.4.3.2 Thermophoresis analysis results in different binding affinity coefficients ( $K_D$ ) for tBid and Bid binding to VDAC1

Although a crucial role of tBid for VDAC1 activity was proposed previously<sup>161</sup>, a convincing characterization of the direct interaction between these proteins was missing. To address this problem, thermophoresis measurements of AlexaFluor 532 C5 maleimide-labeled recombinant mVDAC1 with purified Bid and tBid were performed and revealed apparent dissociation constants ( $K_D$ ) of  $37.1 \pm 1.12 \mu\text{M}$  for tBid- and  $1420 \pm 3.04 \mu\text{M}$  for Bid binding to VDAC1, respectively (Figure 66 C). These  $K_D$  values indicated a 38-fold stronger binding of tBid to VDAC1 compared to the binding of full length Bid. Nonspecific binding of Bid/tBid to  $\beta$ -barrels or detergent micelles was ruled out since no tBid/Bid binding was detected in experiments using either the Escherichia coli outer membrane protein G (OmpG) or empty detergent micelles. In consequence these *in vitro* observations suggested a highly specific mode of interaction between VDAC1 and tBid (Figure 66 A).

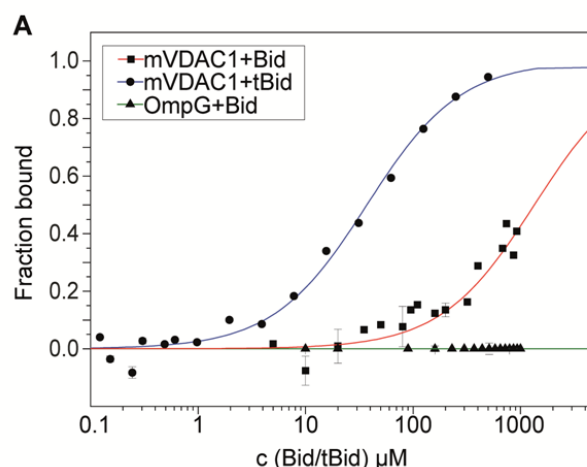


**Figure 66: Thermophoresis measurements revealed  $K_D$  values for Bid/tBid binding to VDAC1.**

Thermophoresis measurements confirmed the specific and direct interaction between Bid/tBid and VDAC1 and revealed  $K_D$  values of  $37.1 \mu\text{M}$  for tBid- (dots, blue line) and  $1420 \mu\text{M}$  for Bid- (squares, red line) binding to fluorescently labeled mVDAC1. The concentration of Bid/tBid was varied from 15 nM to 500  $\mu\text{M}$ , whereas a constant concentration of 50 nM for mVDAC1 and OmpG was used. After 20 min incubation at RT in the dark the mixtures were loaded to MST-grade capillaries and thermophoresis studies were performed using the Monolith



NT-115. Fluorescently labeled OmpG was used as a negative control to exclude unspecific interaction between tBid and  $\beta$ -barrels: Addition of Bid to OmpG leads to no significant change in the thermophoretic signal (triangle, green line). Bars represent SD of three independent measurements. Thermophoresis measurements were kindly performed by Barbara Mertins (Group of Prof Essen, Department of Chemistry, University of Marburg, Marburg, Germany).

### 3.4.3.3 tBid facilitates a reduction in the VDAC1 channel's conductance, while DIDS addition promotes a VDAC1 channel closure

Based on this data, showing that tBid and Bid both bind to VDAC1, the impact of this interaction on VDAC1 channel activity was further examined. It was previously described that addition of tBid to membrane reconstituted VDAC1 leads to a reduced conductivity state of VDAC1 in black lipid membrane (BLM) measurements and a Bid-induced VDAC closure was hypothesized even though a physical interaction of VDAC with tBid had not been demonstrated<sup>161</sup>.

Indeed, the addition of tBid to mVDAC1-containing planar lipid bilayers (BLM), facilitated a reduction in the channel's conductance but did not promote formation of the expected VDAC1 sub-conducting closed states. Native mVDAC1 exhibited the expected gating behavior, responding linearly to the application of both positive and negative potentials, and alternating between high and low conducting states<sup>128, 129, 154</sup>. In line with previous findings<sup>188</sup>, in voltage ranges of -40 to +40 mV native-like mVDAC1 occupied the fully open S0 state with a conductance of  $3.94 \pm 0.04$  nS and the closed S1 and S2 states with conductances of  $2.61 \pm 0.01$  nS and  $1.90 \pm 0.06$  nS respectively (Figure 67 A). Following the addition of recombinant tBid, the channel's conductance suffered a 23% reduction ( $3.05 \pm 0.24$  nS, N=131) with respect to that of the S0 state (unpaired T-test:  $P=10^{-4}$ ) (Figure 67 A, blue squares, B). Furthermore, tBid induced minor yet atypical fast channel switching transitions (Figure 67 C). Since the tBid-lowered conductance differed significantly from the closed-state S1 and S2 conductances (unpaired T-test:  $P=10^{-4}$ ) it seems highly likely that the tBid-VDAC1 interaction promotes a conformational change of the VDAC1 channel rather than its full closure. The effect of tBid addition on VDAC1 channels was further compared with the VDAC1 channel behavior after addition of the VDAC inhibitor DIDS. Notably, addition of DIDS to reconstituted mVDAC1 resulted in a 1.6-fold reduction of VDAC1 conductance ( $2.47 \pm 0.03$  nS, N = 50) (Figure 67 D), and no switching transitions were recorded for up to one hour. Since the lowered conductance mediated by DIDS is between the closed S1 and S2 states of VDAC1, it suggests that DIDS directly alters VDAC1 gating and affects channel closure. Based on this observation, it is highly likely that DIDS occupies the same binding side as tBid albeit with higher affinity, since tBid assumedly fails to interact with mVDAC1 in DIDS presence.

In conclusion, these data clearly demonstrated not only a highly specific interaction between recombinant Bid/tBid and VDAC1 but also indicate the impact of this interaction on the VDAC1 channel's behavior *in vitro*.

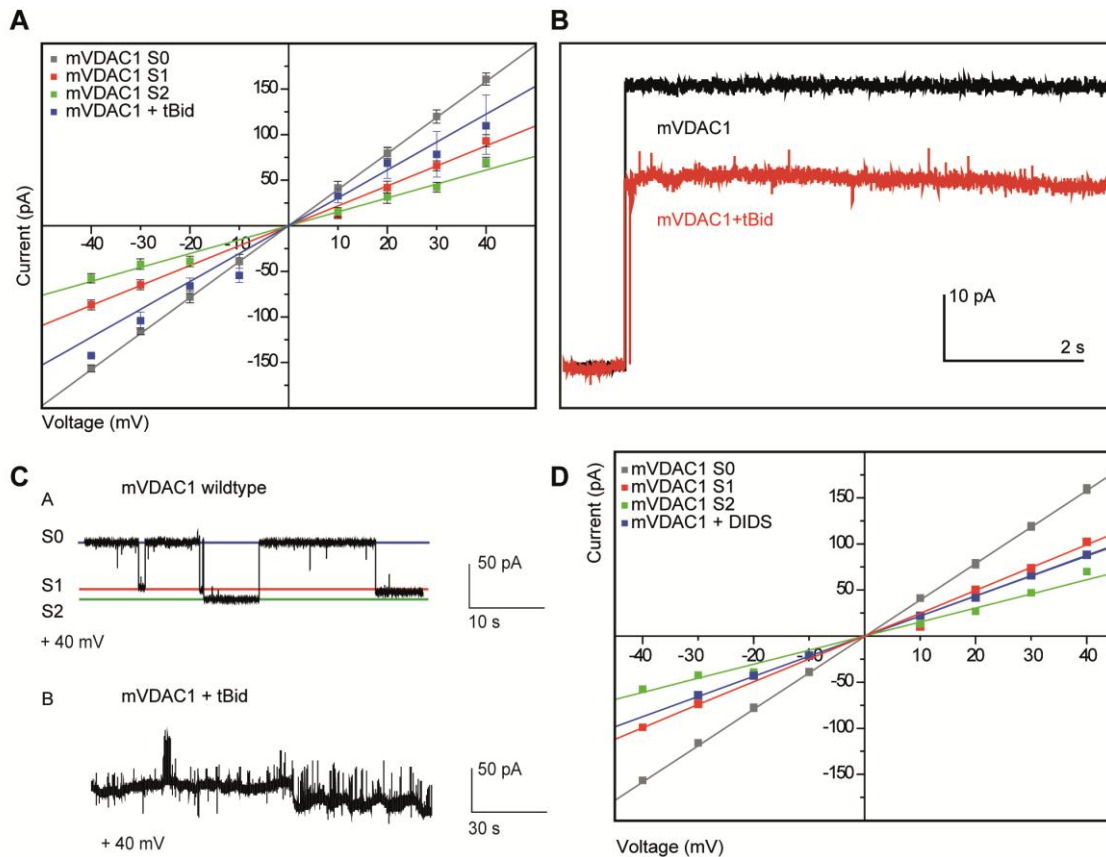


**Figure 67: tBid promotes a reduction in the VDAC1 channel's conductances, while DIDS triggers VDAC1 closure**

**A**, The conductance values of the corresponding VDAC1 channel states were determined by using Ohm-plots. Reconstituted native mVDAC1 responded linearly to application of both positive and negative potentials, alternating between an open (S0; grey) and two major (S1; red and S2; green) closed states. After tBid addition to the cis-side of the BLM chamber, the overall conductance of the channel drops to 77% compared to S0 (blue). Determined conductances: S0;  $3.9 \pm 0.0$  nS, S1;  $2.6 \pm 0.0$  nS; S2;  $1.9 \pm 0.1$  nS and after tBid addition;  $3.0 \pm 0.2$  nS. Bars represent standard errors of a minimum of 10 replicates per measurement. **B**, Representative traces of mVDAC1 (black), mVDAC1 after tBid (red) and DIDS (green) addition at +10 mV. Addition of tBid resulted in a reduced VDAC1 channel conductivity by approximately 23% compared to the open state of mVDAC1 (S0). **C**, **A**: representative trace of the mVDAC1 gating activity at +40 mV. The observed S0, S1 and S2 states, in the +40 mV trace, are indicated by blue, red and green lines respectively. **B**: representative trace of mVDAC1 after addition of tBid at +40 mV. The channel shows minor yet atypical fast channel switching events. **D**, Ohm-plots were used for determining the VDAC1 channel conductance before and after addition of the VDAC inhibitor DIDS. Reconstituted native mVDAC1 responded linearly to application of both positive and negative potentials and revealed the expected gating behavior as described in **A**. DIDS addition to the cis-side exhibited a 1.6-fold reduction in its conductance ( $2.47 \pm 0.03$  nS,  $N=50$ , blue). BLM measurements were kindly performed by the group of Prof Essen (Department of Chemistry, University of Marburg, Marburg, Germany).

### 3.4.4 Direct interaction of Bid and VDAC1 in cultured neurons

Encouraged by the findings above, a further aim was to examine if the Bid-VDAC1 interaction measured *in vitro* can be transferred to cell culture and *in vivo* models. Initially this goal was probed in the hippocampal HT-22 neurons subjected to the toxic effects of glutamate thereby analyzing the proposed interplay between Bid and VDAC1 in relationship to intrinsic cell death mechanisms. Indeed, immunoprecipitation studies using protein extracts from this neuronal cell line provided the first evidence of the interaction of Bid and VDAC1 in living cells, as western blot analysis revealed an increased binding of VDAC1 to Bid after glutamate challenge (Figure 68 A). Notably, 12 h after glutamate exposure, a 70 kDa protein bound to Bid was detected by the applied anti-VDAC1 antibody (Figure 68 A), indicating that activated Bid binds to VDAC1 dimers that may form upon glutamate treatment. This finding is consistent with previous studies showing that VDAC1 dimerization and oligomerization increase substantially upon apoptosis induction<sup>239, 240</sup>. As VDAC1 is discussed as a component of the permeability transition pore (PTP), which is a multi-protein complex consisting of VDAC, the adenine nucleotide transporter (ANT), the matrix protein cyclophilin D, and likely other proteins<sup>23, 40, 241, 242</sup>, co-immunoprecipitations of Bid with VDAC1 from HT-22 cells did not necessarily indicate the direct association of these two proteins as other proteins may also be involved in a higher complex. The proposed direct interaction of Bid and VDAC1 was finally confirmed by co-immunoprecipitations of endogenous VDAC1 and FLAG-VDAC1 expressed in the HT-22 cells (Figure 68 B, C). Both, VDAC1- and FLAG-VDAC1 immune complexes revealed an increasing binding of Bid between 6-15 h after glutamate exposure (Figure 68 B, C). The fact that a direct binding of Bid and VDAC1 only occurred after glutamate exposure indicates that this interaction is an essential step in mitochondrial death pathways.

As immortalized HT-22 hippocampal neurons, lack ionotropic NMDA and AMPA/kainate receptors, cell death is initiated through glutathione depletion after glutamate-induced inhibition of the glutamate-cystine antiporter<sup>243</sup>. Consequently, the HT-22 model of glutamate-induced oxidative stress only partly reflects the mechanisms of neuronal death after acute brain injury. In primary cortical neurons, glutamate-induced excitotoxicity involves an immediate increase in the intracellular  $\text{Ca}^{2+}$ -concentration through activation of NMDA receptors. However, this initial calcium overload triggers the increase of reactive oxygen species and the subsequent mitochondrial damage as it occurs likewise in the HT-22 cells.

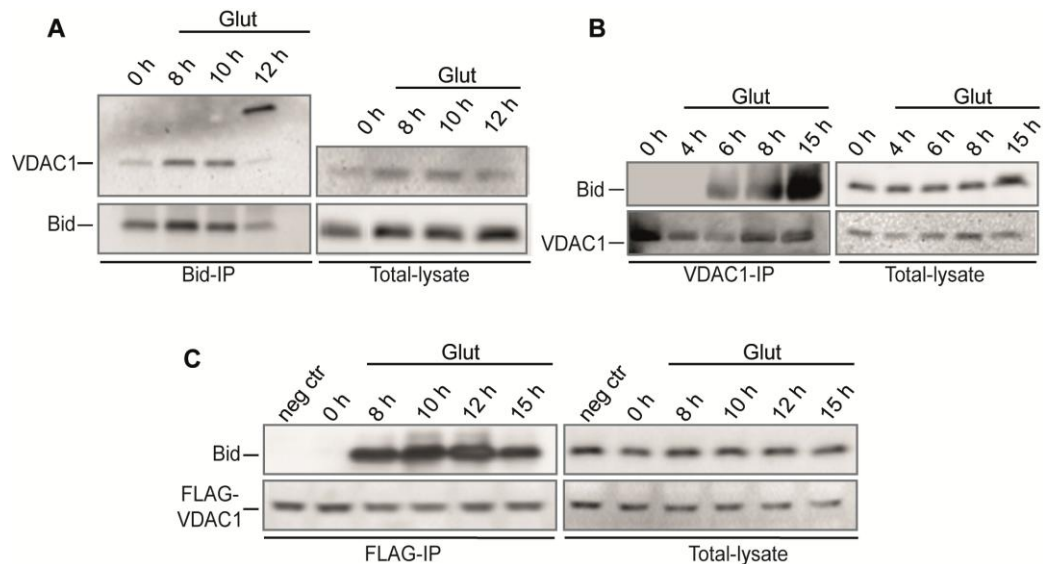


**Figure 68: Direct interaction of Bid and VDAC1 after the onset of glutamate exposure in HT-22 cells.**

Immunoprecipitation analyses of Bid and VDAC1 protein revealed a direct interaction between Bid and VDAC1 6-15 h after glutamate exposure of HT-22 cells. **A**, Immunoprecipitation of Bid protein was prepared from 2.5 mg total protein lysate of HT-22 cells exposed to 3 mM glutamate at the indicated time points of 8-12 h. Western blot panels on the left side show results from the Bid pull down and on the right side total protein lysates with 30  $\mu$ g protein. Eight hours after the onset of glutamate a pronounced binding of VDAC1 to Bid is detected. 12 h after glutamate exposure a 70 kDa protein was detected by the applied VDAC1 antibody (Santa Cruz, VDAC1-N18), indicating VDAC1 dimerization. **B**, Immunoprecipitation of endogenous VDAC1 protein confirmed the direct interaction between VDAC1 and Bid in glutamate-treated HT-22 cells. Western blot panels on the left side reveal an increasing Bid binding to pull down VDAC1 between 6 h to 15 h after the glutamate challenge. Total protein lysates, depicted on the right side, were used as controls. **C**, HT-22 cells were transfected with a FLAG-VDAC1 encoding plasmid and treated with glutamate 24 h after transfection. Western blot analysis of Flag-immunoprecipitations of FLAG-VDAC1 protein from HT-22 cells exposed to 5 mM glutamate at the indicated time points of 0 h-15 h confirm the increasing Bid binding to VDAC1 during cell damage. To rule out unspecific binding of Bid to the FLAG-tag, a negative control containing only a FLAG-plasmid without VDAC1 sequence was used as control. Western blot panels on the right side show total protein lysates, confirming an equal expression of FLAG-VDAC1 in the indicated protein samples. All western blots are representatives of at least 3-4 independent experiments.

To confirm, the relevance of the described Bid-VDAC1 interplay as an essential key in the mechanisms of neuronal death after brain injury and to exclude a cell type specific appearance, the proposed interaction was confirmed in the model of glutamate-induced excitotoxicity in primary cortical neurons (PCN) (Figure 69). Therefore, primary mouse cortical neurons were exposed to 25  $\mu$ M glutamate solution after 7-9 days in culture, when ionotropic glutamate receptors were expressed and the neurons are highly sensitive to glutamate. Immunoprecipitations were performed 4 h to 22 h after excitotoxicity and confirmed the direct interaction between Bid and VDAC1 (Figure 69). In line with our findings in HT-22 cells, the Bid-VDAC1 interaction was also clearly detected at later time points after glutamate-induced excitotoxicity in PCNs, while no binding was detected under control conditions (Figure 69).

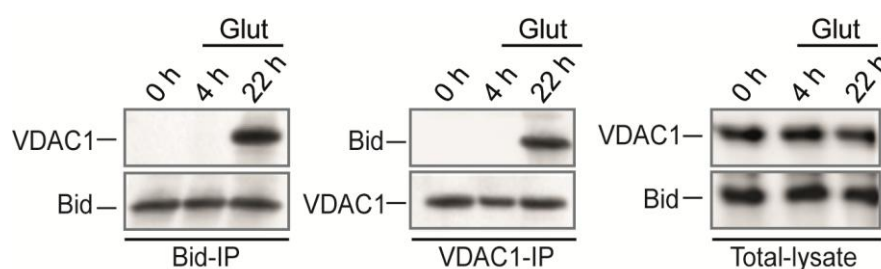


**Figure 69: Direct interaction between Bid and VDAC1 in primary cortical neurons.**

Immunoprecipitations of endogenous Bid and VDAC1 protein (left side) and total protein lysates (right side) from primary cortical neurons exposed to 25  $\mu$ M glutamate at the indicated time points. Bid and VDAC1 immunoprecipitations were prepared from 1 mg to 1.5 mg total protein lysate from PCNs 0 h, 4 h and 22 h after the induction of glutamate-induced excitotoxicity. PCNs were treated on day 7-9 after culturing to ensure NMDA receptor expression. While no interaction was detected in controls and after 4 h excitotoxicity, a direct interaction was revealed 22-24 h after treatment. Total lysates confirm the equal expression of both proteins in all samples. The data are representative western blots from 4 independent experiments.

### 3.4.5 Direct interaction of Bid and VDAC1 during ischemic brain damage *in vivo*

The described cell culture findings on both a neuronal cell line and primary neurons led to further examinations in whole organisms, in a model of cerebral ischemia (Figure 70 A, B, C). The model of transient middle cerebral artery occlusion (MCAo) was conducted by Uta Mamrak and the following immunoprecipitations were performed together with Lilja Meissner at the Ludwig-Maximilians-University in Munich, Germany.

The C57BL/6 mice were subjected to 60 min of transient focal ischemia by introducing a silicon-coated nylon filament into the internal carotid artery to occlude the middle cerebral artery (MCA), followed by reperfusion. Co-immunoprecipitation studies were performed from tissue homogenates of the cortical penumbra 2 h, 6 h and 24 h after the onset of ischemia, respectively. In these homogenates, Bid-VDAC1 interaction became detectable at 6 h and 24 h after ischemia in all mice subjected to transient MCAo. While the interaction significantly increased over 6-24 h in the ischemic brain tissue, no interaction was found at early time-points, i.e. 2 h after ischemia or in the contralateral controls (Figure 70 A, B, C).

Consequently, these data confirmed the importance of the Bid-VDAC1 association in glutamate-induced cell death in HT-22 cells and primary neurons, further highlighting the relevance of this interaction in an *in vivo* model for human disease.

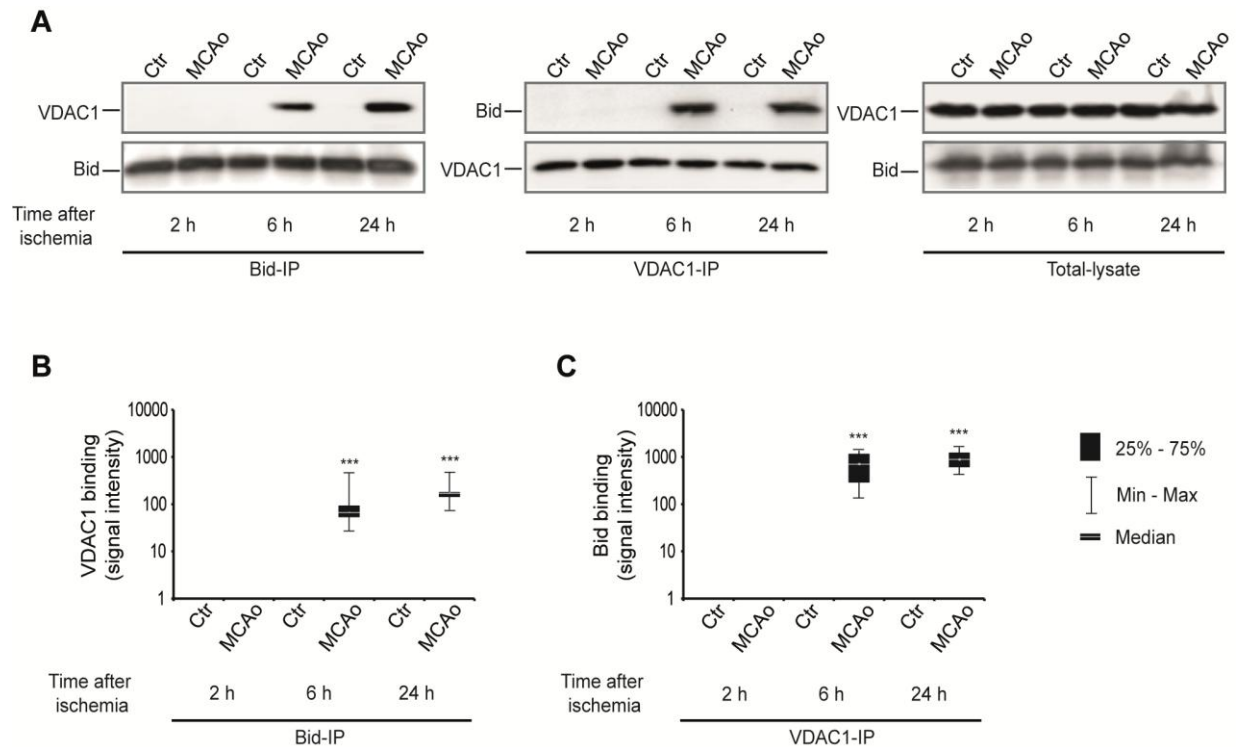


**Figure 70: Direct interaction of Bid and VDAC1 during ischemic brain damage *in vivo*.**

**A**, Western blot analyses reveal results from immunoprecipitation studies of Bid (left panel) and VDAC1 protein (middle panel) and total protein lysates (right panel) from control (ctr) and ischemic (MCAo) brain tissue of mice 2 h, 6 h, and 24 h after transient middle cerebral artery occlusion (MCAo). 6 h and 24 h after transient ischemia a direct interaction of Bid and VDAC1 was detected, while no interaction was observed at early time points (2 h) after MCAo. Contralateral controls showed no interaction at all, confirming the relevance of the Bid-VDAC1 binding during neuronal injury. **B**, **C**, Box-plots reveal significant VDAC1-Bid binding (**B**) and Bid-VDAC1 binding (**C**) in brain tissue of mice 6 h and 24 h after ischemia (MCAo). Data were collected from 6 mice per time-point. (Bottom and top of the box represent first and third quartile (25-75%), band inside the box predicts median and whiskers are shown from minimum to maximum, \*\*\* p < 0.001, ANOVA, Kruskal-Wallis test).

### 3.4.6 Interaction of Bid and VDAC1 determines mitochondrial demise and cell death in HT-22 cells

Combining the data above, a specific and direct interaction between tBid and VDAC1 is clearly demonstrated, with the protective effects of the VDAC inhibitor DIDS in the present cell death models (3.4.2), it is highly likely that both proteins, Bid and VDAC1, interfere together in the mechanisms of intrinsic cell death triggered by oxidative stress and indeed point to VDAC1 as a possible target for Bid and its active form tBid to regulate mitochondrial integrity and function. Although DIDS is well accepted as a VDAC inhibitor<sup>158, 231</sup>, which may also inhibit VDAC2 and VDAC3, as well as other anion channels<sup>244</sup>, it cannot achieve sufficient specificity for inhibition of the isoform of interest, i.e. VDAC1.

To gain further insight in the signaling events downstream of the Bid-VDAC1 interplay, the impact of VDAC1 in Bid-mediated hallmarks of cell death in HT-22 cells was analyzed by using siRNA-mediated VDAC1 silencing.

### 3.4.6.1 VDAC1 gene silencing attenuates glutamate-induced cell death in HT-22 cells

Specific down regulation of VDAC1 was achieved by two different sequences of VDAC1-targeting siRNA (VDAC1 siRNA1 and VDAC1 siRNA2). Both siRNA sequences significantly reduced the expression of VDAC1 whereas control scrambled siRNA (scr siRNA) did not alter VDAC1 levels in HT-22 cells as assessed by RT-PCR and Western blot analysis (Figure 71 A). In contrast, expression levels of VDAC2 were not altered by VDAC1 gene silencing (Figure 71 B), confirming the specific targeting of the isoform VDAC1. To investigate the effect of reduced VDAC1 protein levels, cell morphology as well as cell viability of glutamate exposed cells were analyzed. Unlike control cells, VDAC1- depleted cells sustained their normal spindle-shaped morphology (Figure 71 C) and were rescued from glutamate-induced toxicity as revealed by MTT assay (Figure 71 D,E) and fluorescence-activated cell sorting (FACS) analysis of annexinV/propidium iodide-stained HT-22 cells (Figure 72 A, B). Moreover, real-time cell analysis (RTCA) of cellular impedance, depicted as normalized cell index (NCI) over at least 22 h, indicated a significant reduction in cell viability within a small time window of 2-4 h for glutamate-exposed control and non-functional scrambled (scr) siRNA-treated cells, yet a sustained protection over time in cells pre-treated with 20 nM of VDAC1 siRNA (Figure 72 C, D). Notably, RTCA-recordings revealed, that siRNA cells proliferate slower than un-transfected control cells, which is in line with siRNA mediated reduction in cell viability detected by the MTT assay (Figure 72 C, D and Figure 71D, E)



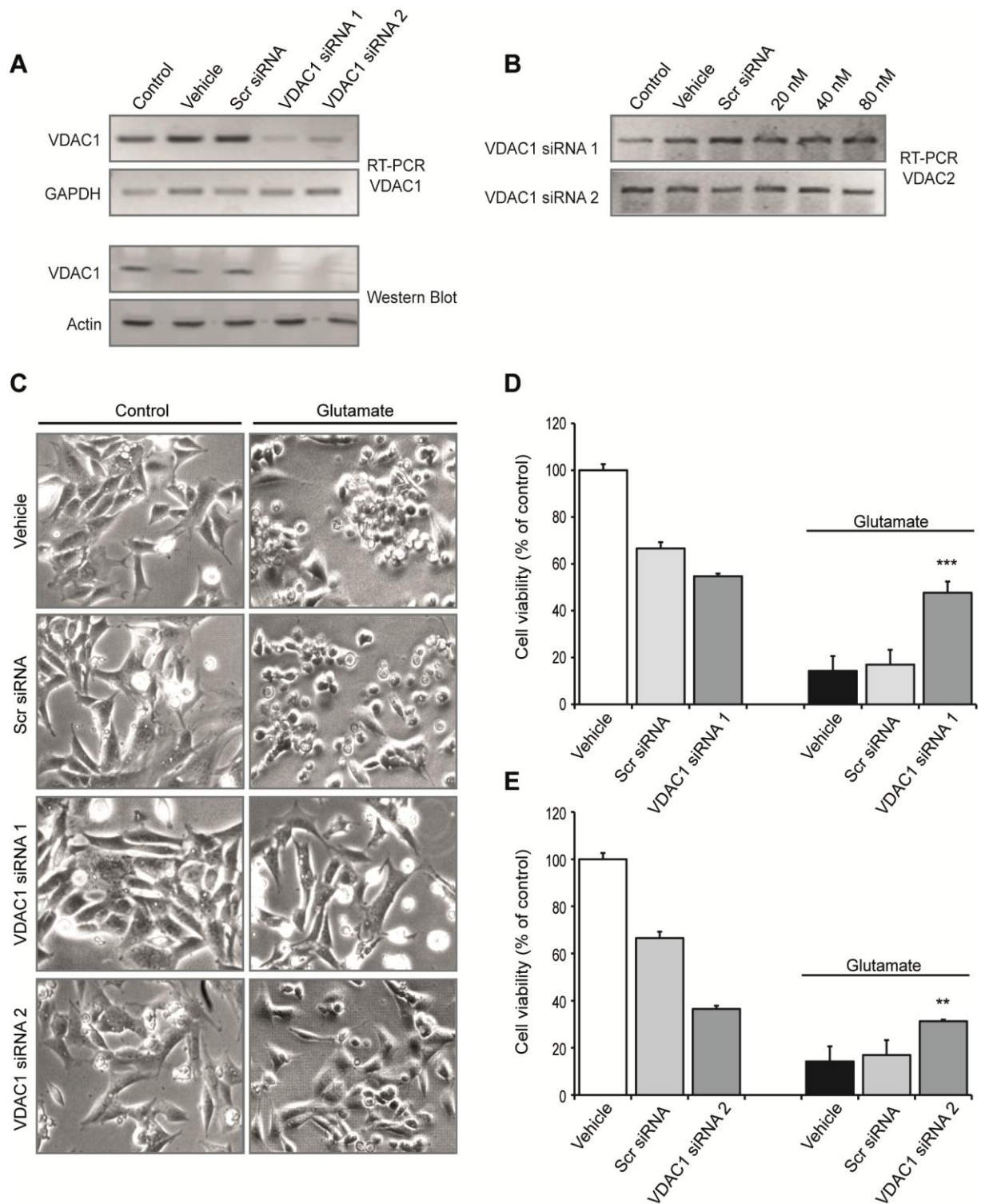


**Figure 71: VDAC1 knockdown by different VDAC1 sequences attenuates glutamate-induced toxicity in HT-22 cells.**

**A**, VDAC1 knockdown by two different VDAC1 siRNA sequences was verified by RT-PCR analysis of VDAC1 mRNA (upper panels) and western blot analysis of VDAC1 protein (lower panels) 48 h after application of 20 nM VDAC1 siRNA 1 or siRNA 2. **B**, RT-PCR analysis of VDAC2 mRNA levels ruled out unspecific knockdown by VDAC1 siRNA1 and siRNA2 in concentrations of 20 nM to 80 nM. **C**, Morphological phenotype from glutamate-induced apoptosis is preserved by VDAC1 silencing. Photomicrographs (10 x 0.25 NA objective) reveal morphological changes of non-transfected HT-22 cells (vehicle) and cells transfected with scr siRNA (20 nM) 16 h after the glutamate (3 mM) challenge. **D**, **E**, Cell viability was determined by MTT assay 16 h after glutamate treatment (3 mM) of HT-22 cells transfected with the respective VDAC1 siRNA sequences (VDAC1 siRNA 1,



20 nM, **D** and VDAC1 siRNA 2, 20 nM, **E**). **D**, MTT assay confirmed the protective effect of VDAC1 siRNA 1 against glutamate toxicity. **E**, Likewise siRNA 1, VDAC1 siRNA 2 provided significant protection against glutamate toxicity. All experiments were repeated at least three times and data are provided as mean  $\pm$  SD (\*\* $p < 0.01$ , \*\*\* $p < 0.001$  compared to glutamate treated vehicle and scr siRNA, ANOVA, Scheffé's test).

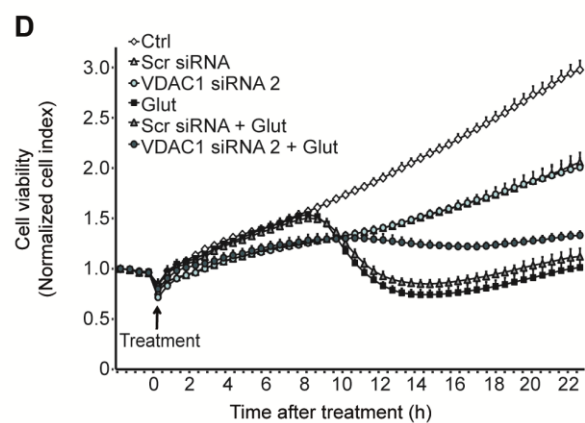
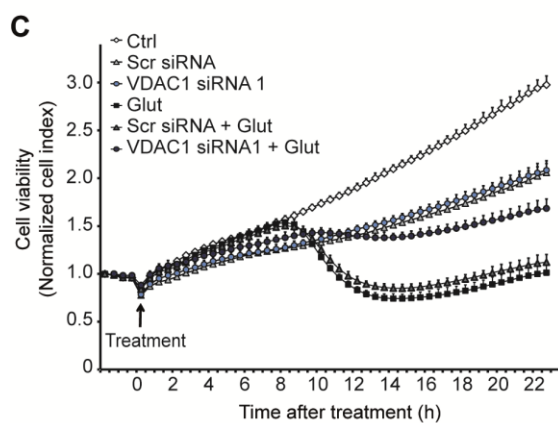
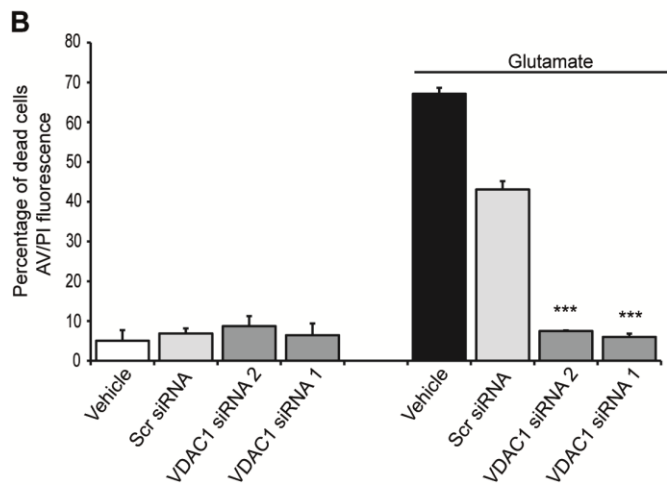
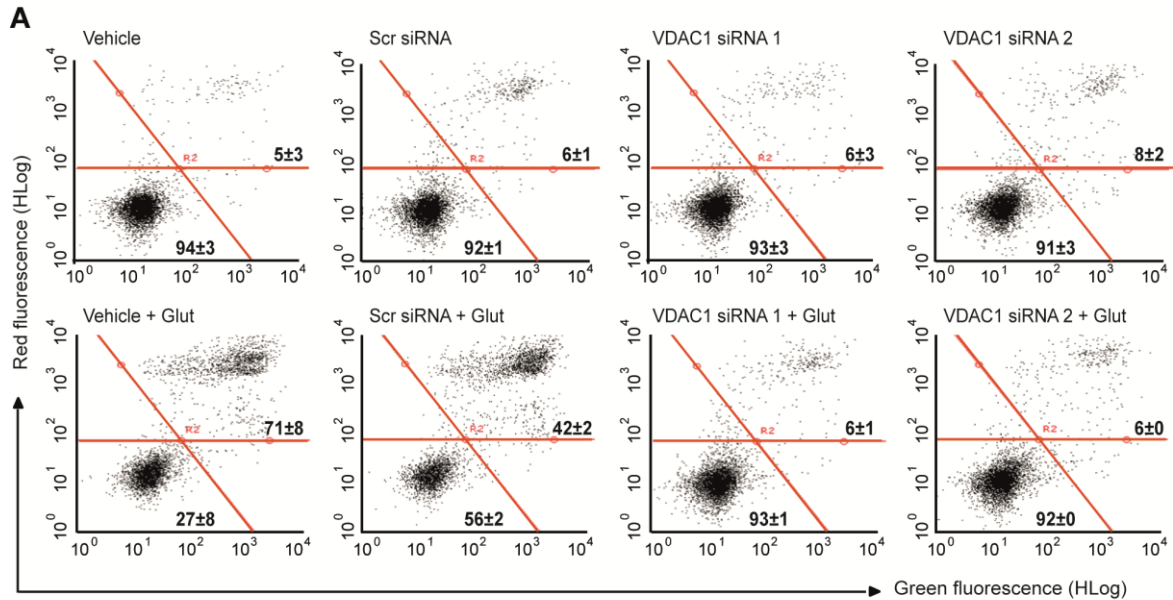


**Figure 72: VDAC1 depletion prevents glutamate-induced cell death**

VDAC1-depleted HT-22 cells are resistant to cell death induced by glutamate. **A**, HT-22 cells were transfected with either VDAC1 siRNA 1 or VDAC1 siRNA 2 (both 20 nM) and exposed to toxic glutamate solution (5 mM, 17.5 h) 24 h after transfection. FACS-analysis of annexin-V/propidium iodide-stained HT-22 cells depicts dead cells (AV+/PI+) in the upper right corner and healthy cells (AV-/PI-) in the lower left corner. Percentages of cells are provided as mean values  $\pm$  SD for three cell groups treated as indicated in the corresponding quadrants. Glut, glutamate 5 mM, 17.5 h. VDAC1 depleted cells show significantly lower percentages of AV+/PI+ cells compared to vehicle control and scrambled (scr) siRNA treated cells. **B**, Quantification of AV/PI-FACS analyses (**A**) confirmed significant prevention of cell death by both VDAC siRNAs. **C, D**, VDAC1 siRNA transfected HT-22 cells were seeded in 96-well E-plates at a density of 8,000-10,000 cells per well and cell proliferation and cell death was monitored by the real-time cell analyzer (RTCA, xCELLigence) over 23 h after exposure of cells to 4 mM glutamate. **C**, Note the persistent protective effect of VDAC1 siRNA 1 transfected cells (dark blue circle) against glutamate-induced cell death (Glut, 4 mM) compared to control (Ctrl) or scr siRNA treated cells. **D**, VDAC1 siRNA 2 transfected cells (dark green circle) are similarly protected against glutamate-induced cell death (Glut, 4 mM) as VDAC1 siRNA 1-treated cells. For statistical analysis all experiments were independently repeated three to five times with  $n=3-4$  (**A, B**) or  $n=8$  (**C, D**) per treatment condition. Data are provided as mean  $\pm$  SD (\*\*\* $p < 0.001$  compared to glutamate treated vehicle and scr siRNA, ANOVA, Scheffe 'test).

**3.4.6.2 Preservation of mitochondrial integrity and function by VDAC1 gene silencing****3.4.6.2.1 VDAC1 deficiency maintains mitochondrial energy metabolism and respiration and prevents glutamate-induced ROS formation**

Further investigations on the impact of VDAC1 in pathways of intrinsic death included measurements of ATP-levels, mitochondrial oxygen consumption rate (OCR) and ROS formation. Consistent with recent studies, revealing that down-regulation of VDAC1 decreases ATP production and cell growth<sup>39, 141</sup>, and in line with the results obtained by DIDS-mediated VDAC inhibition (Figure 60), VDAC1 depleted cells revealed reduced ATP levels under control conditions compared to vehicle or scr siRNA-treated cells (Figure 73 A, B). This reduction in basal ATP generation observed upon silencing of VDAC1 confirms the major role of VDAC1 for nucleotide transport and might be attributed to limited transport of ADP into the mitochondria followed by impaired ATP synthesis<sup>141</sup>. However, the further accelerated ATP depletion after glutamate-induced cell injury was significantly prevented by both VDAC1 siRNAs (Figure 73 A, B), confirming preserved mitochondrial integrity and active energy metabolism in VDAC1 deficient cells. Additional evidence for rescued metabolic functions in mitochondria by VDAC1 silencing was derived from OCR measurements (Figure 73 C-F). Glutamate exposure significantly reduced mitochondrial maximum respiration as well as mitochondrial respiratory capacity in control cells (non-treated and scr siRNA treated cells), whereas mitochondrial respiration remained unaffected in VDAC1-depleted cells (Figure 73 C-F). Notably, the preservation of mitochondrial energy production and respiration achieved by both VDAC1 siRNA sequences was much more pronounced than the effects obtained by DIDS (Figure 60). This might indicate that inhibition

of VDAC by DIDS is reversible and causes a transient protection, while VDAC1 gene silencing is sufficient to provide a sustained protection over time (Figure 71).

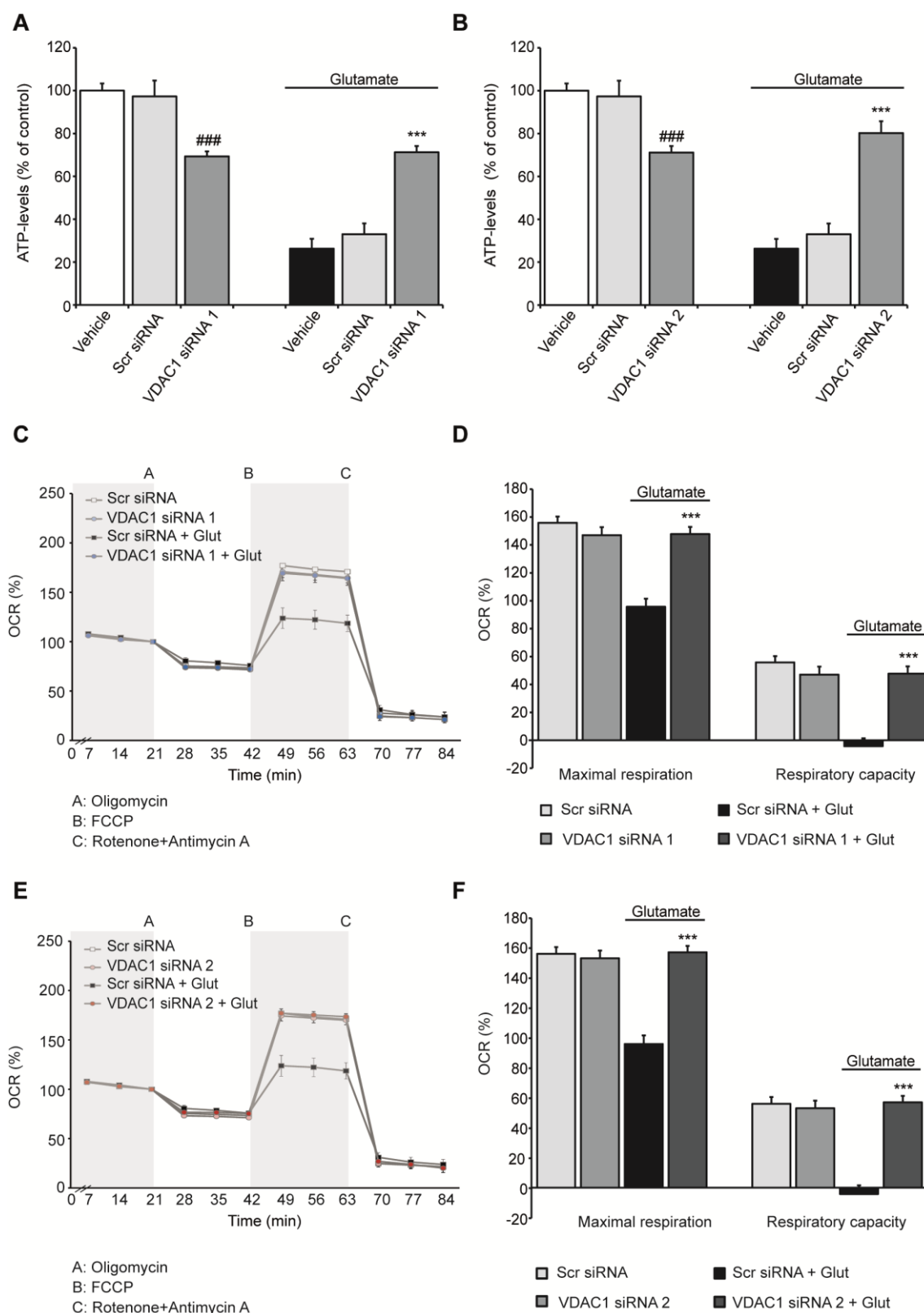


**Figure 73: VDAC1 deficiency maintains mitochondrial energy metabolism and respiration.**

HT-22 cells were transfected with scr siRNA (20 nM) or either VDAC1 siRNA 1 or VDAC1 siRNA 2 (20 nM) and treated with glutamate (4-5 mM, 17-20 h). A, B, Alteration of ATP levels by VDAC1 gene silencing were determined by ATP-luminescence measurements. ATP-levels from VDAC1 siRNA 1 (A) and VDAC1 siRNA 2 (B)

transfected HT-22 cells were analyzed in the presence or absence of glutamate (5 mM, 20 h). VDAC1 knockdown decreased ATP levels under control conditions, but restores ATP production after glutamate exposure. The experiment was repeated three times with  $n = 8$  and results are predicted mean  $\pm$  SD (#### $p < 0.001$  compared to vehicle and scr siRNA controls, \*\*\* $p < 0.001$  compared to glutamate treated vehicle and scr siRNA treated cells, ANOVA, Scheffé's test). C-F, VDAC1 siRNA preserves mitochondrial maximum respiration and respiratory capacity. Mitochondrial respiration, indicated as oxygen consumption rate (OCR) was analyzed by the Seahorse Bioscience system using the XF Mito Stress kit. D, E, Quantification of OCR revealed percentages of mitochondrial maximum respiration and respiratory capacity in VDAC1 depleted HT-22 cells compared to untransfected controls and scrambled (scr) siRNA transfected cells. VDAC depletion does not affect mitochondrial respiration under control conditions and preserves mitochondrial respiratory function after the onset of glutamate exposure. Experiment was independently repeated 5 times with  $n = 6$  and data are provided as mean  $\pm$  SD (\*\*\* $p < 0.001$  compared to scr siRNA treated cells, ANOVA, Scheffé's test).

Furthermore, VDAC1 deficiency protected against increases in ROS as shown by the determination of lipid peroxides 18 h after the onset of glutamate (Figure 74 A, B), suggesting a strong impact of VDAC1 on Bid-dependent irreversible mitochondrial damage and the subsequently accelerated ROS formation<sup>116</sup>. Overall, these data indicate a clear involvement of VDAC1 in intrinsic death pathways established at the level of mitochondria in the applied model of glutamate toxicity. It appeared that a disturbed interaction between VDAC1 and Bid was the underlying mechanism of the protective effects mediated by VDAC1 silencing.

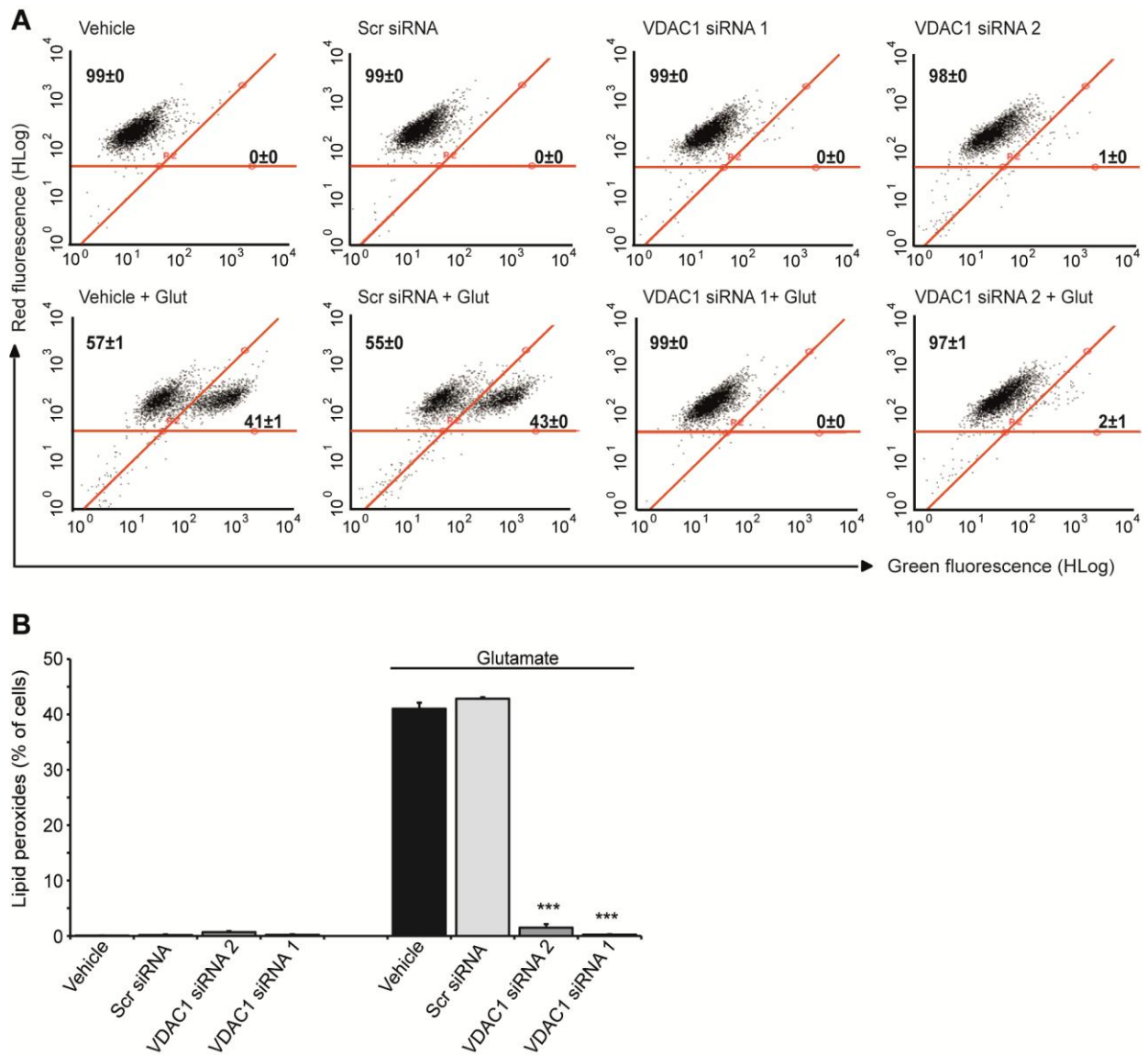


**Figure 74: Glutamate-induced ROS production is prevented by VDAC1 silencing.**

**A, B** BODIPY-FACS analysis of lipid peroxidation in HT-22 cells transfected with VDAC1 siRNA 1 or VDAC1 siRNA 2 (both 20 nM) in comparison to control and scrambled (scr) siRNA transfected cells. The pronounced formation of lipid peroxides 18 h after the onset of glutamate exposure (4 mM) was significantly prevented by VDAC1 silencing as fluorescence detection of ROS revealed a significant reduction in green fluorescence in VDAC1 depleted cells compared to vehicle and scr siRNA transfected cells. Values are averages (%)  $\pm$  SD for three indicated treatment groups, each with 10,000 cells per flow measurement. Low green fluorescence represents healthy cells without lipid peroxidation (upper left corner) whereas high values of green fluorescence indicate increased formation of lipid peroxides in apoptotic cells (upper right corner). **B**, Quantification of lipid peroxides in in VDAC1-depleted HT-22 cells confirms that VDAC1 deficiency completely prevents the formation of ROS 18 h after the onset of glutamate (4 mM). The experiments were repeated three times and the results presented as mean  $\pm$  SD (\*\*\*)  $p < 0.001$  compared to scr siRNA treated cells, ANOVA, Scheffé's test).

### 3.4.6.2.2 VDAC1 is required for Bid-mediated mitochondrial injury

Recent studies revealed a pivotal role of Bid in the balance of mitochondrial fission and fusion, and a Bid-mediated permeabilization of the outer mitochondrial membrane<sup>24, 97, 200</sup>. The channel porin VDAC1 is also thought to participate in mitochondrial-membrane permeabilization, loss of  $\Delta\psi_m$ , and the release of pro-apoptotic mitochondrial proteins, such as cytochrome c, AIF and Smac/DIABLO<sup>143, 144, 159, 160, 245</sup>. The precise mechanism of VDAC1 activation towards mitochondrial impairment, however, is not yet clarified and remains highly controversial<sup>144, 151</sup>. To further investigate whether the direct interaction between Bid and VDAC1 provides a convergence point in the aforementioned mechanisms, it should be examined whether the protective effect of pharmacological VDAC inhibition and VDAC1 depletion in the model of glutamate-induced toxicity was associated with preserved mitochondrial morphology and membrane potential.

In agreement with previous findings and the results presented above, glutamate exposure triggered detrimental mitochondrial fission (Figure 75 A)<sup>24, 200</sup> in HT-22 cells, whereas VDAC1 gene silencing sustained the native-like mitochondrial morphology (category I) and prevented the peri-nuclear accumulation of the fragmented organelles (category III) (Figure 75 A). Quantification of changes in mitochondrial morphology confirmed the glutamate-induced shift from cells containing long elongated mitochondria (category I) to damaged cells containing highly fragmented organelles (category III) that was significantly prevented by both VDAC1 siRNAs (Figure 75 B, C).

These findings are in line with further effects of VDAC1 siRNA towards the integrity of mitochondrial membranes. FACS analysis of TMRE-stained HT-22 cells revealed that both VDAC1 siRNAs prevented the loss of  $\Delta\psi_m$  (Figure 76 A, B), a key event of glutamate- and tBid-induced cell injury<sup>24, 246</sup>.

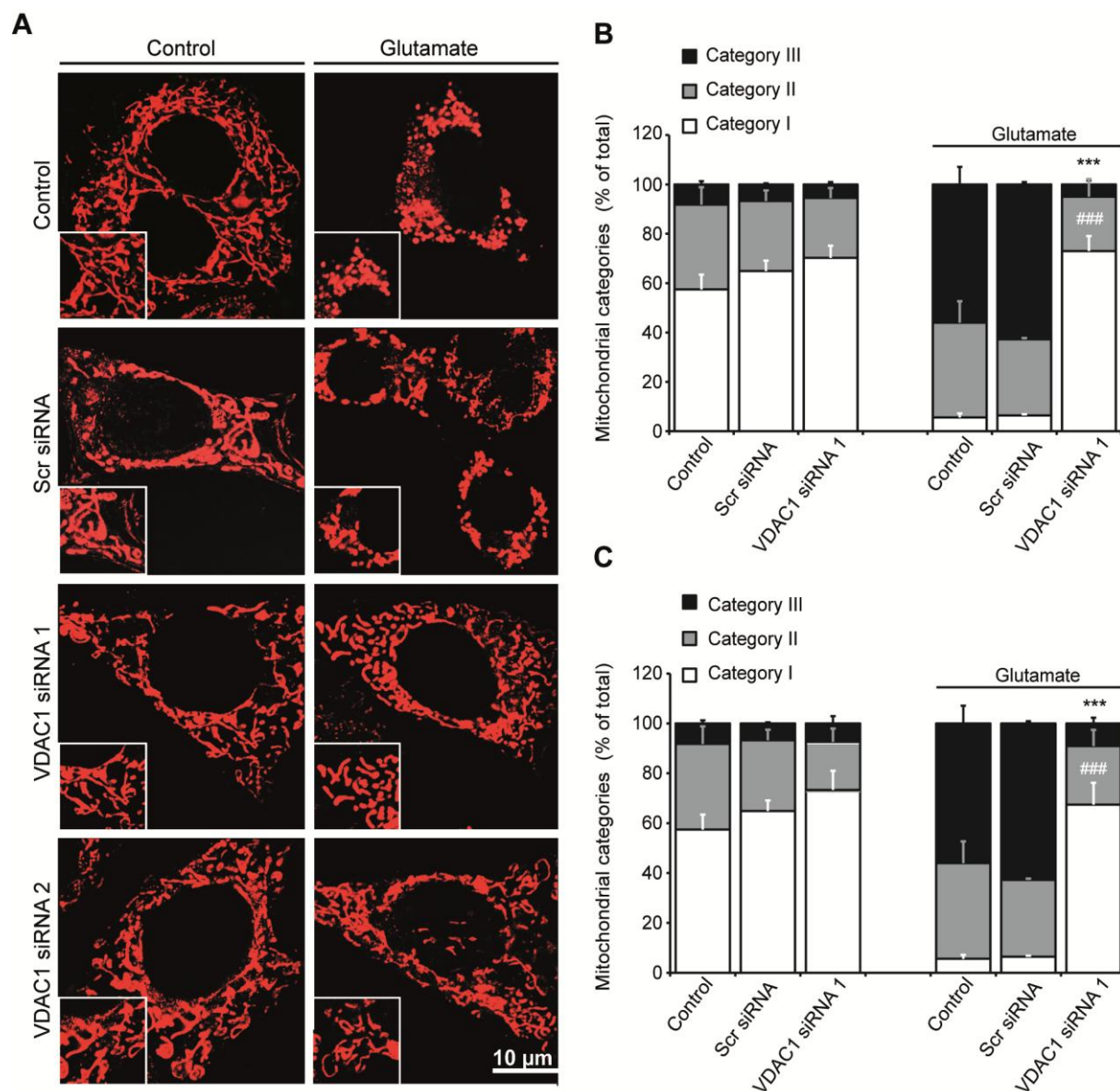


**Figure 75: VDAC1 depletion prevents glutamate-induced mitochondrial fission.**

**A**, Confocal fluorescence photomicrographs reveal protection against glutamate-induced mitochondrial fragmentation in VDAC1 siRNA 1 and VDAC1 siRNA 2 (both 20 nM) transfected HT-22 neurons. Cells were stained with MitoTracker red 30 min before glutamate treatment (5 mM, 17 h). Glutamate induced mitochondrial fission in control vehicle and *scr* siRNA transfected cells, which is prevented by VDAC1 gene depletion. **B**, **C**, Quantification of mitochondrial morphology: Category 1: elongated, fused mitochondria distributed throughout the whole cytosol, category II: intermediate, slightly fragmented mitochondria and category III strongly fragmented mitochondria and peri-nuclear accumulation of the organelles. Data represent the mean  $\pm$  SD of three independent experiments ( $###p < 0.001$  compared to category I glutamate treated control and *scr* siRNA;  $***p < 0.001$  compared to category III glutamate treated control and *scr* siRNA, ANOVA, Scheffé's test).



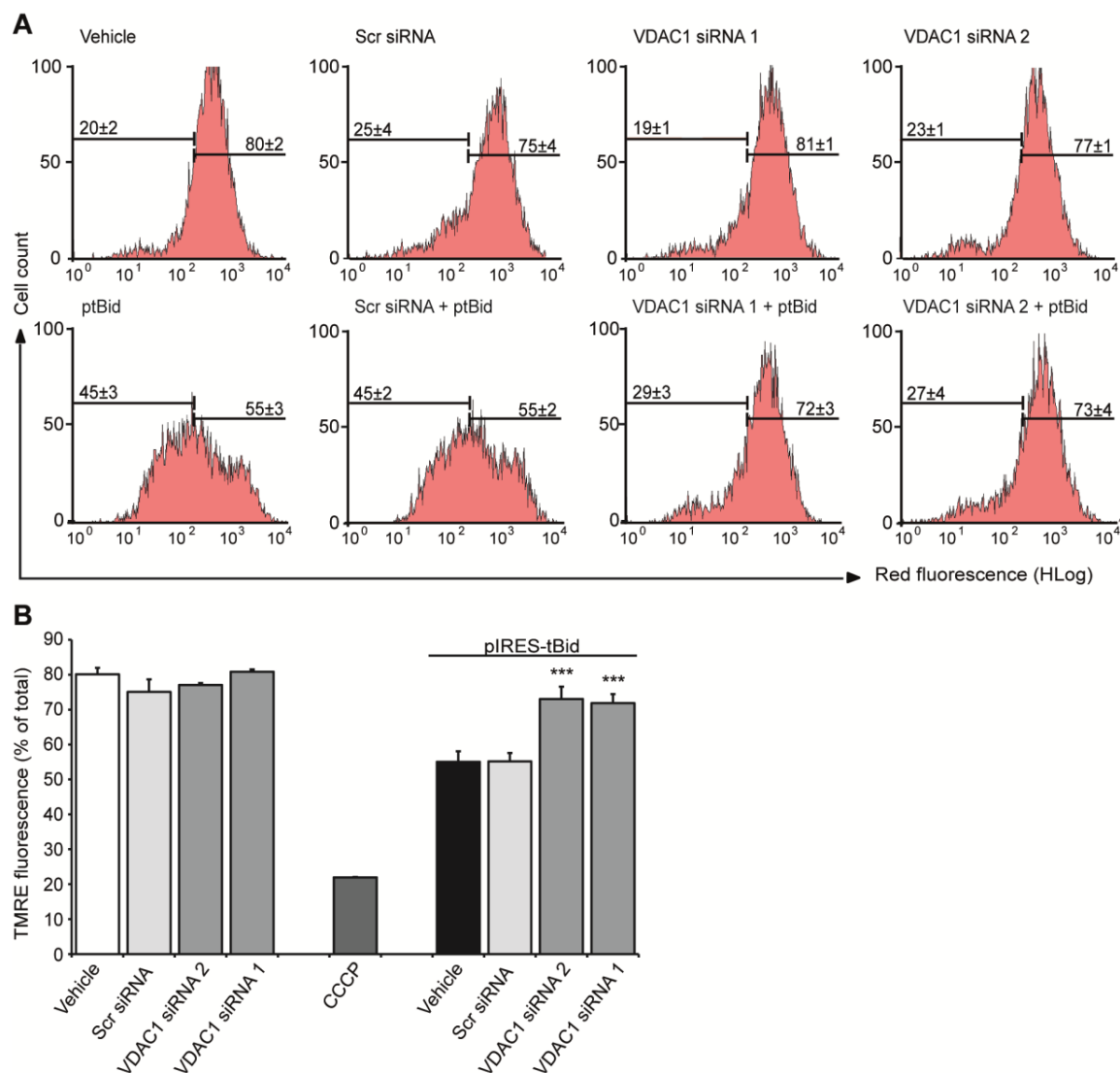


**Figure 76: Preservation of mitochondrial membrane potential by VDAC1 gene silencing.**

HT-22 cells were cultured in 24-well plates at a density of 33,000 cells per well and transfected with either VDAC1 siRNA 1 or VDAC1 siRNA 2 (both 20 nM). **A**, TMRE-FACS recordings of mitochondrial membrane potential ( $\Delta\psi_m$ ) were performed 17 h after glutamate treatment (4 mM) and staining of HT-22 cells with MitoPT™ TMRE dye. Glutamate exposed vehicle and *scr* siRNA transfected HT-22 cells showed significant reduction of red fluorescence, indicating loss of  $\Delta\psi_m$ , while both VDAC1 siRNAs prevented breakdown of  $\Delta\psi_m$  as indicated by preservation of red fluorescence comparable to control cells. Numbers are mean percentages  $\pm$  SD of TMRE fluorescence for  $n=3$  indicated treatment groups. High red fluorescences indicate intact mitochondria (right side), drop of red fluorescence depict loss of  $\Delta\psi_m$  (left side). **B**, Quantification of TMRE fluorescence (**A**) confirms the preservation of  $\Delta\psi_m$  in VDAC1 depleted HT-22 cells. CCCP was used as the positive damage-control for a fast depolarization of the mitochondrial membrane. The experiment was independently repeated four times and values are given as mean  $\pm$  SD (\*\* $p < 0.001$  compared to glutamate-treated vehicle and *scr* siRNA treated cells, ANOVA, Scheffé's test).



### 3.4.6.3 tBid is not able to induce loss of $\Delta\psi_m$ and cell death without functional VDAC1

The observation that the pronounced protection against various hallmarks of glutamate toxicity achieved by DIDS (3.4.2) as well as by VDAC1 gene silencing was similar to the protective effects of the Bid inhibitor BI-6c9 (3.1)<sup>24, 116, 200</sup> and comparable to the sustained protective effects of Bid gene silencing as shown in previous studies<sup>63, 97</sup>, strongly strengthened the hypothesis that the direct interaction between both proteins represents the mechanism behind Bid-mediated impairments of mitochondrial integrity and function. To confirm that both Bid and VDAC1, are indeed equally involved in the mechanisms of intrinsic cell death, HT-22 cells were transfected with a tBid-encoding plasmid (ptBid), and various endpoints of cell death were investigated in the presence or absence of VDAC1 protein expression. Over-expression of tBid induced the described characteristic alteration in the morphology (vehicle, *scr* siRNA, see also 3.1.2), contrary to VDAC1-silenced cells whose morphology remained unaffected (Figure 77 A). FACS analysis after annexin-V/propidium iodide-staining confirmed the protective effect of VDAC1 deficiency against tBid-induced toxicity (Figure 77 B, C).

VDAC1 could finally be confirmed as a required target for tBid-mediated loss of  $\Delta\psi_m$  (Figure 78 A, B). TMRE staining of tBid-over-expressing HT-22 cells (ptBid, *scr* siRNA + ptBid) revealed a tBid-induced decline in  $\Delta\psi_m$  by approximately 40 % of control cells, which was completely prevented by VDAC1 gene silencing (Figure 78 A, B). The fact that tBid caused neither breakdown of  $\Delta\psi_m$  nor cell death at all in VDAC1 depleted cells confirmed that a direct interplay between tBid and VDAC1 is required to induce toxicity.

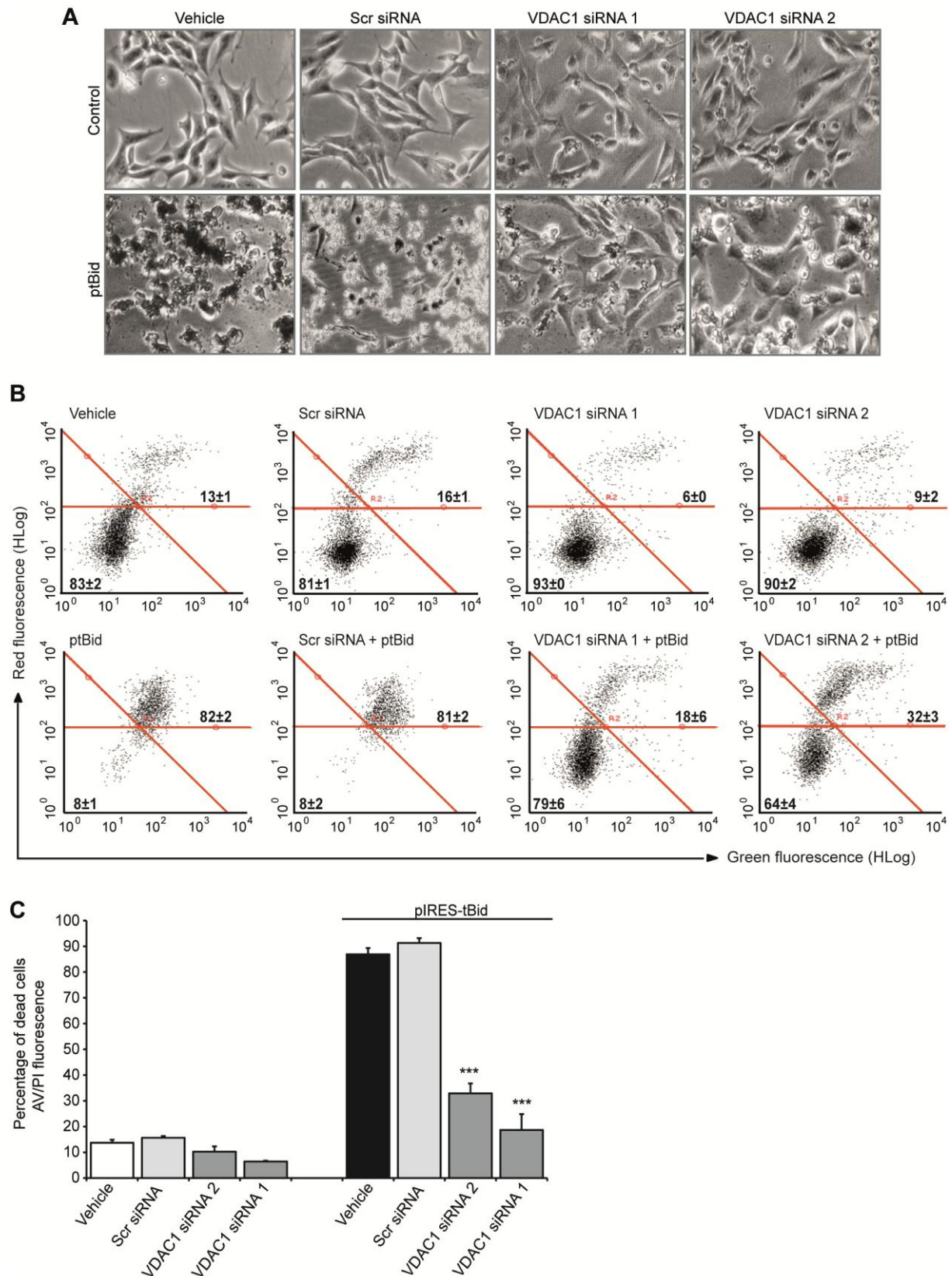


**Figure 77: VDAC1 siRNA 1 and siRNA 2 prevent tBid-induced toxicity.**

HT-22 cells transfected with VDAC1 siRNA 1 or VDAC1 siRNA 2 (both 20 nM) were post-transfected (24 h) with a tBid encoding plasmid (ptBid). Cells treated only with attractene (vehicle) or *scr* siRNA transfected cells were used as controls. Seventeen to eighteen hours after tBid over-expression cell morphology (A) and cell death (B, C) were analyzed. **A**, Photomicroscopy (10 x 0.25 NA objective) reveals that VDAC1-depletion preserves the spindle-shape morphology of HT-22 cells 17 h after tBid over-expression (ptBid) compared to vehicle and *scr*

siRNA treated cells which show extensive morphological alterations: cells appear shrunken, rounded up and detach from the bottom of the culture dishes. **B**, FACS-recordings of annexin-V/propidium iodide stained HT-22 cells show resistance of VDAC1-depleted cells to tBid-induced cell death. HT-22 cells were stained with AV/PI and 10,000 cells per treatment condition were analyzed for cell death by flow cytometry (AV<sup>+</sup>/PI<sup>+</sup>: dead cells, upper right corner, AV<sup>+</sup>/PI<sup>-</sup>: healthy cells, lower left corner) Numbers are mean values (%)  $\pm$  SD for three indicated treatment groups in the corresponding quadrants. **C**, Quantification of AV<sup>+</sup>/PI<sup>+</sup> cells confirmed that VDAC1 depleted cells (VDAC siRNA 1 and 2) are protected against tBid- induced cell death. All experiments were independently repeated three to five times and results are reported as mean  $\pm$  SD (\*\*\*p < 0.001 compared to pIRES-tBid transfected vehicle and *scr* siRNA treated cells, ANOVA, Scheffé's test).

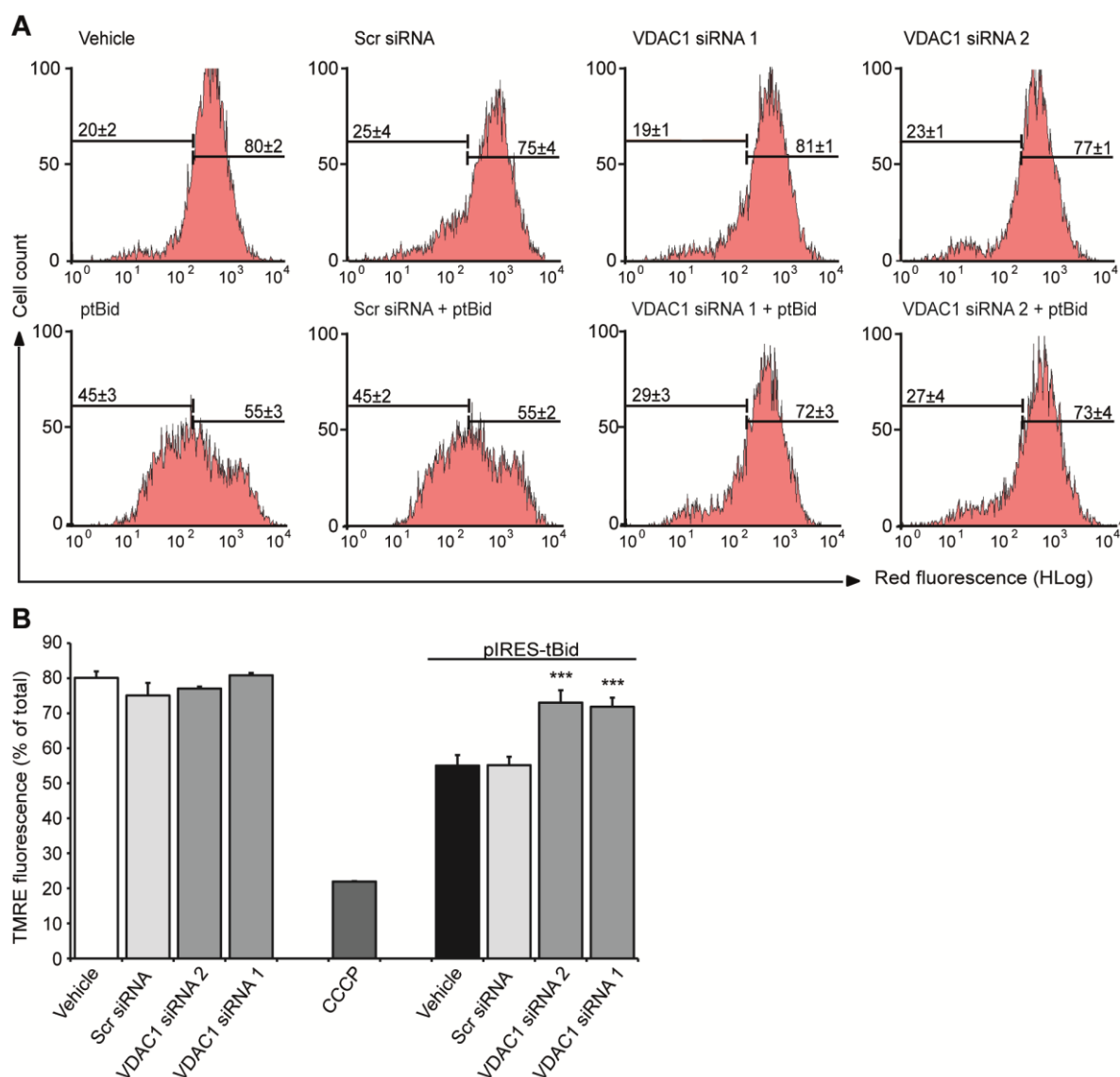


**Figure 78: VDAC1 silencing prevents tBid-induced loss of  $\Delta\psi_m$ .**

TMRE-FACS measurements of mitochondrial membrane potential 18 hours after tBid over-expression. **A**, HT-22 cells were transfected with VDAC1 siRNA 1 or VDAC1 siRNA 2. Cells transfected with an empty pcDNA3.1+ vector were used as control (vehicle). After tBid-induced cell death was morphological detectable, all treatments groups were stained with MitoPT<sup>TM</sup> TMRE dye and fluorescence was detected by FACS measurements. Numbers are mean percentages  $\pm$  SD of  $n = 3$  per treatment group, indicating loss of  $\Delta\psi_m$  (left side) or intact  $\Delta\psi_m$  (right side). The tBid-induced drop in red fluorescence was prevented in VDAC1-depleted cells compared to cells transfected with scramble (*scr*) siRNA. **B**, Quantification of TMRE fluorescence revealed significant loss of  $\Delta\psi_m$  in cells over-expressing tBid which was restored by both VDAC1 siRNA sequences. The experiment was

independently repeated five times and data are reported as mean  $\pm$  SD (\*\*p < 0.001 compared to pIRES-tBid transfected vehicle and *scr* siRNA, n=3, ANOVA, Scheffé test).

#### 3.4.6.4 VDAC1 induced cytotoxicity requires Bid

*Vice versa*, it was previously reported that VDAC1 over-expression induces depolarization of the inner membrane<sup>147</sup> and thereby apoptotic cell death characterized by enhanced nuclear fragmentation<sup>141, 149</sup>. Such VDAC1 induced toxicity could be blocked by different agents shown to inhibit VDAC channel activity, e.g. DIDS<sup>148</sup>, ruthenium red (RuR) or hexokinase (HK)<sup>149</sup>, substantiating that VDAC1 expression levels appear to be critical for mitochondria mediated apoptosis. Nevertheless, it was still questioned how the enhanced VDAC1 expression causes cell death. To further investigate whether the proposed interaction between Bid and VDAC1 is important for VDAC1 induced cytotoxicity, HT-22 cells were transfected with FLAG-tagged VDAC1 and analyzed by fluorescent confocal microscopy (Figure 79 A, B, Figure 80 A, B). Although VDAC1 is present in high abundance in the mitochondrial outer membrane (OMM), various studies have revealed that VDAC is also localized at low abundance to cell compartments other than mitochondria<sup>247-249</sup>. To confirm the mitochondrial localization of the over-expressed FLAG-VDAC1, mitochondria of HT-22 cells were visualized by co-transfection of cells with mito-GFP or by staining with MitoTracker red. Confocal microscopy pictures revealed the co-localization of FLAG-VDAC1 and mito-GFP as well as the VDAC1 co-localization with MitoTracker red stained mitochondria, both confirming the localization of FLAG-VDAC1 in the OMM (Figure 79 A, B, merge, Figure 80 A, B). Of note, co-localization was not completely observed, indicating the partial exposure of VDAC1 to the cytoplasm as also expected by previous studies<sup>137, 250</sup>.

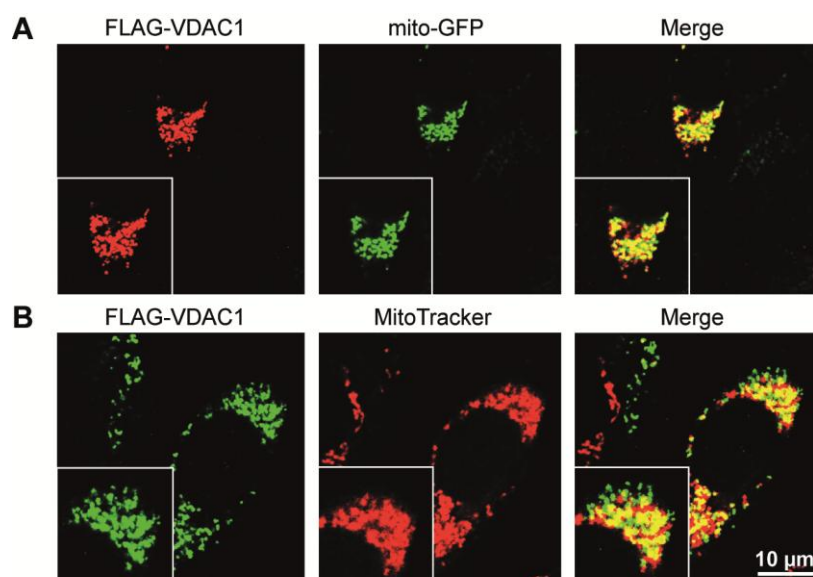


**Figure 79: Mitochondrial localization of FLAG-VDAC1**

Localization of FLAG-VDAC1 in the mitochondrial outer membrane was confirmed by confocal fluorescence microscopy. **A**, HT-22 cells were co-transfected with plasmids encoding FLAG-VDAC1 and mito-GFP. 24 h- 48 h after transfection, FLAG-VDAC1 was immunostained using the primary anti-FLAG antibody and the secondary Dylight 648 antibody. Confocal fluorescence microscopy revealed the co-localization of FLAG-VDAC1 and mito-GFP (merge), indicating the mitochondrial localization of over-expressed VDAC1. **B**, Co-localization of VDAC1 and mitochondria was confirmed by immunostaining of FLAG-VDAC1 with the Alexa Fluor 488 antibody (green) and visualization of mitochondria by MitoTracker red. Note, that co-localization appears not completely, indicating the localization of VDAC1 in the outer mitochondrial membrane with the C-terminus outside of mitochondria.

Twenty four to forty eight hours after plasmid transfection, VDAC1 over-expression resulted in cell death, as characterized by fragmented mitochondria and rounded cells (Figure 80 A, upper panel, Figure 80 B, lower panel), indicating that mitochondrial injury and cell death was triggered by VDAC1 expression levels. In contrast, control cells only transfected with mito-GFP showed elongated mitochondria and spindle-like cell morphology (Figure 80 B, upper panel). In continuation, it was examined, if the VDAC1-induced cytotoxicity is linked to the pro-apoptotic effects of Bid. Interestingly, pre-incubation of cells with 10  $\mu$ M of the Bid inhibitor BI6c9 preserved cell morphology and prevented death of VDAC1 transfected cells (Figure 80 A, lower panel). Since mitochondria of FLAG-VDAC1 over-expressing cells appeared highly fragmented, whereas mitochondria in mito-GFP transfected cells remained elongated, it is likely that VDAC1 over-expression causes toxicity via detrimental effects at the level of mitochondria. The results substantiated the required association of both proteins and suggested that the Bid inhibitor BI6c9 interfered with VDAC1-Bid interactions thereby protecting the cells against cell death induced by VDAC1 over-expression.

In conclusion, these data demonstrate a direct interaction of tBid and Bid with the mitochondrial porin VDAC1, which is obviously highly relevant for determining mitochondrial demise and intrinsic cell death in cultivated cells and *in vivo*. The results predict that neither tBid nor VDAC1 alone are able to trigger mitochondrial injury and cell death without their

respective binding partner. This finding strongly indicates that the proposed Bid-VDAC1 interaction provides a converging point for the mechanisms of MOMP that were previously considered separately, as they were either contributed solely to the Bcl-2 family proteins or to VDACs.

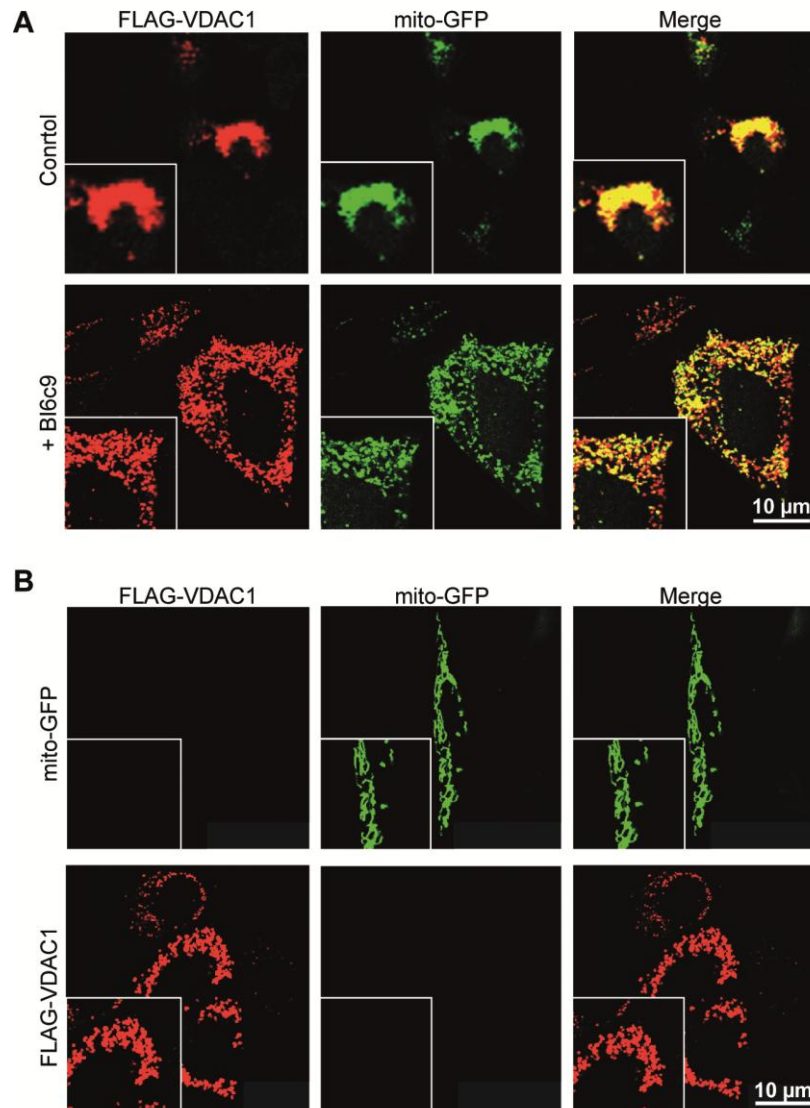


**Figure 80: VDAC1 induced cytotoxicity is inhibited by the Bid inhibitor BI6c9.**

HT-22 cells were co-transfected with FLAG-VDAC1 and mito-GFP in the presence and absence of the Bid inhibitor BI6c9 (10 μM). Localization of VDAC1 and cell morphology was analyzed by confocal fluorescence microscopy 24-48 h after plasmid transfection and immunostaining of FLAG-VDAC1 using the anti-FLAG antibody followed by incubation with Dylight 648. Pictures were taken immediately after immunostaining. **A**, Localization of VDAC1 in the mitochondrial outer membrane was confirmed by co-localization of VDAC1 with mito-GFP. Note, that over-expression of FLAG-VDAC1 resulted in highly fragmented mitochondria, the perinuclear accumulation of the organelles and rounded cells (A, upper panel, B, lower panel). Pre-incubation of HT-22 cells with the Bid inhibitor BI-6c9 (10 μM) prevented the VDAC1-induced cytotoxicity (A, lower panel). **B**, Confocal fluorescence microscopy of control cells transfected only with mito-GFP (upper panel) or FLAG-VDAC1 (lower panel), respectively. Note, that mito-GFP-transfected control cells show elongated mitochondria distributed through the whole cytosol (B, upper panel), whereas cells transfected with FLAG-VDAC1 revealed category II to category III mitochondria (B, lower panel).



### 3.5 VDAC2 plays a minor role in neuronal intrinsic cell death pathways

Besides the involvement of VDAC1 in the regulation of mitochondrial membrane depolarization and the following apoptotic pathways, the mitochondrial outer membrane protein VDAC2, a VDAC isoform present in low abundance<sup>251</sup>, has been recently described as a crucial component in mitochondrial cell death signaling<sup>93, 251, 252</sup>, recruiting pro-apoptotic Bcl-2 family proteins to the outer mitochondrial membrane (OMM)<sup>93</sup>. Interestingly, in non-neuronal mouse embryonic fibroblasts (MEFs) a regulatory function of VDAC2 in the Bak-mediated cell death cascade has been described by linking the isoform to tBid-mediated loss of  $\Delta\Psi_m$  and cell death<sup>93</sup>. These studies suggested that a direct association between VDAC2 and Bak inhibits Bak activation and apoptosis and further reported a tBid-mediated Bak displacement from the VDAC2-Bak complex and thereby a tBid-induced recruitment of Bak to the mitochondria<sup>93</sup>. While these studies revealed a specific involvement of VDAC2 in non-neuronal apoptosis, the role of VDAC2 in neuronal cell death is unknown so far. Therefore, the further work addressed the question, if a regulatory role of VDAC2 can be also determined in the neuronal Bid-mediated death signaling, or if the described Bid-VDAC1 interaction might be the neuronal mirror of the emerging non-neuronal tBid-VDAC2-Bak concepts of apoptosis.

#### 3.5.1 VDAC2 gene silencing provides only transient protective effects against glutamate-induced toxicity

To investigate the role of VDAC2 in neuronal cell death, the impact of VDAC2 gene depletion was analyzed in the model of glutamate-induced toxicity in HT-22 cells.

Specific down-regulation of VDAC2 in HT-22 neurons was achieved by transfection of cells with two different sequences of VDAC2-targeting siRNA (VDAC2 siRNA a and VDAC2 siRNA b) at concentrations of 20 nM, 40 nM and 80 nM (Figure 81 A-D). Both sequences of VDAC2 siRNA were sufficient to reduce cellular VDAC2 mRNA- as well as VDAC2 protein-levels as verified by RT-PCR (Figure 81 A, C) and western blot analysis (Figure 81 B, D). Of note, concentrations of 20 nM siRNA reduced VDAC2 mRNA-levels by approximately 40% compared to vehicle and scramble siRNA-treated cells, whereas a complete deficiency of VDAC2 mRNA was obtained at siRNA-concentrations of 40 nM and 80 nM (Figure 81 A). Therefore, further functional analyses were performed using 40 to 80 nM of siRNA approach. Determination of VDAC1 mRNA expression levels confirmed a specific targeting of VDAC2 by both VDAC2 siRNAs at concentrations of 40-80 nM (Figure 81 E).

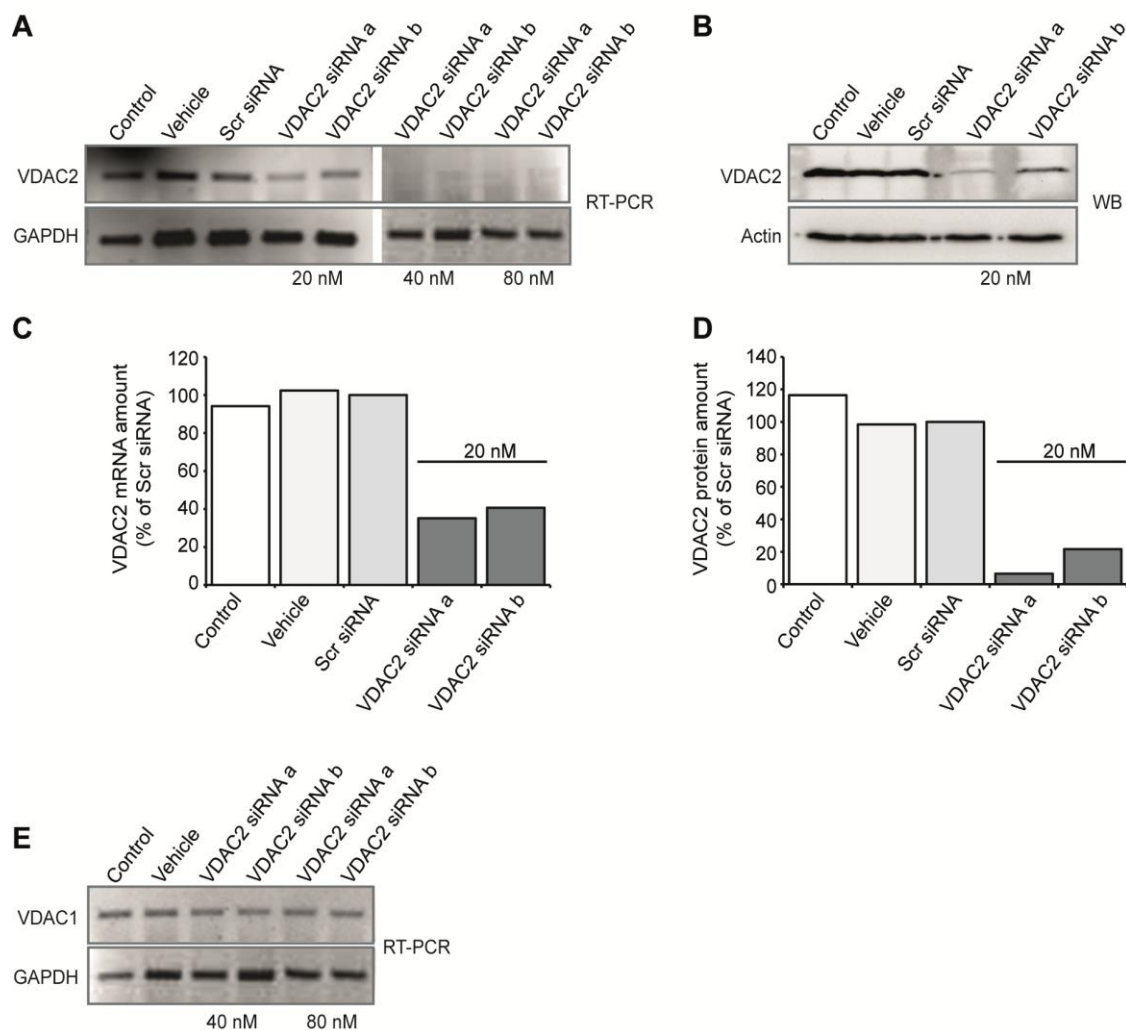


**Figure 81: VDAC2 gene silencing by two different VDAC2 siRNA sequences.**

HT-22 cells were transfected with two different sequences of VDAC2 siRNA (siRNA a and siRNA b) at concentrations of 20 ng, 40 ng and 80 ng. Specific knockdown of VDAC2 was verified by RT-PCR (**A**) and western blot analysis (**B**) 48 h after transfection of HT-22 cells. VDAC2 expression of VDAC2 siRNA transfected cells was compared to non-transfected cells (control), cells treated with the transfection reagent Lipofectamin RNAiMax (vehicle) and cells transfected with non-functional scrambled siRNA (*scr* siRNA). **C**, Quantification of VDAC2 mRNA amount 48 h after transfection of HT-22 with 20 nM VDAC2 siRNA a and VDAC2 siRNA b. **D**, Quantification of VDAC2 protein amount 48 h after transfection of HT-22 with 20 nM VDAC2 siRNA a and VDAC 2 siRNA b. **E**, Unspecific knockdown of VDAC1 by VDAC2 siRNA was ruled out by PCR analysis. Data are representatives of 3-5 independent transfection experiments.

The effect of VDAC2 deficiency upon apoptosis was investigated by analyses of cell morphology and cell viability of HT-22 cells 16-18 h after the onset of glutamate exposure. In contrast to the reported results in VDAC2-depleted MEF cells<sup>93</sup>, revealing a resistance of VDAC2<sup>-/-</sup> cells to tBid-mediated apoptosis, VDAC2 deficiency was only slightly protective in HT-22 neurons. After glutamate exposure, HT-22 cells showed their typical morphological phenotype, which was only partly protected by VDAC2 silencing using VDAC2 siRNA a. However, a more pronounced protection against glutamate cytotoxicity was achieved by transfection of cells with VDAC2 siRNA b, preserving the spindle shape cell morphology



(Figure 82 A). This observation could be confirmed by FACS-analysis of annexin-V/propidium iodide-stained HT-22 neurons (Figure 82 B, C), depicting no significant protection of cells treated with VDAC2 siRNA a. In contrast, VDAC2-depletion by VDAC2 siRNA b attenuated glutamate-toxicity by approximately 40% compared to glutamate-treated control cells (Figure 82 B, C). Quantification of cell viability determined by MTT assay finally substantiated the lack of protection by VDAC2 siRNA a, yet a concentration-dependent enhancement of cell viability in cells transfected with VDAC2 siRNA b (Figure 82 D). Since control scrambled siRNA could not attenuate cell viability after glutamate-induced damage in HT-22 cells, un-specific effects of the siRNA approach were ruled out (Figure 82 A-D).

Since potency and time of protection varies in different experiments depending on the cell passage, density and thereby glutamate-sensitivity of HT-22 cells, the protective potential of VDAC2 silencing was further analyzed by real-time detection of cell death using the xCELLigence system (Figure 83 A, B). Therefore, cell impedance of HT-22 neurons, transfected as indicated, was monitored over at least 18 h after glutamate-treatment, revealing a delayed cell death in VDAC2 siRNA b transfected cells (Figure 83 B) up to a persistent protection at a siRNA concentration of 80 nM. In line with the cell viability data obtained by FACS and MTT analysis, transfection of cells with VDAC2 siRNA a achieved only a short and transient protective effect with a delay of cell death of 1-3 hours compared to controls exposed to glutamate (Figure 83 A).

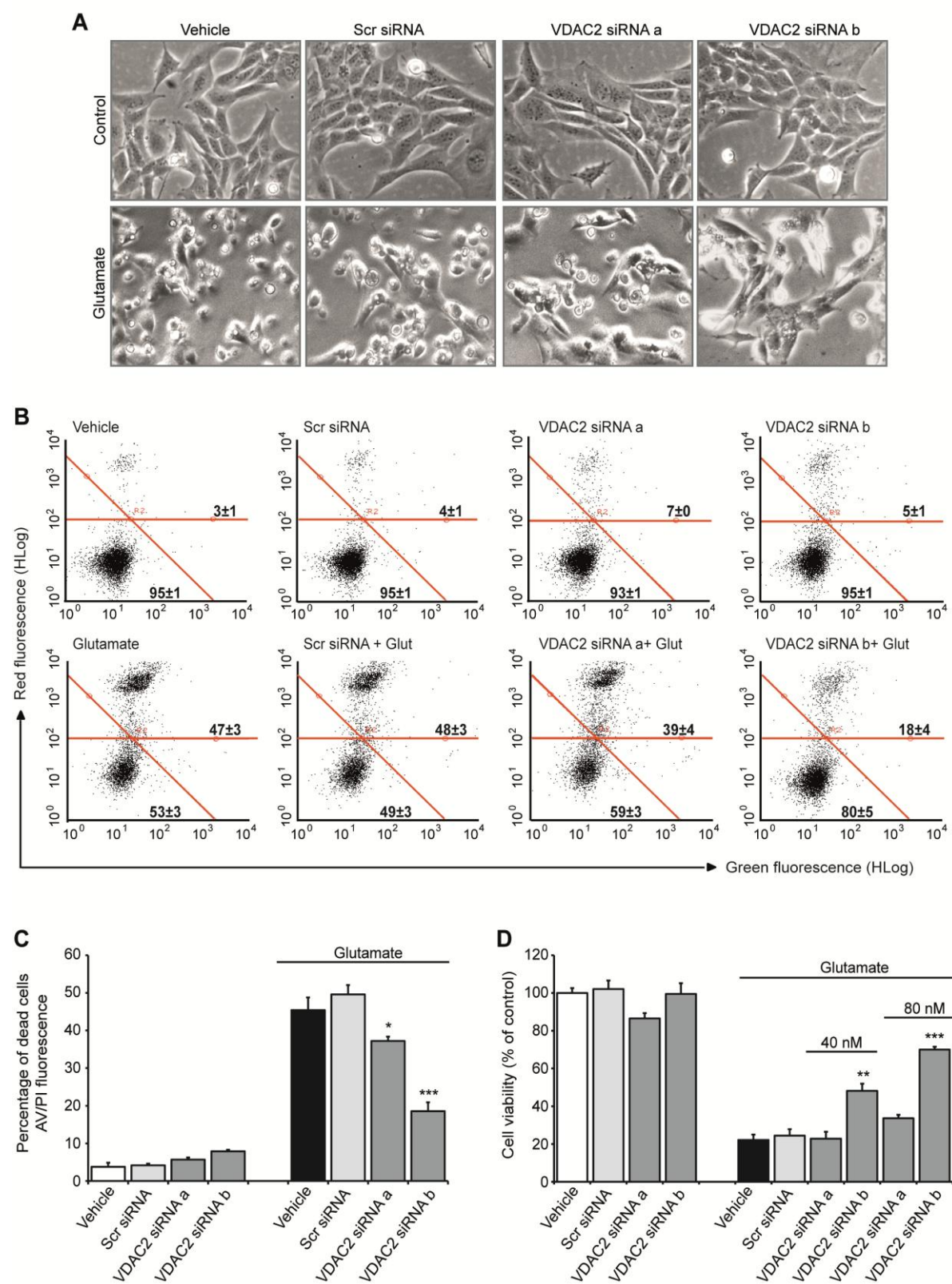


**Figure 82: VDAC2 knockdown by different VDAC2 siRNA sequences provides slight protection against glutamate toxicity.**

HT-22 cells were transfected with VDAC2 siRNA a and VDAC2 siRNA b (40 nM and 80 nM) and challenged with glutamate (4 mM) 48 h after transfection. **A**, Photomicrographs (10 x 0.25 NA objective) reveal the phenotype of glutamate-induced cell death, which is slightly prevented by VDAC2 siRNA a and VDAC2 siRNA b (both 40 nM). **B**, FACS analysis of annexin-V/propidium iodide-stained HT-22 cells depicts dead cells in the upper right corner

and healthy cells in the lower left corner. Glutamate induced cell death of about 47-48% in vehicle and *scr* siRNA treated cells, which is only prevented by knockdown of VDAC2 using VDAC2 siRNA b. Numbers are mean percentages  $\pm$  SD for three cell groups treated as indicated in the corresponding quadrants. Glut, Glutamate, 4 mM. **C**, Quantification of AV<sup>+</sup>/PI<sup>-</sup>-stained HT-22 cells 48 h after transfection with 40 nM of either VDAC2 siRNA a or VDAC2 siRNA b and the onset of glutamate exposure (4 mM, 16-18 h) confirms slightly protective effects of VDAC2 siRNA a, that are achieved more pronounced by VDAC2 siRNA b (\* $p < 0.05$ ; \*\*\* $p < 0.001$ ;  $n=4$ , compared to glutamate-treated vehicle and scrambled (*scr*) siRNA). **D**, MTT assay 65 h after transfection with both VDAC2 siRNA sequences at concentrations of 40 nM and 80 nM confirms a concentration-dependent protection of VDAC2 siRNA b, while no significant protection was obtained by VDAC2 siRNA a (\*\* $p < 0.01$ ; \*\*\* $p < 0.001$ ;  $n=8$ , compared to glutamate-treated vehicle and scrambled (*scr*) siRNA). All experiments were repeated at least three times and data are provided as mean  $\pm$  SD with  $n=4-8$ . All statistics were obtained using ANOVA, Scheffé's test.

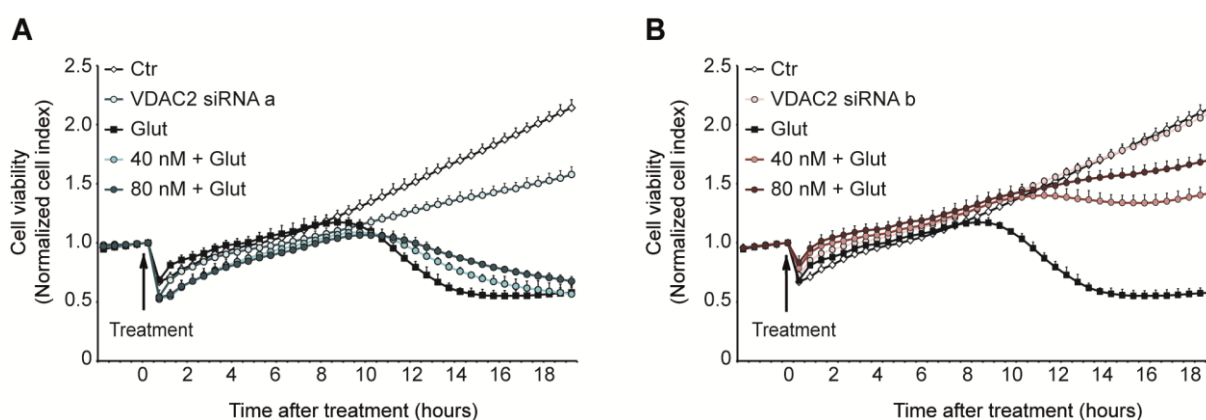


**Figure 83: VDAC2 siRNA attenuates glutamate-induced cell death in a concentration-dependent manner.**

**A, B**, HT-22 cells were cultured in 96-well E-plates at densities of 8,000- 10,000 cells per well and transfected with VDAC2 siRNA a and VDAC2 siRNA b 48 h prior to glutamate exposure (Glut, 4 mM). **A**, VDAC2 siRNA a revealed only short and transient protection against glutamate-induced cell death compared to cells transfected with scrambled (*scr*) siRNA ( $n=8$ ). **B**, VDAC2 siRNA b predicts stronger protection at concentrations of 40 nM and a persistent protection over time at concentrations of 80 nM ( $n=8$ ).

Interestingly, although a more pronounced and complete depletion of VDAC2 protein expression levels was achieved by specific VDAC2 knockdown using the VDAC2 siRNA a sequence, almost no protective effects could be observed in any of the endpoint or real-time analyses of cell viability. Transfection of HT-22 neurons with the siRNA sequence b exerted less reduction in the VDAC2 protein expression levels (Figure 81 B), yet a significant, even though slight protection against glutamate-induced cell death. Notably, the protection achieved with relative high concentrations of VDAC2 siRNA b (40 nM and 80 nM) was still not as pronounced as the protective effects achieved by knockdown of the isoform VDAC1 using less siRNA concentration of 20 nM. In addition, preliminary data obtained from VDAC2 knockdown experiments using 20 nM of VDAC2 siRNA revealed no protection at all in the model of glutamate-induced toxicity, suggesting a minor role of VDAC2 in neuronal cell death compared to the crucial and essential role of VDAC1.

### 3.5.2 Mitochondrial membrane potential is not affected by VDAC2 silencing

To gain broader insight into the question if Bid-mediated mitochondrial demise and cell death could be regulated by VDAC2, as proposed by previous studies<sup>93</sup>, the impact of VDAC2 deficiency on mitochondrial membrane potential ( $\Delta\psi_m$ ) was investigated, since the previous experiments clearly confirmed a Bid/tBid-mediated breakdown of  $\Delta\psi_m$  in the present HT-22 cell line.

Again in contrast to the findings of Roy et al.<sup>93</sup>, a VDAC2 dependence of Bid/tBid-induced MOMP could not be revealed in HT-22 neurons. TMRE-FACS analysis predicted that glutamate-induced toxicity in non-silenced control and *scr* siRNA treated cells is accompanied with a pronounced loss of  $\Delta\psi_m$ , which could be only slightly prevented by transfection of cells with VDAC2 siRNA b (Figure 84 A, B). In line with the findings above, VDAC2 siRNA a was not sufficient to preserve the breakdown of  $\Delta\psi_m$  and did not exert protection against glutamate induced mitochondrial injury (Figure 84 A, B), demonstrating that Bid-mediated glutamate-induced MOMP is not dependent on VDAC2 expression levels.

These data strongly indicate that VDAC2 does not play a major role in Bid-mediated mitochondrial demise and cell death signaling in neurons, although VDAC2 might be important for non-neuronal apoptotic pathways that are triggered by the Bak/Bax assembly. This hypothesis is substantiated by several previous studies, reporting the absence of functional Bak in neurons, indicating separate pathways for non-neuronal and neuronal apoptosis<sup>253-255</sup>. However, further analyses are required to investigate whether neuronal VDAC2 is dispensable for mitochondrial injury and cell death at all or if there might be a regulatory function of VDAC2 in the neuronal death signaling that hasn't been investigated so far.

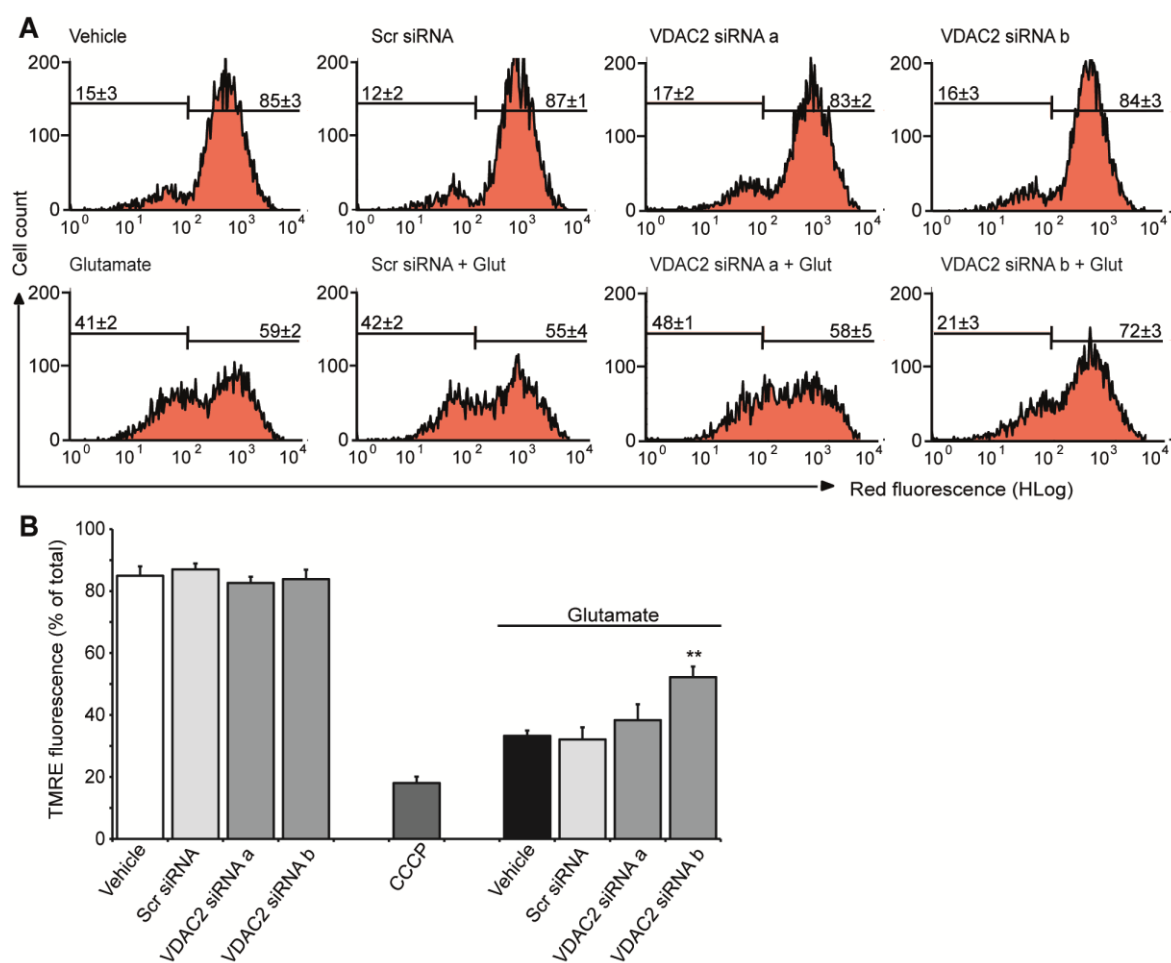


**Figure 84: Mitochondrial membrane potential is only slightly affected by VDAC2 silencing.**

Mitochondrial membrane potential ( $\Delta\psi_m$ ) of HT-22 cells was analyzed 72 h after transfection with VDAC2 siRNA a and b (40 nM) and glutamate treatment (6 mM, 17 h). **A**, TMRE-FACS recordings reveal loss of  $\Delta\psi_m$  17 h after the onset of glutamate exposure. Numbers are mean percentages  $\pm$  SD of TMRE fluorescence for  $n = 3$  indicated treatment groups. High red fluorescence indicates intact mitochondria (right side), drop of red fluorescence depicts loss of  $\Delta\psi_m$  (left side). Glutamate-induced reduction in red fluorescence was detected in vehicle and scrambled (scr) siRNA treated cells as well after transfection with VDAC2 siRNA a. VDAC2 siRNA b was only slightly protective against this breakdown of the mitochondrial membrane potential. **B**, Quantification of TMRE fluorescence of VDAC2 depleted HT-22 cells in the presence and absence of glutamate. CCCP was used as a positive damage-control which causes a fast breakdown of the mitochondrial membrane potential. Glutamate-induced loss of  $\Delta\psi_m$  was only prevented by VDAC2 siRNA b (40 nM), while VDAC2 siRNA a showed no protective effects. The experiment was independently repeated three times with  $n = 3$  per treatment group, data are provided as mean  $\pm$  SD (\*\* $p < 0.01$  compared to glutamate treated vehicle, ANOVA, Scheffé test).

## 4 Discussion

The present thesis highlights the pro-apoptotic protein Bid as a druggable target for mitoprotection and suitable for crystal structure analysis. Furthermore, the data of this study provided new insights in the underlying mechanisms of Bid-dependent mitochondrial injury that is a convergence point for different proposed mechanisms of MOMP which were previously attributed either to the activity of apoptogenic Bcl-2 family proteins or to protein complexes containing the voltage-dependent anion channel VDAC.

Key decision points in the sequence of glutamate-induced impairments in mitochondrial integrity and function, such as MOMP, disturbed mitochondrial energy production and respiration, the accelerated production of ROS as well as imbalance in mitochondrial fission and fusion occur in a Bid-dependent manner. As inhibition of Bid protects against such mitochondrial demise, the present thesis focused on Bid as a target for mitoprotection. To this aim, the first part of the study addressed the identification of small-molecule ligands targeting Bid. Seven compounds obtained from three structural diverse chemical classes were identified as highly protective against glutamate- and tBid-induced toxicity in the present HT-22 neurons. The results provide strong evidence that inhibition of Bid was the underlying mechanism of the observed protective effects. The most promising compounds prevented not only cell death, but also restored  $\Delta\psi_m$ , ATP levels as well as mitochondrial respiration after induction of oxidative stress and over-expression of tBid in HT-22 cells. Overall, this part of the study indicated these compounds as potent scaffolds for future optimizations and further applications in model systems of brain damage *in vivo*.

The second part of the work provides important requisites for the use of recombinant Bid proteins for the first Bid crystallization trials and further structure-guided drug design. Protocols for effective expression and purification of different recombinant Bid constructs were optimized and scaled up, yielding 15-50 mg Bid variant per liter culture thereby providing sufficient amounts for crystallization screening. One of the designed Bid constructs was successfully crystallized and X-ray diffraction data of 3.75 to 3.95 Å resolution could be obtained, confirming that the appropriate constructs of Bid are suitable for crystal structure analysis. Optimizations in construct design and crystallization approach were explored in order to improve the diffraction properties of the Bid crystals obtained in this thesis. Over-expression of the diverse Bid constructs in HT-22 cells revealed their non-apoptotic function, indicating their behavior as a 'full-length Bid like protein', in contrast to the detrimental effects of tBid over-expression.

In addition, the work here included the validation of a model system for membrane permeabilization in order to analyze the effect of recombinant Bid proteins and Bid inhibitors on artificial lipid membranes that mimic the mitochondrial outer membrane. A particular focus

here was on the role of cardiolipin in Bid-mediated MOMP. The data demonstrated that only cleaved Bid, but not full-length Bid was able to induce pore formation and membrane destabilization of CF-containing liposomes and planar lipid bilayers and that membrane targeting of Bid was dependent on the presence of CL. The combination of cBid and Bax was sufficient to increase fluorescence release and pore-opening, whereas Bax alone showed no effect. These results indicate an ordered series of events that occur on mitochondrial membranes to induce MOMP and the release of death promoting proteins.

Lastly, the present thesis demonstrates for the first time a direct interaction of Bid with the voltage-dependent anion channel VDAC1 as an essential key for mitochondrial damage in cultured neurons and *in vivo*. Co-immunoprecipitation experiments, thermophoresis, and lipid bilayer measurements revealed VDAC1 as a binding partner for Bid. Most intriguingly, Bid-VDAC1 interaction significantly increased over 6-24 h in ischemic brain tissue of mice subjected to transient focal cerebral ischemia, indicating the relevance of this interaction in neuronal cell death. To investigate the role of VDAC1, the anion channel blocker DIDS as well as siRNA-mediated VDAC1 gene silencing was applied in the present models of glutamate- and tBid-induced toxicity. Both, DIDS and VDAC1 siRNA, significantly attenuated Bid-mediated impairments in mitochondrial oxygen consumption and ATP production, as well as hallmarks of intrinsic death pathways, such as mitochondrial fission, increased mitochondrial ROS production and breakdown of the mitochondrial membrane potential. These data highlight a critical role for VDAC1 as a mitochondrial receptor for activated Bid and indicate the Bid-VDAC interaction as a major control point of life and death at the level of mitochondria *in vitro* and *in vivo*. In contrast, only a minor role in neuronal cell death was suggested for the isoform VDAC2, as VDAC2 gene silencing provided only transient protective effects against glutamate-induced toxicity and could not restore  $\Delta\psi_m$ . Therefore, the data implicate the observed Bid-VDAC1 interaction as a new mechanism in neuronal cells that might mirror the emerging concepts of the Bid-VDAC2-Bak interplay in cell death pathways of non-neuronal cells.

#### 4.1 Targeting Bid for protection against mitochondrial injury and neuronal cell death

The present thesis confirmed the pro-apoptotic protein Bid as a key player in mitochondrial pathways of neuronal cell death triggered by oxidative stress and thereby substantiated the detrimental involvement of Bid in neurological diseases associated with impairments in mitochondrial integrity and function. The involvement of Bid in the neuronal cell death cascade was mainly characterized in immortalized mouse hippocampal HT-22 neurons exposed to toxic glutamate concentrations. As these neuronal cells lack ionotropic glutamate receptors, glutamate-induced cell death is mediated by inhibition of the cellular cystine import, subsequent glutathione depletion, enhanced formation of reactive oxygen species (ROS) through increased lipid peroxidation and Bid-dependent mitochondrial damage<sup>165, 166</sup>. Furthermore, it was shown that glutamate-induced Bid transactivation to mitochondria triggers the release of AIF, which in turn translocates to the nucleus and induces a nuclear condensation and DNA fragmentation<sup>97</sup>. The crucial role for Bid in the model of glutamate-induced oxidative stress was confirmed by the approach of siRNA-mediated Bid gene silencing and pharmacological Bid inhibition<sup>24, 97, 116</sup>. The fact that inhibition of Bid as well as Bid depletion were sufficient to protect against various features of mitochondrial injury, including the breakdown of the  $\Delta\psi_m$ , mitochondrial fission, impaired energy supply and mitochondrial ROS formation, indicates Bid as a target for mitoprotection.

Previous studies demonstrated an involvement of Bid in neuronal injury revealing that reduced Bid expression prevented cell death in a model of oxygen glucose deprivation (OGD) in primary cultured neurons, and genetic depletion of Bid also reduced brain damage in models of cerebral ischemia and brain trauma *in vivo*<sup>98, 202</sup>. Moreover, recent reports showed that both proteins, full-length Bid as well as its truncated form tBid, are sufficient to induce mitochondrial dysfunction and cell death in neurons and only differ in kinetics and cell death pathways<sup>58</sup>. While tBid is suggested to induce rapid mitochondrial damage in a caspase-dependent manner, full-length Bid is thought to be involved in caspase-independent apoptosis with slower kinetics<sup>59</sup>. In the currently applied model system of glutamate toxicity in HT-22 cells, activated full-length Bid as well as tBid may both contribute to neuronal cell death pathways. Pharmacological Bid inhibition was sufficient to prevent the glutamate-induced translocation of full-length Bid to mitochondria and the subsequent accumulation of the fragmented organelles and additionally attenuated mitochondrial injury and cell death after over-expression of tBid. It should be noted, that the p15 tBid fragment was hardly detectable in cytosolic or mitochondrial fractions of glutamate-exposed HT-22 cells. However, this does not necessarily indicate the absence of tBid in the model of glutamate-induced cell death, but suggests that upon glutamate exposure the caspase-8 cleaved Bid



(cBid) translocates to the mitochondria where the separation of the p7 and p15 Bid (tBid) fragment could occur rapidly and in a small time window after membrane targeting<sup>72</sup>.

Overall, these findings in model systems of neuronal death *in vitro* and *in vivo* strongly suggested that targeting Bid is a promising approach to develop pharmaceutical drugs for mitoprotection with high relevance for novel therapeutic strategies in neurological diseases where mitochondrial demise is prominent. Indeed, it was recently demonstrated, that pharmacological inhibition of Bid with the available inhibitor BI-6C9, which was used as positive control for protection in the present study, strongly reduced tBid-induced release of Smac/DIABLO from isolated mitochondria at concentrations as low as 20  $\mu\text{M}$  *in vitro* and prevented effectively tBid-mediated cell death in mitochondria- and cell-based assays of caspase-dependent cell death<sup>99</sup>. In particular, the available Bid-inhibitors developed by Becattini et al. reduced caspase-3 activity in tBid-transfected HeLa cells at 50  $\mu\text{M}$  and persistently blocked caspase activity at 100  $\mu\text{M}$ <sup>99</sup>. This thesis revealed that the key events of glutamate-induced caspase-independent cell death, such as MOMP, mitochondrial fission and ATP depletion as well as impairments in mitochondrial respiration were apparently Bid-dependent and could be prevented by BI-6c9 at concentrations of 10  $\mu\text{M}$ . However, despite the pronounced neuroprotective potency of BI-6c9 *in vitro*, it failed so far to protect brain tissue *in vivo*. Since the solubility of BI-6c9 is dependent on the serum-content of the culture media, BI-6c9 is not applicable to serum free conditions in cell culture models. A further aspect is the relatively high molecular weight of BI-6c9 that might hamper the penetration of the blood-brain barrier, and metabolically unstable substructures, such as the 4-(4-aminophenyl)sulfanylaniline structure, might cause a fast peripheral metabolism resulting in molecules with less activity.

The small-molecule compounds that were developed in this thesis based on the structure of BI-6c9, provided protective effects against glutamate-induced cell death at concentrations of 5  $\mu\text{M}$  up to 50  $\mu\text{M}$ , and attenuated tBid-induced toxicity even at concentrations as low as 1  $\mu\text{M}$ . The observed protective effect in the model of oxidative stress is promising, since the screened compounds may provide a protective benefit against pathological pathways occurring in neurodegenerative diseases where oxidative stress triggers the onset of neuronal cell death. The finding that the newly synthesized structures preserved cell viability in HT-22 cells after tBid over-expression strongly support the specificity of the small-molecules to provide mitoprotection by targeting the pro-apoptotic protein Bid. Key features of mitochondrial dysfunction, such as impairments in energy metabolism and loss of mitochondrial membrane potential described as 'point of no return' in the cells' commitment to die<sup>19</sup> were effectively prevented by the most promising thiazolidin-2,4-diones. Further, the data demonstrated the compounds' ability to preserve oxygen consumption rate of HT-22 cells and thereby mitochondrial respiration and bioenergetics, described to be defective in

neurodegenerative disorders<sup>204</sup>. The fact that the compounds provided almost full protection against mitochondrial dysfunction indicated that the molecules acted upstream of mitochondria. This supports even more the hypothesis that the protective effects are mediated by inhibiting Bid. The specific targeting of Bid was further substantiated by virtual docking analysis revealing that the compounds fitted nicely into the hydrophobic groove on the surface of the Bid protein. Indeed, the Bid-ligand binding could be confirmed very recently by fluorescence based assays and label-free EnSpire analysis (data not shown)<sup>256</sup>. Furthermore, latest investigations revealed that these compounds are able to inhibit the translocation of Bid to mitochondria and were also protective against glutamate-induced excitotoxicity in cultured primary cortical neurons (data not shown). Therefore, the data obtained from this thesis indicate that Bid is a druggable target that promises novel strategies for future therapeutic perspectives for treatment of diseases associated with mechanisms of Bid-dependent mitochondrial cell death. The relevance of targeting Bid in the brain has been further confirmed by recent studies, reporting that chemical inhibition of Bid exerted antidepressant-like effects in behavioral models *in vivo*, such as the forced swim test, the tail suspension test and learned helplessness paradigms, indicating that Bid might be also a target of a new class of antidepressants<sup>257-259</sup>. However, it remains to be validated whether Bid inhibitors are suitable for long-term systemic use and whether Bid-antagonists can alleviate neurodegenerative or depressive symptoms in human patients. It is further an open question whether these compounds cause side effects due to inhibition of apoptosis pathways, albeit Bid-deficient mice are viable and develop normally<sup>260, 261</sup>. In addition, side effects caused by the chemical structure of the thiazolidindiones comparable to that observed by the thiazolidinediones (TZDs) used for treatment of type II diabetes is unlikely. Those anti-diabetic compounds, also known as glitazones (e.g. Rosiglitazone) act through activation of peroxisome proliferator-activated receptors (PPAR $\gamma$ ). The PPAR $\gamma$ -binding was responsible for several side effects, such as increased risk of cardiovascular events, hepatitis and potential liver failure causing the withdrawn of some glitazones. In contrast to those thiazolidinedione-based PPAR ligands that need to possess a free N-H, all of the Bid-targeting thiazolidinediones screened here are N-substituted, and thus a binding to PPAR's and the resulting side effects are not expected. However, one should keep in mind that the data obtained in this thesis are preclinical and have to be transferred to *in vivo* studies. Further optimizations should be performed in order to improve the protective potency of the compounds to nanomolar concentrations required for first PK studies and observations *in vivo*.

In conclusion, this part of the thesis identified seven small-molecules as potent inhibitors against neuronal cell death and indicates the inhibition of Bid as the key mechanism of their protective properties. In particular, the compounds provided significant protection against

glutamate toxicity and tBid-over-expression in hippocampal HT-22 cells, and further prevented detrimental impairments of mitochondrial integrity and function, thereby inhibiting the final execution of intrinsic cell death. Future optimization of the structures should result in compounds with favorable pharmaceutical properties that are applicable in model systems of cell death *in vivo* and furthermore in pharmaceutical drugs that are suitable for therapeutic strategies not only in the treatment of neurodegenerative diseases, such as Alzheimer's disease and Parkinson's disease, but also for therapeutic interventions in ischemic stroke, mood disorders e.g. major depression, liver inflammation, or other diseases where a role of Bid has been implicated.

## 4.2 Bid protein crystallization – a pipeline for structural knowledge and structure-guided drug design

The atomic resolution structures of a protein provides not only a deep and unique understanding of the molecular protein function and sheds light on chemical interactions and the inner working of the cells<sup>206</sup>, but is also an indispensable tool for the development of highly selective inhibitors of a target protein. Since X-ray crystal structures can account for geometric properties of ligand-protein complexes, they enable a rational and structure-guided drug design that facilitates the further improvement of physico-chemistry and affinity properties of small-molecule compounds. Thus, crystal structures serve as the basis for developing pharmaceuticals against diseases where the target protein plays a major role in the underlying pathology<sup>262, 263</sup>. While several previous studies, reported the advantage of crystal structures for the development of selective inhibitors of other Bcl-2 family proteins, such as Bax, Bcl-xl, or Mcl-1<sup>68, 105, 109, 121, 122</sup>, to date similar drug discovery campaigns for the pro-apoptotic protein Bid were hampered by the absence of appropriate crystal structures of isolated Bid. So far only small Bid BH3-peptides were co-crystallized in combination with the pro-apoptotic protein Bax and used to explore the activation of Bax<sup>121</sup>. However, an atomic resolution structure of full-length Bid is not available. Figure 85 depicts the general workflow which has been pursued within this thesis for obtaining a basis for Bid protein crystallization.

Since every protein has its own distinctive chemical properties and there is no comprehensive theory to guide a successful crystallization, macromolecular crystal growth is largely empirical in nature, demanding patience, perseverance and intuition<sup>189, 207, 209</sup>, starting not at the stage of the obtaining crystals, but much earlier at the selection of the protein. It has been described, that full-length protein constructs versus truncations, chemical modifications and mutations can dramatically influence the crystal formation<sup>207</sup>, a phenomenon that was also observed in the present thesis. Although purification of full-length Bid allowed for harvesting reasonable amounts of the protein, several crystallization screens

failed to yield Bid crystals. Based on previous experiences collected for the construct design and crystallization of the related proteins, Bcl-2, Bcl-xl and Mcl-1<sup>68, 121, 122</sup> it was suggested that flexible regions in the structure of the Bid protein interfere with the crystallization process. Indeed, the present study revealed that truncation of the disordered N-terminus and loop region of full-length Bid enhanced the ability to reach high protein concentration as well as the tendency for obtaining crystals within the first screens. Therefore, the truncation of full-length Bid is an important advance, absolutely essential for obtaining the first diffracting Bid crystals. Notably, the choice of an appropriate protein construct may already cause differences in the expression efficiency, as it was observed in case of the tBid plasmid. While the expression of the active and pro-apoptotic truncated Bid in *E. coli* was completely refused, bacterial expression of the newly designed Bid constructs (Bid 1-Bid 4) succeeded in high protein amounts (Step1).

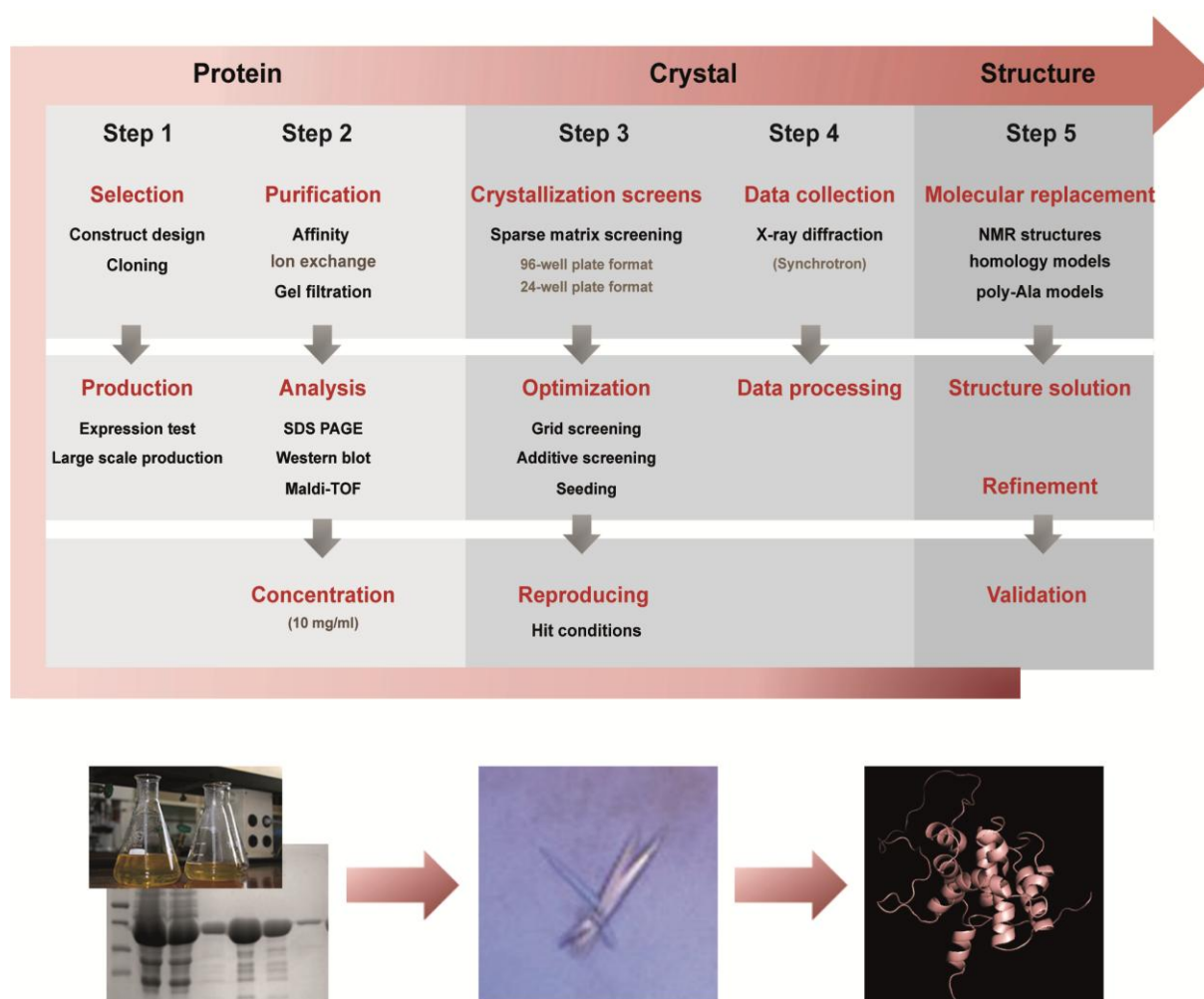


**Figure 85: Workflow from construct design to protein crystallography.**

Pipeline from Bid construct design, cloning, expression and protein purification to Bid protein crystallography. **Step 1:** The pro-apoptotic protein Bid was selected for purification and crystallization studies. Different Bid constructs were designed and respective plasmids were cloned suitable for protein expression in *E. coli*. Large scale production yielded in high protein amount suitable for step 2. **Step 2:** Protein purification: Depending on the protein construct and the respective purification tag, protein purification was performed by 2-3 chromatography steps as indicated. The purity of the protein was estimated by SDS-PAGE followed by coomassie staining and

western blot analysis. To guarantee the identity of the protein MalDI-ToF analysis were performed. The proteins were concentrated to approximately 10 mg/ml. **Step 3:** Protein crystallization was performed by the vapor-diffusion technique and initial screening was conducted using the Qiagen NeXtal-screening suites containing a wide sector of different crystallization conditions differing in pH, precipitants, buffer and salts. Hit conditions, yielding the first protein crystals were further optimized by additive screening, seeding or grid screens. Hit conditions were further reproduced. **Step 4:** Obtained protein crystals were analyzed by X-ray diffraction. Synchrotron measurements of protein crystals took place either at the Helmholtz-Zentrum Berlin using the MX Beamline 14.1, BESSY II or at the DESY Hamburg using the EMBL MX1 and MX2 beamline at the PETRA III ring. **Step 5:** First molecular replacement trials were performed using Phaser with search models from various sources (Bid NMR structures (PDB), homology models and poly-Ala models). So far no MR solution could be identified. Of note, if protein purification, crystallization screens or data processing was not satisfying, all steps were repeated beginning at step 1. Pictures predict protein expression and protein analysis (step 1), the first Bid crystal obtained during this work, and the NMR solution structure of Bid (1DDB) used for molecular replacement.

The second step in the crystallization pipeline included the preparation of a pure homogenous protein sample, which is often a key factor in obtaining crystals that diffract to high resolution<sup>189, 264</sup>. As recommended for the initial crystallization screening, highly pure protein (> 98%) could be achieved for all of the designed and purified Bid constructs and concentration efficiency could be clearly increased by cutting the His-tag of full-length Bid and further by removal of the flexible loop and N-terminal region, confirming the protein itself as an important variable during the crystallization approach. The most important parameters that affect protein solubility and thereby crystallization are reported to be protein concentration, precipitant type and concentration, pH and temperature<sup>189, 265-268</sup>. Notably, it is essential to carefully review the screening outcomes within the first crystallization process, bearing in mind that even negative results provide precious information<sup>207, 264</sup>. Initial crystallization screens revealed that all Bid constructs tended to heavy precipitates in the presence of cadmium, zinc or nickel ions, while most promising conditions often consisted cryoprotectants such as PEGs (PEG 3350, PEG 4000) or higher concentrations of MPD (20-50 % (V/V)).

Regardless of the screening condition, temperature was an important variable to evaluate. As Bid is temperature stable protein, crystallization screens could be performed at 4°C and 18°C, revealing even the most promising results at the higher temperature.

Beside these chemical and physical parameters, the choice of the crystallization method can affect the crystallization result<sup>189, 269, 270</sup>. In accordance to the PDB, the present thesis utilized the vapor diffusion technique as the most popular method used in obtaining the majority of the X-ray structures for which the crystallization method was reported<sup>189</sup>. A couple of promising conditions with crystalline material as well as 3D crystals were observed within the initial Bid crystallization trials, but unfortunately they were often not suitable for X-ray diffraction analysis or diffracted only at low resolution. This was not surprising, as it has been estimated, that only 10 %-20 % of the crystals produced in the first level of screening are diffracting crystals, while the majority requires further refinement<sup>189</sup>. Optimizations performed

for Bid crystallization included not only the variation of parameters such as buffer and precipitant concentration as well as pH, but also contained the approach of crystal seeding and addition of diverse additives. Compared to the initial screening, which is generally fraught with the greater risk, as many proteins refuse to form crystals, the systematic alteration of the initial conditions proves the more demanding and more time consuming step<sup>120, 267</sup>. Crystallization screens performed with full-length Bid succeeded only in microcrystals and could not be optimized to 3D-crystals. So far, crystallization trials for Bid2 and Bid4 yielded only microcrystals and further optimizations have to be performed for those constructs. In contrast, diffracting crystals of Bid construct 1 were already observed within the initial crystallizations screenings, indicating two promising conditions which were used for further optimization trials.

However, despite all performed optimization trials, the best diffracting pattern (step 4 data collection) were observed from the initial “hit” crystals obtained from JSCG+ condition 79 and cryo condition 5. While those initial crystals yielded resolution ranges between 3.75 Å–3.95 Å, several other crystals obtained from optimization trials were recorded with lower resolutions between 3.8 Å and 6 Å and indexing of diffraction data was not always possible. Data collection of the both “hit” crystals, obtained from the abovementioned conditions, reached a high redundancy (6.3) and completeness (99.4 %) and the X-ray diffraction signal-to-noise ratio ( $I/\sigma$ ) was  $> 2$ , which is in general required for good-quality structures<sup>119</sup>. However, no unique X-ray structure solution for Bid could be obtained so far. It should be noted, that many protein crystals do not diffract to atomic resolution as a result of inherent mobility and solvent content surrounding the protein molecule. Additionally, significant amounts of solvents, which were ~44 % for the present Bid crystals, cause the susceptibility of crystals to damage by X-rays, although such radiation damage was reduced by collecting the data at 100 K. Of note, successful structure elucidation for related proteins has been achieved from crystals obtained from similar conditions as those for the Bid crystals. As recently reported, Bax crystals were grown from conditions consisting of 10 % PEG3350, 20 % MPD, 0.5 % CHAPS and 0.1 M Tris (pH 8.0)<sup>121</sup> and the first diffracting Bcl-xl crystals were obtained from 28-31 % PEG 4000, 0.2 M ammonium acetate, 0.1 sodium citrate (pH 7.5)<sup>68</sup>. In consideration of the fact, that the truncated Bid constructs share a high structural similarity to the crystallized Bcl-xl- and Bax protein and considering that the most promising Bid crystals were as well obtained in similar conditions containing either PEG3350/PEG4000 or MPD and at pH values of 7.5 to 8.0, it might be likely that further optimizations of the presented conditions yield high resolution crystals of Bid.

Beside further structure elucidation trials using the here obtained Bid diffraction data via molecular replacement, further optimization trials could include the following ideas: In addition to variations of temperature, pH and concentration of precipitants, the concentration

of the respective Bid constructs is a significant variable. It has been described that the protein concentration can differ from as low as 2 mg/ml to as much as 100 mg/ml for successful crystallization outcomes<sup>120, 264, 266, 268</sup>. Moreover, the presence or absence of ligands, inhibitors, metal ions or coenzymes are relevant considerations, even though the influence of those has to be empirically defined for the particular Bid construct<sup>209</sup>. As substrates and inhibitors are reported to maintain a protein in a more compact and stable form<sup>209</sup>, it might be possible to achieve a greater degree of structural homogeneity by complexing the protein with a ligand before attempting its crystallization<sup>189</sup>. Thus, it is worthwhile to explore complexes of the Bid protein with the newly synthesized Bid inhibitors or the addition of cofactors<sup>271</sup> at these early stages of Bid crystallization, as such complexes could be inherently even more interesting as the apo-Bid protein. However, co-crystallization of the Bid 1 protein with the available BI-6c9 failed to yield crystals so far, probably reasoned by the poor solubility of the inhibitory compound rather than by the general impossibility of protein-ligand crystal growth. Furthermore, ligand binding could be associated with more or less severe changes in the arrangement of the helical organization of Bid as well as in the Bid crystal form as it was also suggested by similar approaches crystallizing the Bcl-xl protein in complex with inhibitors (PDB entries 1MAZ versus 2YXJ)<sup>68, 272</sup>. However, previous reports substantiate the advantage of such crystallization approaches for the identification and improvement of selective protein-binding compounds<sup>272-274</sup>, and are thereby indispensable for further optimization of the here presented Bid inhibitors. Therefore, it would be worthwhile to address the crystallization of diverse protein-ligand complexes, even if those might require additional screening campaigns to find suitable conditions in dependence on the ligand chemotype to be analyzed. Beside these considerations, further Bid protein engineering approaches are desirable, since length and type of the truncation or further mutations may significantly influence the crystallization and diffraction ability of the Bid protein.

Although, further crystallization studies have to be performed to finally elucidate the crystal structure of Bid allowing for a campaign of structure-based development of Bid inhibitors, the present thesis provided already a suitable pipeline from Bid construct design to Bid crystallization. The presented work gained insights in the chemical behavior of the Bid protein by identifying the removal of disordered and flexible regions of the Bid structure as essential for protein solubility and crystal growth. Indicating the crucial importance of construct design, the performed crystallization screenings succeeded in the first diffracting Bid crystals reported so far. Overall, these results reveal the Bid crystallization approach as a powerful tool for a better understanding of Bid activation and function as well as a promising set up for further Bid-inhibiting drug discovery and pharmaceutical research.

### 4.3 Mechanisms of Bid-mediated MOMP and mitochondrial impairments

The present thesis substantiates the crucial involvement of Bid in the regulation of MOMP and mitochondrial injury. Several previous studies reported that upon its activation and translocation to mitochondria, Bid provokes impaired mitochondrial integrity and disturbed mitochondrial dynamics and function<sup>24, 63, 97, 116</sup>, but the precise mechanism how Bid triggers mitochondrial dysfunction is not fully understood. Mitochondrial outer membrane permeabilization (MOMP) is considered as the most critical event and 'point of no return' in the mitochondrial apoptotic pathway<sup>5, 18, 19</sup> promoting apoptosis by releasing IMS pro-apoptotic proteins such as cytochrome c and AIF to the cytosol. However, so far, the mechanisms of MOMP are still elusive and several models have been proposed. Recently, it has been suggested that MOMP might be closely linked to the molecular machinery involved in mitochondrial fission<sup>24, 275, 276</sup>, reporting that mitochondrial fragmentation occurs concomitantly with cytochrome c release<sup>276</sup>.

Alternatively, MOMP has been proposed to be initiated at the inner mitochondrial membrane (IMM) by an increase in permeability to small molecules, a subsequent osmotic swelling and distension of the IMM followed by rupture of the MOM. This phenomenon is promoted by increases in cytosolic  $\text{Ca}^{2+}$  and/or ROS<sup>23, 277</sup>.

A further model of MOMP refers to the mitochondrial permeability transition pore (mPTP). The permeability transition pore complex (PTPC) is described as a large multi-protein complex constituted of several components. Major components of the PTPC are the voltage-dependent anion channel (VDAC), the adenine nucleotide translocator (ANT) and cyclophilin D (CypD), although their precise involvement in MOMP is not yet clear<sup>23</sup>. Both, opening and closing of the mPTP are discussed to trigger MOMP. On the one hand closure of the mPTP is thought to result in osmotic swelling, mitochondrial membrane rupture and the non-specific release of intermembrane space proteins. On the other hand opening of the mPTP or oligomerization of VDAC is reported to be important for cytochrome c release<sup>19, 130</sup>.

Last but not least, MOMP has been related to the members of the Bcl-2 family proteins<sup>5, 44</sup>. The pro-apoptotic multi-domain proteins Bax and Bak are thought to be directly responsible for MOMP by creating protein-permeable pores in the outer mitochondrial membrane. Pro-apoptotic BH3-only proteins, such as activated Bid or Bim can directly induce conformational changes in Bax/Bak, which triggers their oligomerization and pore-formation. Furthermore, a pivotal role for the mitochondrial lipid cardiolipin (CL) has been shown for Bcl-2 family-mediated MOMP<sup>80, 82, 91, 278</sup>.

CL is described to act as an anchor for cytochrome c at the inner mitochondrial membrane (IMM) and CL peroxidation is thought to be required for weakening of this interaction and full release of cytochrome c<sup>279</sup>. Thus, CL seems to play an active role in MOMP as substantiated



by the finding that inhibition of CL peroxidation prevents Smac/DIABLO release<sup>279</sup>. CL is prominently found in the IMM within cristae, but has been also described to be located at the contact sites between MOM and IMM<sup>80</sup>. Notably, also tBid and Bcl-2 have been reported to cluster at the same contact points<sup>81</sup> and further studies showed that the mPTP spans the IMM and MOM in close proximity to the IMM/MOM contact sites<sup>23</sup>. In particular, a CL affinity for VDAC has been reported suggesting that the specific lipid composition of the mitochondrial membrane and/or contact sites influence MOM permeability by regulating VDAC and mPTP gating<sup>131</sup>. However, it is discussed whether MOMP is mainly mediated by the PTPC, conformation changes of the Bcl-2 family proteins and pore-formations and/or protein-protein and protein-membrane-interactions.

Although it might depend on the cellular model, the apoptotic stimulus and the experimental conditions<sup>85, 277</sup>, it seems to be likely that the abovementioned mechanisms underlying MOMP might work in a coordinated manner. The present thesis reveals that Bid-mediated MOMP and mitochondrial demise seem to require both the mitochondrial lipid CL as well as a component of the PTPC, namely VDAC1. *In vitro* studies revealed the essential role of CL for cBid-mediated membrane destabilization and cell culture and *in vivo* studies highlighted the direct interaction between Bid and VDAC1 as essential for mitochondrial demise. Thus this thesis connects the proposed mechanisms of MOMP, as discussed below.

#### **4.3.1 Role of cardiolipin in cBid/Bax mediated pore formation – a model system of membrane permeabilization**

It was an aim of the present study to address the function of recombinant Bid and Bax on artificial lipid membranes and to explore the participation of Bid in MOMP. While attempting to establish the use of liposomes as model system for Bid-mediated membrane permeabilization and the screening of Bid-targeting compounds, the lipid constitution of the mitochondrial outer membrane was recreated. As a particular focus of the applied membrane assay was on the specific role of cardiolipin (CL) in Bid-mediated membrane integration and membrane permeabilization, the studies were performed in the presence and the absence of CL. It was previously reported that Bid and its truncated form tBid preferentially associate with liposomes containing CL levels comparable to those found in mitochondrial membranes<sup>81, 91</sup>, and the absolute requirement of CL for tBid binding was reported by studies involving CL-deficient yeast strains<sup>280, 281</sup>. Previous reports revealed that liposomes require the presence of at least 7 mol % CL in their membranes to undergo optimal permeabilization induced by cleaved Bid and Bax<sup>91, 219, 282</sup>, and other groups reported even the requirement of 20 mol % CL for tBid binding to liposomes<sup>80</sup>. However the physiological relevance of CL and the nature of tBid/Bax-mediated permeabilization remained controversial. While several

studies reported that CL facilitates Bax insertion, oligomerization and permeabilization of the membranes in liposomes<sup>82, 91, 219, 283</sup>, the physiological role of CL in Bax-mediated cell death was questioned by reports concluding that the apoptotic function of Bax occurs independent of CL, revealing the ability of Bax to trigger MOMP in mutants lacking CL synthase<sup>280, 284, 285</sup>. In contrast to the controversial requirement of CL for Bax, several studies suggest CL as a direct mitochondrial receptor for activated Bid<sup>77, 80, 219, 220, 286</sup>. It has been shown that CL increases the binding of both cBid and tBid to pure lipid vesicles as well as to MOM and thereby suggested the direct involvement of CL for Bid mediated apoptosis<sup>80, 281, 286</sup>. The work here reveals the role of cardiolipin for the specific targeting of activated Bid to lipid membranes by comparing the pore-forming ability of Bid, cBid and Bax in liposomes containing PE and PC to the protein-induced permeabilization of liposomes consisting 26 mol % CL in addition. Noteworthy, in accordance to several other studies using artificial mitochondrial membranes<sup>69, 91</sup> the relatively high CL concentration was related to the enhanced content of CL at the IMM/MOM contact sites reported to be approximately 20 %<sup>221</sup>, and might not necessarily reflect the physiological conditions 4-6 % CL of in the IMM. tBid is thought to bind to the outer mitochondrial membrane at both contact and non-contact sites<sup>81, 88</sup>, but also reported to preferentially insert into the negative lipids of the mitochondrial contact sites between IMM and MOM<sup>287</sup>. Previous studies reported that the tBid-CL binding occurs at the mitochondrial contact sites and is accompanied with a remodeling of the mitochondrial cristae, permeability transition and cytochrome c release<sup>85, 220</sup>.

In line with the abovementioned findings, a cBid-induced permeabilization of CF-containing liposomes was only obtained in the presence of CL, while liposomes lacking CL were not disturbed. The cBid mediated CF-release was observed at relatively high concentrations up to micromolar ranges compared to the required concentrations for truncated tBid used in previous studies generating tBid by OG-induced separation of the p7 and p15 fragment of caspase-8 cleaved Bid (cBid)<sup>215, 219</sup>. This suggests that both cBid and tBid differ in their catalytical efficiency dependent on the exposed hydrophobicity which is increased in the case of tBid<sup>61</sup>. Furthermore, a membrane-destabilizing ability for full-length Bid could not be detected in any liposomes containing and lacking CL. Although this is in opposite to previous studies reporting a CL-binding and pro-apoptotic activity for full-length Bid<sup>86, 87, 89</sup>, the observed failure of full-length Bid for membrane permeabilization substantiates the hypothesis that the hydrophobic structures of Bid have to be exposed for Bid recruitment to membrane. The important role of CL for cBid activity on artificial lipid membranes could be further confirmed by preliminary studies using planar lipid bilayers, revealing a pore-forming ability of cBid dependent on the CL-content.

In contrast to the necessity of CL for the recruitment of activated Bid to lipid membranes, CL seems not to be required for the pro-apoptotic protein Bax. Bax alone was not able to induce

pore-formation of BLMs or destabilization of liposomes independent on the presence or absence of CL. In contrast, the data clearly revealed the important presence of activated Bid on lipid membranes prior to Bax addition. A cBid/Bax-mediated increase in fluorescence release was observed when both proteins were incubated before co-addition to liposomes and conductance of BLMs was enhanced after addition of both proteins to the *cis* chamber. These results are in line with several other studies reporting the necessity of activated Bid for Bax induced liposome permeabilization<sup>71, 215, 218, 288</sup>. Intriguingly, a cBid/Bax-induced CF-release could not be detected when Bax was the first protein in the assay.

These results indicate that the described events, resulting in efficient pore formation, occur in an ordered sequence, requiring the initial binding of activated Bid to lipid membranes, particularly to CL, and the subsequent activation of Bax. That both, Bid-lipid binding and protein-interaction can occur in parallel is substantiated by previous observations, revealing that activated Bid targets mitochondrial membranes independent of the BH3-domain which is required for its interactions with Bax or Bak<sup>220</sup>. These studies revealed that the helix  $\alpha$ H6 of Bid was responsible for targeting Bid to mitochondrial CL and for the subsequent reorganization of mitochondrial cristae. A key property of CL could be the ability to alter the membrane curvature and to promote the formation of non-bilayer structures. tBid was found to induce negative membrane curvature<sup>289</sup> and structural distortion of the lipid bilayer following its interaction with CL<sup>290</sup>. Cristae reorganization and disruption of mitochondrial membrane organization might facilitate either Bax oligomerization or pore formation, or both, as an enrichment of Bax oligomers has been found at the mitochondrial fission sites, where CL may also be enriched<sup>225</sup>. Further reports additionally described the relevance of Bid-CL binding for disruption of mitochondrial bioenergetics<sup>220, 286</sup>, thereby supporting the importance of the Bid-CL interaction for both, mitochondrial targeting and pro-apoptotic activity of Bid. The suggested specificity of CL for Bid binding has been further substantiated by studies using proteo-liposomes revealing that the CL dependence was only seen when Bax was activated by cleaved Bid, but not by other activator BH3-only proteins such as Bim<sup>77</sup>. Interestingly, these studies further suggested the importance of at least one factor other than CL that facilitated the Bid/Bax-induced membrane permeabilization<sup>77</sup>, and assumed that other mitochondrial proteins are required. The idea that CL might not be the only receptor for targeting of activated Bid to mitochondria was in line with previous studies revealing that tBid binds only to CL in presences of membranes but not to free CL<sup>80</sup>. Further reports suggested that under physiological conditions the formation of protein-channels by tBid or Bax molecules might occur together with and/or in dependence of MOM-resident membrane proteins, such as VDACs or Mtch2<sup>72, 94, 95, 142, 159</sup>. Therefore, CL may be a physiological receptor for tBid although its function may overlap or synergize with Mtch2 or other mitochondrial proteins that target Bid to membranes.

However, it remains to be shown whether CL is absolutely required for Bid-mediated apoptosis. It has to be determined if a tBid/cBid-CL interaction functions by changing membrane structure and curvature thereby promoting Bax oligomerization and release of proteins from the IMS, or if CL is just a membrane receptor for cBid/tBid to promote further protein-protein interaction that trigger MOMP. Either way, it is likely that tBid might act as a bi-functional molecule, first binding to mitochondrial membranes through interaction with the mitochondrial lipid cardiolipin, destabilizing mitochondrial membrane structure and interacting with other proteins such as Mitch2, VDAC and/or Bax to trigger AIF and cytochrome c release as the final execution of intrinsic apoptotic cell death.

Although these considerations remain to be determined at the cellular level, the presented liposome channel assay is an appropriate model system to investigate Bid-mediated mitochondrial membrane permeabilization. Further studies should address the effect of activated Bid on liposomes and BLM with reconstituted Mitch2 or VDACS in the presence and absence of CL to investigate if the suggested mechanisms occur in parallel or depend on each other. Furthermore, the assay is a suitable model system for analyzing the inhibitory effects of small-molecules targeting activated Bid, as for example shown for the Bid inhibitor BI-6c9 which decreased the cBid/Bax-induced CF-release. Therefore the system allows the screening of novel compounds that selectively target Bid and inhibit membrane integration and pore formation of activated Bid and/or Bax in a cell free system. Thus, the liposome assay is a useful method to identify compounds which should block mitochondrial membrane depolarization and related intrinsic pathways of cell death.

#### **4.4 The role of the voltage-dependent anion channel VDAC1 in Bid-mediated mitochondrial demise and cell death**

The present study demonstrated a pivotal role for the voltage-dependent anion channel 1 (VDAC1) in Bid-mediated mitochondrial apoptotic pathways. The data revealed that Bid-mediated mitochondrial fission, loss of mitochondrial membrane integrity, accumulation of detrimental ROS as well as impairments in mitochondrial energy metabolism and respiration depend on VDAC1 activity. Thus it is indicated that both proteins Bid and VDAC1 are equally involved in the mechanisms of mitochondrial intrinsic cell death signaling. VDACS have been proposed as important regulators of the intrinsic apoptotic pathway and increasing evidence indicates that both anti- and pro-apoptotic proteins, such as Bcl-2, Bcl-xl, Bax and Bid interact with VDAC to regulate mitochondrial pathways of apoptosis<sup>157, 159, 160, 162</sup>. However, published reports about whether and how Bcl-2 family proteins interact with VDAC and how they might alter VDAC channel activity, towards closure or opening, are highly controversial<sup>157, 161-163, 291, 292</sup>. For instance, Bcl-xl has been reported to facilitate the open

configuration of VDAC channels thereby maintaining the permeability of the mitochondrial outer membrane to ATP and ADP<sup>153</sup>, but Bcl-xl has also been shown to induce VDAC channel closure and thus to prevent apoptosis<sup>154, 157</sup>. Moreover, Bax has been discussed to interact with VDAC1 to induce channel opening<sup>159</sup> and is further reported to form a heteromeric complex with VDAC1 to promote cytochrome c release<sup>142, 159, 293</sup>. In contrast, others showed that Bid but not Bax modulates VDAC channel conductance<sup>161</sup>, yet it is further discussed that tBid/Bax-mediated cytochrome c release occurs independently of VDAC<sup>163</sup>.

The presented thesis now highlights new insights into the mechanisms of Bid-dependent cell death and the involvement of VDAC1 in mitochondrial apoptosis. VDAC1 function can be modulated by various physiological ligands, such as adenine nucleotides or NADH as well as non-physiological compounds, such as Koenig's polyanion<sup>227</sup>, ruthenium red (RuR), 4,4'-diisothiocyanatostilbene-2,2'-disulfonic acid (DIDS)<sup>135</sup> or the PS oligonucleotide G3139<sup>230</sup>. However, specific inhibitors for the subunit VDAC1 are missing. In the present thesis, the commonly-used non-specific anion channel blocker DIDS<sup>232, 294</sup> was used in order to gain an initial insight to the question whether VDACS might play a role in Bid-mediated intrinsic cell death pathways. Previous studies reported protective effects of DIDS against various pathologies, including for example STS-induced apoptosis in leukemia cells, neuronal volume-dependent apoptosis and delayed neuronal death in hippocampal neurons<sup>233, 234</sup>. The protective effects achieved by DIDS are usually attributed to inhibition of anion channels or anion exchangers and associated reductions of Cl<sup>-</sup> or ROS flux that regulate cell volume and diverse downstream cell death pathways<sup>234</sup> mediated by toll-like receptors, protein kinase C and matrix metalloproteinases among others<sup>232, 234, 295</sup>. Furthermore, DIDS has been used as a well accepted VDAC inhibitor in several *in vitro* and cell-based assays, revealing that DIDS blocks VDAC channel conductance and VDAC-induced apoptosis<sup>158, 231</sup>. In contrast to the protective effects mediated by DIDS, it has been also reported that DIDS inhibits cellular proliferation in some cell types and induces apoptosis in tumor cells as well as in hippocampal neurons<sup>234</sup>. However, the effects of DIDS and their underlying mechanisms might depend on the cell type and the nature of the cell death stimuli.

The present thesis demonstrated that DIDS exerted significant protective effects in the currently used model systems of glutamate- and tBid-induced toxicity in hippocampal HT-22 cells and indicated that these effects might be mainly mediated through pathways downstream of Bid activation. This suggestion is based on the findings showing that that DIDS preserved not only cell viability but also mitochondrial morphology,  $\Delta\psi_m$ , ATP levels and mitochondrial respiration after induction of oxidative stress in HT-22 cells, and further prevented the secondary increase in lipid peroxidation, which was associated with mitochondrial damage. All of these cellular features, indicating intact mitochondria, were shown to be defective in Bid-induced toxicity and were further reported to be affected by

VDACs<sup>143, 144</sup>. In addition, the data revealed that DIDS was also sufficient to prevent tBid-induced loss of  $\Delta\psi_m$  and cell death, substantiating that DIDS acts at the level of mitochondria and provides protection through inhibition of anion channels localized in the MOM, likely VDACs. The fact that the protective effect of DIDS against several hallmarks of glutamate-induced Bid-mediated toxicity was comparable to the protective effects achieved by the Bid inhibitor BI-6c9 further suggested that the respective mechanisms behind both substances are correlated to each other, although DIDS might exert additional unspecific effects. Therefore it was assumed that DIDS acts via inhibition of mitochondrial VDACs and that there might be a close relationship between the involvement of Bid and VDAC in apoptosis. This hypothesis was finally substantiated by the finding that VDAC1 gene silencing exerted pronounced protection against glutamate- and tBid-induced cell death comparable to the effects achieved by DIDS.

#### 4.4.1 Direct interaction of Bid and VDAC1 determines mitochondrial demise

Based on the abovementioned considerations, the present thesis addressed the suggested interplay between Bid and VDAC and demonstrated, for the first time, a direct interaction of tBid and Bid with VDAC1, a process with high relevance for mitochondrial integrity and intrinsic cell death signaling. The proposed interaction was not only observed at the physical and functional level using recombinant proteins, but also occurs in cell-based death models of glutamate-induced toxicity in HT-22 cells and primary neurons, and *in vivo*. Therefore, the data suggested that the proposed Bid/tBid-VDAC1 interaction is essential for mitochondrial demise and cell death in cultivated cells as well as during pathological conditions in whole organisms. This conclusion was substantiated by the observation that pronounced VDAC1/Bid interaction occurs only after glutamate exposure of HT-22 cells and primary neurons and significantly increased over 6-24 h in ischemic brain tissue of mice subjected to transient focal cerebral ischemia. Therefore, the data suggested that both proteins, Bid and VDAC1, interfere together in neuronal cell death signaling, and pointed to VDAC1 as a mitochondrial receptor for activated Bid to regulate mitochondrial integrity and function. This hypothesis was confirmed by the findings that VDAC1 gene silencing was sufficient to prevent Bid-mediated impairments in mitochondrial morphology and  $\Delta\psi_m$  as well as disturbed mitochondrial bioenergetics and attenuated glutamate toxicity in neuronal cells. Indicating a clear involvement of VDAC1 in the applied cell death models, the data suggested that a disturbed interaction between Bid and VDAC1 is the underlying mechanisms of the protective effects mediated by DIDS and VDAC1 gene silencing. This was affirmed by the data demonstrating that neither glutamate nor tBid were able to trigger mitochondrial dysfunction, MOMP and cell toxicity without functional VDAC1, and, *vice versa* VDAC1 over-expression did not induce mitochondrial fragmentation and cytotoxicity without Bid. Thus, the present thesis indicated that the association of both proteins is a key decision point for promoting

mitochondrial dysfunction and cell death thereby combining the abovementioned and long-standing debate whether MOMP is regulated by the Bcl-2 family members or by the PTPC.

However, what is the precise mechanism of this interaction and how does it affect the downstream signaling cascades?

In agreement with previous studies reporting the oligomeric assembly of VDAC1 coupled to cell death stimuli with increasing conformational changes upon apoptotic signaling<sup>239, 240</sup>, the data revealed dimeric VDAC1 around 12 h of glutamate treatment, i.e. when mitochondrial demise marks the final execution phase of intrinsic cell death. Interestingly, this dimeric assembly still interacted with Bid, indicating that the Bid-VDAC1 interaction might trigger the formation of VDAC1 oligomers. Furthermore, the presented *in vitro* data revealed that the binding affinity of tBid to VDAC1 is 38-fold higher than for the binding of full length Bid to VDAC1 and suggested that tBid is the more effective partner for a direct interaction with VDAC1. In cells exposed to toxic glutamate levels, cleavage of full-length Bid to its active form tBid, or dissociation of the cleaved Bid fragments likely takes place at the mitochondrial membrane nearby the VDAC channel. In fact, earlier observations suggested that tBid most likely affects VDAC following its association with lipid membranes<sup>161</sup> and recent reports showed that separation of the N- and C-terminal tBid fragments occurs rapidly upon initial binding of tBid to the mitochondrial outer membrane<sup>72</sup>. Thus after dissociation of the N-terminal p7 tBid fragment, tBid could bind to VDAC1 with high affinity to regulate its gating behavior. While it has been described that tBid induces VDAC1 channel closure<sup>161</sup>, the mechanism by which Bid alters channel gating, either directly or indirectly, was not reported. The data here revealed that the VDAC1 channel can adopt two major closed states at 40% and 60% of its original conductance<sup>188</sup>. Following tBid/Bid binding a reduction of the overall current was observed in BLM measurements, indicating that Bid-VDAC1 interaction induces a conformational change of the VDAC1 channel, rather than its full closure. In line with previous studies suggesting the importance of the N-terminus of VDAC for its channel gating and protein-interactions<sup>188, 242</sup>, deformations of the VDAC channel may squeeze the N-terminal  $\alpha$ -helix out of the hydrophilic cavity and therefore enable helix-mediated interactions with certain substrates and protein effectors. In accordance, a simplified model for the Bid/tBid-VDAC1 interaction can be suggested: upon cell death stimuli full-length Bid targets VDAC1 to induce a first conformational change of the channel. Cleavage of Bid and the dissociation of the cleaved p7 Bid fragment, which occurs rapidly upon initial binding of cBid to the mitochondrial outer membrane<sup>72</sup>, may promote a tighter binding of tBid to VDAC1. The tBid-VDAC1 complex with a reduced channel current further enables the exposure of the N-terminal  $\alpha$ -helix of VDAC1 to the inner mitochondrial space (IMS). Since tBid binding reduces the overall pore diameter of VDAC1, the tBid-VDAC1 complex might reflect a transitional state that further catalyzes the formation of VDAC1 homo-oligomers or hetero-oligomers with

other pro-apoptotic proteins, e.g. Bax, to sequester a pore formation enabling the release of death promoting factors into the cytosol and the subsequent cell death (Figure 86).

Interestingly, the addition of DIDS to reconstituted VDAC1 in BLMs resulted in a completely dysfunctional VDAC1 channel and no opening or closing events could be detected once DIDS was added. The fact that in the presence of DIDS, tBid fails to interact with BLM reconstituted mVDAC1, and additionally was not able to induce loss of  $\Delta\psi_m$  and cell death at all in HT-22 cells, indicates that DIDS induces the closed state of the VDAC channel thereby prohibits channel deformation by tBid. As DIDS facilitates a channel state that is likewise a nonfunctional VDAC1 channel, it is not surprising that in cells VDAC1 gene depletion and DIDS promote similar protective effects against various features of Bid-dependent cell death pathways.

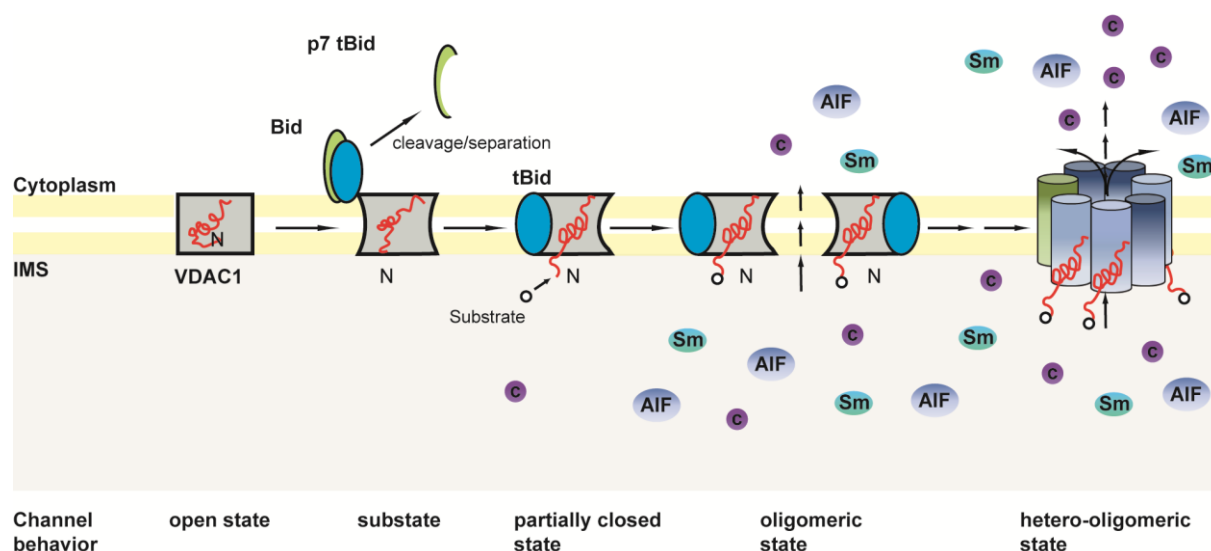


**Figure 86: Proposed model of the direct interaction of Bid and VDAC1.**

Upon apoptotic stimuli, Bid and VDAC1 interact in a direct manner. The association of full length Bid with VDAC1 induces a first conformational change of VDAC1 resulting in a reduction of the pore diameter. The initial binding of Bid with membrane integrated VDAC1 facilitates Bid cleavage and the separation of the p7 tBid fragment, which benefits the tighter binding of the cleaved p15 tBid fragment to VDAC1. The tBid-VDAC1 complex might reflect a transitional state with a reduced overall current that enables the exposure of the VDAC1  $\alpha$ -helix to the inner mitochondrial space (IMS). The exposure of the  $\alpha$ -helix to the IMS allows for further associations with several substrates including  $\text{Ca}^{2+}$ , ATP/ADP or even other proteins present in the IMS. The partially closed state of VDAC1 together with the exposed  $\alpha$ -helix catalyzes the further formation of VDAC1 oligomers or hetero-oligomers to sequester a pore diameter that enables the release of death promoting factors, such as apoptotic inducing factor (AIF), cytochrome c (c) and Smac/DIABLO (Sm), into the cytosol and the subsequent cell death.

If other proteins are involved in the interplay between Bid/tBid and VDAC1 remains to be determined, although the nature of the more complex interactions may be dictated by cell type and the nature of the apoptotic stimulus. Although Bax and Bak are discussed to physically interact with VDACs, they might not necessarily be involved in the tBid-VDAC1 complex. Since neurons do not express full-length Bak and in non-neuronal cells an



interaction of Bak and VDAC has been only demonstrated for the VDAC2 isoform<sup>296</sup>, it is likely that the proposed tBid-VDAC1 complex occurs independently of Bak. In contrast, Bax is widely expressed in neurons and discussed to interact with VDAC1, but so far no direct interaction between Bax and VDAC1 could be detected on the cellular level<sup>155</sup>. Although further studies are required to investigate whether the here proposed interaction might involve or even depends on Bax, a prerequisite role of Bax in the current cell death models is not expected, since previous studies revealed that Bax inhibitory peptides were not protective and Bax siRNA exerted only slightly protective effects in the model of glutamate-toxicity in HT-22 cells<sup>297</sup>. *In vitro* and *in vivo* studies using Bax<sup>-/-</sup> knockout cells and mice would be required to gain a deeper insight if Bax might be involved in the Bid-VDAC1 interplay. In any case, the direct interaction between tBid and VDAC1 seems to be essential for the subsequent impaired mitochondrial function and cell death, since deficiency of either Bid or VDAC1 is sufficient to provide protection, even if Bax is involved in the complex. Co-crystallization of recombinant Bid and VDAC1 is subject of the current studies to provide a more detailed understanding of the proposed Bid-VDAC1 interaction and to determine structural sequences of both proteins that mediate their association and the subsequent conformational changes of the VDAC1 channel. Determining the respective residues of Bid that are required for VDAC1 binding is further worthwhile to examine if a Bid-Bax interaction could take place in parallel or if a Bid-Bax interplay would be competitive to the Bid-VDAC1 interaction. Structural insights into the Bid-VDAC1 complex would further enabling for structure-guided drug campaigns and suggest a rationale for discovering antagonists that hinder the association of both proteins thereby inhibiting the subsequent mitochondrial demise.

In conclusion, the presented data highlight VDAC1 as a mitochondrial receptor for Bid and its cleaved form tBid following introduction of apoptotic stimuli in neuronal cells (Figure 87). This interaction provides a convergence point for the proposed mechanisms of MOMP which were previously attributed solely to either the activity of apoptogenic BH3-only proteins or to VDACS. Targeting the tBid-VDAC1 interaction has high impact for therapeutic perspectives for neurological diseases, where mitochondrial demise is a major feature.

#### **4.5 Bid-mediated mitochondrial demise in neurons is independent on VDAC2**

In addition to the crucial involvement of VDAC1 in Bid-mediated neuronal cell death pathways, the present thesis addressed the role of the isoform VDAC2 in the current model of glutamate-induced toxicity. Similar to VDAC1, VDAC2 is a mitochondrial outer membrane protein with channel forming ability but present in low abundance<sup>251</sup>. Previous studies

indicated a specific the role of VDAC2 in mitochondrial cell death signaling describing the association of VDAC2 with pro-apoptotic Bak<sup>251</sup> and providing evidence for VDAC2 dependence of Bak targeting to the mitochondria<sup>252</sup>. Those studies revealed that VDAC2 binds to Bak in un-stimulated mouse embryonic fibroblasts (MEFs) and that this sequestration is disrupted upon apoptotic signals, releasing Bak to carry out its pro-apoptotic function<sup>251</sup>. In line with these reports, Roy and colleagues linked the isoform VDAC2 to the apoptotic activity of tBid revealing that VDAC2<sup>-/-</sup> MEFs are insensitive to tBid-induced loss of  $\Delta\Psi_m$ , cytochrome c release and apoptosis<sup>298</sup>. These studies suggested that VDAC2 is needed for tBid-mediated cell death by recruiting Bak to mitochondria and suggested that the Bak-VDAC2-tBid axis is more efficient at initiating apoptosis than the Bax-tBid pathway<sup>93</sup>. Further reports demonstrated a direct interaction between VDAC2 and Bak in un-stimulated HCT116 cells which was reduced after Fas- and STS-stimulation<sup>296</sup>, although the specific response to tBid was not addressed. Thus, in non-neuronal cells, VDAC2 seems to have a specific role in tBid-mediated cell death. However, in neuronal cells, the apoptotic mechanism might differ from that in non-neuronal cells, since a neuroprotective function for Bak and a specific role of VDAC2 in neuronal cell death has not been reported so far. The present thesis revealed that in contrast to the essential role of VDAC1, VDAC2 might be dispensable for Bid-mediated mitochondrial demise in neurons. This conclusion was drawn based on the findings that VDAC2 gene silencing achieved only minor protective effects in the model of glutamate-induced toxicity. Furthermore, the data demonstrated that in neurons Bid-mediated MOMP was not dependent on VDAC2, revealing that glutamate-induced loss of  $\Delta\Psi_m$  was not prevented by VDAC2 depletion. Although VDAC2 might be important for non-neuronal cell death mediated by the tBid/Bak/Bax assembly, the data suggest a minor role of VDAC2 in neuronal cells. In regard to the reported absence of full-length Bak in neurons, indicating different non-neuronal and neuronal cell death mechanisms, the present thesis suggest that the proposed Bid-VDAC1 interaction in neurons mirrors the emerging non-neuronal tBid-VDAC2-Bak pathway of apoptosis.

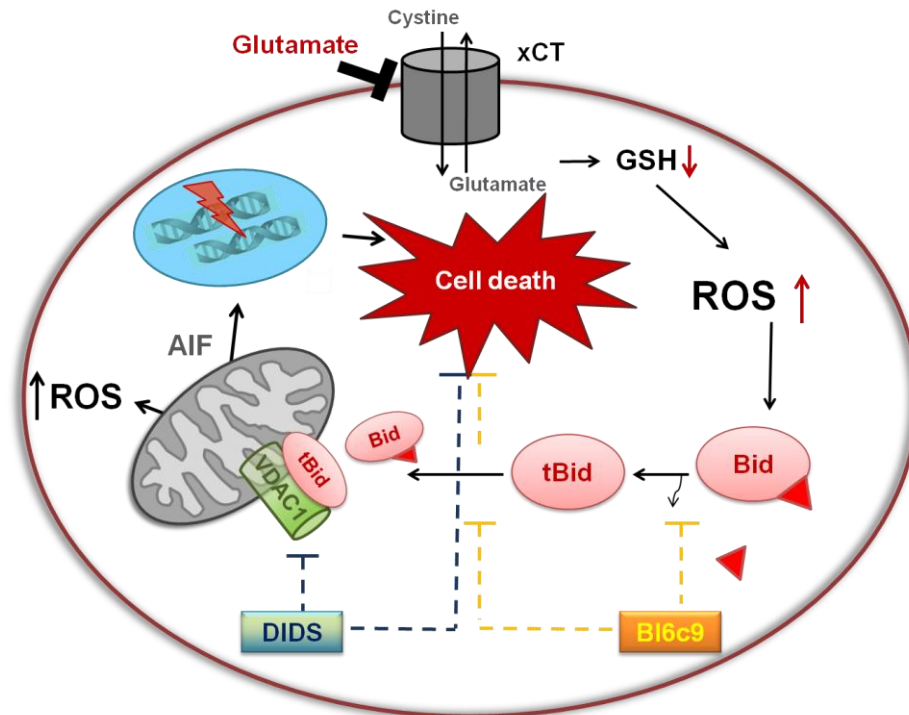


**Figure 87: Proposed role of VDAC1 and Bid in neuronal apoptosis based on the findings in the glutamate-toxicity model in HT-22 cells.**

The model of glutamate-induced toxicity in HT-22 cells was demonstrated as a suitable model to investigate neuronal apoptosis. In this model system, oxidative stress, as it is induced by different neurodegenerative diseases, cerebral ischemia and others, leads to a detrimental increase of reactive oxygen species that trigger the following cleavage and activation of the pro-apoptotic protein Bid. Upon transactivation Bid initiates the point of no return in the mitochondrial cell death pathway: the depolarization of mitochondrial outer membrane (MOMP). The present thesis revealed an essential role for the voltage-dependent anion channel VDAC1 in the model of glutamate-induced toxicity and points to VDAC1 as a mitochondrial receptor for Bid to trigger mitochondrial demise and cell death. Both, over-expression of tBid as well as over-expression of VDAC1 induced mitochondrial fragmentation, loss of  $\Delta\psi_m$  and cell death in HT-22 neurons. Upon the Bid/tBid–VDAC1 interaction, breakdown of the mitochondrial membrane potential, ATP depletion, impairments in mitochondrial respiration and finally the release of AIF and Cyt C trigger the final execution of mitochondrial apoptosis. Inhibition of either factor, VDAC1 and Bid, is sufficient to block the other's detrimental effect on mitochondria and execution of neuronal cell death. The Bid inhibitor BI-6c9 and Bid siRNA prevented the translocation of both, full-length Bid and tBid, to the mitochondria. Down-regulation of VDAC1 by siRNA as well as the anion channel blocker DIDS significantly preserved mitochondrial integrity and function, MOMP and reduced glutamate toxicity in neuronal cells. In contrast to VDAC1, VDAC2 down-regulation was not sufficient to provide protection against glutamate-induced Bid-mediated apoptosis. Therefore, inhibition of the Bid/VDAC1 interaction is a promising therapeutic target to prevent mitochondrial demise, a crucial hallmark of neuronal cell death in acute and chronic neurodegenerative diseases, where glutamate toxicity and oxidative stress are prominent.

## 5 Summary

Mitochondrial demise is a key feature of the progressive neuronal death in age-related neurodegenerative diseases such as Alzheimer's disease or Parkinson's disease and after acute brain injury. Oxidative stress or impaired calcium homeostasis converge at mitochondria where the permeabilization of the mitochondrial outer membrane (MOMP) are considered as 'point of no return' in the cell's commitment to die. The pro-apoptotic Bcl-2 family protein Bid has been identified as a key regulator of mitochondrial injury and mitochondrial pathways of neuronal cell death. Upon its transactivation to mitochondria, Bid induces mitochondrial fragmentation and MOMP thereby accelerating the production of reactive oxygen species (ROS) and the release of death promoting factors into the cytosol that trigger the final steps of intrinsic cell death. The pivotal role of Bid in neuronal cell death has been further shown in models of cerebral ischemia and traumatic brain injury *in vivo*. Since it has been shown that inhibition of Bid maintains mitochondrial integrity and function thereby preventing mitochondrial cell death, Bid serves as a target for mitoprotection and neuronal cell survival. However, the precise mechanisms how Bid triggers mitochondrial impairment and disruption are still unknown and have to be explored to achieve efficient strategies for inhibition of Bid-mediated cell death pathways.

Therefore, the present study was aimed to elucidate the mechanisms of Bid-dependent mitochondrial demise and addressed the associated Bid-protein interactions. Furthermore, the thesis focused on Bid crystallization campaigns and the development of Bid-inhibiting compounds with high impact for novel therapeutic perspectives in neurological diseases. Bid-mediated cell death pathways were mainly addressed in immortalized mouse hippocampal HT-22 neurons exposed to toxic glutamate concentrations that induce oxidative stress through glutathione depletion. The findings were additionally confirmed in a model of tBid-induced toxicity by over-expressing tBid in the HT-22 cell line and *in vitro* studies using recombinant proteins.

The first part of the present study focused on the development of small-molecule ligands that target Bid for mitoprotection and neuronal cell survival. Seven compounds, obtained from three diverse chemical structure classes, were identified as effective inhibitors against glutamate- and tBid-induced cell injury. Most promising compounds were obtained from the class of thiazolidin-2,4-diones, revealing EC<sub>50</sub> values in the lower micromolar range between 6.78  $\mu$ M and 13.27  $\mu$ M. The compounds prevented not only cell death, but also preserved mitochondrial membrane potential, ATP levels as well as mitochondrial respiration after induction of oxidative stress in HT-22 neurons. The data further indicated the inhibition of Bid as the key mechanism behind their neuroprotective properties as substantiated by docking analysis and the compound's protective effect against tBid-induced toxicity. Thus, the

identified compounds indicate potent scaffolds for future structure optimization which should result in small-molecules with favorable pharmaceutical properties, applicable also in model systems of cell death *in vivo* and further promise pharmaceutical perspectives for various neuronal and non-neuronal pathologies where Bid-mediated mitochondrial injury has been implicated.

The second part of the thesis provided a basis for the use of recombinant Bid constructs suitable for Bid crystallization campaigns and further structure-guided drug design. Protocols for the design, expression and purification of different Bid constructs were scaled up, yielding reasonable amounts of Bid protein sufficient for crystallization screening. One of the designed Bid constructs was successfully crystallized obtaining diffraction data of 3.75 to 3.95 Å resolution under synchrotron-X-ray exposure. This observation indicates the appropriate Bid constructs as suitable for Bid crystal structure analysis. In addition, the activity of the novel Bid constructs was verified in the HT-22 cell line. Over-expression of those proteins revealed their non-apoptotic function and indicated their behavior as a 'full-length Bid-like protein', in contrast to toxic effects of tBid-over-expression. The further work investigated the effect of recombinant full-length Bid, caspase-8 cleaved Bid (cBid) and Bax on fluorescence-containing liposomes which mimic the mitochondrial membrane and focused on the role of cardiolipin (CL) in Bid-mediated membrane integration and permeabilization. The results indicated an ordered series of events that occur at mitochondrial membranes to induce MOMP and the release of death promoting proteins, revealing the requirement of CL for the recruitment of cBid to membranes and the role for Bax to enhance cBid-induced fluorescence release.

The last part of the thesis demonstrated for the first time a direct interaction of Bid and VDAC1 with high relevance for Bid-mediated mitochondrial demise and neuronal cell death. The Bid-VDAC1 interaction significantly increased after glutamate-exposure of HT-22 cells and primary cortical neurons *in vitro* and after transient focal cerebral ischemia *in vivo*. The role of VDAC1 in Bid-dependent cell death signaling was verified by the protective effects of the anion channel blocker DIDS and VDAC1 siRNA in the present models of glutamate- and tBid-induced toxicity. Functional analysis revealed that both, Bid and VDAC1, cooperate during neuronal apoptosis to mediate impairments in mitochondrial oxygen consumption and ATP production, as well as mitochondrial fission, increased mitochondrial ROS production and the breakdown of the mitochondrial membrane potential. Inhibition of either factor, Bid or VDAC1, was sufficient to block the other's detrimental effect on mitochondria and the execution of intrinsic cell death. These findings strongly indicated the proposed Bid-VDAC1 interaction as a converging point for the mechanisms of MOMP that were previously contributed solely to either Bcl-2 family proteins or to VDACS. In contrast, only a minor role in Bid-mediated cell death signaling was suggested for the mitochondrial porin VDAC2, as

VDAC2 gene silencing could not protect against glutamate-induced injury. Therefore the data implicate a specific role for VDAC1 as mitochondrial receptor for activated Bid at the control point of life and death at the level of mitochondria *in vitro* and *in vivo*.

Overall, the present thesis highlights the pro-apoptotic protein Bid as a promising druggable target for mitoprotection and neuronal survival and indicates recombinant Bid constructs as suitable for Bid crystal structure analysis. Furthermore, the data gained new insights in the mechanisms of Bid-dependent mitochondrial injury and the involvement of VDAC1 in mitochondrial apoptosis, connecting the controversial hypothesis of MOMP initiated by Bid and Bcl-2 family proteins or VDAC-mediated mPTP, respectively. Targeting the Bid-VDAC1 interaction serves as a promising therapeutic approach aiming at preserved mitochondrial function and neuronal survival with high relevance for the treatment of neurological disorders, where oxidative stress and mitochondrial demise are prominent.

## 6 Zusammenfassung

Mitochondriale Prozesse des Zelltods spielen eine entscheidende Rolle für den progressiven Verlust von Neuronen bei neurodegenerativen Erkrankungen (M. Alzheimer, M. Parkinson) und nach akuter Hirnschädigung durch Schädel-Hirn-Trauma oder zerebraler Ischämie. Eine Schlüsselfunktion nimmt hierbei das pro-apoptotische Bcl-2 Protein Bid ein. Durch die Aktivierung und mitochondriale Translokation von Bid kommt es zur Schädigung und Fragmentierung von Mitochondrien und letztlich zur Freisetzung von weiteren pro-apoptotischen Faktoren (AIF, Cytochrom C, Smac/DIABLO), die den Untergang der Neurone steuern. Um in Zukunft Bid als potentiell Target für die Therapie von akuten und chronischen neurologischen sowie nicht neurologischen Erkrankungen nutzen zu können, müssen die bisher ungeklärten Mechanismen der Bid-induzierten mitochondrialen Schädigung, sowie die Interaktionen von aktiviertem Bid mit weiteren am Zelltod beteiligten Proteine aufgeklärt werden.

Ziel dieser Arbeit war daher die Untersuchung Bid-abhängiger, mitochondrialer Zelltod Mechanismen und beteiligter Protein-Wechselwirkungen. Darüber hinaus stand die Entwicklung neuer Leitstrukturen für protektive Bid-Inhibitoren sowie die Etablierung erster Kristallisationsansätze verschiedener Bid Konstrukte im Fokus dieser Arbeit. Als Modellsysteme mitochondrialer Prozesse des Zelltods dienten vor allem immortalisierte hippocampale Neurone (HT-22 Zellen), in denen eine Behandlung mit Glutamat den durch oxidativen Stress gekennzeichneten Zelltod induziert. Als weiteres Schädigungsmodell wurde die Überexpression von aktiviertem Bid (tBid) eingesetzt. Zum Nachweis von Proteininteraktionen wurden weiterhin eine primäre neuronale Zellkultur und ein *in vivo*-Modell der zerebralen Ischämie verwendet, sowie verschiedene Untersuchungen mit rekombinanten Proteinen durchgeführt.

Im ersten Teil der vorliegenden Arbeit wurden neue niedermolekulare Bid-Inhibitoren aus drei strukturell verschiedenen Substanzklassen mittels Zellviabilitätsmessungen auf neuroprotektive Effekte geprüft. Sieben Substanzen zeigten nicht nur deutliche Protektion gegenüber dem Glutamat- und tBid-induzierten Zelltod, sondern konnten ebenso die Bid-abhängige mitochondriale Schädigung verhindern. Durch die Applikation dieser Substanzen konnten HT-22 Zellen vor dem Verlust des mitochondrialen Membranpotentials, dem Abfall intrazellulärer ATP Level sowie vor Störungen der mitochondrialen Atmung nach oxidativem Stress geschützt werden. Die hier gezeigten Verbindungen stellen daher wichtige Leitstrukturen für die Weiterentwicklung potenzieller Bid-Inhibitoren als Neuroprotektiva dar.

Der zweite Teil dieser Arbeit beschäftigte sich mit der Kristallisation von rekombinantem Bid Protein, welche als Basis für ein grundlegendes Verständnis der molekularen Proteinfunktion sowie der Struktur-basierten Wirkstoffentwicklung dient. Hier wurde die Expression und

Reinigung verschiedener rekombinanter Bid Konstrukte etabliert und hoch gereinigtes Bid Protein für erste Kristallisationsätze verwendet. Durch Verfolgung wichtiger Strategien im Konstruktdesign konnte eines der verwendeten Bid Konstrukte erfolgreich kristallisiert werden und lieferte eine Strukturauflösung von 3.75 bis 3.95 Å unter Synchrotronstrahlung. Die Arbeit konnte somit eine grundlegende Basis für die weitere Optimierung der hier erhaltenden Kristalle legen und sollte eine zukünftige Aufklärung der Kristallstruktur von Bid ermöglichen. Eine Überprüfung der verschiedenen Bid-Konstrukte im Zellsystem zeigte ein nicht-apoptotisches Verhalten im Gegensatz zur Überexpression von toxischem tBid. Im weiteren Rahmen dieser Promotionsarbeit wurde der Effekt der rekombinanten Proteine Bid, cBid und Bax auf Fluoreszenz-Liposomen getestet, um die Mechanismen der Bid-abhängigen mitochondrialen Membranpermeabilisierung zu untersuchen. Es konnte hier eine Schlüsselrolle für das mitochondriale Lipid Cardiolipin gezeigt werden, in dessen Abhängigkeit Caspase-8 aktiviertes Bid (cBid) eine Membrandestabilisierung vermittelte, welche durch die Koexistenz von Bax gesteigert werden konnte.

Der letzte Teil der Arbeit konnte erstmals eine direkte Interaktion zwischen Bid und dem mitochondrialen Porin VDAC1 in kultivierten Neuronen sowie in einem *in vivo* Modell der zerebralen Ischämie nachweisen. Die Inhibition von VDAC1 mittels Einsatz des Anionen-Kanal-Blockers DIDS sowie der Verwendung von VDAC1 siRNA konnte sowohl die Funktion als auch die Integrität der Mitochondrien nach Glutamat- und tBid-induzierter Schädigung schützen und bestätigte somit die essentielle Rolle von VDAC1 im Bid-abhängigen Zelltod. Weitere Untersuchungen zeigten erstmalig, dass beide Proteine, Bid und VDAC1, gleichermaßen im neuronalen Zelltod involviert sind und offensichtlich zusammen eine Schädigung der mitochondrialen Membran induzieren. Die Hemmung eines der beiden Proteine war ausreichend, um die toxischen Effekte des Partnerproteins zu hemmen und so den Funktionsverlust der Neurone zu verhindern. Im Gegensatz dazu konnte gezeigt werden, dass die Isoform VDAC2 nur eine untergeordnete Rolle im Bid-induzierten Zelltod in Neuronen spielt.

Die nachgewiesene Bid-VDAC1 Wechselwirkung besitzt hohe Relevanz für die mitochondrialen Prozesse des Zelltods. Damit verbindet die vorliegende Arbeit die bisher kontrovers betrachteten Mechanismen der mitochondrialen Membranschädigung, die zuvor entweder auf die alleinige Aktivität der Bcl-2 Proteine oder auf VDACs zurückgeführt wurde. Mit der Identifizierung neuer potentieller Bid-Inhibitoren sowie durch Etablierung wichtiger Grundlagen für die Aufklärung der Kristallstruktur von Bid, stellt die Arbeit einen wesentlichen Beitrag für die strukturbasierte Wirkstoffentwicklung und Therapie verschiedener neurologischer und nicht neurologischer Erkrankungen dar, in welchen Bid-abhängige mitochondriale Prozesse des Zelltods eine wesentliche Rolle spielen.



## 7 Abbreviations

<b>A1</b>	Bcl-2 related gene A1
<b>AD</b>	Alzheimer's disease
<b>AIF</b>	Apoptosis inducing factor
<b>ALS</b>	Amyotrophic lateral sclerosis
<b>AMP</b>	Adenosine monophosphate
<b>ANOVA</b>	Analysis of variance
<b>APAF-1</b>	Apoptosis protease-activating factor-1
<b>ATP</b>	Adenosinetriphosphate
<b>Bad</b>	Bcl-2 antagonist of cell death
<b>Bak</b>	Bcl-2 antagonist/killer 1
<b>Bax</b>	Bcl-2 associated protein X
<b>BCA</b>	Bicinchonic acid
<b>Bcl-2</b>	B-cell lymphoma-2
<b>Bcl-xl</b>	Bcl-2-related gene, long isoform
<b>BH</b>	Bcl-2 homology
<b>BI</b>	Bid inhibitor
<b>Bid</b>	Bcl-2 interacting domain death antagonist
<b>Bim</b>	Bcl-2-interacting mediator of cell death
<b>BLM</b>	Black lipid bilayers
<b>BSA</b>	Bovine serum albumin
<b>BODIPY</b>	4,4-Difluoro-5-(4-phenyl-1,3-butadienyl)-4-bora 3a,4a-diaza-sindacene-3-undecanoic acid
<b>Bp</b>	Base pairs
<b>°C</b>	Grad Celcius
<b>Ca<sup>2+</sup></b>	Calcium
<b>CAD</b>	Caspase-activated deoxyribonuclease
<b>cBid</b>	Caspase-8 cleaved Bid
<b>CCCP</b>	Carbonyl cyanide 3-chlorophenylhydrazone
<b>CL</b>	Cardiolipin
<b>Cl<sup>-</sup></b>	Chlorid
<b>CNS</b>	Central nervous system
<b>CO<sub>2</sub></b>	Carbon dioxide
<b>Cu<sup>1+</sup></b>	Copper
<b>Cyp D</b>	Cyclophilin D

<b>Cyt C</b>	Cytochrome C
<b>DAPI</b>	4',6-Diamidino-2-phenylindole
<b>DED</b>	Death effector domain
<b>DIDS</b>	4,4-diisothio-cyanatostilbene-2,2'-disulfonic acid
<b>DMEM</b>	Dulbecco's Modified Eagle Medium
<b>DMSO</b>	Dimethyl sulfoxide
<b>DNA</b>	Deoxyribonucleic acid
<b>DTT</b>	D,L-Dithiotreitol
<b>EDTA</b>	Ethylenediamine-tetra-acetic acid
<b>EGTA</b>	Ethylene glycol-bis(2-aminoethylether)- <i>N,N,N',N'</i> - tetraacetic acid
<b>FACS</b>	Fluorescence-activated cell sorting
<b>FasL</b>	Fas-ligand
<b>FCS</b>	Fetal calf serum
<b>GAPDH</b>	Glyceraldehyde-3-phosphate-dehydrogenase
<b>GFP</b>	Green fluorescence protein
<b>GSH</b>	Gluthatione
<b>Glut</b>	Glutamate
<b>Gpx 4</b>	Glutathione peroxidase 4
<b>GSH</b>	Glutathione
<b>h</b>	hour
<b>HCL</b>	Hydrochloric acid
<b>HEPES</b>	4-(2-Hydroxyethyl)piperazine-1-ethanesulfonic acid
<b>HD</b>	Huntington's disease
<b>HRP</b>	Horseradish peroxidase
<b>IAP</b>	Inhibitors of apoptosis
<b>ICAD</b>	Inactive caspase-activated desoxyribonuclease
<b>IMM</b>	Inner mitochondrial membrane
<b>IPTG</b>	Isopropyl- $\beta$ -D-thiogalactopyranosid
<b>kDa</b>	Kilo Dalton
<b>12/15 LOX</b>	12/15 Lipoxygenase
<b>MCA</b>	Middle carotid artery
<b>MCAO</b>	Middle carotid artery occlusion
<b>Mcl-1</b>	Myeloid cell leukemia 1
<b>MEF</b>	Mouse embryonic fibroblast

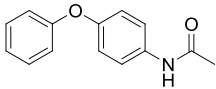
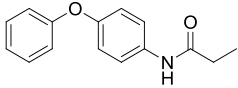
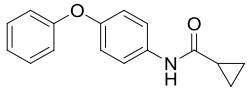
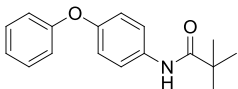
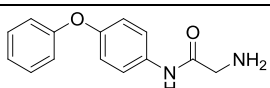
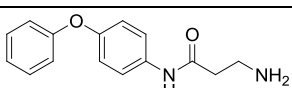
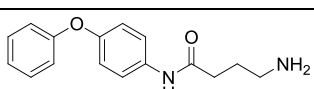
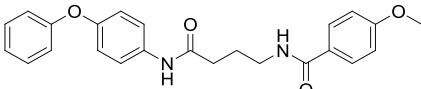
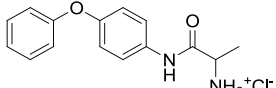
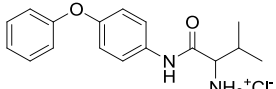
<b>MEM+</b>	Eagle's minimum essential medium
<b>mGFP</b>	Mitochondrial targeting green fluorescent protein
<b>mM</b>	Millimolar
<b>MOM</b>	Mitochondrial outer membrane
<b>MOMP</b>	Mitochondrial outer membrane permeabilization
<b>mPTP</b>	Mitochondrial permeability transition pore
<b>mtDNA</b>	Mitochondrial DNA
<b>MTT</b>	3-(4,5-Dimethylthiazol-2-yl)-2,5-diphenyltetrazolium bromide
<b>NADH</b>	Nicotinamide adenine dinucleotide
<b>NaHCO<sub>3</sub></b>	Sodium hydrogen carbonate
<b>NaOH</b>	Sodium hydroxide
<b>nM</b>	Nanomolar
<b>NMDA</b>	N-methyl-D-aspartic acid
<b>OG</b>	Octylglucosid
<b>OGD</b>	Oxygen-glucose deprivation
<b>Omi/HtrA2</b>	High temperature requirement protein A2
<b>PBS</b>	Phosphate buffered saline
<b>PC</b>	Phosphatidylcholin
<b>PCR</b>	Polymerase chain reaction
<b>PCD</b>	Programmed cell death
<b>PD</b>	Parkinson's disease
<b>PDB</b>	Protein data bank
<b>pDsRed2-Bid</b>	Plasmid encoding for a fusion protein of red fluorescent protein and Bid under control of the CMV promoter/enhancer
<b>PE</b>	Phosphatidylethanolamin
<b>PEG</b>	Polyethyleneglycole
<b>PEI</b>	Polyethylenimine
<b>PFA</b>	Paraformaldehyde
<b>PH</b>	Potentia hydrogenii
<b>PI</b>	Propidium iodide
<b>PS</b>	Phosphorothioate
<b>PTP</b>	Permeability transition pore
<b>PTPC</b>	Permeability transition pore complex
<b>PVDF</b>	Polyvinylidenfluorid

<b>ROS</b>	Reactive oxygen species
<b>RT</b>	Room temperature
<b>RuR</b>	Ruthenium red
<b>Scr</b>	Scrambled
<b>SD</b>	Standard deviation
<b>SDS</b>	Sodium dodecyl sulfate
<b>SDS-PAGE</b>	Sodium dodecyl sulfate polyacrylamide gel electrophoresis
<b>siRNA</b>	Small interfering ribonucleic acid
<b>Smac/DIABLO</b>	Second mitochondria – derived activator of caspase/direct IAP binding protein with low pI
<b>STS</b>	Staurosporin
<b>TBE</b>	Tris/borate/EDTA
<b>TBI</b>	Traumatic brain injury
<b>tBid</b>	truncated Bid
<b>TBS</b>	Tris-buffered solution
<b>TBST</b>	Tris-buffered solution with Tween 20
<b>TE</b>	Trypsin-EDTA
<b>TEMED</b>	Tetramethylenethylenediamin
<b>TMRE</b>	Tetramethylrhodamin ethal ester
<b>TNF</b>	Tumor necrosis factor
<b>U</b>	Unit(s)
<b>V</b>	Volt
<b>VDAC</b>	Voltage-dependent anion channel
<b>xCT</b>	glutamine-cystine antiporter
<b>XIAP</b>	X-chromosomal linked inhibitor of apoptosis
<b>μ</b>	Micro
<b>μM</b>	Micromolar

## 8 Appendix

**Table 67: Neuroprotective properties of 4-phenoxyanilines**

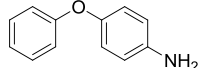
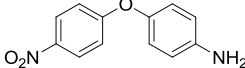
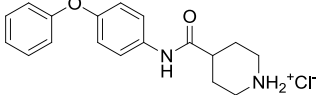
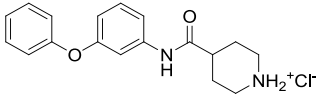
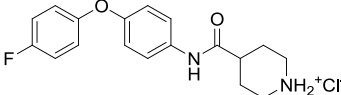
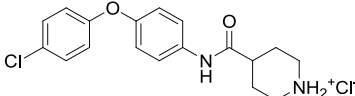
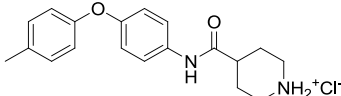
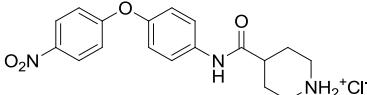
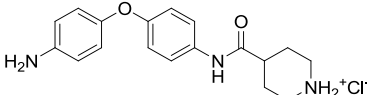
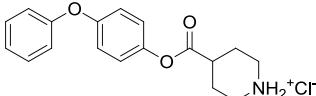
Chemical structures and neuroprotective activities of representative *N*-acyl 4-phenoxyanilines against glutamate-induced toxicity as achieved by the first screening and determined by MTT assay. Results are representatives of 3-8 independent experiments each with  $n = 8$  (\* $p < 0.05$ ; \*\* $p < 0.01$ ; \*\*\* $p < 0.001$  compared to glutamate treated controls, ANOVA Scheffé's test; N/A<sup>α</sup>, not active: compound revealed no toxic effects in HT-22 cells at concentrations from 1  $\mu\text{M}$  up to 100  $\mu\text{M}$ ).

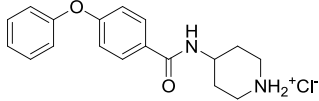
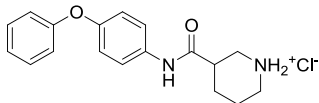
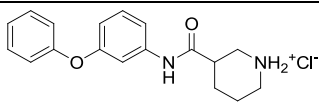
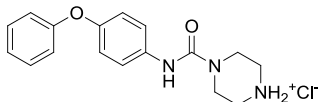
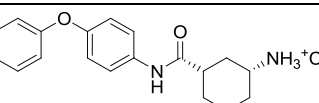
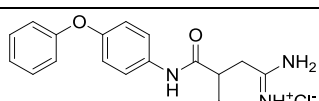
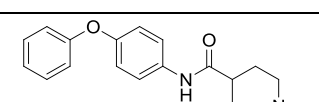
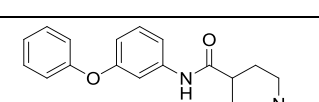
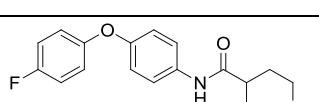
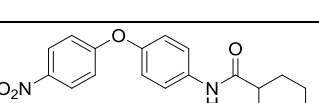
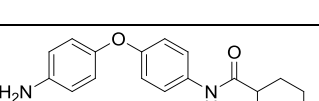
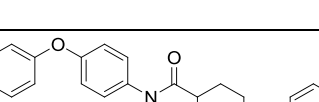
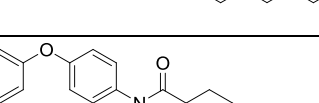
Compound name	Structure	Neuroprotective activity					Cytotoxicity ( $\mu\text{M}$ , $p < 0.001$ )
		compound concentration ( $\mu\text{M}$ )					
		1	10	25	50	100	
SCHL 24366		---	---	---	---	---	N/A <sup>α</sup>
SCHL 24370		---	---	***	***	***	$\geq 100$
SCHL 28131		---	---	---	---	---	N/A <sup>α</sup>
SCHL 28132		---	---	---	---	***	N/A <sup>α</sup>
SCHL 24388		---	---	---	***	***	$\geq 100$
SCHL 24395		---	---	---	---	***	$\geq 100$
SCHL 24396		---	---	---	---	---	N/A <sup>α</sup>
SCHL 24382		---	---	---	---	---	$\geq 100$
SCHL 28073		---	---	*	**	***	N/A <sup>α</sup>
SCHL 28074		---	---	---	---	***	$\geq 100$



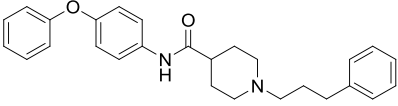
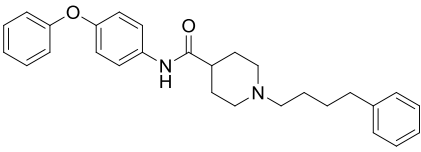
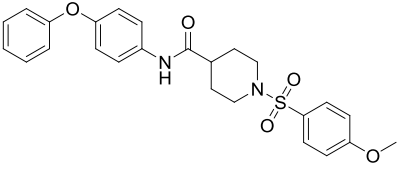
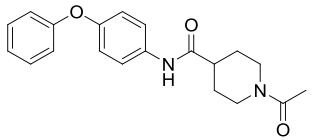
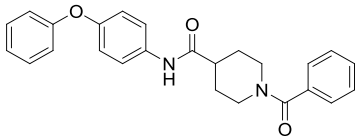
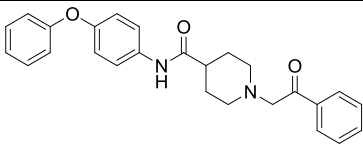
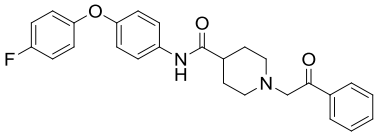
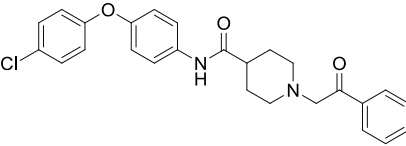
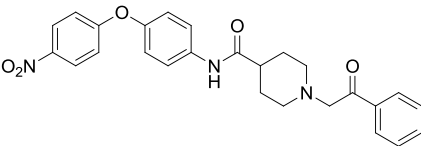
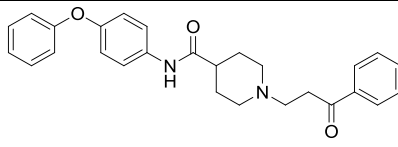
**Table 68: Neuroprotective properties of isonipecotic acid derivatives**

Chemical structures and neuroprotective activities of representative isonipecotic acid derivatives against glutamate-induced toxicity as achieved by the first screening and determined by MTT assay. Results are representatives of 3-8 independent experiments each with  $n = 8$  (\* $p < 0.05$ ; \*\* $p < 0.01$ ; \*\*\* $p < 0.001$  compared to glutamate treated controls, ANOVA Scheffé's test; N/A<sup>a</sup>, not active: compound revealed no toxic effects in HT-22 cells at concentrations from 1  $\mu\text{M}$  up to 100  $\mu\text{M}$ ).

Compound name	Structure	Neuroprotective activity					Cytotoxicity ( $\mu\text{M}$ , $p < 0.001$ )
		compound concentration ( $\mu\text{M}$ )					
		1	10	25	50	100	
SCHL 28001		---	***	***	***	***	$\geq 50$
SCHL 28002		*	***	***	***	***	N/A <sup>a</sup>
SCHL 24519		***	***	***	***	***	N/A <sup>a</sup>
SCHL 24017		---	---	---	***	***	$\geq 100$
SCHL 28025		---	---	***	***	---	$\geq 100$
SCHL 28049		---	***	***	***	---	$\geq 100$
SCHL 28069		---	---	***	---	---	$\geq 100$
SCHL 28038		---	***	***	***	***	$\geq 100$
SCHL 28052		---	***	***	***	***	N/A <sup>a</sup>
SCHL 28146		---	---	---	***	***	$\geq 100$

SCHL 24543		---	***	***	***	---	≥ 100
SCHL 24537		---	***	***	***	---	≥ 100
SCHL 24062		---	---	***	*	---	≥ 100
SCHL 24545		---	---	***	***	***	N/A <sup>a</sup>
SCHL 24546		---	**	***	***	---	≥ 100
SCHL 24553		---	*	***	***	***	N/A <sup>a</sup>
SCHL 24518		---	**	***	***	***	≥ 100
SCHL 24551		---	---	*	***	***	≥ 100
SCHL 24555		---	---	---	***	***	N/A <sup>a</sup>
SCHL 28086		---	***	***	---	---	≥ 100
SCHL 28119		---	***	***	***	***	N/A <sup>a</sup>
SCHL 24520		---	---	*	*	***	≥ 100
SCHL 24524		---	***	***	***	***	≥ 100



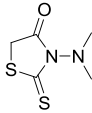
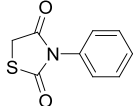
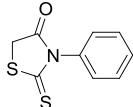
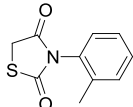
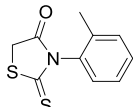
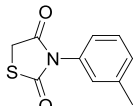
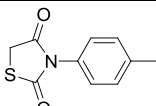
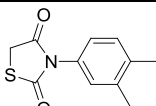
SCHL 24522		**	***	***	---	---	$\geq 100$
SCHL 28129		---	---	---	---	---	$\geq 10$
SCHL 24379		---	---	---	---	---	N/A <sup>a</sup>
SCHL 24380		---	---	---	---	---	N/A <sup>a</sup>
SCHL 24381		---	---	---	---	***	N/A <sup>a</sup>
SCHL 28037		---	---	---	---	---	N/A <sup>a</sup>
SCHL 28045		---	---	*	*	*	N/A <sup>a</sup>
SCHL 28053		---	***	***	***	***	$\geq 100$
SCHL 28047		---	***	***	***	***	$\geq 100$
SCHL 24540		---	---	---	---	---	$\geq 100$

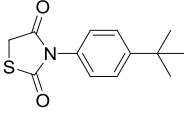
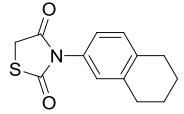
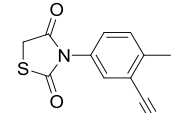
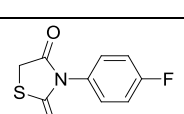
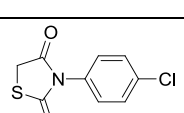
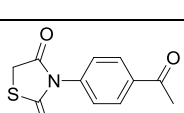
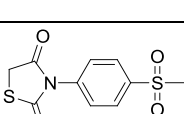
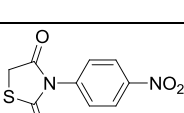
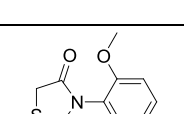
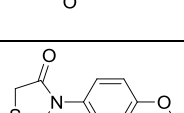
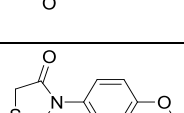
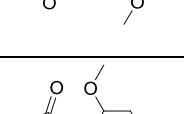




**Table 69: Neuroprotective properties of *N*-phenyl substituted thiazolidindiones.**

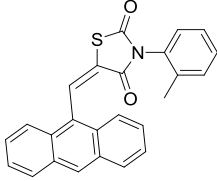
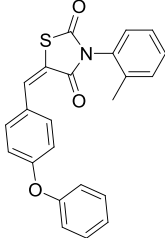
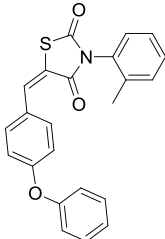
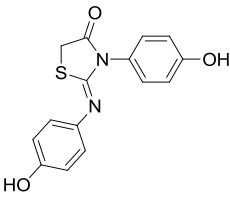
Neuroprotective activity of the compounds against glutamate-toxicity in HT-22 cells was determined within the first screening approach by MTT assay. EC<sub>50</sub> are given as the mean drug concentration required for inhibiting cell death by 50 % compared to controls. Toxicity values indicate toxic drug concentrations found to induce cell death without co-treatment with glutamate. (\*\*\*p < 0.001 compared to glutamate treated control, ANOVA Scheffé's test; N/A<sup>α</sup>, not active – substance revealed no toxic properties at concentrations of 0.1 μM up to 100 μM; N/D<sup>β</sup>, not determinable – EC<sub>50</sub> values could not be calculated due to lack of protective effects. The results presented are representatives of 4-6 independent experiments (MTT assay).

Compound name	Structure	EC <sub>50</sub> (μM)	Neuroprotective activity					Cytotoxicity (μM, p < 0.001)
			compound concentration (μM)					
			0.1	1	5	10	50	
SCHL 30049		N/D <sup>β</sup>	---	---	---	---	---	N/A <sup>α</sup>
SCHL 24292		9.87	---	---	***	***	***	N/A <sup>α</sup>
SCHL 30042		18.10	---	---	---	***	***	N/A <sup>α</sup>
SCHL 24277		6.78	---	---	***	***	***	N/A <sup>α</sup>
SCHL 30026		19.30	---	---	---	---	***	N/A <sup>α</sup>
SCHL 24262		11.87	---	---	**	***	***	N/A <sup>α</sup>
SCHL 24258		18.10	---	---	---	***	***	N/A <sup>α</sup>
SCHL 24310		9.59	---	---	***	***	***	N/A <sup>α</sup>

SCHL 24324		20.85	---	---	---	*	**	N/A <sup>a</sup>
SCHL 24309		9.60	---	---	---	***	***	N/A <sup>a</sup>
SCHL 24338		9.28	---	---	*	***	***	N/A <sup>a</sup>
SCHL 30024		19.98	---	---	---	*	***	N/A <sup>a</sup>
SCHL 30037		19.73	---	---	---	---	***	N/A <sup>a</sup>
SCHL 24293		13.20	---	---	***	***	***	N/A <sup>a</sup>
SCHL 24305		15.71	---	---	***	***	***	N/A <sup>a</sup>
SCHL 30021		19.50	---	---	---	---	***	N/A <sup>a</sup>
SCHL 30025		19.46	---	---	---	*	***	N/A <sup>a</sup>
SCHL 24386		13.68	---	---	*	***	***	N/A <sup>a</sup>
SCHL 24213		9.39	---	---	***	***	***	N/A <sup>a</sup>
SCHL 24239		14.94	---	---	---	***	***	≥ 50



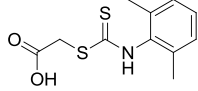
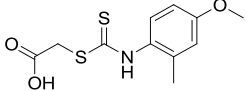
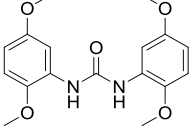
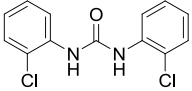
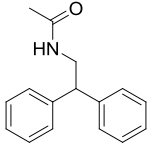
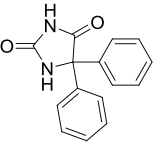
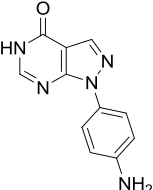
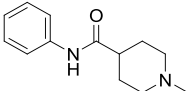


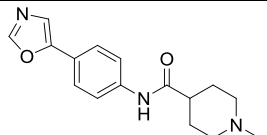
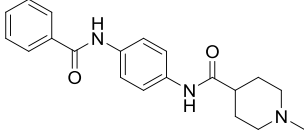
SCHL 30011		N/D <sup>β</sup>	---	---	---	---	---	N/A <sup>α</sup>
SCHL 30010		N/D <sup>β</sup>	---	---	---	---	---	≥ 100
SCHL 30008		N/D <sup>β</sup>	---	---	---	*	*	≥ 50
SCHL 24100		N/D <sup>β</sup>	---	---	---	---	---	N/A <sup>α</sup>



**Table 70: Neuroprotective properties of miscellaneous chemical compounds.**

Structures and neuroprotective activities of novel chemical compounds against glutamate-induced toxicity as achieved by the first screening and determined by MTT assay. Results are representatives of 3-8 independent experiments each with  $n = 8$  (\* $p < 0.05$ ; \*\*  $p < 0.01$ ; \*\*\*  $p < 0.001$  compared to glutamate treated controls, ANOVA Scheffé's test; N/A<sup>α</sup>, not active: compound revealed no toxic effects in HT-22 cells at concentrations from 1  $\mu\text{M}$  up to 100  $\mu\text{M}$ ).

Compound name	Structure	Neuroprotective activity					Cytotoxicity ( $\mu\text{M}$ , $p < 0.001$ )
		compound concentration ( $\mu\text{M}$ )					
		1	10	25	50	100	
SCHL 30032		---	---	---	---	---	N/A <sup>α</sup>
SCHL 30040		---	---	---	---	---	N/A <sup>α</sup>
SCHL 30002		---	---	---	---	---	N/A <sup>α</sup>
SCHL 30027		---	---	---	---	***	N/A <sup>α</sup>
SCHL 24398		---	---	---	---	---	N/A <sup>α</sup>
SCHL 24401		---	---	---	---	---	N/A <sup>α</sup>
SCHL 24394		---	---	***	***	***	N/A <sup>α</sup>
SCHL 24552		---	---	---	---	---	N/A <sup>α</sup>

SCHL 24554		---	---	---	---	---	N/A <sup>α</sup>
SCHL 24549		---	---	---	---	---	N/A <sup>α</sup>

## 9 References

1. Franklin, J. L. Redox regulation of the intrinsic pathway in neuronal apoptosis. *Antioxid. Redox. Signal.* **14**, 1437-1448 (2011).
2. Mattson, M. P. Apoptosis in neurodegenerative disorders. *Nat. Rev. Mol. Cell Biol.* **1**, 120-129 (2000).
3. Gorman, A. M. Neuronal cell death in neurodegenerative diseases: recurring themes around protein handling. *J. Cell Mol. Med.* **12**, 2263-2280 (2008).
4. Yuan, J. Neuroprotective strategies targeting apoptotic and necrotic cell death for stroke. *Apoptosis.* **14**, 469-477 (2009).
5. Galluzzi, L. *et al.* Molecular definitions of cell death subroutines: recommendations of the Nomenclature Committee on Cell Death 2012. *Cell Death. Differ.* **19**, 107-120 (2012).
6. Majno, G. & Joris, I. Apoptosis, oncosis, and necrosis. An overview of cell death. *Am. J. Pathol.* **146**, 3-15 (1995).
7. Vanden Berghe, T., Linkermann, A., Jouan-Lanhouet, S., Walczak, H. & Vandenabeele, P. Regulated necrosis: the expanding network of non-apoptotic cell death pathways. *Nat. Rev. Mol. Cell Biol.* **15**, 135-147 (2014).
8. Liu, Q. *et al.* Akt and mTOR mediate programmed necrosis in neurons. *Cell Death. Dis.* **5**, e1084 (2014).
9. Rosenbaum, D. M. *et al.* Necroptosis, a novel form of caspase-independent cell death, contributes to neuronal damage in a retinal ischemia-reperfusion injury model. *J. Neurosci. Res.* **88**, 1569-1576 (2010).
10. Yuan, J., Lipinski, M. & Degtarev, A. Diversity in the mechanisms of neuronal cell death. *Neuron* **40**, 401-413 (2003).
11. Zong, W. X. & Thompson, C. B. Necrotic death as a cell fate. *Genes Dev.* **20**, 1-15 (2006).
12. Kerr, J. F., Wyllie, A. H. & Currie, A. R. Apoptosis: a basic biological phenomenon with wide-ranging implications in tissue kinetics. *Br. J. Cancer* **26**, 239-257 (1972).
13. Oppenheim, R. W. Cell death during development of the nervous system. *Annu. Rev. Neurosci.* **14**, 453-501 (1991).
14. Graham, S. H. & Chen, J. Programmed cell death in cerebral ischemia. *J. Cereb. Blood Flow Metab* **21**, 99-109 (2001).
15. Kroemer, G., Petit, P., Zamzami, N., Vayssiere, J. L. & Mignotte, B. The biochemistry of programmed cell death. *FASEB J.* **9**, 1277-1287 (1995).
16. Mattson, M. P., Duan, W., Pedersen, W. A. & Culmsee, C. Neurodegenerative disorders and ischemic brain diseases. *Apoptosis.* **6**, 69-81 (2001).
17. Darwish, R. S. Regulatory mechanisms of apoptosis in regularly dividing cells. *Cell Health and Cytoskeleton* **2010,2**, 59-68 (2010).

18. Galluzzi, L., Blomgren, K. & Kroemer, G. Mitochondrial membrane permeabilization in neuronal injury. *Nat. Rev. Neurosci.* **10**, 481-494 (2009).
19. Kroemer, G., Galluzzi, L. & Brenner, C. Mitochondrial membrane permeabilization in cell death. *Physiol Rev.* **87**, 99-163 (2007).
20. Chan, D. C. Mitochondria: dynamic organelles in disease, aging, and development. *Cell* **125**, 1241-1252 (2006).
21. Chipuk, J. E., Bouchier-Hayes, L. & Green, D. R. Mitochondrial outer membrane permeabilization during apoptosis: the innocent bystander scenario. *Cell Death. Differ.* **13**, 1396-1402 (2006).
22. Culmsee, C. & Landshamer, S. Molecular insights into mechanisms of the cell death program: role in the progression of neurodegenerative disorders. *Curr. Alzheimer Res.* **3**, 269-283 (2006).
23. Green, D. R. & Kroemer, G. The pathophysiology of mitochondrial cell death. *Science* **305**, 626-629 (2004).
24. Grohm, J., Plesnila, N. & Culmsee, C. Bid mediates fission, membrane permeabilization and peri-nuclear accumulation of mitochondria as a prerequisite for oxidative neuronal cell death. *Brain Behav. Immun.* **24**, 831-838 (2010).
25. Susin, S. A. *et al.* Molecular characterization of mitochondrial apoptosis-inducing factor. *Nature* **397**, 441-446 (1999).
26. Droge, W. Free radicals in the physiological control of cell function. *Physiol Rev.* **82**, 47-95 (2002).
27. Phillis, J. W., Horrocks, L. A. & Farooqui, A. A. Cyclooxygenases, lipoxygenases, and epoxygenases in CNS: their role and involvement in neurological disorders. *Brain Res. Rev.* **52**, 201-243 (2006).
28. Ott, M., Gogvadze, V., Orrenius, S. & Zhivotovsky, B. Mitochondria, oxidative stress and cell death. *Apoptosis.* **12**, 913-922 (2007).
29. Coyle, J. T. & Puttfarcken, P. Oxidative stress, glutamate, and neurodegenerative disorders. *Science* **262**, 689-695 (1993).
30. Culmsee, C. & Krieglstein, J. Ischaemic brain damage after stroke: new insights into efficient therapeutic strategies. International Symposium on Neurodegeneration and Neuroprotection. *EMBO Rep.* **8**, 129-133 (2007).
31. Greenlund, L. J., Deckwerth, T. L. & Johnson, E. M., Jr. Superoxide dismutase delays neuronal apoptosis: a role for reactive oxygen species in programmed neuronal death. *Neuron* **14**, 303-315 (1995).
32. Lin, M. T. & Beal, M. F. Mitochondrial dysfunction and oxidative stress in neurodegenerative diseases. *Nature* **443**, 787-795 (2006).
33. Simon, H. U., Haj-Yehia, A. & Levi-Schaffer, F. Role of reactive oxygen species (ROS) in apoptosis induction. *Apoptosis.* **5**, 415-418 (2000).

34. Tan, S., Sagara, Y., Liu, Y., Maher, P. & Schubert, D. The regulation of reactive oxygen species production during programmed cell death. *J. Cell Biol.* **141**, 1423-1432 (1998).
35. Landes, T. & Martinou, J. C. Mitochondrial outer membrane permeabilization during apoptosis: the role of mitochondrial fission. *Biochim. Biophys. Acta* **1813**, 540-545 (2011).
36. Martinou, J. C. & Youle, R. J. Mitochondria in apoptosis: Bcl-2 family members and mitochondrial dynamics. *Dev. Cell* **21**, 92-101 (2011).
37. Giacomello, M., Drago, I., Pizzo, P. & Pozzan, T. Mitochondrial Ca<sup>2+</sup> as a key regulator of cell life and death. *Cell Death. Differ.* **14**, 1267-1274 (2007).
38. Bolanos, J. P., Moro, M. A., Lizasoain, I. & Almeida, A. Mitochondria and reactive oxygen and nitrogen species in neurological disorders and stroke: Therapeutic implications. *Adv. Drug Deliv. Rev.* **61**, 1299-1315 (2009).
39. Desagher, S. & Martinou, J. C. Mitochondria as the central control point of apoptosis. *Trends Cell Biol.* **10**, 369-377 (2000).
40. Kroemer, G., Zamzami, N. & Susin, S. A. Mitochondrial control of apoptosis. *Immunol. Today* **18**, 44-51 (1997).
41. Halestrap, A. P., McStay, G. P. & Clarke, S. J. The permeability transition pore complex: another view. *Biochimie* **84**, 153-166 (2002).
42. Rao, V. K., Carlson, E. A. & Yan, S. S. Mitochondrial permeability transition pore is a potential drug target for neurodegeneration. *Biochim. Biophys. Acta*(2013).
43. Garcia-Saez, A. J. The secrets of the Bcl-2 family. *Cell Death. Differ.* **19**, 1733-1740 (2012).
44. Youle, R. J. & Strasser, A. The BCL-2 protein family: opposing activities that mediate cell death. *Nat. Rev. Mol. Cell Biol.* **9**, 47-59 (2008).
45. Chipuk, J. E. *et al.* Mechanism of apoptosis induction by inhibition of the anti-apoptotic BCL-2 proteins. *Proc. Natl. Acad. Sci. U. S. A* **105**, 20327-20332 (2008).
46. Hardwick, J. M. & Youle, R. J. SnapShot: BCL-2 proteins. *Cell* **138**, 404, 404 (2009).
47. Kuwana, T. *et al.* BH3 domains of BH3-only proteins differentially regulate Bax-mediated mitochondrial membrane permeabilization both directly and indirectly. *Mol. Cell* **17**, 525-535 (2005).
48. Krajewska, M. *et al.* Expression of Bcl-2 family member Bid in normal and malignant tissues. *Neoplasia*. **4**, 129-140 (2002).
49. Krajewska, M. *et al.* Dynamics of expression of apoptosis-regulatory proteins Bid, Bcl-2, Bcl-X, Bax and Bak during development of murine nervous system. *Cell Death. Differ.* **9**, 145-157 (2002).
50. Krajewski, S. *et al.* Immunohistochemical analysis of Mcl-1 protein in human tissues. Differential regulation of Mcl-1 and Bcl-2 protein production suggests a unique role for Mcl-1 in control of programmed cell death in vivo. *Am. J. Pathol.* **146**, 1309-1319 (1995).

51. Krajewski, S. *et al.* Upregulation of bax protein levels in neurons following cerebral ischemia. *J. Neurosci.* **15**, 6364-6376 (1995).
52. Sun, Y. F., Yu, L. Y., Saarma, M., Timmusk, T. & Arumae, U. Neuron-specific Bcl-2 homology 3 domain-only splice variant of Bak is anti-apoptotic in neurons, but proapoptotic in non-neuronal cells. *J. Biol. Chem.* **276**, 16240-16247 (2001).
53. Chipuk, J. E., Moldoveanu, T., Llambi, F., Parsons, M. J. & Green, D. R. The BCL-2 family reunion. *Mol. Cell* **37**, 299-310 (2010).
54. Shamas-Din, A., Kale, J., Leber, B. & Andrews, D. W. Mechanisms of action of Bcl-2 family proteins. *Cold Spring Harb. Perspect. Biol.* **5**, a008714 (2013).
55. Wang, K., Yin, X. M., Chao, D. T., Milliman, C. L. & Korsmeyer, S. J. BID: a novel BH3 domain-only death agonist. *Genes Dev.* **10**, 2859-2869 (1996).
56. Kamer, I. *et al.* Proapoptotic BID is an ATM effector in the DNA-damage response. *Cell* **122**, 593-603 (2005).
57. Zinkel, S. S. *et al.* A role for proapoptotic BID in the DNA-damage response. *Cell* **122**, 579-591 (2005).
58. Konig, H. G. *et al.* Full length Bid is sufficient to induce apoptosis of cultured rat hippocampal neurons. *BMC. Cell Biol.* **8**, 7 (2007).
59. Ward, M. W. *et al.* Real time single cell analysis of Bid cleavage and Bid translocation during caspase-dependent and neuronal caspase-independent apoptosis. *J. Biol. Chem.* **281**, 5837-5844 (2006).
60. Li, H., Zhu, H., Xu, C. J. & Yuan, J. Cleavage of BID by caspase 8 mediates the mitochondrial damage in the Fas pathway of apoptosis. *Cell* **94**, 491-501 (1998).
61. Billen, L. P., Shamas-Din, A. & Andrews, D. W. Bid: a Bax-like BH3 protein. *Oncogene* **27 Suppl 1**, S93-104 (2008).
62. Brustovetsky, N., Dubinsky, J. M., Antonsson, B. & Jemmerson, R. Two pathways for tBID-induced cytochrome c release from rat brain mitochondria: BAK- versus BAX-dependence. *J. Neurochem.* **84**, 196-207 (2003).
63. Culmsee, C. & Plesnila, N. Targeting Bid to prevent programmed cell death in neurons. *Biochem. Soc. Trans.* **34**, 1334-1340 (2006).
64. Chou, J. J., Li, H., Salvesen, G. S., Yuan, J. & Wagner, G. Solution structure of BID, an intracellular amplifier of apoptotic signaling. *Cell* **96**, 615-624 (1999).
65. McDonnell, J. M., Fushman, D., Milliman, C. L., Korsmeyer, S. J. & Cowburn, D. Solution structure of the proapoptotic molecule BID: a structural basis for apoptotic agonists and antagonists. *Cell* **96**, 625-634 (1999).
66. Yin, X. M. Bid, a BH3-only multi-functional molecule, is at the cross road of life and death. *Gene* **369**, 7-19 (2006).
67. Suzuki, M., Youle, R. J. & Tjandra, N. Structure of Bax: coregulation of dimer formation and intracellular localization. *Cell* **103**, 645-654 (2000).

68. Muchmore, S. W. *et al.* X-ray and NMR structure of human Bcl-xL, an inhibitor of programmed cell death. *Nature* **381**, 335-341 (1996).
69. Kudla, G. *et al.* The destabilization of lipid membranes induced by the C-terminal fragment of caspase 8-cleaved bid is inhibited by the N-terminal fragment. *J. Biol. Chem.* **275**, 22713-22718 (2000).
70. Zha, J., Weiler, S., Oh, K. J., Wei, M. C. & Korsmeyer, S. J. Posttranslational N-myristoylation of BID as a molecular switch for targeting mitochondria and apoptosis. *Science* **290**, 1761-1765 (2000).
71. Lovell, J. F. *et al.* Membrane binding by tBid initiates an ordered series of events culminating in membrane permeabilization by Bax. *Cell* **135**, 1074-1084 (2008).
72. Shamas-Din, A. *et al.* tBid undergoes multiple conformational changes at the membrane required for Bax activation. *J. Biol. Chem.* **288**, 22111-22127 (2013).
73. Sutton, V. R., Wowk, M. E., Cancilla, M. & Trapani, J. A. Caspase activation by granzyme B is indirect, and caspase autoprocessing requires the release of proapoptotic mitochondrial factors. *Immunity*. **18**, 319-329 (2003).
74. Chen, M. *et al.* Bid is cleaved by calpain to an active fragment in vitro and during myocardial ischemia/reperfusion. *J. Biol. Chem.* **276**, 30724-30728 (2001).
75. Polster, B. M., Basanez, G., Etxebarria, A., Hardwick, J. M. & Nicholls, D. G. Calpain I induces cleavage and release of apoptosis-inducing factor from isolated mitochondria. *J. Biol. Chem.* **280**, 6447-6454 (2005).
76. Cirman, T. *et al.* Selective disruption of lysosomes in HeLa cells triggers apoptosis mediated by cleavage of Bid by multiple papain-like lysosomal cathepsins. *J. Biol. Chem.* **279**, 3578-3587 (2004).
77. Schafer, B. *et al.* Mitochondrial outer membrane proteins assist Bid in Bax-mediated lipidic pore formation. *Mol. Biol. Cell* **20**, 2276-2285 (2009).
78. Grinberg, M. *et al.* tBID Homooligomerizes in the mitochondrial membrane to induce apoptosis. *J. Biol. Chem.* **277**, 12237-12245 (2002).
79. Crimi, M. & Esposti, M. D. Apoptosis-induced changes in mitochondrial lipids. *Biochim. Biophys. Acta* **1813**, 551-557 (2011).
80. Lutter, M. *et al.* Cardiolipin provides specificity for targeting of tBid to mitochondria. *Nat. Cell Biol.* **2**, 754-761 (2000).
81. Kim, T. H. *et al.* Bid-cardiolipin interaction at mitochondrial contact site contributes to mitochondrial cristae reorganization and cytochrome C release. *Mol. Biol. Cell* **15**, 3061-3072 (2004).
82. Lucken-Ardjomande, S., Montessuit, S. & Martinou, J. C. Contributions to Bax insertion and oligomerization of lipids of the mitochondrial outer membrane. *Cell Death. Differ.* **15**, 929-937 (2008).
83. Lutter, M., Perkins, G. A. & Wang, X. The pro-apoptotic Bcl-2 family member tBid localizes to mitochondrial contact sites. *BMC. Cell Biol.* **2**, 22 (2001).

84. Ott, M., Zhivotovsky, B. & Orrenius, S. Role of cardiolipin in cytochrome c release from mitochondria. *Cell Death. Differ.* **14**, 1243-1247 (2007).
85. Scorrano, L. *et al.* A distinct pathway remodels mitochondrial cristae and mobilizes cytochrome c during apoptosis. *Dev. Cell* **2**, 55-67 (2002).
86. Eskes, R., Desagher, S., Antonsson, B. & Martinou, J. C. Bid induces the oligomerization and insertion of Bax into the outer mitochondrial membrane. *Mol. Cell Biol.* **20**, 929-935 (2000).
87. Esposti, M. D., Erler, J. T., Hickman, J. A. & Dive, C. Bid, a widely expressed proapoptotic protein of the Bcl-2 family, displays lipid transfer activity. *Mol. Cell Biol.* **21**, 7268-7276 (2001).
88. Esposti, M. D., Cristea, I. M., Gaskell, S. J., Nakao, Y. & Dive, C. Proapoptotic Bid binds to monolysocardiolipin, a new molecular connection between mitochondrial membranes and cell death. *Cell Death. Differ.* **10**, 1300-1309 (2003).
89. Sorice, M. *et al.* Cardiolipin and its metabolites move from mitochondria to other cellular membranes during death receptor-mediated apoptosis. *Cell Death. Differ.* **11**, 1133-1145 (2004).
90. Cristea, I. M. & Degli, E. M. Membrane lipids and cell death: an overview. *Chem. Phys. Lipids* **129**, 133-160 (2004).
91. Kuwana, T. *et al.* Bid, Bax, and lipids cooperate to form supramolecular openings in the outer mitochondrial membrane. *Cell* **111**, 331-342 (2002).
92. Korsmeyer, S. J. *et al.* Pro-apoptotic cascade activates BID, which oligomerizes BAK or BAX into pores that result in the release of cytochrome c. *Cell Death. Differ.* **7**, 1166-1173 (2000).
93. Roy, S. S., Ehrlich, A. M., Craigen, W. J. & Hajnoczky, G. VDAC2 is required for truncated BID-induced mitochondrial apoptosis by recruiting BAK to the mitochondria. *EMBO Rep.* **10**, 1341-1347 (2009).
94. Robinson, A. J., Kunji, E. R. & Gross, A. Mitochondrial carrier homolog 2 (MTCH2): the recruitment and evolution of a mitochondrial carrier protein to a critical player in apoptosis. *Exp. Cell Res.* **318**, 1316-1323 (2012).
95. Zaltsman, Y. *et al.* MTCH2/MIMP is a major facilitator of tBID recruitment to mitochondria. *Nat. Cell Biol.* **12**, 553-562 (2010).
96. Kook, S. *et al.* Caspase-cleaved arrestin-2 and BID cooperatively facilitate cytochrome C release and cell death. *Cell Death. Differ.* **21**, 172-184 (2014).
97. Landshamer, S. *et al.* Bid-induced release of AIF from mitochondria causes immediate neuronal cell death. *Cell Death. Differ.* **15**, 1553-1563 (2008).
98. Plesnila, N. *et al.* BID mediates neuronal cell death after oxygen/ glucose deprivation and focal cerebral ischemia. *Proc. Natl. Acad. Sci. U. S. A* **98**, 15318-15323 (2001).
99. Becattini, B. *et al.* Targeting apoptosis via chemical design: inhibition of bid-induced cell death by small organic molecules. *Chem. Biol.* **11**, 1107-1117 (2004).



100. Bempohl, D., You, Z., Korsmeyer, S. J., Moskowitz, M. A. & Whalen, M. J. Traumatic brain injury in mice deficient in Bid: effects on histopathology and functional outcome. *J. Cereb. Blood Flow Metab* **26**, 625-633 (2006).
101. Yin, X. M. *et al.* Bid-mediated mitochondrial pathway is critical to ischemic neuronal apoptosis and focal cerebral ischemia. *J. Biol. Chem.* **277**, 42074-42081 (2002).
102. Henshall, D. C. *et al.* Cleavage of bid may amplify caspase-8-induced neuronal death following focally evoked limbic seizures. *Neurobiol. Dis.* **8**, 568-580 (2001).
103. Yamamoto, A. *et al.* Endoplasmic reticulum stress and apoptosis signaling in human temporal lobe epilepsy. *J. Neuropathol. Exp. Neurol.* **65**, 217-225 (2006).
104. Becattini, B. *et al.* Rational design and real time, in-cell detection of the proapoptotic activity of a novel compound targeting Bcl-X(L). *Chem. Biol.* **11**, 389-395 (2004).
105. Czabotar, P. E. & Lessene, G. Bcl-2 family proteins as therapeutic targets. *Curr. Pharm. Des* **16**, 3132-3148 (2010).
106. Degterev, A. *et al.* Identification of small-molecule inhibitors of interaction between the BH3 domain and Bcl-xL. *Nat. Cell Biol.* **3**, 173-182 (2001).
107. Kitada, S. *et al.* Discovery, characterization, and structure-activity relationships studies of proapoptotic polyphenols targeting B-cell lymphocyte/leukemia-2 proteins. *J. Med. Chem.* **46**, 4259-4264 (2003).
108. Leone, M. *et al.* Cancer prevention by tea polyphenols is linked to their direct inhibition of antiapoptotic Bcl-2-family proteins. *Cancer Res.* **63**, 8118-8121 (2003).
109. Lessene, G. *et al.* Structure-guided design of a selective BCL-X(L) inhibitor. *Nat. Chem. Biol.* **9**, 390-397 (2013).
110. Manion, M. K. & Hockenbery, D. M. Targeting BCL-2-related proteins in cancer therapy. *Cancer Biol. Ther.* **2**, S105-S114 (2003).
111. O'Neill, J. W. & Hockenbery, D. M. Bcl-2-related proteins as drug targets. *Curr. Med. Chem.* **10**, 1553-1562 (2003).
112. Osford, S. M., Dallman, C. L., Johnson, P. W., Ganesan, A. & Packham, G. Current strategies to target the anti-apoptotic Bcl-2 protein in cancer cells. *Curr. Med. Chem.* **11**, 1031-1039 (2004).
113. Sattler, M. *et al.* Structure of Bcl-xL-Bak peptide complex: recognition between regulators of apoptosis. *Science* **275**, 983-986 (1997).
114. Becattini, B. *et al.* Structure-activity relationships by interligand NOE-based design and synthesis of antiapoptotic compounds targeting Bid. *Proc. Natl. Acad. Sci. U. S. A* **103**, 12602-12606 (2006).
115. Tzung, S. P. *et al.* Antimycin A mimics a cell-death-inducing Bcl-2 homology domain 3. *Nat. Cell Biol.* **3**, 183-191 (2001).
116. Tobaben, S. *et al.* Bid-mediated mitochondrial damage is a key mechanism in glutamate-induced oxidative stress and AIF-dependent cell death in immortalized HT-22 hippocampal neurons. *Cell Death. Differ.* **18**, 282-292 (2011).

117. Anguissola, S. *et al.* Bid and calpains cooperate to trigger oxaliplatin-induced apoptosis of cervical carcinoma HeLa cells. *Mol. Pharmacol.* **76**, 998-1010 (2009).
118. Kohler, B. *et al.* Bid participates in genotoxic drug-induced apoptosis of HeLa cells and is essential for death receptor ligands' apoptotic and synergistic effects. *PLoS. One.* **3**, e2844 (2008).
119. Acharya, K. R. & Lloyd, M. D. The advantages and limitations of protein crystal structures. *Trends Pharmacol. Sci.* **26**, 10-14 (2005).
120. McPherson, A. & Gavira, J. A. Introduction to protein crystallization. *Acta Crystallogr. F. Struct. Biol. Commun.* **70**, 2-20 (2014).
121. Czabotar, P. E. *et al.* Bax crystal structures reveal how BH3 domains activate Bax and nucleate its oligomerization to induce apoptosis. *Cell* **152**, 519-531 (2013).
122. Stewart, M. L., Fire, E., Keating, A. E. & Walensky, L. D. The MCL-1 BH3 helix is an exclusive MCL-1 inhibitor and apoptosis sensitizer. *Nat. Chem. Biol.* **6**, 595-601 (2010).
123. Thomas, S. *et al.* Targeting the Bcl-2 family for cancer therapy. *Expert. Opin. Ther. Targets.* **17**, 61-75 (2013).
124. Weyhenmeyer, B., Murphy, A. C., Prehn, J. H. & Murphy, B. M. Targeting the anti-apoptotic Bcl-2 family members for the treatment of cancer. *Exp. Oncol.* **34**, 192-199 (2012).
125. Shoshan-Barmatz, V. & Mizrahi, D. VDAC1: from structure to cancer therapy. *Front Oncol.* **2**, 164 (2012).
126. Shoshan-Barmatz, V. & Golan, M. Mitochondrial VDAC1: function in cell life and death and a target for cancer therapy. *Curr. Med. Chem.* **19**, 714-735 (2012).
127. Bayrhuber, M. *et al.* Structure of the human voltage-dependent anion channel. *Proc. Natl. Acad. Sci. U. S. A* **105**, 15370-15375 (2008).
128. Hiller, S. *et al.* Solution structure of the integral human membrane protein VDAC-1 in detergent micelles. *Science* **321**, 1206-1210 (2008).
129. Ujwal, R. *et al.* The crystal structure of mouse VDAC1 at 2.3 Å resolution reveals mechanistic insights into metabolite gating. *Proc. Natl. Acad. Sci. U. S. A* **105**, 17742-17747 (2008).
130. Rostovtseva, T. K., Tan, W. & Colombini, M. On the role of VDAC in apoptosis: fact and fiction. *J. Bioenerg. Biomembr.* **37**, 129-142 (2005).
131. Rostovtseva, T. K. & Bezrukov, S. M. VDAC regulation: role of cytosolic proteins and mitochondrial lipids. *J. Bioenerg. Biomembr.* **40**, 163-170 (2008).
132. Shoshan-Barmatz, V. & Ben-Hail, D. VDAC, a multi-functional mitochondrial protein as a pharmacological target. *Mitochondrion.* **12**, 24-34 (2012).
133. De, S. D. *et al.* VDAC1 selectively transfers apoptotic Ca<sup>2+</sup> signals to mitochondria. *Cell Death. Differ.* **19**, 267-273 (2012).

134. Keinan, N., Pahima, H., Ben-Hail, D. & Shoshan-Barmatz, V. The role of calcium in VDAC1 oligomerization and mitochondria-mediated apoptosis. *Biochim. Biophys. Acta* **1833**, 1745-1754 (2013).
135. Shoshan-Barmatz, V., Israelson, A., Brdiczka, D. & Sheu, S. S. The voltage-dependent anion channel (VDAC): function in intracellular signalling, cell life and cell death. *Curr. Pharm. Des* **12**, 2249-2270 (2006).
136. Shoshan-Barmatz, V. *et al.* VDAC, a multi-functional mitochondrial protein regulating cell life and death. *Mol. Aspects Med.* **31**, 227-285 (2010).
137. Colombini, M. VDAC: the channel at the interface between mitochondria and the cytosol. *Mol. Cell Biochem.* **256-257**, 107-115 (2004).
138. Lemasters, J. J. & Holmuhamedov, E. Voltage-dependent anion channel (VDAC) as mitochondrial governor--thinking outside the box. *Biochim. Biophys. Acta* **1762**, 181-190 (2006).
139. Rostovtseva, T. & Colombini, M. VDAC channels mediate and gate the flow of ATP: implications for the regulation of mitochondrial function. *Biophys. J.* **72**, 1954-1962 (1997).
140. Rostovtseva, T. K. & Bezrukov, S. M. ATP transport through a single mitochondrial channel, VDAC, studied by current fluctuation analysis. *Biophys. J.* **74**, 2365-2373 (1998).
141. Abu-Hamad, S., Sivan, S. & Shoshan-Barmatz, V. The expression level of the voltage-dependent anion channel controls life and death of the cell. *Proc. Natl. Acad. Sci. U. S. A* **103**, 5787-5792 (2006).
142. Shimizu, S., Ide, T., Yanagida, T. & Tsujimoto, Y. Electrophysiological study of a novel large pore formed by Bax and the voltage-dependent anion channel that is permeable to cytochrome c. *J. Biol. Chem.* **275**, 12321-12325 (2000).
143. Shimizu, S., Matsuoka, Y., Shinohara, Y., Yoneda, Y. & Tsujimoto, Y. Essential role of voltage-dependent anion channel in various forms of apoptosis in mammalian cells. *J. Cell Biol.* **152**, 237-250 (2001).
144. Tsujimoto, Y. & Shimizu, S. The voltage-dependent anion channel: an essential player in apoptosis. *Biochimie* **84**, 187-193 (2002).
145. Tajeddine, N. *et al.* Hierarchical involvement of Bak, VDAC1 and Bax in cisplatin-induced cell death. *Oncogene* **27**, 4221-4232 (2008).
146. Yuan, S. *et al.* Voltage-dependent anion channel 1 is involved in endostatin-induced endothelial cell apoptosis. *FASEB J.* **22**, 2809-2820 (2008).
147. Tomasello, F. *et al.* Outer membrane VDAC1 controls permeability transition of the inner mitochondrial membrane in cellulo during stress-induced apoptosis. *Cell Res.* **19**, 1363-1376 (2009).
148. Godbole, A., Varghese, J., Sarin, A. & Mathew, M. K. VDAC is a conserved element of death pathways in plant and animal systems. *Biochim. Biophys. Acta* **1642**, 87-96 (2003).

149. Zaid, H., Abu-Hamad, S., Israelson, A., Nathan, I. & Shoshan-Barmatz, V. The voltage-dependent anion channel-1 modulates apoptotic cell death. *Cell Death. Differ.* **12**, 751-760 (2005).
150. Madesh, M. & Hajnoczky, G. VDAC-dependent permeabilization of the outer mitochondrial membrane by superoxide induces rapid and massive cytochrome c release. *J. Cell Biol.* **155**, 1003-1015 (2001).
151. Galluzzi, L. & Kroemer, G. Mitochondrial apoptosis without VDAC. *Nat. Cell Biol.* **9**, 487-489 (2007).
152. Tsujimoto, Y. & Shimizu, S. Role of the mitochondrial membrane permeability transition in cell death. *Apoptosis.* **12**, 835-840 (2007).
153. Vander Heiden, M. G. *et al.* Bcl-xL promotes the open configuration of the voltage-dependent anion channel and metabolite passage through the outer mitochondrial membrane. *J. Biol. Chem.* **276**, 19414-19419 (2001).
154. Abu-Hamad, S. *et al.* The VDAC1 N-terminus is essential both for apoptosis and the protective effect of anti-apoptotic proteins. *J. Cell Sci.* **122**, 1906-1916 (2009).
155. Keinan, N., Tyomkin, D. & Shoshan-Barmatz, V. Oligomerization of the mitochondrial protein voltage-dependent anion channel is coupled to the induction of apoptosis. *Mol. Cell Biol.* **30**, 5698-5709 (2010).
156. Shoshan-Barmatz, V., Keinan, N. & Zaid, H. Uncovering the role of VDAC in the regulation of cell life and death. *J. Bioenerg. Biomembr.* **40**, 183-191 (2008).
157. Arbel, N., Ben-Hail, D. & Shoshan-Barmatz, V. Mediation of the antiapoptotic activity of Bcl-xL protein upon interaction with VDAC1 protein. *J. Biol. Chem.* **287**, 23152-23161 (2012).
158. Scharstuhl, A., Mutsaers, H. A., Pennings, S. W., Russel, F. G. & Wagener, F. A. Involvement of VDAC, Bax and ceramides in the efflux of AIF from mitochondria during curcumin-induced apoptosis. *PLoS. One.* **4**, e6688 (2009).
159. Shimizu, S., Narita, M. & Tsujimoto, Y. Bcl-2 family proteins regulate the release of apoptogenic cytochrome c by the mitochondrial channel VDAC. *Nature* **399**, 483-487 (1999).
160. Tsujimoto, Y. & Shimizu, S. VDAC regulation by the Bcl-2 family of proteins. *Cell Death. Differ.* **7**, 1174-1181 (2000).
161. Rostovtseva, T. K. *et al.* Bid, but not Bax, regulates VDAC channels. *J. Biol. Chem.* **279**, 13575-13583 (2004).
162. Shimizu, S., Shinohara, Y. & Tsujimoto, Y. Bax and Bcl-xL independently regulate apoptotic changes of yeast mitochondria that require VDAC but not adenine nucleotide translocator. *Oncogene* **19**, 4309-4318 (2000).
163. Baines, C. P., Kaiser, R. A., Sheiko, T., Craigen, W. J. & Molkenin, J. D. Voltage-dependent anion channels are dispensable for mitochondrial-dependent cell death. *Nat. Cell Biol.* **9**, 550-555 (2007).

164. Albrecht, P. *et al.* Mechanisms of oxidative glutamate toxicity: the glutamate/cystine antiporter system xc<sup>-</sup> as a neuroprotective drug target. *CNS. Neurol. Disord. Drug Targets*. **9**, 373-382 (2010).
165. Burdo, J., Dargusch, R. & Schubert, D. Distribution of the cystine/glutamate antiporter system xc<sup>-</sup> in the brain, kidney, and duodenum. *J. Histochem. Cytochem.* **54**, 549-557 (2006).
166. Murphy, T. H., Miyamoto, M., Sastre, A., Schnaar, R. L. & Coyle, J. T. Glutamate toxicity in a neuronal cell line involves inhibition of cystine transport leading to oxidative stress. *Neuron* **2**, 1547-1558 (1989).
167. Sagara, Y. *et al.* Cellular mechanisms of resistance to chronic oxidative stress. *Free Radic. Biol. Med.* **24**, 1375-1389 (1998).
168. Cheung, N. S., Pascoe, C. J., Giardina, S. F., John, C. A. & Beart, P. M. Micromolar L-glutamate induces extensive apoptosis in an apoptotic-necrotic continuum of insult-dependent, excitotoxic injury in cultured cortical neurones. *Neuropharmacology* **37**, 1419-1429 (1998).
169. Choi, D. W. Glutamate neurotoxicity in cortical cell culture is calcium dependent. *Neurosci. Lett.* **58**, 293-297 (1985).
170. Henke, N. *et al.* The plasma membrane channel ORAI1 mediates detrimental calcium influx caused by endogenous oxidative stress. *Cell Death. Dis.* **4**, e470 (2013).
171. Tan, S., Schubert, D. & Maher, P. Oxytosis: A novel form of programmed cell death. *Curr. Top. Med. Chem.* **1**, 497-506 (2001).
172. Kazhdan, I., Long, L., Montellano, R., Cavazos, D. A. & Marciniak, R. A. Targeted gene therapy for breast cancer with truncated Bid. *Cancer Gene Ther.* **13**, 141-149 (2006).
173. Wei, M. C. *et al.* tBID, a membrane-targeted death ligand, oligomerizes BAK to release cytochrome c. *Genes Dev.* **14**, 2060-2071 (2000).
174. Morimoto, B. H. & Koshland, D. E., Jr. Excitatory amino acid uptake and N-methyl-D-aspartate-mediated secretion in a neural cell line. *Proc. Natl. Acad. Sci. U. S. A* **87**, 3518-3521 (1990).
175. Liu, Y., Peterson, D. A., Kimura, H. & Schubert, D. Mechanism of cellular 3-(4,5-dimethylthiazol-2-yl)-2,5-diphenyltetrazolium bromide (MTT) reduction. *J. Neurochem.* **69**, 581-593 (1997).
176. Diemert, S. *et al.* Impedance measurement for real time detection of neuronal cell death. *J. Neurosci. Methods* **203**, 69-77 (2012).
177. Wu, M. *et al.* Multiparameter metabolic analysis reveals a close link between attenuated mitochondrial bioenergetic function and enhanced glycolysis dependency in human tumor cells. *Am. J. Physiol Cell Physiol* **292**, C125-C136 (2007).
178. Gohil, V. M. *et al.* Nutrient-sensitized screening for drugs that shift energy metabolism from mitochondrial respiration to glycolysis. *Nat. Biotechnol.* **28**, 249-255 (2010).
179. Walker, J. M. The bicinchoninic acid (BCA) assay for protein quantitation. *Methods Mol. Biol.* **32**, 5-8 (1994).

180. Plesnila, N. *et al.* BID mediates neuronal cell death after oxygen/ glucose deprivation and focal cerebral ischemia. *Proc. Natl. Acad. Sci. U. S. A* **98**, 15318-15323 (2001).
181. Plesnila, N. *et al.* Nuclear translocation of apoptosis-inducing factor after focal cerebral ischemia. *J. Cereb. Blood Flow Metab* **24**, 458-466 (2004).
182. Rarey, M., Kramer, B., Lengauer, T. & Klebe, G. A fast flexible docking method using an incremental construction algorithm. *J. Mol. Biol.* **261**, 470-489 (1996).
183. Schneider, N. *et al.* Substantial improvements in large-scale redocking and screening using the novel HYDE scoring function. *J. Comput. Aided Mol. Des* **26**, 701-723 (2012).
184. Schneider, N., Lange, G., Hindle, S., Klein, R. & Rarey, M. A consistent description of HYdrogen bond and DEhydration energies in protein-ligand complexes: methods behind the HYDE scoring function. *J. Comput. Aided Mol. Des* **27**, 15-29 (2013).
185. Stierand, K. & Rarey, M. From modeling to medicinal chemistry: automatic generation of two-dimensional complex diagrams. *ChemMedChem.* **2**, 853-860 (2007).
186. Chung, C. T., Niemela, S. L. & Miller, R. H. One-step preparation of competent *Escherichia coli*: transformation and storage of bacterial cells in the same solution. *Proc. Natl. Acad. Sci. U. S. A* **86**, 2172-2175 (1989).
187. Gill S.C. & Hippel P.H. Calculation of Protein Extinction Coefficients from Amino Acid Sequence Data. *Analytical Biochemistry* **182**, 319-326 (1989).
188. Mertins, B. *et al.* Flexibility of the N-terminal mVDAC1 segment controls the channel's gating behavior. *PLoS. One.* **7**, e47938 (2012).
189. Bergfors T.M. *Protein Crystallization*(IUL,2009).
190. Mueller, U. *et al.* Facilities for macromolecular crystallography at the Helmholtz-Zentrum Berlin. *J. Synchrotron. Radiat.* **19**, 442-449 (2012).
191. Kabsch, W. XDS. *Acta Crystallogr. D. Biol. Crystallogr.* **66**, 125-132 (2010).
192. Krug, M., Weiss, M. S., Heinemann, U. & Mueller, U. XDSAPP: a graphical user interface for the convenient processing of diffraction data using XDS. *Appl. Cryst.* **45**, 568-572 (2012).
193. McCoy, A. J. *et al.* Phaser crystallographic software. *J. Appl. Crystallogr.* **40**, 658-674 (2007).
194. Friedlander, R. M. Apoptosis and caspases in neurodegenerative diseases. *N. Engl. J. Med.* **348**, 1365-1375 (2003).
195. Guegan, C. *et al.* Instrumental activation of bid by caspase-1 in a transgenic mouse model of ALS. *Mol. Cell Neurosci.* **20**, 553-562 (2002).
196. Waldmeier, P. C. Prospects for antiapoptotic drug therapy of neurodegenerative diseases. *Prog. Neuropsychopharmacol. Biol. Psychiatry* **27**, 303-321 (2003).
197. Arnoult, D. Mitochondrial fragmentation in apoptosis. *Trends Cell Biol.* **17**, 6-12 (2007).

198. Danial, N. N. & Korsmeyer, S. J. Cell death: critical control points. *Cell* **116**, 205-219 (2004).
199. Autret, A. & Martin, S. J. Emerging role for members of the Bcl-2 family in mitochondrial morphogenesis. *Mol. Cell* **36**, 355-363 (2009).
200. Grohm, J. *et al.* Inhibition of Drp1 provides neuroprotection in vitro and in vivo. *Cell Death. Differ.* **19**, 1446-1458 (2012).
201. Sasaki, Y. F. *et al.* The alkaline single cell gel electrophoresis assay with mouse multiple organs: results with 30 aromatic amines evaluated by the IARC and U.S. NTP. *Mutat. Res.* **440**, 1-18 (1999).
202. Culmsee, C. *et al.* Apoptosis-inducing factor triggered by poly(ADP-ribose) polymerase and Bid mediates neuronal cell death after oxygen-glucose deprivation and focal cerebral ischemia. *J. Neurosci.* **25**, 10262-10272 (2005).
203. Wu, M. *et al.* Multiparameter metabolic analysis reveals a close link between attenuated mitochondrial bioenergetic function and enhanced glycolysis dependency in human tumor cells. *Am. J. Physiol Cell Physiol* **292**, C125-C136 (2007).
204. Clerc, P. & Polster, B. M. Investigation of mitochondrial dysfunction by sequential microplate-based respiration measurements from intact and permeabilized neurons. *PLoS. One.* **7**, e34465 (2012).
205. Azarias, G. *et al.* Glutamate transport decreases mitochondrial pH and modulates oxidative metabolism in astrocytes. *J. Neurosci.* **31**, 3550-3559 (2011).
206. Dessau, M. A. & Modis, Y. Protein Crystallization for X-ray Crystallography. *JoVE* **47**, (2011).
207. Benvenuti, M. & Mangani, S. Crystallization of soluble proteins in vapor diffusion for x-ray crystallography. *Nat. Protoc.* **2**, 1633-1651 (2007).
208. Chayen, N. E. Turning protein crystallisation from an art into a science. *Curr. Opin. Struct. Biol.* **14**, 577-583 (2004).
209. McPherson, A. Introduction to protein crystallization. *Methods* **34**, 254-265 (2004).
210. Ku, B., Liang, C., Jung, J. U. & Oh, B. H. Evidence that inhibition of BAX activation by BCL-2 involves its tight and preferential interaction with the BH3 domain of BAX. *Cell Res.* **21**, 627-641 (2011).
211. Steuber, H. . Personal Communication (2011)
212. Stoka, V. *et al.* Lysosomal protease pathways to apoptosis. Cleavage of bid, not procaspases, is the most likely route. *J. Biol. Chem.* **276**, 3149-3157 (2001).
213. Sarig, R. *et al.* BID-D59A is a potent inducer of apoptosis in primary embryonic fibroblasts. *J. Biol. Chem.* **278**, 10707-10715 (2003).
214. Bleicken, S., Garcia-Saez, A. J., Conte, E. & Bordignon, E. Dynamic interaction of cBid with detergents, liposomes and mitochondria. *PLoS. One.* **7**, e35910 (2012).

215. Hetz, C. *et al.* Bax channel inhibitors prevent mitochondrion-mediated apoptosis and protect neurons in a model of global brain ischemia. *J. Biol. Chem.* **280**, 42960-42970 (2005).
216. Kale, J., Liu, Q., Leber, B. & Andrews, D. W. Shedding light on apoptosis at subcellular membranes. *Cell* **151**, 1179-1184 (2012).
217. Roucou, X., Montessuit, S., Antonsson, B. & Martinou, J. C. Bax oligomerization in mitochondrial membranes requires tBid (caspase-8-cleaved Bid) and a mitochondrial protein. *Biochem. J.* **368**, 915-921 (2002).
218. Roucou, X., Rostovtseva, T., Montessuit, S., Martinou, J. C. & Antonsson, B. Bid induces cytochrome c-impermeable Bax channels in liposomes. *Biochem. J.* **363**, 547-552 (2002).
219. Terrones, O. *et al.* Lipidic pore formation by the concerted action of proapoptotic BAX and tBID. *J. Biol. Chem.* **279**, 30081-30091 (2004).
220. Gonzalez, F. *et al.* Mechanistic issues of the interaction of the hairpin-forming domain of tBid with mitochondrial cardiolipin. *PLoS. One.* **5**, e9342 (2010).
221. Jalmar, O., Garcia-Saez, A. J., Berland, L., Gonzalez, F. & Petit, P. X. Giant unilamellar vesicles (GUVs) as a new tool for analysis of caspase-8/Bid-FL complex binding to cardiolipin and its functional activity. *Cell Death. Dis.* **1**, e103 (2010).
222. Jalmar, O. *et al.* Caspase-8 binding to cardiolipin in giant unilamellar vesicles provides a functional docking platform for bid. *PLoS. One.* **8**, e55250 (2013).
223. Korytowski, W., Basova, L. V., Pilat, A., Kernstock, R. M. & Girotti, A. W. Permeabilization of the mitochondrial outer membrane by Bax/truncated Bid (tBid) proteins as sensitized by cardiolipin hydroperoxide translocation: mechanistic implications for the intrinsic pathway of oxidative apoptosis. *J. Biol. Chem.* **286**, 26334-26343 (2011).
224. Petit, P. X. *et al.* Interaction of the alpha-helical H6 peptide from the pro-apoptotic protein tBid with cardiolipin. *FEBS J.* **276**, 6338-6354 (2009).
225. Raemy, E. & Martinou, J. C. Involvement of cardiolipin in tBID-induced activation of BAX during apoptosis. *Chem. Phys. Lipids* **179**, 70-74 (2014).
226. De, P., V *et al.* Characterization of human VDAC isoforms: a peculiar function for VDAC3? *Biochim. Biophys. Acta* **1797**, 1268-1275 (2010).
227. Colombini, M., Yeung, C. L., Tung, J. & Konig, T. The mitochondrial outer membrane channel, VDAC, is regulated by a synthetic polyanion. *Biochim. Biophys. Acta* **905**, 279-286 (1987).
228. Konig, T. *et al.* Interaction of a synthetic polyanion with rat liver mitochondria. *Biochim. Biophys. Acta* **462**, 380-389 (1977).
229. Konig, T., Stipani, I., Horvath, I. & Palmieri, F. Inhibition of mitochondrial substrate anion translocators by a synthetic amphipathic polyanion. *J. Bioenerg. Biomembr.* **14**, 297-305 (1982).
230. Stein, C. A. & Colombini, M. Specific VDAC inhibitors: phosphorothioate oligonucleotides. *J. Bioenerg. Biomembr.* **40**, 157-162 (2008).



231. Han, D., Antunes, F., Canali, R., Rettori, D. & Cadenas, E. Voltage-dependent anion channels control the release of the superoxide anion from mitochondria to cytosol. *J. Biol. Chem.* **278**, 5557-5563 (2003).
232. Yao, H., Felfly, H., Wang, J., Zhou, D. & Haddad, G. G. DIDS protects against neuronal injury by blocking Toll-like receptor 2 activated-mechanisms. *J. Neurochem.* **108**, 835-846 (2009).
233. Inoue, H., Ohtaki, H., Nakamachi, T., Shioda, S. & Okada, Y. Anion channel blockers attenuate delayed neuronal cell death induced by transient forebrain ischemia. *J. Neurosci. Res.* **85**, 1427-1435 (2007).
234. Pamerter, M. E., Perkins, G. A., Gu, X. Q., Ellisman, M. H. & Haddad, G. G. DIDS (4,4-diisothiocyanatostilbenedisulphonic acid) induces apoptotic cell death in a hippocampal neuronal cell line and is not neuroprotective against ischemic stress. *PLoS. One.* **8**, e60804 (2013).
235. Himi, T., Ishizaki, Y. & Murota, S. I. 4,4'-diisothiocyano-2',2'-stilbenedisulfonate protects cultured cerebellar granule neurons from death. *Life Sci.* **70**, 1235-1249 (2002).
236. Maeno, E., Ishizaki, Y., Kanaseki, T., Hazama, A. & Okada, Y. Normotonic cell shrinkage because of disordered volume regulation is an early prerequisite to apoptosis. *Proc. Natl. Acad. Sci. U. S. A* **97**, 9487-9492 (2000).
237. Tauskela, J. S. *et al.* Protection of cortical neurons against oxygen-glucose deprivation and N-methyl-D-aspartate by DIDS and SITS. *Eur. J. Pharmacol.* **464**, 17-25 (2003).
238. Xue, J., Zhou, D., Yao, H. & Haddad, G. G. Role of transporters and ion channels in neuronal injury under hypoxia. *Am. J. Physiol Regul. Integr. Comp Physiol* **294**, R451-R457 (2008).
239. Geula, S., Naveed, H., Liang, J. & Shoshan-Barmatz, V. Structure-based analysis of VDAC1 protein: defining oligomer contact sites. *J. Biol. Chem.* **287**, 2179-2190 (2012).
240. Mader, A., Abu-Hamad, S., Arbel, N., Gutierrez-Aguilar, M. & Shoshan-Barmatz, V. Dominant-negative VDAC1 mutants reveal oligomeric VDAC1 to be the active unit in mitochondria-mediated apoptosis. *Biochem. J.* **429**, 147-155 (2010).
241. Zamzami, N., Brenner, C., Marzo, I., Susin, S. A. & Kroemer, G. Subcellular and submitochondrial mode of action of Bcl-2-like oncoproteins. *Oncogene* **16**, 2265-2282 (1998).
242. Shoshan-Barmatz, V. & Gincel, D. The voltage-dependent anion channel: characterization, modulation, and role in mitochondrial function in cell life and death. *Cell Biochem. Biophys.* **39**, 279-292 (2003).
243. Schubert, D. & Piasecki, D. Oxidative glutamate toxicity can be a component of the excitotoxicity cascade. *J. Neurosci.* **21**, 7455-7462 (2001).
244. Pusch, M., Zifarelli, G., Murgia, A. R., Picollo, A. & Babini, E. Channel or transporter? The CLC saga continues. *Exp. Physiol* **91**, 149-152 (2006).

245. Shoshan-Barmatz, V., Keinan, N., bu-Hamad, S., Tyomkin, D. & Aram, L. Apoptosis is regulated by the VDAC1 N-terminal region and by VDAC oligomerization: release of cytochrome c, AIF and Smac/Diablo. *Biochim. Biophys. Acta* **1797**, 1281-1291 (2010).
246. Öxler, E. M., Dolga, A. & Culmsee, C. AIF depletion provides neuroprotection through a preconditioning effect. *Apoptosis*. **17**, 1027-1038 (2012).
247. Bathori, G. *et al.* Extramitochondrial porin: facts and hypotheses. *J. Bioenerg. Biomembr.* **32**, 79-89 (2000).
248. De, P., V, Messina, A., Lane, D. J. & Lawen, A. Voltage-dependent anion-selective channel (VDAC) in the plasma membrane. *FEBS Lett.* **584**, 1793-1799 (2010).
249. Shoshan-Barmatz, V. & Israelson, A. The voltage-dependent anion channel in endoplasmic/sarcoplasmic reticulum: characterization, modulation and possible function. *J. Membr. Biol.* **204**, 57-66 (2005).
250. De, P., V *et al.* New functions of an old protein: the eukaryotic porin or voltage dependent anion selective channel (VDAC). *Ital. J. Biochem.* **52**, 17-24 (2003).
251. Cheng, E. H., Sheiko, T. V., Fisher, J. K., Craigen, W. J. & Korsmeyer, S. J. VDAC2 inhibits BAK activation and mitochondrial apoptosis. *Science* **301**, 513-517 (2003).
252. Setoguchi, K., Otera, H. & Mihara, K. Cytosolic factor- and TOM-independent import of C-tail-anchored mitochondrial outer membrane proteins. *EMBO J.* **25**, 5635-5647 (2006).
253. Fannjiang, Y. *et al.* BAK alters neuronal excitability and can switch from anti- to pro-death function during postnatal development. *Dev. Cell* **4**, 575-585 (2003).
254. Jakobson, M., Lintulahti, A. & Arumae, U. mRNA for N-Bak, a neuron-specific BH3-only splice isoform of Bak, escapes nonsense-mediated decay and is translationally repressed in the neurons. *Cell Death. Dis.* **3**, e269 (2012).
255. Jakobson, M., Jakobson, M., Llano, O., Palgi, J. & Arumae, U. Multiple mechanisms repress N-Bak mRNA translation in the healthy and apoptotic neurons. *Cell Death. Dis.* **4**, e777 (2013).
256. Doti, N. Personal Communication (2014)
257. Drzyzga, L. R., Marcinowska, A. & Obuchowicz, E. Antiapoptotic and neurotrophic effects of antidepressants: a review of clinical and experimental studies. *Brain Res. Bull.* **79**, 248-257 (2009).
258. Malkesman, O. *et al.* Targeting the BH3-interacting domain death agonist to develop mechanistically unique antidepressants. *Mol. Psychiatry* **17**, 770-780 (2012).
259. McKernan, D. P., Dinan, T. G. & Cryan, J. F. "Killing the Blues": a role for cellular suicide (apoptosis) in depression and the antidepressant response? *Prog. Neurobiol.* **88**, 246-263 (2009).
260. Yin, X. M. *et al.* Bid-deficient mice are resistant to Fas-induced hepatocellular apoptosis. *Nature* **400**, 886-891 (1999).

261. Zinkel, S. S. *et al.* Proapoptotic BID is required for myeloid homeostasis and tumor suppression. *Genes Dev.* **17**, 229-239 (2003).
262. Mohammad, R., Giri, A. & Goustin, A. S. Small-molecule inhibitors of Bcl-2 family proteins as therapeutic agents in cancer. *Recent Pat Anticancer Drug Discov.* **3**, 20-30 (2008).
263. Porter, J. *et al.* Tetrahydroisoquinoline amide substituted phenyl pyrazoles as selective Bcl-2 inhibitors. *Bioorg. Med. Chem. Lett.* **19**, 230-233 (2009).
264. McPherson, A. & DeLucas, L. Crystal-growing in space. *Science* **283**, 1459 (1999).
265. Landsberg, M. J., Bond, J., Gee, C. L., Martin, J. L. & Hankamer, B. A method for screening the temperature dependence of three-dimensional crystal formation. *Acta Crystallogr. D. Biol. Crystallogr.* **62**, 559-562 (2006).
266. McPherson, A. Crystallization of proteins by variation of pH or temperature. *Methods Enzymol.* **114**, 125-127 (1985).
267. McPherson, A. Crystallization of macromolecules: general principles. *Methods Enzymol.* **114**, 112-120 (1985).
268. McPherson, A. & Kuznetsov, Y. G. Mechanisms, kinetics, impurities and defects: consequences in macromolecular crystallization. *Acta Crystallogr. F. Struct. Biol. Commun.* **70**, 384-403 (2014).
269. Chayen, N. E. Comparative studies of protein crystallization by vapour-diffusion and microbatch techniques. *Acta Crystallogr. D. Biol. Crystallogr.* **54**, 8-15 (1998).
270. Rayment, I. Small-scale batch crystallization of proteins revisited: an underutilized way to grow large protein crystals. *Structure.* **10**, 147-151 (2002).
271. Smits, S. H., Mueller, A., Grieshaber, M. K. & Schmitt, L. Coenzyme- and His-tag-induced crystallization of octopine dehydrogenase. *Acta Crystallogr. Sect. F. Struct. Biol. Cryst. Commun.* **64**, 836-839 (2008).
272. Lee, E. F. *et al.* Crystal structure of ABT-737 complexed with Bcl-xL: implications for selectivity of antagonists of the Bcl-2 family. *Cell Death. Differ.* **14**, 1711-1713 (2007).
273. Petros, A. M. *et al.* Fragment-based discovery of potent inhibitors of the anti-apoptotic MCL-1 protein. *Bioorg. Med. Chem. Lett.* **24**, 1484-1488 (2014).
274. Zhou, H. *et al.* Design of Bcl-2 and Bcl-xL inhibitors with subnanomolar binding affinities based upon a new scaffold. *J. Med. Chem.* **55**, 4664-4682 (2012).
275. Perfettini, J. L., Roumier, T. & Kroemer, G. Mitochondrial fusion and fission in the control of apoptosis. *Trends Cell Biol.* **15**, 179-183 (2005).
276. Suen, D. F., Norris, K. L. & Youle, R. J. Mitochondrial dynamics and apoptosis. *Genes Dev.* **22**, 1577-1590 (2008).
277. Zamzami, N. & Kroemer, G. The mitochondrion in apoptosis: how Pandora's box opens. *Nat. Rev. Mol. Cell Biol.* **2**, 67-71 (2001).
278. Gonzalez, F. & Gottlieb, E. Cardiolipin: setting the beat of apoptosis. *Apoptosis.* **12**, 877-885 (2007).

279. Kagan, V. E. *et al.* Cytochrome c acts as a cardiolipin oxygenase required for release of proapoptotic factors. *Nat. Chem. Biol.* **1**, 223-232 (2005).
280. Gonzalez, F., Bessoule, J. J., Rocchiccioli, F., Manon, S. & Petit, P. X. Role of cardiolipin on tBid and tBid/Bax synergistic effects on yeast mitochondria. *Cell Death. Differ.* **12**, 659-667 (2005).
281. Gonzalez, F. *et al.* tBid interaction with cardiolipin primarily orchestrates mitochondrial dysfunctions and subsequently activates Bax and Bak. *Cell Death. Differ.* **12**, 614-626 (2005).
282. Yethon, J. A., Epand, R. F., Leber, B., Epand, R. M. & Andrews, D. W. Interaction with a membrane surface triggers a reversible conformational change in Bax normally associated with induction of apoptosis. *J. Biol. Chem.* **278**, 48935-48941 (2003).
283. Lucken-Ardjomande, S., Montessuit, S. & Martinou, J. C. Bax activation and stress-induced apoptosis delayed by the accumulation of cholesterol in mitochondrial membranes. *Cell Death. Differ.* **15**, 484-493 (2008).
284. Iverson, S. L., Enoksson, M., Gogvadze, V., Ott, M. & Orrenius, S. Cardiolipin is not required for Bax-mediated cytochrome c release from yeast mitochondria. *J. Biol. Chem.* **279**, 1100-1107 (2004).
285. Polcic, P. *et al.* Cardiolipin and phosphatidylglycerol are not required for the in vivo action of Bcl-2 family proteins. *Cell Death. Differ.* **12**, 310-312 (2005).
286. Liu, J., Weiss, A., Durrant, D., Chi, N. W. & Lee, R. M. The cardiolipin-binding domain of Bid affects mitochondrial respiration and enhances cytochrome c release. *Apoptosis.* **9**, 533-541 (2004).
287. Van, M. N., Kajava, A. V., Bonfils, C., Martinou, J. C. & Harricane, M. C. Interactions of Bax and tBid with lipid monolayers. *J. Membr. Biol.* **207**, 1-9 (2005).
288. Satsoura, D. *et al.* Interaction of the full-length Bax protein with biomimetic mitochondrial liposomes: a small-angle neutron scattering and fluorescence study. *Biochim. Biophys. Acta* **1818**, 384-401 (2012).
289. Epand, R. F., Martinou, J. C., Fornallaz-Mulhauser, M., Hughes, D. W. & Epand, R. M. The apoptotic protein tBid promotes leakage by altering membrane curvature. *J. Biol. Chem.* **277**, 32632-32639 (2002).
290. Terrones, O. *et al.* BIM and tBID are not mechanistically equivalent when assisting BAX to permeabilize bilayer membranes. *J. Biol. Chem.* **283**, 7790-7803 (2008).
291. Ott, M., Norberg, E., Zhivotovsky, B. & Orrenius, S. Mitochondrial targeting of tBid/Bax: a role for the TOM complex? *Cell Death. Differ.* **16**, 1075-1082 (2009).
292. Shimizu, S. & Tsujimoto, Y. Proapoptotic BH3-only Bcl-2 family members induce cytochrome c release, but not mitochondrial membrane potential loss, and do not directly modulate voltage-dependent anion channel activity. *Proc. Natl. Acad. Sci. U. S. A* **97**, 577-582 (2000).
293. Banerjee, J. & Ghosh, S. Bax increases the pore size of rat brain mitochondrial voltage-dependent anion channel in the presence of tBid. *Biochem. Biophys. Res. Commun.* **323**, 310-314 (2004).

294. Wangemann, P. *et al.* Cl(-)-channel blockers in the thick ascending limb of the loop of Henle. Structure activity relationship. *Pflugers Arch.* **407 Suppl 2**, S128-S141 (1986).
295. Pamenter, M. E. *et al.* DIDS prevents ischemic membrane degradation in cultured hippocampal neurons by inhibiting matrix metalloproteinase release. *PLoS. One.* **7**, e43995 (2012).
296. Chandra, D., Choy, G., Daniel, P. T. & Tang, D. G. Bax-dependent regulation of Bak by voltage-dependent anion channel 2. *J. Biol. Chem.* **280**, 19051-19061 (2005).
297. Landshamer, S. Thesis/Dissertation (2007)
298. Roy, M. J., Vom, A., Czabotar, P. E. & Lessene, G. Cell death and the mitochondria: therapeutic targeting of the BCL-2 family-driven pathway. *Br. J. Pharmacol.*(2013).

## 10 Index of Tables

Table 1: Primers used for RT-PCR.....	21
Table 2: Kits .....	23
Table 3: Materials for protein purification.....	24
Table 4: Materials for protein crystallization.....	25
Table 5: Sterile plastic ware.....	25
Table 6: HT-22 standard growth medium.....	27
Table 7: Phosphate buffered saline (PBS), pH 7.4 .....	27
Table 8: Standard Trypsin/EDTA solution.....	27
Table 9: HT-22 cells – cell densities .....	28
Table 10: 5% PEI .....	28
Table 11: Neurobasal medium.....	29
Table 12: Hank´s balanced salt solution (1 x HBSS) ph 7.2.....	30
Table 13: Eagle´s minimum essential medium (MEM) .....	30
Table 14: Protein lysis stock-buffer for HT-22 cells; pH 7.8 .....	45
Table 15: Protein Lysis Buffer for primary neurons and brain tissue; pH 7.4.....	46
Table 16: Stacking gel 3.5 %.....	49
Table 17: Running gel 12.5 % .....	50
Table 18: 5 x SDS-loading buffer.....	50
Table 19: 1 x Electrophoresis buffer .....	50
Table 20: 1 x 10 % Transfer buffer (Semi-Dry-Blotting), pH 8.3 .....	51
Table 21: 1 x 20% Transfer buffer (Tank-Blotting), pH 8.3.....	51
Table 22: 1 x TBS/Tween 20, pH 7.5.....	51
Table 23: 5 % Blocking buffer.....	51
Table 24: Stripping buffer, pH 2.....	52
Table 25: PCR sample preparation: VDAC1, VDAC2, Bid .....	54
Table 26: PCR sample preparation GAPDH .....	54
Table 27: RT-PCR cyler program – murine GAPDH .....	55
Table 28: RT-PCR cyler program – murine VDAC1 .....	55
Table 29: RT-PCR cyler program – murine VDAC2 .....	55
Table 30: RT-PCR cyler program – murine Bid.....	56
Table 31: PCR sample preparation - G12-mBid, A13-mBid .....	60
Table 32: PCR sample preparation - Y47-mBid, D51-mBid .....	60
Table 33: RT-PCR Cyler program – G12-mBid and A13-mBid.....	61
Table 34: RT-PCR Cyler program – Y47-mBid and D51-mBid.....	61
Table 35: PCR sample preparation- A13-mBid constructs.....	62
Table 36: RT-PCR Cyler program A13-mBid constructs .....	63

Table 37: Protein standard lysis buffer .....	66
Table 38: Protein lysis buffer for GSTrap purification.....	66
Table 39: Buffer for His-Catcher Nickel Gravity Columns (PJK GmbH) .....	67
Table 40: Buffer for HisTrap affinity columns (HisTrap™ FF 5 ml).....	68
Table 41: Buffer for GSTrap affinity columns and Glutathione and HiCap Cartridges .....	68
Table 42: Buffer for HiTrap ion exchange columns (HiTrap Q HP, 5 ml) .....	69
Table 43: Buffer for HiLoad gel filtration columns (HiLoad™ 16/600 Superdex 75 pg) .....	69
Table 44: Programmed method for ÄKTA- wash and storage.....	70
Table 45: Programmed method for ÄKTA - IMAC- Ni-Affinity chromatography .....	72
Table 46: Programmed method for ÄKTA – Ion Exchange Gradient elution .....	73
Table 47: Programmed method for ÄKTA – Gel filtration (full-length Bid) .....	74
Table 48: Programmed method for ÄKTA – sample application.....	75
Table 49: ÄKTA installed method – GST-tagged purification GSTrap.....	76
Table 50: Programmed method for ÄKTA – GST-affinity chromatography.....	76
Table 51: Programmed method for ÄKTA – Gel filtration (Bid constructs).....	77
Table 52: Molar extinction coefficients and A280 factors .....	81
Table 53: Lipids (Avanti Polar lipids).....	82
Table 54: Initial screens and set ups tested for the different Bid constructs .....	90
Table 55: Optimization of Bid 22 crystals I, 4°C + 18°C .....	91
Table 56: Optimization of Bid 22 crystals II, 4°C + 18°C .....	91
Table 57: Optimization of Bid construct 1 I, 21°C.....	92
Table 58: Optimization of Bid construct 1 II, 21°C.....	92
Table 59: Opti-Grid 96 of Bid construct 1 I, 4°C + 18°C .....	92
Table 60: Opti-Grid 96 of Bid construct 1 II, 4°C + 18°C .....	93
Table 61: Scoring system used for interpretation of crystallization drop results .....	95
Table 62: Neuroprotective properties of <i>N</i> -acyl phenoxyanilines. ....	107
Table 63: Neuroprotective properties of <i>N</i> -phenyl substituted thiazolidinediones.....	118
Table 64: Neuroprotective properties of <i>N</i> -aryl substituted pyrazolopyrimidinone (19).....	129
Table 65: Gene alignment of novel Bid constructs and mouse full-length Bid .....	141
Table 66: Statistics for data collection and processing for Bid 1. ....	149
Table 67: Neuroprotective properties of 4-phenoxyanilines .....	237
Table 68: Neuroprotective properties of isonipecotic acid derivatives .....	239
Table 69: Neuroprotective properties of <i>N</i> -phenyl substituted thiazolidindiones.....	244
Table 70: Neuroproctive properties of miscellaneous chemical compounds. ....	249

## 11 Index of Figures

Figure 1: Intrinsic and extrinsic pathways of apoptotic cells death. ....	3
Figure 2: Simplified overview of the Bcl-family proteins. ....	6
Figure 3: Molecular structure and protease-cleavage sites of Bid. ....	8
Figure 4: Structures of Bid-binding fragments and the resulting Bid inhibitors. ....	12
Figure 5: Simplified model of glutamate-induced toxicity in HT-22 cells. ....	16
Figure 6: Chemical structure of the Bid inhibitor BI-6c9. ....	32
Figure 7: Chemical structure of 4,4'-Diisothio-cyanatostilbene-2,2'-disulfonic acid (DIDS). ....	32
Figure 8: Reduction of yellow MTT to purple colored formazan. ....	35
Figure 9: Formation of light from ATP and luciferin. ....	37
Figure 10: Mito Stress Profile. ....	38
Figure 11: Vapor-diffusion techniques: A) sitting-drop, B) hanging-drop. ....	88
Figure 12: Neuroprotective potency of BI-6c9 – half maximal effective concentration. ....	100
Figure 13: tBid-induced cell death in HT-22 cells. ....	102
Figure 14: tBid-induced loss of $\Delta\psi_m$ is prevented by BI-6c9. ....	103
Figure 15: Synthesis strategy for development of novel Bid inhibitors. ....	105
Figure 16: Structures of fragment BI-2A7 and the replacement 4-phenoxyaniline. ....	106
Figure 17: Neuroprotective activity of compound 6 in HT-22 cells exposed to glutamate. ....	108
Figure 18: Neuroprotective activities of compounds 8 and 9 against glutamate-induced cell death. ....	109
Figure 19: Compound 11 provides neuroprotection against glutamate-induced cell death. ....	110
Figure 20: Molecular docking of compounds 8 and 11 into the 3D-structure of Bid. ....	111
Figure 21: Real-time detection of cellular impedance confirms neuroprotective properties of <i>N</i> -acyl-phenoxyanilines. ....	112
Figure 22: Neuroprotective activities of <i>N</i> -acyl-phenoxyanilines against tBid-induced neuronal cell death. ....	114
Figure 23: <i>N</i> -acyl-phenoxyanilines provide slightly protective effects against tBid-induced toxicity in low concentrations as 1 $\mu$ M. ....	115
Figure 24: Concentration-dependent toxic effects of <i>N</i> -acyl-phenoxyanilines. ....	115
Figure 25: Development of thiazolidine-2,4-dione structure 13 based on the structure of BI-6C9 (5). ....	117
Figure 26: <i>N</i> -phenyl substituted thiazolidinediones provide maximal neuroprotection at concentrations of 20 $\mu$ M and higher. ....	119
Figure 27: <i>N</i> -Phenyl substituted thiazolidinediones provide neuroprotection against glutamate-induced toxicity. ....	121
Figure 28: Real time monitoring of cell impedance confirms concentration-dependent neuroprotection mediated by thiazolidindiones. ....	122



Figure 29: <i>N</i> -Phenyl substituted thiazolidinediones attenuate tBid-induced neuronal cell death.....	124
Figure 30: 2D and 3D-representation of the binding mode of compound 13 for inhibition of Bid.....	125
Figure 31: <i>N</i> -Phenyl substituted thiazolidinediones preserve mitochondrial integrity and function. ....	126
Figure 32: <i>N</i> -Phenyl substituted thiazolidinediones preserve mitochondrial respiration .....	128
Figure 33: <i>N</i> -aryl substituted pyrazolopyrimidinone protects against glutamate-induced toxicity in a concentration dependent manner.....	130
Figure 34: Compound 19 prevents tBid-induced neuronal cell death. ....	131
Figure 35: Effective expression of full length Bid. ....	133
Figure 36: Purification of full length Bid by Äkta-chromatography. ....	135
Figure 37: Purified His <sub>6</sub> -Bid. ....	135
Figure 38: Gel filtration of full length His <sub>6</sub> -Bid.....	136
Figure 39: Recovery of full-length Bid during chromatography purification and MALDI-TOF analysis. ....	137
Figure 40: Highly flexible regions of full-length Bid .....	140
Figure 41: Strategy for design of novel truncated Bid constructs. ....	140
Figure 42: Effective expression of truncated Bid constructs.....	142
Figure 43: Purification of Bid 1 (pGEX-Δ12-Y47).....	144
Figure 44: MALDI-TOF analysis of Bid1 (pGEX-Δ12-Y47).....	145
Figure 45: Successful result of Bid 1 crystallization. ....	146
Figure 46: Bid 1 crystals obtained from opti grid conditions. ....	147
Figure 47: Bid 1 crystals used for data collection and typical diffraction pattern.....	149
Figure 48: Purification of Bid 2 (pGEX-Δ12-D51).....	150
Figure 49: MALDI-TOF analysis of purified Bid 2 (pGEX-Δ12-D51).....	151
Figure 50: Purification of highly pure Bid 4 protein (pGEX-Δ13-D51).....	152
Figure 51: MALDI-TOF analysis of purified Bid 4 (pGEX-Δ13-D51).....	153
Figure 52: Functional analysis of Bid constructs. ....	155
Figure 53: Liposome channel activity assay as model system for membrane permeabilization. ....	157
Figure 54: Cleavage of full-length Bid with caspase 8.....	158
Figure 55: Permeabilization of cardiolipin-containing liposomes is induced by Bid in a concentration dependent manner, but not by full-length Bid. ....	159
Figure 56: cBid-mediated permeabilization of cardiolipin-containing liposomes is increased by pre-incubation with Bax, and slightly reduced by the Bid inhibitor BI6c9. ....	161
Figure 57: Expression levels of VDAC1 and VDAC2 in HT-22 cells.....	163

Figure 58: DIDS protects against glutamate-induced toxicity. ....	165
Figure 59: DIDS attenuates apoptotic and necrotic cell death. ....	166
Figure 60: The anion channel blocker DIDS maintains mitochondrial energy metabolism and respiratory activity. ....	168
Figure 61: DIDS prevents glutamate-induced ROS formation. ....	169
Figure 62: DIDS prevents mitochondrial fission and loss of $\Delta\psi_m$ . ....	172
Figure 63: tBid-induced toxicity in HT-22 cells is prevented by DIDS. ....	173
Figure 64: DIDS prevents tBid-induced loss of $\Delta\psi_m$ . ....	174
Figure 65: Direct interaction between recombinant Bid/tBid and VDAC1. ....	175
Figure 66: Thermophoresis measurements revealed $K_D$ values for Bid/tBid binding to VDAC1. ....	176
Figure 67: tBid promotes a reduction in the VDAC1 channel's conductances, while DIDS triggers VDAC1 closure. ....	178
Figure 68: Direct interaction of Bid and VDAC1 after the onset of glutamate exposure in HT-22 cells. ....	180
Figure 69: Direct interaction between Bid and VDAC1 in primary cortical neurons. ....	181
Figure 70: Direct interaction of Bid and VDAC1 during ischemic brain damage <i>in vivo</i> . ....	182
Figure 71: VDAC1 knockdown by different VDAC1 sequences attenuates glutamate-induced toxicity in HT-22 cells. ....	184
Figure 72: VDAC1 depletion prevents glutamate-induced cell death. ....	186
Figure 73: VDAC1 deficiency maintains mitochondrial energy metabolism and respiration. ....	187
Figure 74: Glutamate-induced ROS production is prevented by VDAC1 silencing. ....	189
Figure 75: VDAC1 depletion prevents glutamate-induced mitochondrial fission. ....	191
Figure 76: Preservation of mitochondrial membrane potential by VDAC1 gene silencing. ....	192
Figure 77: VDAC1 siRNA 1 and siRNA 2 prevent tBid-induced toxicity. ....	194
Figure 78: VDAC1 silencing prevents tBid-induced loss of $\Delta\psi_m$ . ....	195
Figure 79: Mitochondrial localization of FLAG-VDAC1. ....	197
Figure 80: VDAC1 induced cytotoxicity is inhibited by the Bid inhibitor BI6c9. ....	198
Figure 81: VDAC2 gene silencing by two different VDAC2 siRNA sequences. ....	200
Figure 82: VDAC2 knockdown by different VDAC2 siRNA sequences provides slight protection against glutamate toxicity. ....	202
Figure 83: VDAC2 siRNA attenuates glutamate-induced cell death in a concentration-dependent manner. ....	203
Figure 84: Mitochondrial membrane potential is only slightly affected by VDAC2 silencing. ....	205
Figure 85: Workflow from construct design to protein crystallography. ....	212
Figure 86: Proposed model of the direct interaction of Bid and VDAC1. ....	224

Figure 87: Proposed role of VDAC1 and Bid in neuronal apoptosis based on the findings in the glutamate-toxicity model in HT-22 cells. ....227

## 12 Publications

### 12.1.1 Original papers

**S. Oppermann**, F. Schrader, K. Elsässer, A.M. Dolga, L. Krause, N. Doti, C. Wegscheid-Gerlach, M. Schlitzer, C. Culmsee, *Novel N-Phenyl substituted thiazolidinediones protect neuronal cells against glutamate- and tBid-induced toxicity.* (resubmitted)

**S. Oppermann**, M.T. Barho, K., F.Schrader, I. Degenhardt, K. Elsässer, C. Wegscheid-Gerlach, C. Culmsee, M. Schlitzer, *N-Acyl derivatives of phenoxyaniline as novel neuroprotective agents.* (submitted)

**S. Oppermann**, B. Mertins, K. Elsässer, C. Krasel, G. Psakis, P. Reiß, A.M. Dolga, M. Bünemann, L.O. Essen, C. Culmsee, *Interaction of tBid and VDAC1 determines mitochondrial demise.* (submitted)

### 12.1.2 Poster presentations

#### 2014

**S. Oppermann**, B. Mertins, C. Krasel, L. Meissner, G. Psakis, P. Reiß, A.M. Dolga, N. Plesnila, M. Bünemann, L.O. Essen, C. Culmsee, The interaction of Bid and VDAC1 is essential for neuronal cell death in vitro and in vivo, *8<sup>th</sup> International Symposium on Neuroprotection and Neurorepair*, Magdeburg, Germany **(2014)**

**S. Oppermann**, B. Mertins, L. Meissner, C. Krasel, G. Psakis, P. Reiß, A.M. Dolga, N. Plesnila, M. Bünemann, L.O. Essen, C. Culmsee, Interaction of Bid and VDAC1 determines mitochondrial demise, *Keystone Symposia on mitochondrial Dynamics and Physiology*, Santa Fe, NM, USA **(2014)**

#### 2013

**S. Oppermann**, B. Mertins, C. Krasel, M. Bünemann, L.O. Essen, C. Culmsee, The interaction of tBid with VDAC1 is essential for mitochondrial damage in intrinsic death pathways, *The Cold Spring Harbor Meeting on Cell Death*, Cold Spring Harbor - New York, USA **(2013)**

B. Mertins, G. Psakis, **S. Oppermann**, K. Sivaraman, P. Reiss, C. Krasel, U. Koert, C. Culmsee, L.O. Essen, Conformational flexibility of VDAC and the influence of effectors, *Molecular life science, Gesellschaft für Biochemie und Molekularbiologie (GBM)*, Frankfurt, Germany **(2013)**

**S. Oppermann**, B. Mertins, G. Psakis, S. Schneider, C. Krasel, M. Bünemann, L.O. Essen, C. Culmsee, VDAC1 mediated neuronal cell death requires tBid, *21<sup>th</sup> ECDO Euroconference on Apoptosis*, Paris, France (2013)

**S. Oppermann**, K. Elsässer, F. Schrader, C. Krasel, A.M. Dolga, M. Bünemann, M. Schlitzer, N. Plesnila, C. Culmsee, Novel small molecules provide protection against glutamate and tBid induced toxicity in neuronal hippocampal cells, *21<sup>th</sup> ECDO Euroconference on Apoptosis*, Paris, France (2013)

**S. Oppermann**, S. Schneider, C. Culmsee, The role of VDAC in glutamate toxicity and tBid-induced cell death in HT-22 cells, *Tag der Pharmazie*, Marburg, Germany (2013)

**S. Oppermann**, F. Schrader, K. Elsässer, C. Krasel, H. Steuber, M. Bünemann, M. Schlitzer, N. Plesnila, C. Culmsee, Small molecule inhibitors of the BH3- only protein Bid as novel therapeutic agents in neurodegenerative diseases, *Science to market 2013, European Association of Pharma Biotechnology (EABP)*, Cologne, Germany (2013)

## 2012

**S. Oppermann**, J. Grohm, F. Schrader, C. Krasel, M. Bünemann, M. Schlitzer, G. Klebe, N. Plesnila, C. Culmsee, Novel small molecule inhibitors of Bid provide neuroprotection in vitro, *Annual Meeting of the American Society of Neuroscience*, New Orleans, USA (2012)

**S. Oppermann**, J. Grohm, F. Schrader, C. Krasel, M. Bünemann, M. Schlitzer, N. Plesnila, C. Culmsee, Small molecule Bid inhibitors prevent Drp1- dependent mitochondrial fission and cell death in neurons, *7<sup>th</sup> International Symposium on Neuroprotection and Neurorepair*, Potsdam, Germany (2012)

**S. Oppermann**, K. Elsässer, F. Schrader, S. Glinca, C. Krasel, M. Bünemann, G. Klebe, M. Schlitzer, C. Culmsee, Development of novel Bid inhibitors for therapeutic approaches in models of neuronal cell death, *78. Jahrestagung der Deutschen Gesellschaft für Experimentelle und Klinische Pharmakologie und Toxikologie (DGPT)*, Dresden, Germany (2012)

**S. Oppermann**, K. Elsässer, J. Grohm, F. Schrader, S. Glinca., G. Klebe, M. Schlitzer, C. Culmsee, Development of novel Bid inhibitors for the treatment of neurodegenerative diseases, *Tag der Wissenschaft, MARA*, Marburg, Germany (2012)

**S. Oppermann**, C. Reuther, E.M. Öxler, A.M. Dolga and C. Culmsee, Schädigungsmechanismen in Mitochondrien als neue therapeutische Ansatzpunkte der Neuroprotektion, *Tag der Wissenschaft, MARA*, Marburg, Germany (2012)

## 2011

**S. Oppermann**, K. Elsässer, J. Grohm, F. Schrader, S. Glinca., G. Klebe, M. Schlitzer, C. Culmsee, Development of novel Bid inhibitors for the treatment of neurodegenerative diseases, *Joint meeting of the Austrian and German pharmaceutical societies (DphG)*, Innsbruck, Austria **(2011)**

### 12.1.3 Oral presentations

“Small molecule inhibitors of the BH3-only protein Bid as novel therapeutic agents in neurodegenerative diseases”, *Science to market 2013*, European Association of Pharma Biotechnology (EABP), Cologne, Germany (Selected abstract for oral presentation) **(2013)**

“Evaluation of novel Bid- Inhibitors for therapy of neurodegenerative disease”, oral presentation, Group of Prof Jean-Claude Martinou, University of Geneva, Geneva, Switzerland (Invited) **(2011)**

## 13 Grants

Conference Grant by Cold Spring Harbor Laboratory for research on “The interaction of tBid with VDAC1 is essential for mitochondrial damage in intrinsic death pathways” presented at the CSHL cell death meeting, Cold Spring Harbor, New York. **(2013)**

Travel Award by the Seahorse Bioscience for research on “Novel small molecules provide protection against glutamate and tBid induced toxicity in neuronal hippocampal cells” presented at the 21<sup>st</sup> ECDO Euroconference on Apoptosis, Institut Pasteur, Paris, France. **(2013)**

## 14 Acknowledgements

First and foremost, I would like to express my sincere thanks to my supervisor Prof. Dr. Carsten Culmsee who offered me the fantastic opportunity to work in his lab as a PHD. Within a great and ambitious theme, he gave me not only the possibility to explore exciting scientific questions but also enables me to utilize an amazing range of diverse methods, expanding my horizon to crazy fields that I never would have thought to touch, before starting this thesis. He gave me a lot of free space for own ideas, supported me and my projects in an excellent manner and always had an open door and time for critical discussions. I greatly appreciate the chance he gave me to attend several national and international meetings, which gained me insight into the exciting news in research, and which were always pleasant and unforgettable events, especially the “NY Cold Spring Harbor Cell Death meeting” as a contributing factor for my continued scientific progress. Thank you very much for this!

I would also like to say a big thank to all my collaboration partners. First of all, I would like thank Cornelius Krasel, who always supported me within the “purification and crystallization” project and always had time for questions. He managed to calm me down in any critical “Äkta” situation and helped me to exercise patient during crystal growth, always believing in the day where the crystal diffracts to high resolution. At this point I also want to thank Prof. Dr. Klebe and Dr. Holger Steuber for the possibility to use the crystallization approaches and to join the crazy sleepless synchrotron trips!

I further would like to thank Prof. Dr. Schlitzer for giving me the nice opportunity to work on the development of novel promising Bid inhibitors. I thank Florian Schrader, Marlene Barho and Lena Krause for all the structure syntheses and Dr. Wegscheid-Gerlach for the nice docking solutions and support in paper revision!

I also would like to mention Prof. Dr. Essen and his group members Barbara Mertins and George Psakis, who gave me the great possibility for collaboration within the Bid-VDAC project. I want to thank all of them for the always uncomplicated teamwork, the fruitful meetings, the BLM and thermophoresis data and for carefully editing the manuscript! I am looking forward to Bid-VDAC crystals and a continued collaboration!

A special thank goes to Prof. Nick Plesnila for the possibility for *in vivo* studies, his critical comments on the manuscript and projects and the pleasant time together with Carsten within the Neuroscience conference in New Orleans and the Neurorepair and neuroprotection meeting in Potsdam! Thanks also for the very funny skiing event together with your and our group! I will never forget the “frying pan race” and this huge amount of rice pudding!

I also want to thank all my colleagues and friends, not only in the Culmsee’s lab but also in the Bünemann’s and Kockskämper’s lab! Thank you for your support, your motivation and

constructive discussions regarding research, but also for the good atmosphere in the lab! Especially I want to thank Sebastian, Eva and Maren for being my calming influence on crazy days, for joining the long evenings in the lab and for all the talks we had! I thank Amalia for her great support in paper submission and revision, her big support especially in the last months, as well as for all the nice talks and delicious dinners. Thank you Diana for the tea breaks and our “each other reminder” just in the right time and always with the words “wir schaffen das”. Thank you Maren for all the funny zumba hours, the motivation for the powerful fitness trainings as well as for the private events in the areas around Marburg! Special thanks go also to the “old” group, Julia, Svenja, Sebastian, Anderson, Steffi, Eva and Christina for the good time we had in and outside of the lab, and particularly for all the amazing and periodic meetings throughout whole Germany! I am always looking forward to seeing you again! I thank also my whole lab and especially my office members, for all the funny “pink” situations! Without you I would have never known that everything I touch is pink!

Special thank goes to Katharina and Eileen not only for their excellent technical support but also for the very nice and always refreshing teamwork, and particularly I want to say big thanks to Katharina for her incommensurable help with the first screening of all those small-molecules! I am pretty sure the day will come where the “Joker” substance will appear!

Thank you Emma and Niki for all your support and help with the bureaucratic affairs you managed for me! Thank you Emma for all your critical proof readings of the paper manuscripts as well as for carefully editing this thesis!

I would also like to say thank you to all my “Wahlpflichtfach”-students, who did an excellent job during their time in our lab and supported my work with new enthusiasm and nice results!

Very special thanks to all the friends of mine who always believed in me, supported me outside of the lab and who were always there even without seeing them! Especially, I want to thank you Sina M., Jasmin H., Julia St., Angi G., Silvia P. and Nicole N. for the funny weekend events and phone calls which let me shortly forget the lab! Thank you for always fully understanding my rare time during my research!

Finally I want to say very special thanks to my parents, who supported me wherever possible and always gave me new strength to go on! Thank you for your open door in any time, your open ears in any situation, your incommensurable believe in me and your right words that build me up! I also want to thank my brother Denni and my sisters Anika and Larissa for always believing in me, even without understanding why I am doing “this crazy research stuff” and for all the nice and funny coming together’s at our parents house, which brought me always back down! Cause of you all, I always have a smile in my face when driving back home! Without my family’s support, I would never have been able to complete this thesis!



## 15 Curriculum vitae

### Personal details

Date of birth: 21.05.1986

Place of birth: Haiger, Germany

### Education and career

03/2011 – today	PhD thesis at the Department of Pharmacology and Clinical Pharmacy, Philipps University of Marburg, Germany supervisor: Prof. Dr. Carsten Culmsee
01/2011	Approbation pharmacist
06/2010-03/2011	Temporary job at Hirsch-Apotheke Frankfurt and Central-Apotheke Steinbach, Germany
05/2010-11/2010	Research internship at Merck Serono Darmstadt, Department of Exploratory Development NBE, Darmstadt, Germany
11/2009-05/2010	Pharmacy internship at Hirsch-Apotheke, Frankfurt and Central-Apotheke, Steinbach, Germany
10/2005-10/2009	Studies of pharmacy, Faculty of Pharmacy, Johann-Wolfgang-Goethe-University, Frankfurt, Germany
08/2002-06/2005	Secondary school, Johanneum Gymnasium, Herborn, Germany
08/1996-07/2002	Secondary school, Johann-Textor Gymnasium Haiger, Germany
08/1992-07/1996	Elementary school, Grundschule Langenaubach, Haiger, Germany



